High-Level Coupled-Cluster Characterization of Ethynyl Radical Reactions and Other Small Challenging Molecules

by

Michael Charles Bowman

(Under the Direction of Henry F. Schaefer III)

Abstract

For small molecular systems, convergent quantum chemical methods may be employed to obtain results rivaling experimental accuracy. The first project in this dissertation presents an in-depth methodological study of the gas-phase methyl anion (CH_3^-) with its peculiar basis set dependence. The next project characterizes various constitutional isomers of Ca_2H_2 and Ca_2H_4 with highly accurate coupled-cluster methods and second order vibrational perturbation theory (VPT2). The third project examines the mechanism of the reaction between the ubiquitous ethynyl radical (C_2H) and molecular oxygen (O_2), employing both coupled-cluster methods as well as multi-reference configuration interaction. The fourth project likewise examines reactions with ethnynl radical, but with a focus on hydrogen-abstractions that may occur with various H-atom donors instead. The final chapter summarizes key observations from these computational studies.

INDEX WORDS: Computational Chemistry, Electronic Structure Theory,
Coupled-Cluster Theory, Focal Point Analysis, Basis Set Extrapolation,
Methyl Anion, Calcium Hydride, Ethynyl Radical, Hydrogen
Abstraction

High-Level Coupled-Cluster Characterization of Ethynyl Radical Reactions and Other Small Challenging Molecules

by

Michael Charles Bowman

B.S., Huntington University, 2017

A Dissertation Submitted to the Graduate Faculty of the
University of Georgia in Partial Fulfillment of the Requirements for the Degree.

Doctor of Philosophy

Athens, Georgia

2020

High-Level Coupled-Cluster Characterization of Ethynyl Radical Reactions and Other Small Challenging Molecules

by

Michael Charles Bowman

Major Professor: Henry F. Schaefer

Committee: Gary E. Douberly

Steven E. Wheeler

Electronic Version Approved:

Ron Walcott

Interim Dean of the Graduate School

The University of Georgia

May 2020

Dedication

To my beautiful wife Christine and my precious son Daniel.

I love you both very deeply.

Acknowledgments

The publication of this dissertation has been made possible by numerous friends, colleagues, and family members. I am truly blessed to be surrounded by so many people that have encouraged and supported my graduate work and I would like to briefly mention their contributions:

- First and foremost, I would like to acknowledge my Lord and Savior. Every ounce of intellect and moment of clarity I have is the result of divine grace.

- My parents, Dan and Georgann Bowman. They have always encouraged me to utilize the skills I have been given to honor God.

- My professors at Huntington University were instrumental in the development of my academic interests. I want to specifically thank Dr. Ruth Nalliah, Dr. Timothy Troyer, Dr. Daniel Dobbs, Dr. Brian Rice, and Dr. Jeffrey Lehman for their devotion to teaching me inside and outside the classroom.

- My dear wife, Christine, has walked beside me during difficult weeks of research. She has talked me out of my insecurities as a graduate student, she has listened to countless practice talks without understanding half of the jargon I used, and she has brought me numerous meals when I was working late.

- I would also like to thank my son, Daniel. His playful smiles imbue me with great joy each day and I am grateful whenever he allows me to sleep through the night.

- The chemistry department at Taylor University has graciously minimized my load during the writing of this dissertation. I am honored to have received this opportunity to teach at this excellent institution and I hope that I will be able to serve Taylor University for many years to come.

- My principal investigator, Dr. Schaefer, is largely the reason why I pursued a degree in computational chemistry. He put far more faith in my abilities than I had in myself. I'm not sure if this faith was warranted, but I always strived to live up to his expectations. I greatly benefited from his many years of research experience and it was always clear that he had the well-being of his graduate students as his top priority.

- My committee members, Dr. Wheeler and Dr. Douberly, have challenged me to be critical of my own work, examining the impact of my research. They were excellent teachers and were always willing to discuss research.

- It was a significant pleasure to work alongside my colleagues at the CCQC. Between intellectual discussions in my office and not-so-intellectual discussions in the break-room, they greatly enriched my experience as a graduate student.

- Dr. Justin Turney has been a tremendous resource, serving in multiple regards from maintaining the computer cluster to proofreading numerous drafts.

- The administrative assistants at the CCQC, Sybil Copan and Kathryn Juras, are indispensable because they allow graduate students, like myself, to focus on research.

- My church family at Treasuring Christ Church loved and supported me from the first day I visited. I was blessed to spend my graduate years at a great church.

- To everyone else who contributed either through helpful deed, encouraging word, or diligent prayer, your support was also appreciated.

"If a man will begin with certainties, he shall end in doubts;
but if he will be content to begin with doubts he shall end in certainties."

-Sir Francis Bacon

Contents

List of Figures

List of Tables

List of Symbols or Abbreviations

AE	All-electron computation
ANO	Atomic natural orbital basis set
aug-cc-pVXZ	augmented correlation consistent polarized valence X-ζ basis set
CASPT2	Second order complete active space perturbation theory
CASSCF	Complete active space self-consistent field
CBS	Complete basis set limit
CC	Coupled cluster
CCQC	Center for Computational Quantum Chemistry
CCSD	Coupled cluster with single and double excitations
CCSD(T)	Coupled cluster with single, double, and perturbative triple excitations
CCSDT	Coupled cluster with single, double, and triple excitations
CCSDT(Q)	Coupled cluster with single, double, triple, and perturbative quadruple excitations
CGTO	Contracted Gaussian-type orbital
CI	Configuration interaction
CTST	Canonical transition state theory
cc-pCVXZ	Correlation consistent polarized core-valence X-ζ basis set
cc-pVXZ	Correlation consistent polarized valence X-ζ basis set
cc-pwCVXZ	Correlation consistent polarized weighted core-valence X-ζ basis set
DBOC	Diagonal Born-Oppenheimer correction
DPT2	Second-order direct perturbation theory
d-aug-cc-pVXZ	Doubly augmented cc-pVXZ basis set
EOM-CCSD	Equation of motion coupled cluster with single and double excitations
FC	Frozen-core
FCI	Full configuration interaction
FPA	Focal point analysis
HF	Hartree-Fock
IRC	Intrinsic Reaction Coordinate
ISC	Intersystem crossing
MP2	Second order Møller-Plesset perturbation theory
MRCISD	Multireference configuration interaction with single and double excitations
MRCISD+Q	MRCISD with a Davidson correction for size extensivity.
NBO	Natural Bond Order

PRC	Pre-reactive complex
PoRC	Post-reactive complex
QCISD	Quadratic configuration interaction with single and double excitations
QCISD(T)	Quadratic configuration interaction with single, double, and perturbative triple excitations
QSD	Quadratic steepest descent
RHF	Restricted Hartree–Fock
ROHF	Restricted open-shell Hartree–Fock
RRHO	Rigid rotor harmonic oscillator
SCT	Small curvature tunneling
UHF	Unrestricted Hartree-Fock
TST	Transition state theory
VPT2	Second-order vibrational perturbation theory
VTST	Variational transition state theory
X2C-1e	Exact two-component one electron
ZPVE	Zero-point vibrational energy

Chapter 1

Introduction

1.1 The Schrödinger Equation

The core objective in electronic structure theory is to solve the time-independedent Schrödinger equation[1] for molecular systems:

$$\hat{H}\mathbf{\Psi} = E\mathbf{\Psi} \tag{1.1}$$

where $\hat{H}$ is the Hamiltonian operator, $\mathbf{\Psi}$ is the molecular wavefunction, and $E = \langle \mathbf{\Psi} | \hat{H} | \mathbf{\Psi} \rangle$ is the total energy. The Hamiltonian operator $\hat{H}$ may be written in terms of the following kinetic and potential energy operators:

$$\hat{H} = \hat{T}_e + \hat{T}_N + \hat{V}_{eN} + \hat{V}_{NN} + \hat{V}_{ee} \tag{1.2}$$

where $\hat{T}_e$ is the kinetic energy operator of the electrons, $\hat{T}_N$ is the kinetic energy operator of the nuclei, $\hat{V}_{eN}$ is the electron-nucleus attraction operator, $\hat{V}_{NN}$ is the nucleus–nucleus repulsion operator, and $\hat{V}_{ee}$ is the electron–electron repulsion operator. By assuming atomic

units, these operators are given as:

$$\hat{T}_e = -\sum_i \frac{1}{2}\nabla_i^2 \tag{1.3}$$

$$\hat{T}_N = -\sum_A \frac{1}{2M_A}\nabla_A^2 \tag{1.4}$$

$$\hat{V}_{eN} = -\sum_i \sum_A \frac{Z_A}{r_{iA}} \tag{1.5}$$

$$\hat{V}_{NN} = \sum_{A>B} \frac{Z_A Z_B}{r_{AB}} \tag{1.6}$$

$$\hat{V}_{ee} = \sum_{i>j} \frac{1}{r_{ij}} \tag{1.7}$$

The application of the Schrödinger equation is greatly simplified by assuming the nuclei and electrons move on significantly different timescales based on their relative masses. This assumption is known as the Born–Oppenheimer approximation and it allows for the nuclei to be treated as point particles that are parametrically factored into the Schrödinger equation.[2,3*] This separation allows the computational chemist to determine a potential energy surface (PES) based on the relative electronic energy for the $3N$-dimensional space nuclei may occupy. The potential energy surface is used to obtain many valuable properties such as the relative energies, equilibrium geometries, and frequencies of conformers for a given system.

Under the Born–Oppenheimer approximation, we may define a new Hamiltonian to account for the electronic energy:

$$\hat{H}_e = -\sum_i \frac{1}{2}\nabla_i^2 - \sum_i \sum_A \frac{Z_A}{r_{iA}} + \sum_{i>j} \frac{1}{r_{ij}} \tag{1.8}$$

*The Born–Oppenheimer approximation is widely used in most applications; however, in particular cases such as avoided crossing and reactions involving the transfer of a hydrogen atom the Born–Oppenheimer approximation has been shown to introduce significant error. Approximating the breakdown of the Born–Oppenheimer approximation will be discussed in section 1.5

For hydrogenic systems which consist of only one electron, the final term in equation 1.8 may be safely ignored and the Schrödinger equation can be solved analytically. Unfortunately, there is more than one electron in this universe and an exact analytical solution to the Schrödinger equation does not exist for most molecules. However, as the subsequent chapters demonstrate, an arbitrary level of accuracy may be achieved by applying a hierarchy of computational methods to numerically approximate the solutions to the Schrödinger equation.

1.2 Hartree–Fock Theory

The Pauli exclusion principle states that the interchange of two indistinguishable electrons must result in a change in the sign of the wavefunction.[4] The simplest electronic wavefunction which correctly accounts for the fermionic nature of N electrons is a Slater determinant of the form:[5]

$$\Phi_e = \frac{1}{\sqrt{N!}} \begin{vmatrix} \chi_a(\mathbf{x_1}) & \chi_b(\mathbf{x_1}) & \dots & \chi_n(\mathbf{x_1}) \\ \chi_a(\mathbf{x_2}) & \chi_b(\mathbf{x_2}) & \dots & \chi_n(\mathbf{x_2}) \\ \vdots & \vdots & \ddots & \vdots \\ \chi_a(\mathbf{x_N}) & \chi_b(\mathbf{x_N}) & \dots & \chi_n(\mathbf{x_N}) \end{vmatrix} \tag{1.9}$$

where $\chi_a \ \dots \ \chi_n$ are n spin orbitals and $\mathbf{x_i}$ represent the coordinates and spin of electron i. The electronic Hamiltonian may be divided into one and two electron terms:

$$\hat{H}_e = \sum_i \hat{h}(i) + \sum_{i>j} \frac{1}{r_{ij}} \tag{1.10}$$

$$\hat{h}_i = -\frac{1}{2}\nabla_i^2 - \sum_A \frac{Z_A}{r_{iA}} \tag{1.11}$$

The electronic energy of a Slater determinant may be determined by calculating the expectation value of the electronic Hamiltonian:

$$E = \langle \Phi_e | \hat{H}_e | \Phi_e \rangle \tag{1.12}$$

$$= \sum_i \langle \Phi_e | \hat{h}_i | \Phi_e \rangle + \sum_{i>j} \langle \Phi_e | \frac{1}{r_{ij}} | \Phi_e \rangle \tag{1.13}$$

$$= \sum_i h_{ii} + \sum_{i>j} \langle ij||ij \rangle \tag{1.14}$$

where $h_{ii} = \langle \Phi_e | \hat{h}(i) | \Phi_e \rangle$ and $\langle ij||ij \rangle$ are the two-electron integrals which may be expressed in terms of Coloumb and exchange terms:

$$\langle ij||ij \rangle = \langle \chi_i \chi_j | \chi_i \chi_j \rangle - \langle \chi_i \chi_j | \chi_j \chi_i \rangle \tag{1.15}$$

Hartree–Fock theory seeks to determine the Slater determinant which will provide the lowest energy by variationally optimizing the spin orbitals. Since Hartree–Fock is a variational procedure, the expectation energy obtained from the optimized Slater determinant will always be greater than or equal to the exact non-relativistic energy:

$$E_{\text{HF}} \geq E_{\text{exact}} \tag{1.16}$$

Closed-shell molecules, with no unpaired electrons, are the most common in chemistry. In such cases, it is natural to restrict the molecular orbitals to be paired up by opposite spins. This approach describes the basis of the Restricted Hartree–Fock (RHF) formalism.[6] However, the treatment of molecules with unpaired electrons is not as straight forward. Unrestricted Hartree–Fock (UHF) allows the respective spin orbitals to vary in their spatial components.[7] While this approach seems to maximize the flexibility in the wavefunction, it suffers from an issue known as spin contamination where the expectation value of the $\hat{S}^2$ is greater that

what would be expected from the multiplicity of the electronic state due to the mixing with higher-spin states. In systems with significant spin contamination a different formalism known as restricted open-shell Hartree–Fock (ROHF) is often preferred.[8,9] Similar to RHF, ROHF forces orbitals to be paired up on the basis of spin. While ROHF assumes the correct spin expectation value, it suffers from less obvious faults related to the complexity of the ROHF equations. The choice between UHF and ROHF for open-shell molecules is not trivial and is often determined by several factors including the degree of spin contamination.

For restricted Hartree–Fock, we may work with spatial molecular orbitals, ψ_i, instead of spin orbitals by integrating out the spin. Using the LCAO-MO approximation, the spatial molecular orbitals may be expressed as a linear combination of atomic orbitals:

$$\psi_i = \sum_{\mu} C_{\mu}^{i} \phi_{\mu} \tag{1.17}$$

where ϕ_μ are atomic orbitals and C_μ^i are expansion coefficients for an atomic orbital inside a molecular orbital. The expansion coefficients C_μ^i are usually stored together in a single coefficient matrix $\mathbf{C}$ which describes all the molecular orbitals. The density matrix, $\mathbf{D}$, describes the probability for observing an electron within a certain space in the basis of atomic orbitals. The terms inside the density matrix ($D_{\mu\nu}$) are determined from the expansion coefficients:[†]

$$D_{\mu\nu} = 2 \sum_{i} C_{\mu}^{i} C_{\nu}^{i*} \tag{1.18}$$

Also central to Hartree–Fock theory are the overlap matrix $\mathbf{S}$, which determines the overlap between two basis functions, and the Fock matrix $\mathbf{F}$, which accounts for the energy of one

[†]At the initialization of a Hartree–Fock procedure it is unclear what the expansion coefficients should be, therefore the density matrix is usually set to zero during the first iteration in order to provide an estimate $\mathbf{C}$ and then $\mathbf{C}$ is refined by subsequent iterations

electron in a mean-field of the other electrons. These matrices are evaluated as:

$$S_{\mu\nu} = \langle \psi_\mu | \psi_\nu \rangle \tag{1.19}$$

$$F_{\mu\nu} = \langle \psi_\mu | \hat{h} | \psi_\nu \rangle + \sum_{\rho\sigma} D_{\rho\sigma} \left[\langle \psi_\mu \psi_\rho | \psi_\nu \psi_\sigma \rangle - \frac{1}{2} \langle \psi_\mu \psi_\rho | \psi_\sigma \psi_\nu \rangle \right] \tag{1.20}$$

It may be shown that the optimal molecular orbitals to minimize the Hartree–Fock energy are obtained by iteratively solving the following generalized eigenvalue equation:

$$\mathbf{FC} = \mathbf{SC}\epsilon \tag{1.21}$$

where the eigenvalues, ϵ, correspond to the molecular orbital energies. This eigenvalue problem can be simplified into a standard eigenvalue problem by substituting $\mathbf{F}' = \mathbf{S}^{-\frac{1}{2}}\mathbf{F}\mathbf{S}^{-\frac{1}{2}}$ and $\mathbf{C}' = \mathbf{S}^{\frac{1}{2}}\mathbf{C}$:

$$\mathbf{F}'\mathbf{C}' = \mathbf{C}'\epsilon \tag{1.22}$$

By solving for the transformed coefficient $\mathbf{C}'$ in equation 1.22, a new coefficient matrix ($\mathbf{C}$) is determined and the Hartree–Fock energy is calculated as:

$$E_{\mathrm{HF}} = \sum_{\mu\nu} D_{\mu\nu} \left[\langle \psi_\mu | \hat{h} | \psi_\nu \rangle + \frac{1}{2} \sum_{\rho\sigma} D_{\rho\sigma} \left(\langle \psi_\mu \psi_\rho | \psi_\nu \psi_\sigma \rangle - \frac{1}{2} \langle \psi_\mu \psi_\rho | \psi_\sigma \psi_\nu \rangle \right) \right] + V_{NN} \tag{1.23}$$

where V_{NN} is the nuclear repulsion energy. Using the new coefficient matrix, the Fock matrix in equation 1.20 is re-evaluated and equation 1.22 is solved once more. These iterations continue until the both the Hartree–Fock energy (E_{HF}) and the density matrix ($\mathbf{D}$) converge to a self-consistent solution.

1.3 Basis Sets

In equation 1.17 the LCAO-MO approximation was employed to write molecular orbitals in terms of atomic basis functions; however, this approach first requires accurate atom-centered basis functions to be defined. Based on the solutions to the hydrogenic Schrödinger equation, one might expect Slater type orbitals (STO) of the form

$$\phi_{\mu}^{\mathrm{STO}}(r; a, l, m, n) = N x^{l} y^{m} z^{n} e^{-ar} \tag{1.24}$$

to be the most appropriate. Unfortunately the two electron integrals given in equation 1.15 do not, in general, have analytic solutions for basis functions with an e^{-ar} dependence. This frustration lead Boys to suggest replacing Slater type orbitals with Gaussian type orbitals (GTO) of the form:[10]

$$\phi_{\mu}^{\mathrm{GTO}}(r; \alpha, l, m, n) = N x^{l} y^{m} z^{n} e^{-\alpha r^{2}} \tag{1.25}$$

The overlap of two Gaussian functions is a third Gaussian function; therefore, the evaluation of two electron integrals for GTOs is significantly more efficient than the analogous calculation for Slater type orbitals. Gaussian type orbitals disagree with their Slater type counterparts both near the nucleus as well as a distances further away. In order to reproduce the STOs as closely as possible, contracted Gaussian type orbitals (CGTO) are generated from linear combination of Gaussian type orbitals:[11]

$$\phi_{\mu}^{\mathrm{CGTO}}(r; l, m, n) = \sum_{i} d_{i}^{\mu} \phi_{\mu}^{\mathrm{GTO}}(r; \alpha_{i}, l, m, n) \tag{1.26}$$

where the contraction coefficients d_{i}^{μ} and the exponent factors α_{i} are determined for each element by variationally minimizing electronic energy for that atom.

Next, the number of CGTOs in the basis set must be determined. Naively, one may predict a minimal basis set consisting of only one CGTO per atomic orbital is sufficient. However, the Hartree–Fock energy for molecules is significantly lowered by the addition of CGTOS to valence atomic orbitals. Furthermore, the addition of basis functions with higher angular momentum (e.g. 'd' and 'f' for a carbon atom) is often also necessary to maintain the mathematical flexibility required for an accurate wavefunction.

The correlation-consistent polarized valence basis sets (e.g. cc-pVXZ) developed by Dunning and coworkers are commonly employed in many *ab initio* computations.[12] Each family of basis sets forms an internal hierarchy described by the cardinality of the basis set, where an increase in the cardinality is accompanied by an extra set of valence functions as well a new polarization function with greater angular momenta. In this fashion, correlation-consistent basis sets systematically converge to the hypothetical limit for an infinite basis set known as the complete basis set (CBS) limit. While increasing the size of the basis set increases the accuracy of the computational method, it should be noted that the computational scaling of conventional Hartree–Fock with respect to number of CGTOs, n, is $\mathcal{O}(n^4)$, therefore the accuracy of many *ab initio* methods is limited by size of the basis set that is computationally feasible.

For molecules such as anions or Rydberg states with diffuse electron densities, basis sets are augmented with a set of diffuse basis functions with relatively small exponential factors in order to properly account for the electron density at increased distances away from the nuclei.[13] However, as examined in Chapter 2, it is not always clear how many diffuse functions must be added to the basis set in order to achieve an appropriate balance between accuracy and computational efficiency.

1.4 Correlated Methods

While Hartree–Fock theory can capture up to 99% of the total electronic energy of a system, the remaining 1% is very important to chemistry. In fact, the bulk of modern electronic structure theory has been devoted to accounting for the discrepancy between the Hartree–Fock energy and the exact electronic energy. The correlation energy, E_{corr}, describes the electronic energy on top of the Hartree–Fock energy:

$$E_{\text{corr}} = E - E_{\text{HF}} \tag{1.27}$$

One of the main sources of error within Hartree–Fock theory is the mean-field treatment of electrons, namely that electrons experience a repulsive force based on the averaged electrostatic potential of the other electrons. A more accurate approach would account for the instantaneous position of multiple electrons, allowing the motion of electrons to be dynamically correlated to minimize the repulsive forces. This post-Hartree–Fock correction is known as "dynamic" correlation. The other type of correlation, known as "static" or "non-dynamical", is the direct result of the single-determinant nature of Hartree–Fock theory. While dynamic correlation is encountered for all chemical systems, static correlation is generally only significant for bond-breaking processes or molecules with multiple resonance structures.

It can be shown that both the dynamic and static correlation may be properly accounted for by expanding the wavefunction in terms of Slater determinants with some electrons excited to virtual orbitals. The exact solution to the Schrödinger equation is given as a linear combination of the reference Hartree–Fock determinant and all possible excited determinants:

$$\Psi_{\text{exact}} = c_0 \Phi_e + \sum_{ia} c_i^a \Phi_i^a + \cdots + \sum_{ijkl\ldots abcd\ldots} c_{ijkl\ldots}^{abcd\ldots} \Phi_{ijkl\ldots}^{abcd\ldots} \tag{1.28}$$

where Φ_e is the Hartree–Fock determinant and Φ_i^a is the determinant generated from exciting an electron in orbital i to the virtual orbital a. Equation 1.28 represents the Full Configuration Interaction (FCI) wavefunction. While it is possible to compute the FCI energy of small systems, computing the FCI energy of larger systems is computationally infeasible due to the factorial scaling of the number of excited determinants. The computational demand of FCI is further increased by larger basis sets which increase the number of available virtual orbitals. Therefore, it is necessary to determine methods that approximate the correlation energy with an appropriate balance between accuracy and computational cost.

Configuration interaction (CI) methods simply truncates equation 1.28 based on the number of electrons that must be excited to reach a determinate. For example, CISD uses only the determinates generated from excitating one or two electrons. Unfortunately, the conceptually simple CI theory suffers from a lack of size-consistency. This may be illustrated as a CISD computation on a Helium dimer separated by a near infinite distance. CISD would account for double excitations on either Helium atom, but it would not be able to account for double excitations on both Helium atoms simultaneously. Contrary to expectation for the separate Helium atoms, one would find:

$$E_{\mathrm{CISD}}\left(\mathrm{He}+\mathrm{He}\right) \neq 2E_{\mathrm{CISD}}\left(\mathrm{He}\right) \tag{1.29}$$

The size-consistency error is exacerbated with system size, therefore a reliable correlation method must incorporate excited determinants in a size-consistent manner to guarantee a reliable potential energy surface.

One of the most popular size-consistent correlation methods is coupled-cluster (CC) theory.[14] The CC wavefunction is constructed with an exponential *ansatz*:

$$\Psi_{\mathrm{CC}} = e^{\hat{T}}\Phi_e \tag{1.30}$$

where the cluster operator $\hat{T}$ is given as:

$$\hat{T} = \hat{T}_1 + \hat{T}_2 + \cdots + \hat{T}_N \tag{1.31}$$

Similar to CI theory, a certain truncation of the cluster operator must be chosen. The most common truncation is coupled-cluster with single and double excitations (CCSD) where $\hat{T} = \hat{T}_1 + \hat{T}_2$.[15] When acting on the HF reference wavefunction $\hat{T}_1$ and $\hat{T}_2$ operators generate all the singly and doubly excited determinants with various amplitudes:

$$\hat{T}_1 \Phi_e = \sum_{i}^{\text{occ}} \sum_{a}^{\text{vir}} t_i^a \Phi_i^a \tag{1.32}$$

$$\hat{T}_2 \Phi_e = \sum_{i<j}^{\text{occ}} \sum_{a<b}^{\text{vir}} t_{ij}^{ab} \Phi_{ij}^{ab} \tag{1.33}$$

While CCSD is efficient at recovering dynamic correlation, it often fails to account for most static correlation. It has been shown that expanding the coupled cluster *ansatz* to include triple excitations (CCSDT) greatly improves the accuracy of systems with significant static correlation; however, the $\mathcal{O}(N^8)$ scaling of CCSDT makes it too expensive for even moderately sized systems. Various approaches have been proposed to approximately account for the connected triple excitations in CCSDT at a reduced computational cost, but the most common method is CCSD(T).[16] The robustness of CCSD(T) has been demonstrated by numerous studies over the past three decades and as a result CCSD(T) with a triple-zeta basis set (e.g. cc-pVTZ) has been regarded as the "gold standard" of quantum chemistry.

CCSD(T) is useful to account for systems with mild amounts of static correlation. However, in bond-breaking processes or molecules with multiple resonance structures the amount of static correlation is sometimes too great for CCSD(T) to provide an accurate energy.[‡] The

[‡]The increase in static correlation can be mitigated by expanding the cluster operator to include not only single, double, and triple excitations but also quadruple or even quintuple excitations; however, the large polynomial scaling of the higher order CC methods makes this approach infeasible for systems with even a moderate number of atoms

T_1 diagnostic proposed by Taylor and Lee[17] is often used to determine whether the static correlation is sufficiently low for accurate CCSD(T) results:

$$T_1 = \sqrt{\frac{\sum_i^{\text{occ}} \sum_a^{\text{vir}} \left(t_i^a\right)^2}{n}} \tag{1.34}$$

where t_i^a are the singles amplitudes and n is the number of electrons. For closed-shell systems the recommended maximum value of T_1 is 0.02, while for open-shell systems it is considerably greater at 0.045.[18] Whenever the T_1 diagnostic exceeds this maximum value, correlation methods based on a single HF determinant are not guaranteed to provide accurate energies.

An alternative approach is to replace the single determinant Hartree–Fock reference wavefunction with a multi-reference wavefunction. In multi-configuration self-consistent field (MCSCF) theory, the wavefunction is written as a linear combination of multiple determinants:[19]

$$\Psi_{\text{MCSCF}} = \sum_i c_i \Phi_i \tag{1.35}$$

where the linear expansion coefficients (c_i) and the molecular orbitals are simultaneously optimized. MCSCF computations require the judicious choice of determinants to include in the wavefunction. One possible approach is to list an "active space" consisting of occupied and virtual orbitals obtained in a Hartree–Fock computation and consider all possible determinants generated from excitations within that active space. This approach is known as complete active space self-consistent field (CASSCF) and it is usually described by the total number of orbitals and electrons within the active space. The selection of an active space distinguishes CASSCF from "black box" methods such as HF and CCSD(T) which do not require the same level of user input. Moreover, the extra flexibility provided in the selection of an active space makes the comparison of electronic energies between different conformers difficult and prone to user error.

MCSCF is usually not efficient at capturing dynamic correlation, therefore it is common for the analogs of single-reference correlation methods to be employed on top of a MCSCF reference wavefunction to capture the dynamic correlation. In this sense, multi-reference configuration interaction with single and double excitations (MRCISD) corresponds to the CISD energy computed from a MCSCF reference wavefunction.[20] While MRCISD is not a size-extensive method, a Davidson correction (MRCISD+Q) may be applied to the MRCISD wavefunction to account for size-extensitivity. In practice, MRCISD+Q can be a computationally expensive method depending on the size of the molecule, active space, and basis set, but the electronic energy given from a MRCISD+Q computation provides an accurate description of both the static and dynamic correlation.

1.5 Focal Point Analysis

The determination of accurate electronic energies is central to quantum chemistry as most chemical processes involve some change in energy. However, computing the exact electronic energy for most molecules is an intractable task. Highly accurate energies may be directly computed for molecules with only a few atoms, but the determination of accurate energies for larger molecules is complicated by the large computational scaling of accurate electronic structure methods. Therefore, numerous theoretical studies have examined the most efficient way to compute the electronic energy with a desired balance between accuracy and computational cost.

The incompleteness of the basis set is one of the main limitations in accuracy when solving the multi-electron Schrödinger equation. As mentioned in section 1.3, the Hartree–Fock (HF) energy for a molecule is consistently lowered by the addition of more CGTO basis functions due to the increased flexibility in the molecular orbitals. Furthermore, the correlation energy on top of the HF energy is likewise increased with the presence of additional basis functions in the basis set, as this amendment improves the description of virtual orbitals as well as

the occupied orbitals. The lowest possible HF energy and the largest possible correlation energy for a given correlated method is obtained in the limit of a complete basis set (CBS). The complete basis set consists of an infinite number of basis functions; therefore, the direct evaluation of the CBS energy is a non-starter. However, as mentioned in section 1.3, basis sets such as the cc-pVXZ family by Dunning and co-workers[12] form a hierarchy that systematically converges to the CBS limit. Hence, it is possible to approximate the CBS energy for a given method by extrapolating the energies obtained for that method with increasing sizes for the basis set.

Due to differences in their convergence behavior, it is usually wise to extrapolate the HF energy separately from the correlation energy using different equations. Throughout this dissertation the HF energy is fit to an exponential equation of the form:[21]

$$E_{\mathrm{HF}}(X) = E_{\mathrm{HF}}^{\infty} + ae^{-bX} \tag{1.36}$$

Where X is the cardinality of the basis set (e.g. 2, 3, 4 for DZ, TZ, QZ, etc.) and a and b are constants of the fit. Equation 1.36 requires at least three points to obtain a fit and previous studies have shown HF/cc-pVDZ energies are not accurate enough to be employed in this fit; therefore, the Hartree–Fock energy is usually computed up through a quintuple-zeta (i.e. 5Z) basis set in order to accurately predict the HF/CBS energy. On the other hand, the correlation energy for various correlated methods is extrapolated using an inverse cubic equation:[22]

$$E_{\mathrm{corr}}(X) = E_{\mathrm{corr}}^{\infty} + aX^{-3} \tag{1.37}$$

By extrapolating the HF and CCSD(T) correlation energies separately with equations 1.36 and 1.37, the CCSD(T)/CBS energy ($\Delta E_{\mathrm{CCSD(T)/CBS}}$) may be determined.

While CCSD(T) recovers the majority of the correlation energy, some correlation energy is neglected by the truncation of the coupled cluster *ansatz*. As discussed in section 1.4, the

FCI limit provides an exact description of a multi-electronic wavefunction for a given basis set; however, FCI computations are generally infeasible for even moderately sized systems with small basis sets. Fortunately, coupled-cluster theory provides a convenient hierarchy of size-extensive methods which converge to the FCI limit by incorporating incremental excitations into the cluster operator (e.g. CCSD, CCSDT, CCSDTQ). Perturbative corrections for connected triples excitations [CCSD(T)] and connected quadruple excitations [CCSDT(Q)] are treated as intermediate levels of theory between CCSD and CCSDT and between CCSDT and CCSDTQ, respectively. Furthermore, second order Møller–Plesset perturbation theory (MP2) may be considered as an intermediate level of theory between Hartree–Fock and CCSD. Thus by examining incremental changes in the relative energy between these increasing levels of theory, one can determine the convergence of the correlation energy to the FCI limit.

Focal point analysis (FPA) examines the convergence of the electronic energy to both the CBS limit and the FCI limit as displayed in a focal point table.[23–26] The columns of a focal point table correspond to different electron correlation methods with increasing complexity whereas the rows correspond to different basis sets with increasing cardinality. Table 1.1 provides an example of an incremental focal point table. Each value in Table 1.1 represents an incremental change in the relative energy with respect to the level of theory in the previous column. In general, the incremental changes become smaller proceeding from left to right, signifying the convergence of the relative energy to the FCI limit. Moreover, the differences between consecutive rows on the focal point table become increasingly smaller as the basis set is increased, representing the convergence to the CBS limit for all methods. Due to the large computational cost of performing CCSDT and CCSDT(Q) computations with large basis sets, these values are generally only computed with double zeta or triple zeta basis sets. With larger basis sets, the δT and δ(Q) values are denoted with square brackets because they correspond to additive corrections from the largest basis set the CCSDT and CCSDT(Q) energies were obtained. The values in the bottom row are obtained through extrapolation

Table 1.1: Focal Point Analysis (FPA) of the ethynyl peroxy radical (HCCOO) relative to the $C_2H + O_2$. Energies are in kcal mol^{-1}. δ indicates an incremental change in energy from the previous level of theory. Brackets represent additive corrections or extrapolated values.

Basis	ROHF	$+\delta$MP2	$+\delta$CCSD	$+\delta$(T)	$+\delta$T	$+\delta$(Q)	Net
DZ	−45.61	+14.76	−12.49	−0.35	−0.04	+0.38	[−43.34]
TZ	−47.11	+11.87	−13.46	−0.45	−0.21	[+0.38]	[−48.98]
QZ	−46.82	+10.97	−13.74	−0.48	[−0.21]	[+0.38]	[−49.90]
5Z	−46.75	+10.60	−13.79	−0.50	[−0.21]	[+0.38]	[−50.26]
6Z	−46.66	+10.44	−13.79	−0.50	[−0.21]	[+0.38]	[−50.33]
CBS	[−46.63]	[+10.21]	[−13.78]	[−0.50]	[−0.21]	[+0.38]	[−50.52]

and are likewise denoted with brackets. The total CCSDT(Q)/CBS[§] energy is given as the value in the bottom right corner. Furthermore, by examining the convergence of the focal point table, the uncertainty in the focal point extrapolation may be estimated.

Further corrections are made to the electronic energy to account for approximations used during standard CCSD(T) computations. Most electronic structure packages by default use the frozen-core approximation which assumes determinants where the core electrons have been excited may be ignored in correlated methods. The core-correlation which is neglected under the frozen-core (FC) approximation may be considered by a simple all-electron (AE) CCSD(T) computation (δ_{CORE}). Electrons in the core orbitals of heavy atoms usually have velocities that approach the speed of light, thus scalar relativity would have a significant effect on the size and energy of these orbitals but the Schrödinger does not account for relativity. This assumption may likewise be accounted for by an additive correction for a relativistic treatment of the electronic wavefunction (δ_{REL}) such as second order direct perturbation theory (DPT2)[27] or a spin-free exact two-component one electron (X2C-1e) Hamiltonian.[28] The diagonal Born–Oppenheimer correction (δ_{DBOC}) is a first order correction to the clamped-nuclei approximation (see section 1.1) given as the expectation value of the

[§]This notation is used in this dissertation for brevity; however, it should be noted that the CCSDT(Q) energies are not directly extrapolated to the CBS limit.

nuclear kinetic energy operator.[29,30] In the vast majority of chemical systems the DBOC is very small (≤ 0.02 kcal mol^{-1}); however, for particular cases such as stationary points located near a conical intersection or transition states with a large imaginary frequency the DBOC can be considerably large. These auxiliary corrections are described below:

$$\delta_{\text{CORE}} = \Delta E_{\text{AE-CCSD(T)}} - \Delta E_{\text{FC-CCSD(T)}} \tag{1.38}$$

$$\delta_{\text{REL}} = \Delta E_{\text{AE-CCSD(T)/Rel}} - \Delta E_{\text{AE-CCSD(T)}} \tag{1.39}$$

$$\delta_{\text{DBOC}} = \langle \Psi_e(r;R) | \hat{T}_n | \Psi_e(r;R) \rangle \tag{1.40}$$

When comparing the relative enthalpies of molecules, a final correction must be included to account for the zero-point vibrational energy (δ_{ZPVE}). Altogether the relative enthalpy at 0 K for a molecule is given as:

$$\Delta H_{0\text{K}} = \Delta E_{\text{CCSDT(Q)/CBS}} + \delta_{\text{ZPVE}} + \delta_{\text{CORE}} + \delta_{\text{REL}} + \delta_{\text{DBOC}} \tag{1.41}$$

1.6 Transition State Theory

One of the more practical applications of electronic structure theory is the prediction of accurate rate constants for reactions. Using transition state theory (TST) or other kinetics models, rate coefficients for a multitude of reactions may be determined over a wide range of temperatures and pressures.[31] These theoretical rate constants are especially useful when experimental rate constant have not been obtained under the same conditions.

Canonical transition state theory only requires an accurate description of stationary points on a reactive surface. If we assume for a bimolecular reaction, the reactants form a favorable pre-reactive complex (PRC) prior to reacting, the reaction may be described as:

$$\text{Reactants} \underset{k_{-1}}{\overset{k_1}{\rightleftharpoons}} \text{PRC} \xrightarrow{k_2} \text{Products}$$

The total rate constant for the forwards direction is given as:

$$k_{\text{total}} = k_2 \frac{k_1}{k_{-1} + k_2} \tag{1.42}$$

Given the transition state for this reaction lies above the relative enthalpy of the dissociated reactants we may assume $k_{-1} \gg k_2$ and the rate constant simplifies to:

$$k_{\text{total}} = k_2 K_{\text{eq}} \tag{1.43}$$

Where K_{eq} is the equilibrium constant between the pre-reactive complex and the reactants, which may be calculated as the ratio between their respective canonical partition functions:

$$K_{\text{eq}} = \frac{Q_{\text{PRC}}}{Q_{\text{Reactants}}} \tag{1.44}$$

It may be shown[32*] that the rate constant of the conversion of the PRC into the products (k_2) can be expressed as:

$$k_2 = \kappa \frac{k_B T}{h} \frac{Q_{\text{TS}}(T)}{Q_{\text{PRC}}(T)} \tag{1.45}$$

Where κ is the transmission coefficient which accounts for the quantum tunneling of reactants at energies below the classical barrier height, as well as non-classical reflection at energies above the classical barrier height. By factoring out the relative enthalpy difference between the reactants and transition state saddle point ($\Delta H^{\ddagger}$), the forwards reaction rate may be expressed as:

$$k_{\text{total}} = \kappa(T) \frac{k_B T}{h} \frac{Q_{\text{TS}}(T)}{Q_{\text{Reactants}}(T)} e^{-\Delta H^{\ddagger}/k_B T} \tag{1.46}$$

The exponential term in equation 1.46 is reminiscent of the Arrhenius equation. Moreover, the exponential dependence of k_{total} on $\Delta H^{\ddagger}$, suggests the accurate determination of $\Delta H^{\ddagger}$ is especially important at low temperatures. Even at 300 K, an uncertainty of ± 1.0 kcal

*See Cramer[33] for an intuitive derivation.

mol^{-1} in $\Delta H^{\ddagger}$ corresponds to an uncertainty of a factor of 5.3 in the rate constant. Accurate chemical models usually require rate constants to be accurate within a factor of 2; therefore, it is necessary for $\Delta H^{\ddagger}$ to be converged within subchemical accuracy (≤ 0.5 kcal mol^{-1}) to guarantee reliable theoretical rate constants at moderate to low temperatures.

The transmission coefficient, κ, in equation 1.46 depends on the height and width of the barrier as well as the temperature and the reduced mass of the reaction mode. By assuming the barrier is parabolic with a width that is determined by the imaginary mode frequency at the transition state ($\omega^{\ddagger}$), the transmission coefficient may be calculated as:

$$\kappa(T) = 1 + \frac{1}{24}\left(\frac{h\omega^{\ddagger}}{k_B T}\right)^2 \tag{1.47}$$

This simple approximation, known as the Wigner correction, is sufficient for systems where $\frac{h\omega^{\ddagger}}{k_B T} < 1$.[34] However, a more detailed model is necessary for reactions with more significant contributions from tunneling. Alternatively, the potential energy surface may be approximated as an Eckart barrier.[35] In this case, the transmission probability can be expressed analytically in terms of the relative enthalpy of the PRC, TS, and products as well as $\omega^{\ddagger}$, and the transmission coefficient is evaluated from a Boltzmann weighted integral over the transmission probability.[36] More sophisticated tunneling models, such as small curvature tunneling (SCT), require a description of the potential energy surface beyond the stationary points and account for the multidimensionality of the potential energy surface.[37] These models are sometimes necessary in reactions dominated by tunneling; however, the Eckart tunneling model benefits from some fortuitous cancellation of errors which allows it to be sufficient for many chemical reactions at moderate to high temperature.

The rigid rotor harmonic oscillator (RRHO) approximation is generally employed to calculate the partition functions in equation 1.46. Under the RRHO approximation, the partition function Q is given as a product of the partition function for the different degrees

of freedom in the molecule.

$$Q(T) = q_{\text{trans}}(T)q_{\text{rot}}(T)q_{\text{vib}}(T)q_{\text{elec}}(T) \tag{1.48}$$

For a non-linear molecule, these individual partition functions are calculated as:

$$q_{\text{trans}}(T) = \left(\frac{2\pi M k_B T}{h^2}\right) V \tag{1.49}$$

$$q_{\text{rot}}(T) = \frac{\sqrt{\pi}}{\sigma}\left(\frac{8\pi^2 k_B T}{h^2}\right)^{3/2}\sqrt{I_M} \tag{1.50}$$

$$q_{\text{vib}}(T) = \prod_{i=1}^{3N-6} \frac{1}{1 - e^{h\omega_i/k_B T}} \tag{1.51}$$

$$q_{\text{elec}}(T) = \sum g_i e^{-\epsilon_i/k_B T} \approx g_0 \tag{1.52}$$

Where M, σ, I_M, ω_i, g_i, and ϵ_i respectively are the mass, symmetry index, inertia product, harmonic vibrational frequencies, electronic degeneracies, and electronic energies for each molecule.

Based on equation 1.51, the vibrational modes with the lowest frequencies contribute the most to the partition function at any given temperature. The harmonic frequencies of large amplitude bending modes or hindered rotations can be especially small, which is problematic because these particular modes exhibit a significant amount of anharmonicity. As more vibrational quanta is added to a hindered rotor mode, the wavefunction begins to resemble a free rotor and the spacing of the energy levels increases. On a similar note for large amplitude motions, the potential energy surface with respect to the bending mode is often rectangular-shaped and the spacing between vibrational energy levels also increases with quanta. Therefore, treating these vibrational modes as harmonic oscillators leads to a gross overestimation of the vibrational partition function, especially at moderate to high temperatures. Often, these low frequency anharmonic modes correspond to motion along a single internal coordinate. In such instances, these modes may be projected out of the Hessian

matrix and treated separately. By scanning the potential energy surface and by determining the reduced mass of moment of inertia along this internal coordinate, the numerically exact solutions to the one dimensional Schrödinger equation for the anharmonic mode may be computed and the anharmonic vibrational partition function may be obtained.

In canonical transition state theory, the transition state saddle point on the electronic energy surface serves as the dividing point between the reactants and the products. However, the reaction rate is limited by the relative change in Gibbs free energy along the reaction coordinate and using the saddle point in equation 1.46 instead of the true maximum in ΔG will lead to an overestimation of the rate constant. Variational transition state theory[38,39] (VTST) seeks to amend this error by replacing the saddle point with a generalized transition state that is a function of the reaction coordinate s and minimizing the rate constant as a function of s:

$$k_{VTST}(T) = \min_{s} \frac{k_B T}{h} \frac{Q_{\mathrm{TS}}(T,s)}{Q_{\mathrm{R}}(T)} e^{-\Delta H^{\ddagger}/k_B T} \tag{1.53}$$

By convention $s = 0$ refers to the generalized transition state occurring at the saddle point on the electronic energy surface. For reactions with tight transition states at low temperatures, the variational correction is often small as the saddle point closely resembles a maximum in ΔG. On the other hand at temperatures above 1000 K, the variational correction is non-negligible. Nevertheless, conventional TST may be still be used to determine an upper-bound for the rate constant at high temperatures.

Chapter 2

A Remarkable Case of Basis Set Dependence: The False Convergence Patterns of the Methyl Anion

Reprinted from Bowman, M.C.; Zhang, B.; Morgan, W.J.; Schaefer, H.F., *Mol. Phys.*, 2019, 117, 1069, with permission from Taylor and Francis Publishing.

2.1 Abstract

The gas phase methyl anion, CH_3^-, has been difficult to study experimentally, and the extreme basis set dependence of its molecular properties has presented a comparable challenge to theoreticians. Reliable predictions for the electronic structure of CH_3^- require the use of basis sets capable of describing both the diffuse and valence characteristics of the system. The present study examines the basis set dependence of the equilibrium geometry and harmonic vibrational frequencies of CH_3^-. Both Hartree–Fock and CCSD(T) levels of theories are used with cc-pVXZ (X= D, T, Q, 5, 6) basis sets with up to triple augmentation to describe the diffuse nature of the electron distribution. We find that non-augmented basis sets systematically yield vibrational frequencies that are too high for the umbrella mode and too low for the C–H symmetric and antisymmetric stretch even when extrapolated to the complete basis set limit, displaying false convergence patterns. The inclusion of one set of augmented functions significantly improves the convergence of these properties, but again yields false convergence patterns. Only with the doubly augmented basis set do we approach the basis set limit for the CH_3^- vibrational frequencies.

2.2 Introduction

Carbanions pervade many branches of modern chemistry, appearing most often as transient reaction intermediates. However, they can be used as strong carbon-based nucleophiles when paired with metal cations. Recently the insertion of CO_2 into metal-carbanion complexes has been identified as a possible method of carbon-recycling.[40] With the discovery of large organic molecular anions in Titan's upper atmosphere, gas-phase carbanion chemistry is now of particular interest to astrochemistry.[41–45] Despite the ubiquity of carbanions in chemistry, few studies exist on the methyl anion, the simplest of carbanions.

The methyl anion, CH_3^-, is a challenging system to characterize both experimentally and theoretically. The nature of the extra electron (the electron added to its radical parent) has been a particular subject of debate because of its minuscule binding energy. The earliest theoretical studies predicted the additional electron to be unbound;[46,47] however, in 1978 Ellison, Engelking, and Lineberger were able to demonstrate with photoelectron spectroscopy that CH_3^- was bound by 0.08(3)eV.[48] A much more recent (2015) study by Lineberger, Stanton, and coworkers confirmed this result, obtaining an electron affinity of 0.093(3) eV with high-resolution photoelectron spectroscopy.[49] In practice, when trying to generate CH_3^- through electron capture, the small electron affinity results in competition for free electrons from other species and thus minimizes the amount of CH_3^- actually produced.[50] Furthermore, while the methyl anion can be stabilized in solution with counterions, it is particularly difficult to isolate in the gas phase due to its affinity for hydrogen abstraction.[51–53] In fact, the methyl anion is second only to lithium monoxide anion and diethynylbenzene dianion in terms of gas-phase basicity.[54,55] These physical challenges have led to a scarcity of experimental studies on CH_3^-.

Theoretical work has been done on CH_3^- in light of the experimental obstacles for its production and isolation. However, obtaining an accurate theoretical description of CH_3^- presents its own set of difficulties.[47,56–58] It has long since been known that the methyl anion's potential energy surface along the inversion coordinate is characterized by a double well,[59–61] similar to its isoelectronic counterparts NH_3 and H_3O^+. The vibrational mode along the inversion coordinate, commonly referred to as the umbrella mode ν_2, is of special interest because it can lead to an inversion of chirality during organic and inorganic reactions.[62] The CH_3^- inversion barrier is predicted to be significantly smaller than the inversion barrier of NH_3, lying close to the energy of the fundamental frequency of the umbrella mode.[49,63] Tunneling across this shallow inversion barrier leads to significant splitting in the zero-point vibrational energy and is predicted to cause even more dramatic splitting in the

fundamental frequency of the umbrella mode.[49,57,64,65] Perturbation treatments such as second order vibrational perturbation theory (VPT2) are not able to account for this splitting, but vibrational variational methods are capable of providing this description.

Many early theoretical studies predicted the additional electron on the anion to be unbound,[47,57] but this was due to use of insufficient levels of theory. In 1997, Dixon, Feller, and Peterson[64] predicted an electron affinity of 0.07(1) eV in agreement with Ellison's photoelectron result by extrapolating to the complete basis set (CBS) limit with CCSD(T)/aug-cc-pVXZ where X = D, T, Q. They found that over half of the binding energy could be attributed to the change in the zero-point vibrational energies. Additionally, they computed the energy of the methyl anion at planarity (D_{3h} symmetry) and interpreted the electron to be unbound by 2.15 kcal mol^{-1} at this geometry. In 2015, Lineberger, Stanton, and coworkers performed CCSD(T)/d-aug-pVTZ computations with corrections for extrapolation to the CBS limit and various other effects to obtain an electron affinity of 0.094 eV,[49] and concluded that the electron is bound at planarity. Soon after, Feller published a benchmark study on the application of a convergent coupled cluster theory to computing electron affinities. Feller used a similar approach as Stanton, but added first and second order molecular spin-orbit corrections and replaced the d-aug-cc-pVTZ basis set for the much larger aug-cc-pV8Z basis set, achieving an electron affinity of 0.093(4) eV for the methyl radical.[66]

The diversity in the basis sets applied to this system leads to a methodological question of which basis set provides the most accurate results for a particular molecular property with the least computational cost.[67] However, the basis set dependence of the properties of CH_3^- has not been thoroughly investigated. Augmented basis sets are typically employed in molecules with lone electron pairs because spatially diffuse functions may be necessary for a proper description of the electronic space.[68] In the case of CH_3^- the weakly-bound molecular orbital filled by the extra electron is especially diffuse. As the molecule approaches planarity the electron density becomes even more diffuse, further increasing the need for augmentation

in the basis set.[61,69] While diffuse functions may be necessary to accurately model the electron density of the anion, the addition of diffuse functions increases the computational cost compared to unaugmented basis sets of the same cardinality. Furthermore, augmented basis sets increase the overlap of orbitals on adjacent atoms, which can sometimes lead to numerical instability when the eigenvalues of the overlap matrix approach zero; this is known as linear (or near-linear) dependency.[66] Problems with both computational cost and linear dependency increase with the size of both the system and the basis set, a reason why augmentation beyond doubly augmented cc-pVXZ is rarely employed.

In this work, we thoroughly investigate the basis set dependence of the equilibrium geometry and harmonic vibrational frequencies of the methyl anion at both the Hartree–Fock (HF) and coupled cluster (CC) level of theory. By studying the effects of basis set cardinality and augmentation on the methyl anion we can gain important insight into which basis sets will provide qualitatively correct answers at the lowest computational cost. Furthermore, the basis set dependence of CH_3^- can be used as a guideline for the accurate modelling of other challenging anions.

2.3 Methods

Equilibrium geometries and harmonic vibrational frequencies were computed using both Hartree–Fock and coupled cluster theory with single, double, and perturbative triple excitations [CCSD(T)]. The energy thresholds for the convergence of the HF and CC iterations were 1×10^{-12} and 1×10^{-10} Hartrees, respectively. Similarly, the convergence criteria for the CC amplitudes was 1×10^{-10} Hartrees. The C–H bond length (R_{CH}) and the inversion angle (θ, defined as the angle of the C–H bonds from planarity) were optimized. The geometry optimization included the following convergence criteria: the maximum component of the gradient less than 1×10^{-8} and the root mean square of the gradient less than 1×10^{-9}. The convergence criteria for the aug-cc-pV6Z and d-aug-cc-pV5Z basis sets was loosened to

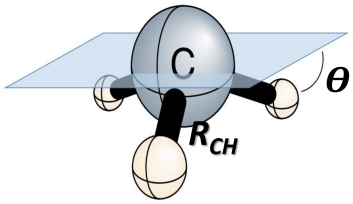

Figure 2.1: Illustration of methyl anion geometrical parameters.

1×10^{-7} and 1×10^{-8} for the maximum component of the gradient and root mean square of the gradient, respectively. Harmonic vibrational frequencies were computed at each optimized geometry using the same level of theory. To compute the harmonic frequencies, numerical Hessians were generated with a step size of 0.005 atomic units. The MOLPRO 2010 software package was used for all computations.[70]

The correlation consistent basis sets of Dunning and coworkers were used (cc-pVXZ, X = D, T, Q, 5, 6).[71,72] The corresponding augmented (aug-cc-pVXZ , X = D, T, Q, 5, 6),[68] doubly-augmented (d-aug-cc-pVXZ , X = D, T, Q, 5),[73] and triply-augmented (t-aug-cc-pVXZ , X = D, T, Q)[70,73] basis sets were also used for comparison.

We examined the convergence of the electronic energy to the complete basis set (CBS) limit using the three-point exponential equation[74] (Eqn. 2.1) for the reference (HF) energy and the two-point inverse cubic equation[75] (Eqn. 2.2) for the correlation [CCSD(T)] energies:

$$E_{\mathrm{ref}}(X) = E_{\mathrm{CBS}} + ae^{-bX} \tag{2.1}$$

$$E_{\mathrm{corr}}(X) = E_{\mathrm{CBS}} + aX^{-3} \tag{2.2}$$

where X is the basis set cardinality (e.g. 2, 3, 4 for DZ, TZ, QZ, etc.). Both the reference and correlation energies were extrapolated for the CCSD(T)/CBS computations. Furthermore, CBS geometries and harmonic vibrational frequencies were computed by applying the

Table 2.1: Relative CCSD(T) Energies (kcal mol^{-1}), Geometries (Å and °), and Harmonic Vibrational Frequencies (cm^{-1}). Values shown are relative to the CBS extrapolation for that family of basis sets, except for the t-aug-cc-pVXZ results which are relative to the d-aug-cc-pVXZ CBS extrapolation.

Basis	ζ	ΔE	R_{CH}	θ	$\omega_1(a_1)$	$\omega_2(a_1)$	$\omega_3(e)$	$\omega_4(e)$
cc-pVXZ	DZ	65.68	0.040	7.37	-199	318	-244	32
	TZ	24.60	0.015	5.24	-117	237	-162	33
	QZ	11.65	0.010	4.01	-79	177	-111	23
	5Z	5.23	0.005	2.24	-38	103	-57	9
	6Z	2.61	0.002	1.13	-17	54	-26	4
	CBS	**0.00**	**1.104**	**20.73**	**2888**	**803**	**2976**	**1422**
aug-cc-pVXZ	DZ	36.95	0.021	2.05	-68	97	-77	-21
	TZ	10.54	0.005	1.14	-31	72	-44	3
	QZ	3.89	0.003	0.76	-19	49	-25	2
	5Z	1.85	0.001	0.38	-9	25	-12	1
	6Z	1.11	0.001	0.12	-4	10	-5	1
	CBS	**0.00**	**1.100**	**19.09**	**2921**	**712**	**3024**	**1418**
d-aug-cc-pVXZ	DZ	35.59	0.016	-0.01	-33	-23	-27	-19
	TZ	9.81	0.002	-0.12	-8	2	-12	5
	QZ	3.49	0.001	-0.03	-3	4	-6	4
	5Z	1.66	0.000	-0.02	-3	2	-4	-1
	CBS	**0.00**	**1.098**	**18.51**	**2929**	**661**	**3040**	**1412**
t-aug-cc-pVXZ	DZ	35.52	0.015	-0.27	-30	-59	-21	-20
	TZ	9.77	0.002	-0.24	-6	-12	-9	6

extrapolation scheme listed above to the single points that define the numerical gradients and Hessians.

2.4 Results and Discussion

Table 2.1 displays the relative differences of computations performed with different basis sets at the CCSD(T) level of theory to the highest cardinality of that augmentation level. Absolute values are provided in the supporting information.

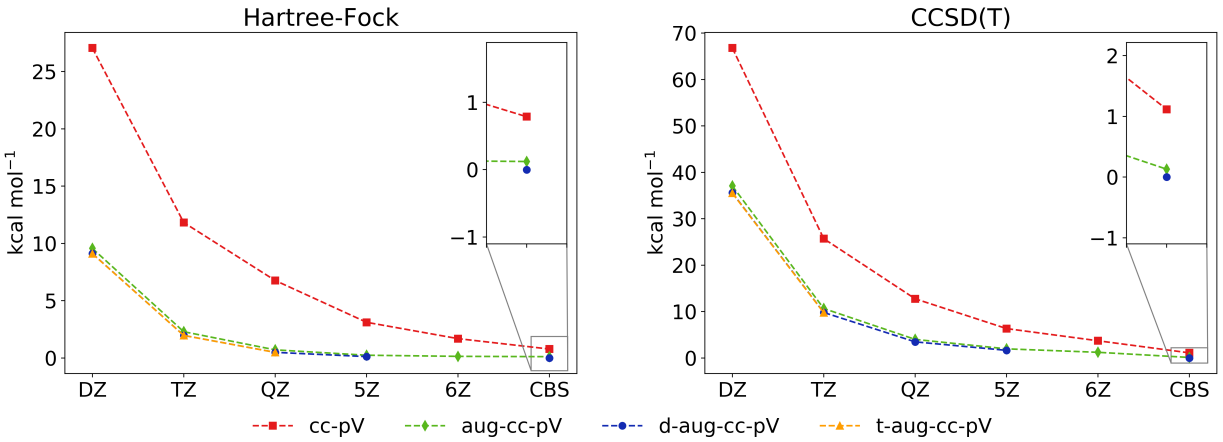

Figure 2.2: Hartree–Fock and CCSD(T) electronic energies relative to the HF and CCSD(T) d-aug-cc-pV(T-5)Z CBS energies respectively.

Figure 2.2 shows the electronic energy of the optimized geometries with different levels of theory and basis sets. The unaugmented cc-pVXZ basis sets (red) show the slowest convergence of all the basis sets for both the Hartree–Fock and CCSD(T) electronic energies. Furthermore, the reference and correlated CBS limit energies with the cc-pVXZ basis sets are over one kcal mol^{-1} away from the CBS energies given by any of the augmented basis sets. The deviation of cc-pVXZ energies from the aug-cc-pVXZ (green) energies increases nearly by a factor of two between the Hartree–Fock and CCSD(T) levels of theory; this demonstrates that the inclusion of diffuse functions is especially necessary with correlated treatments. The distinction between unaugmented basis sets and augmented basis sets is clear: qualitatively different energies are found in both the HF and CCSD(T) energies at all cardinalities. However, this drastic difference is not present between the various levels of augmentation, suggesting that higher levels of augmentation are only required for quantitative accuracy at equilibrium.

A comparison of the computed equilibrium C–H bond distances (R_{CH}) and inversion angles (θ) at the CCSD(T) level of theory is shown in Figure 2.3. An increase in either the cardinality or the augmentation level of the basis set leads to a shorter C–H bond distance

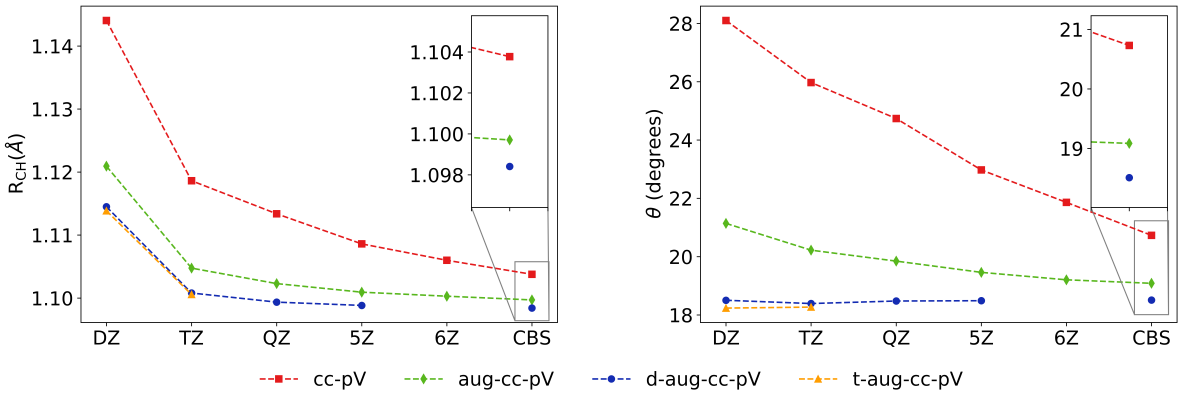

Figure 2.3: CCSD(T) equilibrium geometries. R_{CH} is the C–H bond distance and θ is the angle of the C–H bonds from planarity (as shown in Figure 2.1).

and a smaller inversion angle. This trend is expected, because as the size of the basis set is increased, the electron density is allowed to become more diffuse, minimizing the repulsion of the C–H bonds with the electron pair. The unaugmented cc-pVXZ basis sets demonstrate a 'false convergence' for both the bond distance (0.0054 Å) and the bond angle (2.22°). The doubly augmented d-aug-cc-pVXZ basis set results converge properly and considerably quicker than the aug-cc-pVXZ results. The geometries predicted with the aug-cc-pVXZ basis sets change considerably as we increase the cardinality from TZ through 6Z; however, the d-aug-cc-pVXZ geometries are converged within 0.001 Å and 0.01° at d-aug-cc-pVQZ.

These are the most important results of the present research. The harmonic frequencies of the methyl anion are displayed in Figure 2.4. The C–H antisymmetric and symmetric stretches, $\omega_1(a_1)$ and $\omega_3(e)$, exhibit similar trends: their frequencies increase as the size of the basis set is increased. The trend is likely related to the decrease in the C–H bond distance with increasing basis set size.

The degenerate deformation vibrational mode, $\omega_4(e)$, shows the least basis set dependence out of the four vibrational modes, because the C–H bonds are primarily rotating along the principle axis such that distance between each hydrogen and the carbon center remains about

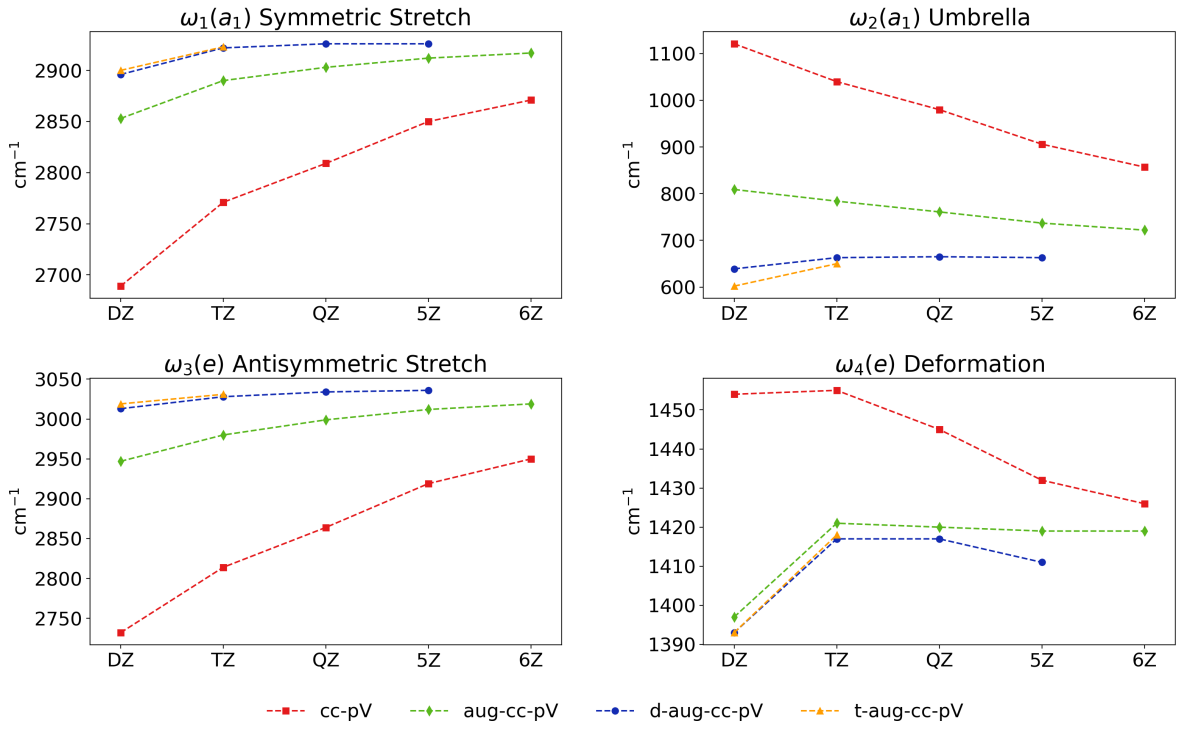

Figure 2.4: CCSD(T) harmonic vibrational frequencies (cm^{-1})

the same. However, as the hydrogens approach one another along this coordinate, the overlap between diffuse hydrogen orbitals increases, leading to linear dependency issues with the d-aug-cc-pV5Z basis set. The deviation of the d-aug-cc-pV5Z degenerate bend frequency from the d-aug-cc-pVTZ and d-aug-cc-pVQZ frequencies is not representative of the overall trend. It may be a consequence of the linear dependency of the d-aug-cc-pV5Z basis set which also limited convergence of the geometry (see methods) in the present study. This deviation is limited to the $\omega_4(e)$ mode.

The basis set dependence of the umbrella motion, $\omega_2(a_1)$ is severe. The d-aug-cc-pVQZ and aug-cc-pVQZ basis sets disagree by nearly 100 cm^{-1} for this mode, which is especially considerable given its low magnitude. Furthermore, the d-aug-cc-pVXZ basis sets remain converged within 1 cm^{-1} from TZ onward, whereas the aug-cc-pVXZ basis sets are relatively unconverged, changing by over 24 cm^{-1} from QZ to 5Z.

Table 2.2: Comparison of CCSD(T) harmonic vibrational frequency for the CH_3^- umbrella mode ($\omega_2(a_1)$). Error is relative to the d-aug-cc-pVXZ CBS frequency.

Basis	ζ	$\omega_2(a_1)$	Error	% Error
cc-pVXZ	TZ	1040	379	57.3
	QZ	980	319	48.3
	5Z	906	245	37.1
	6Z	857	196	29.7
aug-cc-pVXZ	TZ	784	123	18.6
	QZ	761	100	15.1
	5Z	737	76	11.5
	6Z	722	61	9.2
d-aug-cc-pVXZ	TZ	663	2	0.3
	QZ	665	4	0.6
	5Z	663	2	0.3
	CBS	**661**	**0**	**0.0**

The direction and amplitude of the umbrella motion leads to a significant distortion of the anion from its equilibrium structure. The electron density of the lone pair is more concentrated near the carbon atom, repelling the C–H bonds as they approach planarity. However, with a sufficiently augmented basis set, the electron density of the lone pair is significantly more diffuse, minimizing the repulsive interaction. Furthermore, since the umbrella motion approaches the equilibrium geometry of the methyl radical, the electron density is expected to become increasingly diffuse as the molecule approaches a marginally bound planar geometry. Thus, the inclusion of diffuse functions is especially important to describe the umbrella motion of the methyl anion.

A genuinely surprising result of our research is what we call the 'false convergence' of the CH_3^- vibrational frequencies with respect to basis set. This behavior is seen in Table 2.1. We focus on the umbrella frequency $\omega_2(a_1)$ in this discussion. In Table 2.1, the aug-cc-pVXZ CCSD(T) prediction of $\omega_2(a_1)$ appears to have converged at 712 cm^{-1}. However, with the

d-aug-cc-pVXZ basis sets, another apparently convergent CCSD(T) $\omega_2(a_1)$ value is found, namely 661 cm^{-1}. Furthermore, a CBS extrapolation of the unaugmented cc-pVXZ basis set, which remains unconverged at a cardinality of 6Z, provides an estimated CBS limit of 803 cm^{-1} which is in considerable error to the results from augmented basis sets. The conclusion here is that basis sets that might otherwize seem impeccable, for example aug-cc-pV6Z, may have serious shortcomings for anions with low electron affinities

Let us now use Table 2.2 to study the precize convergence patterns for the umbrella frequency $\omega_2(a_1)$. The error was computed relative to the doubly augmented CBS limit of 661 cm^{-1}. Even with the cc-pV6Z basis set, the CCSD(T) value of ω_2 is in error by 196 cm^{-1} or 29.7%. With the larger singly augmented aug-cc-pV6Z basis set the error in ω_2 is still 61 cm^{-1}, corresponding to an error of 9.2%. In contrast, with the doubly augmented sets, even the TZ basis is converged within 2 cm^{-1} of the basis set limit.

Complete basis set (CBS) limit results for both levels of theory along with previous theoretical and experimental results are provided in Table 2.3. Despite the extrapolation, the cc-pVXZ, aug-cc-pVXZ, and d-aug-cc-pVXZ basis sets provide different results for their estimated CBS limit. The discrepancy in the predicted CBS geometries and frequencies is more dramatic with the CCSD(T) method than with Hartree–Fock. This shows that the inclusion of dynamic correlation increases the basis set dependence of the molecular properties in this study. Once more, the umbrella motion of the anion is strongly influenced by the choice of basis set. The difference between the CCSD(T)/aug-cc-pV(T-5)Z CBS and CCSD(T)/d-aug-cc-pV(T-5)Z CBS harmonic frequencies for the umbrella mode is almost 50 cm^{-1}. This difference shows that even in the limiting case of a CBS extrapolation, the description of the umbrella motion is qualitatively different between the aug-cc-pVXZ and d-aug-cc-pVXZ basis sets.

The basis sets used by Lee and Schaefer[69] and by Duke[61] roughly correspond to the aug-cc-pVQZ and d-aug-cc-pVDZ basis sets respectively in overall size and number of diffuse s and

Table 2.3: Equilibrium geometries (Å and °) and harmonic vibrational frequencies (cm^{-1}) of CH_3^-

Method	Basis Set	R_{CH}	θ	$\omega_1(a_1)$	$\omega_2(a_1)$	$\omega_3(e)$	$\omega_4(e)$	Ref.
HF	cc-pV(Q56)Z	1.094	19.7	3007	834	3076	1530	This
	aug-cc-pV(Q56)Z	1.092	18.7	3030	762	3111	1527	work
	d-aug-cc-pV(TQ5)Z	1.091	18.5	3034	744	3118	1527	
CCSD(T)	cc-pV(Q56)Z	1.104	20.7	2888	803	2976	1422	
	aug-cc-pV(TQ5)Z	1.100	19.1	2921	712	3024	1418	
	d-aug-cc-pV(TQ5)Z	1.098	18.5	2929	661	3040	1412	
HF	7s5p2d/3s1p	1.093	19.1					A
HF	10s7p3d/7s2p	1.094	19.4	3019	800	3096	1532	B
CCSD(T)	aug-cc-pVTZ			2891	784	2981	1421	C
CCSD(T)	aug-cc-pVQZ	1.102	19.9	2902	762	2999	1420	D
CCSD(T)	aug-cc-pV5Z	1.097	18.7	2912	738	3012	1419	E
CCSD(T)	d-aug-cc-pVTZ						1417	F
Exp.					460(40)[1]			G
Exp.					444(13)[1]			F

[1] Photoelectron spectroscopy results for the $\nu_2(0^+ \rightarrow 1^+)$ transition

[A] Duke[61], two diffuse s and p functions on the carbon atom

[B] Lee and Schaefer[69], one diffuse s and p function on the carbon and a diffuse s function on the hydrogen

[C] Dixon, Feller, and Peterson[64]

[D] Ragni and coworkers[65]

[E] Feller[66]

[F] Lineberger, Stanton and coworkers[49]

[G] Ellison and coworkers[48]

p functions. The Hartree–Fock equilibrium geometries and harmonic frequencies reported by Lee are in strong agreement with the HF/aug-cc-pVQZ results in this study (see supporting information and Table 2.3), despite the inclusion of the f and g functions in the aug-cc-pVQZ basis. This suggests that the functions of higher polarization may not be as necessary to provide an accurate description of the molecule at the Hartree–Fock level of theory.

The CCSD(T) harmonic frequencies reported by Dixon and coworkers,[64] Ragni and coworkers,[65] Stanton and coworkers,[49] and Feller[66] agree with the harmonic frequencies computed in this study at the same basis set (see Tables 2.1 and 2.3). The considerable difference between the harmonic frequencies and the VPT2 fundamental frequencies reported by Stanton and coworkers,[49] is a result of the anharmonicity of vibrational modes of the methyl anion. The discrepancy between the harmonic frequency of the umbrella mode and the experimentally observed frequency is well accounted for by the vibrational splitting caused by tunnelling across the shallow inversion barrier. The variational treatment used by Stanton and coworkers captures this inversion splitting, providing a qualitatively correct description of the umbrella mode. However, these variational treatments are only as accurate as the potential energy surface computed for the molecule and our harmonic frequency results show that the description of the potential energy surfaces, especially with respect to the inversion coordinate, is highly dependent on the choice of basis set.

Table 2.4 demonstrates how the size of the basis set grows with cardinality and levels of augmentation. The number of two-electron integrals will scale as $O(n^4)$ where n is the total number of orbitals. This polynomial scaling makes the larger basis sets less practical than moderately sized basis sets. For example, the d-aug-cc-pVQZ basis set has approximately twice the number orbitals as the cc-pVQZ basis set, which will require an increase in the number of two-electron integrals by a factor of 16.

Basis sets with a large number of diffuse functions can suffer from near-linear dependency, possibly leading to numerical instability, depending on the choice of quantum chemistry

Table 2.4: Basis set size of correlation consistent basis sets of Dunning and coworkers.

Basis	ζ	Hydrogen	Carbon	CGTOs[1]
cc-pVXZ	DZ	2s1p	3s2p1d	29
	TZ	3s2p1d	4s3p2d1f	72
	QZ	4s3p2d1f	5s4p3d2f1g	145
	5Z	5s4p3d2f1g	6s5p4d3f2g1h	256
	6Z	6s5p4d3f2g1h	7s6p5d4f3g2h1i	413
aug-cc-pVXZ	DZ	3s2p	4s3p2d	50
	TZ	4s3p2d	5s4p3d2f	115
	QZ	5s4p3d2f	6s5p4d3f2g	218
	5Z	6s5p4d3f2g	7s6p5d4f3g2h	367
	6Z	7s6p5d4f3g2h	8s7p6d5f4g3h2i	570
d-aug-cc-pVXZ	DZ	4s3p	5s4p3d	71
	TZ	5s4p3d	6s5p4d3f	158
	QZ	6s5p4d3f	7s6p5d4f3g	291
	5Z	7s6p5d4f3g	8s7p6d5f4g3h	478
t-aug-cc-pVXZ	DZ	5s4p	6s5p4d	92
	TZ	6s5p4d	7s6p5d4f	201
	QZ	7s6p5d4f	8s7p6d5f4g	364

[1] Total number of contracted Gaussian type orbitals (spherical coordinates). Canonical orthogonalization was not implemented in this study, thus the number of CGTOs directly corresponds to the number of molecular orbitals.

package tolerances. The smallest eigenvalue of the overlap matrix $s_{\min}$ is often used as a metric for linear dependency.[66] For reference $s_{\min}$ for the cc-pV5Z, aug-cc-pV5Z, and d-aug-cc-pV5Z computations was 3.12×10^{-3}, 6.38×10^{-5}, and 1.47×10^{-7}, respectively. With 64-bit arithmetic, computers can handle eigenvalues as low as $s_{\min} = 10^{-8}$. However, programs can safely proceed below that threshold by projecting out the molecular orbitals that correspond to the lowest eigenvalues of the overlap matrix.

The d-aug-cc-pVXZ family of basis sets has been shown in this work to give rapid convergence of the molecular properties, outperforming the aug-cc-pVXZ basis sets of higher cardinality. A comparison between doubly augmented basis sets of modest cardinality with singly augmented basis sets of greater cardinality and similar convergence demonstrates the advantages of using a d-aug-cc-pVXZ basis set. The total number of diffuse orbitals within each augmented basis set can be calculated by subtracting the number of CGTOs in the cc-pVXZ computation of the same cardinality. The d-aug-cc-pVTZ basis set has 86 diffuse orbitals whereas the aug-cc-pV5Z basis set has 111 diffuse orbitals. Despite having fewer diffuse orbitals, the difference in the computed geometry and harmonic frequencies between the d-aug-cc-pVTZ and the d-aug-cc-pVXZ CBS is smaller than between the aug-cc-pV5Z and aug-cc-pVXZ CBS results. Additionally, the d-aug-cc-pVTZ computation has less than half the total number of orbitals as the aug-cc-pV5Z computation. In a similar manner, the d-aug-cc-pVQZ basis set has significantly less orbitals than the aug-cc-pV6Z basis set, but shows tighter convergence of the equilibrium geometry and harmonic frequencies to the CBS limit.

A pragmatic solution to achieve a good compromize between the accuracy of a large basis set and the efficiency of a modest basis set is to implement a custom basis set. Since the majority of the electron density is centered around the carbon atom, the basis set of the hydrogens should have a relatively small effect on the molecular properties of the anion compared to the basis set on the carbon atom. Table 2.5 examines the basis set dependence

Table 2.5: Relative CCSD(T) Energies (kcal mol^{-1}), Geometries (Å and °), and Harmonic Frequencies (cm^{-1}). Basis set on the carbon atom is d-aug-cc-pV5Z for each computation. ΔE is calculated by subtracting the d-aug-cc-pV5Z energy.

Hydrogen Basis	ζ	ΔE	R_{CH}	θ	$\omega_1(a_1)$	$\omega_2(a_1)$	$\omega_3(e)$	$\omega_4(e)$
cc-pVXZ	TZ	1.827	1.0998	18.47	2925	665	3033	1415
	QZ	0.685	1.0993	18.50	2927	667	3035	1416
	5Z	0.121	1.0988	18.49	2929	668	3037	1417
aug-cc-pVXZ	TZ	1.741	1.0998	18.49	2924	666	3032	1414
	QZ	0.594	1.0993	18.53	2926	668	3034	1416
	5Z	0.016	1.0989	18.50	2928	668	3036	1417
d-aug-cc-pVXZ	TZ	1.729	1.0998	18.49	2924	665	3032	1414
	QZ	0.575	1.0993	18.52	2926	667	3034	1416
	5Z	0.000	1.0988	18.49	2926	663	3037	1412

of just the hydrogen atoms on molecular properties. If the d-aug-cc-pV5Z basis on the hydrogens is replaced with an unaugmented basis set with the same cardinality (i.e. cc-pV5Z) the electronic energy changes by only 0.12 kcal mol^{-1}, the equilibrium geometry remains nearly the same, and the harmonic frequencies disagree by no more than 5 cm^{-1} relative to the fully augmented results. This shows that the basis set on the hydrogen can dismiss augmentation with little to no loss in accuracy. Such a substitution not only decreases the number of two-electron integrals, but also potentially eliminates the linear dependency issue, as there would be no diffuse functions on the hydrogens to overlap with the diffuse carbon orbitals. Decreasing the cardinality, as opposed to augmentation level, of the basis set of the hydrogen atoms has a more noticeable effect on the molecular properties. However, substitution of cc-pVTZ for the hydrogen atoms, which decreases both the cardinality and the level of augmentation, has a minor effect on the geometry and changes the harmonic frequencies by at most 4 cm^{-1}.

2.5 Conclusions

In this work, we examined the basis set dependence of CH_3^- molecular properties with respect to both the diffuseness of basis functions and the basis set overall size. The addition of diffuse functions rapidly increases the convergence of the electronic energies, equilibrium geometries, and harmonic frequencies. Incorporating a second set of diffuse functions marginally affects the electronic energy of the anion. However, this addition has an important impact on the equilibrium geometry and harmonic frequencies that is required to achieve quantitative accuracy. An unanticipated result of this research is the discovery of 'false convergence' in the prediction of vibrational frequencies as a function of cardinality in the cc-pVXZ and aug-cc-pVXZ families of basis sets.

While conventional large augmented basis sets (such as aug-cc-pV5Z) are sufficient to describe the electronic energy of the anion at equilibrium, we determined that it is more efficient to use a doubly augmented basis set for the equilibrium geometry and harmonic frequencies of the anion. This is because the same accuracy can be achieved at a significantly lower cardinality through double augmentation. On the other hand, subsequent diffuse functions beyond a doubly augmented basis set have little effect on the convergence of the molecular properties studied. The results of this study should guide the efforts of future theoretical studies on other carbanions.

Chapter 3

Convergent Energies and Anharmonic Vibrational Spectra of Ca_2H_2 and Ca_2H_4 Constitutional Isomers

Bowman, M.C.; Douberly, G.E.; Schaefer, H.F., *Phys. Chem. Chem. Phys.*, 2019, 117, 1069.

3.1 Abstract

Three constitutional isomers of both Ca_2H_2 and Ca_2H_4 have been characterized with molecular electronic structure theory. Correlation methods as complete as CCSDT(Q) and basis sets as large as cc-pwCV5Z have been used to converge the relative energies within chemical accuracy ($\leq$ 1 kcal mol^{-1}). Anharmonic vibrational frequencies were computed using second-order vibrational perturbation theory employing CCSD(T)/cc-pwCVTZ cubic and quartic force-fields and a CCSD(T)/cc-pwCVQZ quadratic force field. The monobridged [Ca(μ_2−H)CaH] and dibridged [Ca(μ_2−H)$_2$Ca] isomers of Ca_2H_2 were predicted to lie 6.5 and 12.9 kcal mol^{-1} below the energy of the classical HCaCaH linear isomer, respectively. Despite the energetic favorability of the bridged Ca_2H_2 isomers, we conclude (surprisingly) that only the higher energy linear structure has been observed in the laboratory. At 0 K, the tribridged [Ca(μ_2−H)$_3$CaH] isomer of Ca_2H_4 is predicted to be enthalpically favored by 0.9 kcal mol^{-1} in comparison to the enthalpy of the dibridged [HCa(μ_2−H)$_2$CaH] structure. Comparison of experiment with our computed frequencies suggests that the observed vibrational features arise from both the dibridged *and* the tribridged Ca_2H_4 structures.

3.2 Introduction

Mukherjee, Schuhknecht, and Okuda have reviewed recently the rapidly expanding field of molecular calcium hydrides.[76] Molecular calcium hydrides have a strong affinity to dimerize, forming (L)Ca(μ_2-H)$_2$Ca(L) complexes.[77,78] These dimeric calcium hydrido complexes serve as efficient catalysts for various reactions including hydrogenation,[79,80] hydroboration,[81,82] and hydrosilylation.[83] Solid calcium hydride $[CaH_2]_\infty$ has also been the subject of many studies due to its potential use as a doping agent for hydrogen storage materials.[84–86] While great attention has been given to calcium hydrido complexes in solution and calcium hydride in the solid state, less is known about calcium hydride systems in the gas phase.

In 1991, Xiao, Hauge, and Margrave performed the first FTIR matrix isolation spectroscopic study of the reaction of photoexcited calcium with an excess of H_2.[87] By adjusting the photolysis source and vaporization temperature and by replacing the hydrogen with isotopologues, these authors assigned peaks to the CaH_2, Ca_2H_2, and Ca_2H_4 molecules in krypton and xenon matrices. Later, in 2004, Wang and Andrews performed a related study in solid neon, argon, and hydrogen, but used laser ablation as the calcium source instead of vaporization. These authors made similar assignments for CaH_2, Ca_2H_2, and Ca_2H_4.[88] To our knowledge, Ca_2H_2 and Ca_2H_4 have not been detected in the gas phase. In the present study, we interpret the previous matrix isolation experiments as well as make predictions for how Ca_2H_2 and Ca_2H_4 might be characterized in the gas phase.

As a fourth row element, calcium falls between the lighter alkaline earth metals (Be and Mg) and the heavier metals (Sr and Ba) in terms of polarizability. Calcium's intermediate degree of polarizability makes it difficult to predict *a priori* whether it will behave like its lighter or heavier congeners. For example, many theoretical studies have predicted that CaH_2 should be linear like MgH_2 and BeH_2 instead of bent like SrH_2 and BaH_2.[89–91] However, infrared spectra from Xiao et al and from Wang and Andrews both suggested that CaH_2 was quasilinear.[87,88] This observation was later corroborated by Koput, who used CCSD(T) with quadruple- and quintuple-ζ basis sets to obtain equilibrium bond angles of 167.1° and 164.4°, respectively.[92] The success of coupled cluster methods with large basis sets, over lower levels of theory, in correctly predicting the quasilinearity of CaH_2 demonstrated the necessity for high level *ab initio* characterization for calcium hydride species.

Ab initio studies on M_2H_2 (M = Be, Mg, Ca, Sr, or Ba) alkaline earth metal hydrides have explored local minima corresponding to both linear [HMMH] and bridged [M(μ_2-H)MH or M(μ_2-H)$_2$M] structures.[93–95] For the lighter metal hydrides Be_2H_2 and Mg_2H_2 the linear structure was favored over the bridged structures.[94,96–98] On the other hand, the heavier metal hydrides Sr_2H_2 and Ba_2H_2 have a preference for bridged or branched (e.g. $BaBaH_2$)

structures.[88] In 2003, Magnusson and Petrie examined many M_2H_2 species at the B3LYP and G2 levels of theory and concluded that Ca_2H_2 was similar to its heavier congeners in its preference for bridged structures.[99] However, despite the thermodynamical favorability of the monobridged and dibridged Ca_2H_2 structures, only the linear Ca_2H_2 structure has been experimentally examined.

Dimerization of MH_2 monomers yields M_2H_4 hydrides. Kaupp and Schleyer[100] determined that the factors controlling the monomeric MH_2 bond angle, namely the polarizability of the alkaline metal and d orbital participation in σ-bonding, were also responsible for the bridging preferences in M_2H_4 hydrides. Theoretical and experimental studies alike have shown that Be_2H_4 and Mg_2H_4 possess a dibridged [HM(μ_2-H)$_2$MH] D_{2h} geometry as a global minimum.[93,98,101] Contrarily, Sr_2H_4 and Ba_2H_4 preferentially form tribridged C_{3v} structures [HM(μ_2-H)$_3$M].[88,100] Once again calcium represents an intermediate case between the lighter and heavier alkaline earth metals. MP2 studies performed by Kaupp and Schleyer[100] in 1993 reported that the dibridged structure was preferred over the tribridged by 1.4 kcal mol^{-1}. However, Wang and Andrews later computed the tribridged Ca_2H_4 structure to be lower in energy by 1.2 kcal mol^{-1} at the B3LYP/6-311++G(3df,3pd) level of theory.[88] Wang and Andrews also computed B3LYP harmonic vibrational frequencies for both the dibridged and tribridged Ca_2H_4 isomers, but were unable to confidently determine which isomer was responsible for the Ca_2H_4 bands observed. Given the above modest theoretical treatments, it is currently unclear whether the dibridged or the tribridged Ca_2H_4 structure is the lowest energy constitutional isomer and which structure has been observed in the various matrices.

In the present study, we have performed a high-level *ab initio* characterization of minima and transition states on the Ca_2H_2 and Ca_2H_4 potential energy surfaces to confidently determine the relative enthalpies of calcium hydride species at 0 K. Additionally, we have computed fundamental frequencies for Ca_2H_2 and Ca_2H_4 species to aid the spectroscopic identification of calcium hydrides.

3.3 Methods

Coupled cluster theory with single, double, and perturbative triple excitations [CCSD(T)][102] was used to characterize stationary points on the Ca_2H_2 and Ca_2H_4 surfaces. Contributions from calcium's outer-core ($3s^23p^6$) shell were considered through the use of cc-pwCVXZ (X = D, T, Q, 5) basis sets[103] and by freezing only the ten inner most electrons ($1s^22s^22p^6$) on each calcium atom. Diffuse basis functions (i.e. aug-cc-pVXZ) were added to the relatively electronegative hydrogen atoms to account for the expected negative charge on these atoms.[13] For brevity we will use "XZ" to denote the use of cc-pwCVXZ on calcium atoms and aug-cc-pVXZ on the hydrogen atoms. Preliminary results confirmed that this choice of basis set and electron correlation provided results that converged to experimental values for calcium monohydride (CaH $^2\Sigma^+$). The methods used in this study are also consistent with recent high-level *ab initio* studies performed on the related molecules CaH and CaH_2.[92,104–106]

Equilibrium geometries were optimized at the CCSD(T)/QZ level of theory to a RMS energy gradient of 1.0×10^{-7}. Harmonic vibrational frequencies were obtained for the CCSD(T)/QZ optimized geometries at the same level of theory. The harmonic vibrational frequencies were used to characterize stationary points as minima or transition states. Equilibrium geometries and harmonic vibrational frequencies were obtained using the MOLPRO 2010 package.[70] The connections between transition states and minima were verified using Quadratic Steepest Descent Reaction Path Following[107,108] as implemented in MOLPRO 2010 at the CCSD(T)/DZ level of theory. Full cubic and semidiagonal quartic anharmonic contributions to the vibrational frequencies were computed for local minima at the CCSD(T)/TZ level of theory with second order vibrational perturbation theory (VPT2)[109] as implemented in CFOUR 2.0.[110] The anharmonic contributions were appended to the harmonic vibrational frequencies obtained at the CCSD(T)/QZ level of theory to predict

the fundamental frequencies. Additionally, the dipole moments of CaH, HCa(μ_2−H)Ca and HCa(μ_2−H)$_3$Ca were computed at the CCSD/QZ level of theory.

The electronic energies of stationary points were computed according to the focal point analysis (FPA) of Allen and coworkers.[23–26] Electron correlation treatments up to CCSDT(Q) and basis sets as large as quintuple-ζ (i.e. 5Z) were used in this study. Complete basis set (CBS) energies were obtained for various methods by extrapolating the Hartree-Fock reference energies and correlation energies using a three-point exponential equation[21] and a two-point inverse cubic equation,[22] respectively:

$$E_{\mathrm{ref}}(X) = E_{\mathrm{ref}}^{\infty} + ae^{-bX} \tag{3.1}$$

$$E_{\mathrm{corr}}(X) = E_{\mathrm{corr}}^{\infty} + aX^{-3} \tag{3.2}$$

The CCSDT(Q)/CBS energy was determined by appending CCSDT(Q) and CCSDT additive corrections to the CCSD(T)/CBS energy. The CCSDT(Q) and CCSDT corrections were computed with the MRCC 2015[111] package using DZ and TZ basis sets, respectively. The CCSDT and CCSDT(Q) corrections are reported as a single higher order correlation correction ($\delta_{\mathrm{T(Q)}}$). Further corrections were included to account for the limitations of approximations used to compute the CCSDT(Q)/CBS energy. The impact of calcium's inner-core-correlation was accounted for by a CCSD(T)/QZ all-electron computation. Scalar relativistic effects were considered using second-order direct perturbation theory (DPT2)[27] at the CCSD(T)/TZ level of theory with all the electrons correlated. The correction for the inner-core correlation and the scalar relativistic correction largely cancel each other out, therefore we list only the combined correction (δ_{CR}). An adiabatic diagonal Born-Oppenheimer correction (δ_{DBOC})[29,30] was performed at the HF/QZ level of theory to account for the clamped-nuclei approximation. Finally, the harmonic zero-point vibrational energy (δ_{ZPVE}) was appended to determine the relative enthalpy at zero Kelvin ($\Delta H_{0\mathrm{K}}$). The matrix isolation studies have been performed

at temperatures less than 15K; therefore, it was unnecessary to compute thermal corrections in order to accurately interpret the experimental results. Nevertheless, in order to predict the equilibrium constant between the dibridged and tribridged Ca_2H_4 structures at higher temperatures we have calculated the relative Gibbs free energy [$\Delta G(T)$] for these constitutional isomers using rigid-rotor harmonic-oscillator partition functions.

3.4 Results and Discussion

A plethora of theoretical and experimental research has been reported on the calcium dimer, calcium monohydride, and calcium dihydride. These results provide us with ample comparisons to validate our theoretical methods.

The alkaline earth metals have been shown in several studies to form weakly-bound van der Waals dimers.[112–116] Francis and Weber[117] observed that calcium has an affinity to aggregate into Ca_2 dimers when deposited into solid krypton; therefore, it is likely that Ca_2 was initially present in the matrix isolation experiments of Xiao et al[87] and Wang and Andrews.[98] However, the calcium dimer is a particularly difficult system to model because of its shallow potential well. Table 3.1 compares our Ca_2 results to experimental and previous theoretical studies. Many studies have employed augmented basis sets to model the weak Ca–Ca interaction; however, by comparing the results we obtained using CCSD(T)/cc-pwCVQZ to the results Yang and Wang obtained with CCSD(T)/aug-cc-pCVQZ, we find the addition of diffuse functions has a negligible effect on the molecular properties of Ca_2. On the other hand, incorporation of corrections for iterative triple and perturbative quadruple amplitudes [i.e. CCSDT(Q)] into the CCSD(T) geometry optimization decreases the equilibrium Ca–Ca distance by about 0.05 Å, bringing it into better agreement with experiment. However, we expect the incorporation of quadruple excitations to have a significantly decreased effect on the equilibrium geometries of calcium hydrides. Hence, the error within our Ca_2 theoretical results can be viewed as an upper-bound for the error elsewhere in this study.

Table 3.1: Equilibrium bond distance (r_e, in Å), dissociation energy (D_e, in cm^{-1}), harmonic vibrational frequency (ω_e, in cm^{-1}) and anharmonicity constant ($\omega_e x_e$, in cm^{-1}) for the calcium dimer (Ca_2).

Work	r_e	D_e	ω_e	$\omega_e x_e$
CCSD(T)/QZ[a]	4.337	932	61.1[h]	1.21
CCSDT(Q)/CBS[a]		990		
Experiment[b]	4.277	1075	64.9	1.07
Experiment[c]	4.276	1095	65.1	
Experiment[d]	4.277	1102	64.4	
CCSD(T)/aQZ[e]	4.339	930	61.3	1.15
CCSD(T)/a5Z[f]		983		
CCSDT(Q)/aCBS[e]	4.287	1095	63.8	1.15
CCSD(T)/GRECP[g]	4.283	1136	65.4	

[a] This research
[b] Balfour and Whitlock[114]
[c] Vidal[118]
[d] Allard et al[119,120]
[e] Yang and Wang[121]
[f] Patwoski et al, all electron[122]
[g] Mosyagin et al[123]
[h] $\omega_e x_e$ obtained with CCSD(T)/TZ

Table 3.2: Equilibrium bond distance (r_e, in Å), dissociation energy (D_e, in cm^{-1}), harmonic vibrational frequency (ω_e, in cm^{-1}), anharmonicity constant ($\omega_e x_e$, in cm^{-1}), and dipole moment (μ in Debye) for calcium monohydride (CaH $^2\Sigma^+$).

Work	r_e	D_e	ω_e	$\omega_e x_e$	μ
CCSD(T)/QZ[a]	2.005	14410	1296.6	21.94 [g]	2.52
CCSDT(Q)/CBS[a]		14540			
Experiment[b]			1298.4	19.18	
Experiment[c]	2.003	14360	1298.3	19.10	2.50
MRCI+Q/QZ[e]	2.006	14330	1293.8	18.89	2.55
CCSD(T)/5Z[f]	2.004	14270			2.54

[a] This research
[b] Petitprez et al[124]
[c] Huber and Herzberg[125]
[d] Chen and Steimle[126]
[e] Shayesteh et al[106]
[f] Kerkines and Mavridis[105]
[g] $\omega_e x_e$ obtained with CCSD(T)/TZ

Calcium monohydride is an important astronomical radical, as such it has received significant treatment both experimentally and theoretically. Table 3.2 shows our results for ground state CaH ($^2\Sigma^+$) in comparison to previous theoretical and experimental studies. At the CCSD(T)/QZ level of theory we were able to closely replicate the experimentally observed values for r_e, D_e, ω_e, and μ. This suggests that CCSD(T)/QZ is sufficient to make accurate predictions on the calcium hydrides within this study.

As mentioned in the introduction, the quasilinearity of CaH_2 long evaded a proper theoretical treatment. Table 3.3 lists the equilibrium geometry and fundamental vibrational frequencies of CaH_2 as observed in matrix isolation experiments and as predicted at various levels of theory. We find that our CCSD(T)/QZ optimization predicts CaH_2 to be slightly bent with an equilibrium bond angle of 166.0 degrees, which is in agreement with the prediction by Koput at the CCSD(T)/5Z level of theory[92] as well as the experimental conclusions made by Xiao et al[87] and by Wang and Andrews.[88] However, we found that at the

Table 3.3: Equilibrium bond distance (r_e, in Å), bond angle (θ_e, in degrees), and fundamental frequencies (ν_i, in cm^{-1}) for CaH_2.

Work	r_e	θ_e	ν_1	ν_2	ν_3
CCSD(T)/QZ[a]	2.047	166.0	1295.7[f]	91.2[f]	1214.7[f]
Experiment[b]		166(4)	1289.7		1216.3
Experiment[c]		168(4)	1267.0		1192.0
CCSD(T)/TZ[d]		180.0	1277.7	205.1	1195.8
CCSD(T)/5Z[e]	2.045	164.4	1298.5	116.1	1223.0

[a] This research
[b] Wang and Andrews, Ar matrix[88]
[c] Xiao et al, Kr matrix[87]
[d] Hrenar et al, VCI[127]
[e] Koput, VPT2[92]
[f] δ_ν computed at CCSD(T)/TZ level of theory

CCSD(T)/TZ and CCSD(T)/DZ level of theory CaH_2 had a linear structure as a minimum. Therefore, we propose basis sets of at least quadruple-ζ are necessary to confidently determine the qualitative geometry of calcium hydrides. Furthermore, when considering typical red-shifts associated with the Ar and Kr matrices, our VPT2 frequencies closely match the fundamental frequencies observed in both matrix isolation studies. Based on this, VPT2 with CCSD(T)/TZ cubic and semi-diagonal quartic force fields appears appropriate to predict calcium hydride gas-phase frequencies.

Three equilibrium structures were optimized for the Ca_2H_2 calcium hydride: linear (M1), monobridged (M2), and dibridged (M3). The geometries of Ca_2H_2 stationary points are illustrated in Figure 3.1 and the relevant internal coordinates are provided in Table 3.4. The relative enthalpies of the Ca_2H_2 stationary points are calculated in Table 3.5 and illustrated in Figure 3.2. We have assumed that linear Ca_2H_2 (M1) is initially produced from the combination of two calcium monohydride radicals; however, the exact mechanism for Ca_2H_2 production is currently unclear.

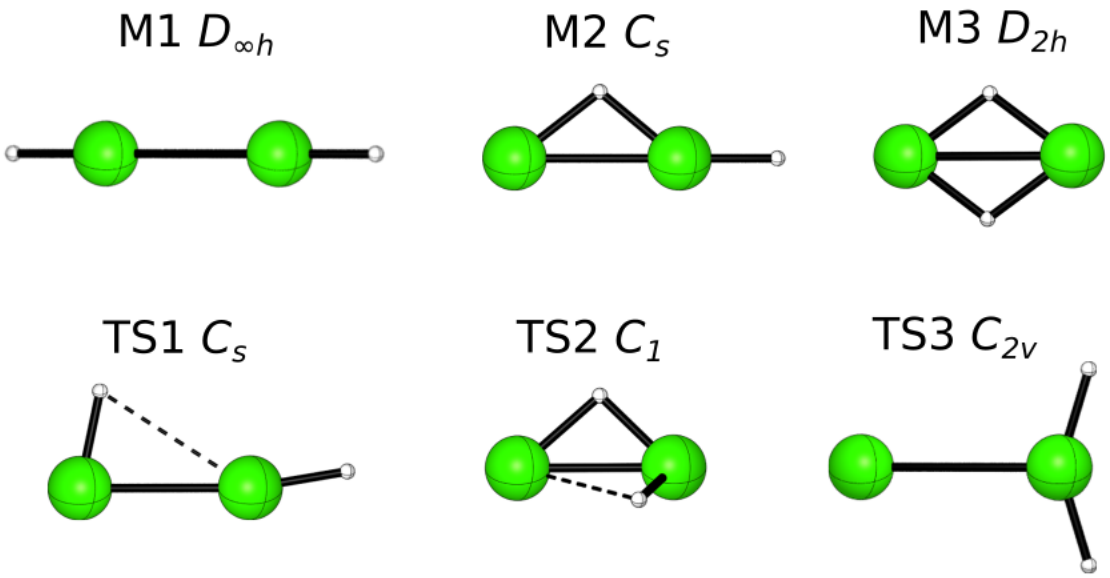

Figure 3.1: Qualitative geometries of Ca_2H_2 stationary points. Bond lengths and angles are given in Table 3.4.

Table 3.4: Internal coordinates (in Å and degrees) of Ca_2H_2 constitutional isomers.

Species	Ca–Ca	Ca–H_t[a]	∠CaH_bCa[a]
M1 [HCaCaH]	3.733	2.024	
M2 [HCa(μ_2−H)Ca]	3.404	2.020	102.6
M3 [Ca(μ_2−H)$_2$Ca]	3.481		106.7
TS1 (M1→M2)	3.517	2.017	
TS2 (M2→M3)	3.183	2.012	94.9
TS3 (M2→M2)	4.049	2.051	

[a] H_t and H_b respectively indicate a terminal hydrogen and a bridging hydrogen

Table 3.5: Enthaplies at 0 K (ΔH_{0K}) in kcal mol^{-1} of Ca_2H_2 isomers. CBS denotes the CCSD(T)/CBS relative energy. δ denotes the change in relative energy with respect to the preceding level of theory or various additional corrections. See Methods section for details.

Species	CBS	$\delta_{T(Q)}$	δ_{CR}	δ_{DBOC}	δ_{ZPVE}	Total
2 CaH	28.93	0.16	0.82	0.15	−2.67	27.23
CaH_2 + Ca	8.20	0.32	−0.00	0.01	−2.56	5.97
TS1 (M1 → M2)	7.55	−0.11	−0.37	0.14	−2.24	5.27
TS2 (M2 → M3)	1.82	−0.19	−0.88	0.18	−0.93	0.01
TS3 (M2 → M2)	2.98	0.15	−0.36	0.10	−2.07	0.62
M1 [HCaCaH]	−2.92	0.10	−0.19	0.11	−1.67	−4.58
M2 [HCa(μ_2−H)Ca]	−9.36	−0.06	−0.68	0.14	−1.08	−11.04
M3 [Ca(μ_2−H)$_2$Ca]	−16.76	0.10	−1.33	0.36	0.20	−17.43
Ca_2 + H_2	0.00	0.00	0.00	0.00	0.00	0.00

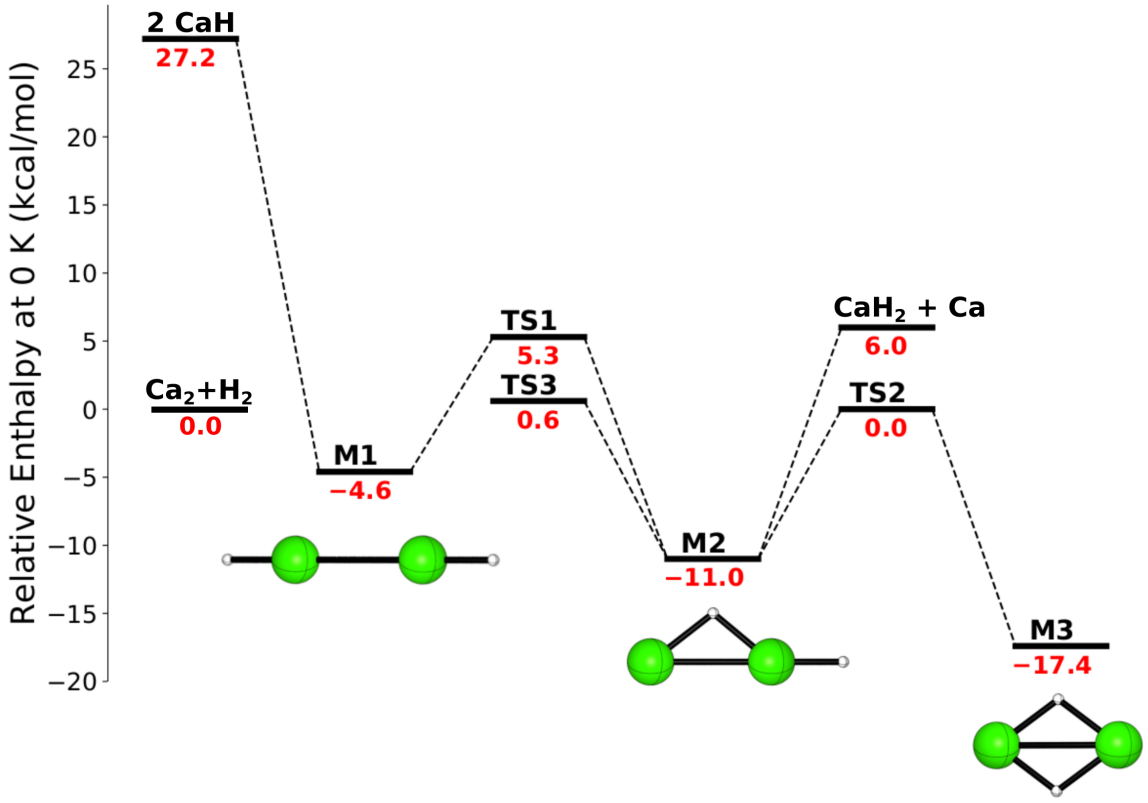

Figure 3.2: Potential enthalpy diagram for Ca_2H_2 at 0 K. TS3 connects M2 to M2'

All three constitutional isomers are thermodynamically favored over the dissociation products, 2 CaH, CaH_2 + Ca, or Ca_2 + H_2. Relaxed potential surface scans revealed the addition of 2 CaH → M1 and CaH_2 + Ca → M2 to proceed without an entrance barrier. On the other hand, it should be noted that the direct insertion of H_2 into Ca_2 is forbidden in C_{2v} symmetry on the ground state potential surface and will encounter a substantial entrance barrier. The dibridged structure is the lowest in enthalpy followed by the monobridged, then linear structures. As previously mentioned, this relative ordering is different than the isovalent Mg_2H_2 and Be_2H_2 isomers,[94,95] but similar to the heavier alkaline earth metal hydrides Sr_2H_2 and Ba_2H_2.[88] The relative differences in enthalpies from monobridged to linear and from dibridged to monobridged are 6.5 and 6.4 kcal mol^{-1}, respectively. These may be compared with the results Magnusson and Petrie[99] obtained with the G2 method: 6.6 and 9.0 kcal mol^{-1}.

A C_{2v} branched ("vinylidene-like") geometry was also optimized for Ca_2H_2. The branched geometry lies 5.2 kcal mol^{-1} above the enthalpy of the linear Ca_2H_2 isomer, but 5.4 kcal mol^{-1} below the dissociation to CaH_2 + Ca. However, this stationary point features a symmetry breaking imaginary mode and was identified as the transition state (TS3) connecting similar monobridged structures. This is in contrast to the heavier alkaline earth metal hydrides Sr_2H_2 and Ba_2H_2, which both exhibit[88] branched minima with B3LYP.

At a photolysis wavelength of 580 nm, Xiao et al[87] observed a bright peak centered at 1237 cm^{-1} in a Kr matrix. By adjusting the H_2 pressure and Ca concentration as well as by replacing H_2 with isotopologues, these authors assigned the 1237 cm^{-1} peak to linear Ca_2H_2. In a similar manner, Wang and Andrews[88] observed a peak at 1240 cm^{-1} in their neon matrix and assigned it to linear Ca_2H_2. The fundamental frequencies and intensities of Ca_2H_2 minima are provided in Table 3.6. Our VPT2 analysis predicts a bright absorption band for the asymmetric Ca-H stretch in linear Ca_2H_2 at 1245 cm^{-1}. This result agrees well

Table 3.6: Fundamental vibrational frequencies of Ca_2H_2 isomers with anharmonic intensities. Frequencies are given in cm^{-1} and intensities are given in km mol^{-1}.

Species	Frequencies (Intensities)
M1 [HCaCaH] linear	1264 (σ_g, 0), 1245 (σ_u, 1684), 167 (π_g, 0), 151 (σ_g, 0), 140 (π_u, 428)
M2 [HCa(μ_2−H)Ca] monobridged	1270 (a', 742), 985 (a', 17), 792 (a', 832), 220 (a', 251), 159 (a', 28), 144 (a'', 318)
M3 [Ca(μ_2−H)$_2$Ca] dibridged	1005 (b_{3u}, 41), 985 (a_g, 0), 956 (b_{1g}, 0), 801 (b_{2u}, 123), 422 (b_{1u}, 5), 217 (a_g, 0)

with the band observed in solid neon (1240 cm^{-1})[88] and krypton (1237 cm^{-1}),[87] given the expected red-shift of the bands due to the neon and krypton matrices.

While both matrix isolation studies made assignments for the linear Ca_2H_2 asymmetric stretching frequency, neither study assigned frequencies to the lower in energy monobridged or dibridged Ca_2H_2 isomers. The monobridged structure has bright absorption bands at 1270 and 792 cm^{-1}, corresponding to the Ca-H stretch and Ca-H-Ca stretches, respectively. The most intense vibrational mode of the dibridged constitutional isomer is the Ca-H-Ca asymmetric stretch at 801 cm^{-1}, which is similar to the Ca-H-Ca stretch of the monobridged structure. While the 1270 cm^{-1} monobridged Ca-H stretch might coincide with the linear Ca_2H_2 asymmetric stretch, neither experimental study reported peaks in the 800-750 cm^{-1} region where the Ca-H-Ca stretching frequencies would occur. Therefore, the absence of a vibrational band around 800 cm^{-1} in both studies suggests that the monobridged and dibridged Ca_2H_2 isomers were not present in any matrix. This result is especially perplexing, because in related studies with isovalent magnesium hydride, the dibridged Mg_2H_2 structure was observed alongside the linear Mg_2H_2 structure even though the dibridged Mg_2H_2 structure is higher in energy.[97]

It is currently unclear how Ca_2H_2 is produced, but the lack of experimental observation (despite substantial predicted oscillator strength) of the bridged Ca_2H_2 calcium hydrides

suggests that the linear Ca_2H_2 is initially produced and is kinetically hindered from converting to the enthalpically favored monobridged or dibridged structures. One possibility is that the photolysis source excites the calcium dimer to the $^1\Sigma_u^+$ or $^1\Pi_u$ state,[128] allowing the calcium dimer to react with H_2. An alternative mechanism would be two calcium monohydride monomers are initially formed from the photolysis of calcium in the matrix and recombine to produce Ca_2H_2. In either case, the excess internal energy released from the formation of linear Ca_2H_2 isomer would need to be quenched by the matrix before the linear structure isomerizes to a more favorable isomer. In Figure 3.2, we have assumed the latter to be the principle mechanism for Ca_2H_2 production. Transition states between Ca_2H_2 species were optimized in order to determine the feasibility of interconversion between these constitutional isomers. The barriers from the linear to monobridged structure (TS1) and from the monobridged to dibridged structure (TS2) were determined to be 9.9 and 11.0 kcal mol^{-1}, respectively. Given the moderate barrier to interconversion, it is plausible that the excess internal energy from the photolytic reaction of $Ca_2 + H_2 \rightarrow Ca_2H_2$ dissipates into the surrounding matrix before the linear isomer can undergo interconversion to a more thermodynamically stable isomer. Nevertheless, it is conceivable that the monobridged and dibridged isomers could be produced within these matrices through tunneling of the hydrogen atoms. We suggest that future studies examine the timescales for tunneling between the linear isomer to the monobridged and dibridged structures.

The monobridged and dibridged structures are more likely to be produced in the gas phase, where the excess internal energy would not be quenched as quickly. The monobridged structure has a a permanent dipole moment of 2.79 Debye units whereas the other Ca_2H_2 isomers do not have a dipole moment. Because the Ca-H-Ca stretching frequencies of the dibridged and monobridged isomer are very similar, microwave spectroscopy could be used to distinguish the monobridged Ca_2H_2 isomer from the dibridged isomer in the gas phase. We

Table 3.7: Internal coordinates (in Å and degrees) of Ca_2H_4 constitutional isomers.

Species	Ca–Ca	Ca–H_t[a]	∠CaH_bCa[a]
M4 [HCa(μ_2−H)$_2$CaH]	3.438	2.032	103.3
M5 [Ca(μ_2−H)$_3$CaH]	3.006	2.048	86.7
M6 [Ca(μ_2−H)$_4$Ca]	2.655		75.4
TS4 (M4→M5)	3.233	2.034	96.4
TS5 (M5→M6)	2.753		78.9
TS6 (M5→M5)	3.323	2.093	97.6

[a] H_t and H_b respectively indicate a terminal hydrogen and a bridging hydrogen

encourage future experimental characterizations of calcium hydride to attempt to observe monobridged and dibridged Ca_2H_2 in the gas phase.

Three minima and transition states were optimized on the Ca_2H_4 surface: dibridged (M4, D_{2h}), tribridged (M5, C_{3v}), and tetrabridged (M6, D_{4h}). The geometries of Ca_2H_4 stationary points are depicted in Figure 3.3 and the relevant internal coordinates for Ca_2H_4 stationary points are given in Table 3.7. There is a clear trend in Table 3.7; as the number of bridging hydrogens is increased, the Ca–Ca bond distance and Ca-H-Ca bond angle both decrease. These trends can be intuitively assigned to the increased electrostatic attraction between calcium and hydrogen and increased electrostatic repulsion of bridging hydrogens, respectively. The relative enthalpies of these Ca_2H_4 stationary points are calculated in Table 3.8 and illustrated in Figure 3.4. We have assumed that dibridged Ca_2H_4 (M4) is directly produced from the dimerization of two CaH_2 monomers. Alternatively, tribridged Ca_2H_4 (M5) could also result from the dimerization of CaH_2, but a relaxed potential surface scan suggested that the direct production of dibridged Ca_2H_4 (M4) is more favorable. All three structures are bound with respect to dissociation to Ca_2 + 2 H_2 or two CaH_2 monomers; however, the dibridged and tribridged isomers are significantly more thermodynamically favorable than the tetrabridged isomer.

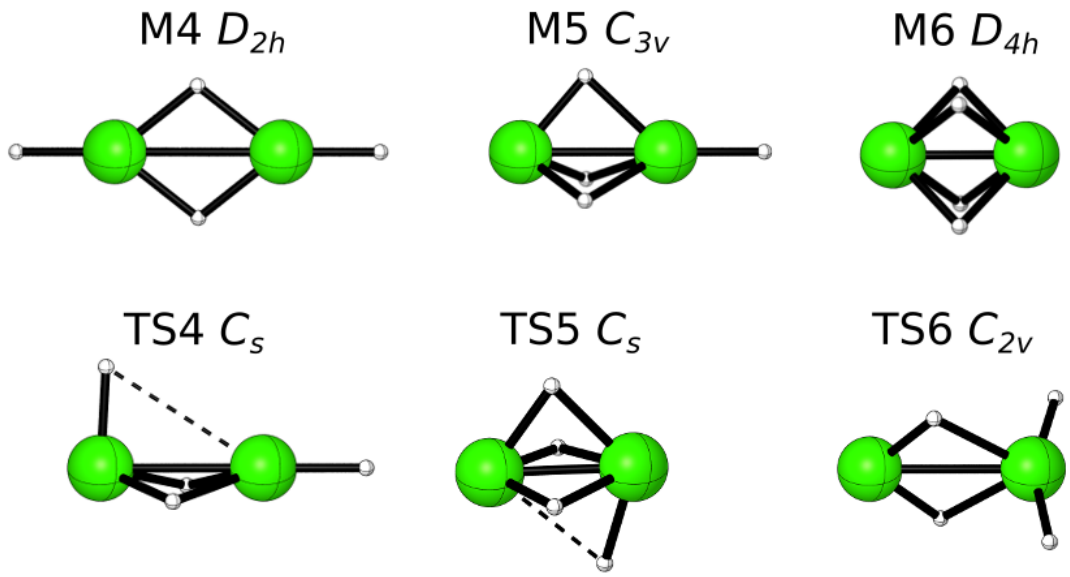

Figure 3.3: Qualitative geometries of Ca_2H_4 stationary points. Bond lengths and angles are given in Table 3.7.

Table 3.8: Enthaplies at 0 K (ΔH_{0K}) in kcal mol^{-1} of Ca_2H_4 isomers. CBS denotes the CCSD(T)/CBS relative energy. δ denotes the change in relative energy with respect to the preceding level of theory or various additional corrections. See Methods section for details.

Species	CBS	$\delta_{T(Q)}$	δ_{CR}	δ_{DBOC}	δ_{ZPVE}	Total
2 CaH_2	13.55	0.30	−0.33	0.18	−5.03	8.67
TS6 (M5 → M5)	−7.77	0.10	−1.82	0.20	−1.42	−10.72
TS5 (M5 → M6)	−16.63	−0.10	−2.40	0.23	0.34	−18.57
M6 [$Ca(\mu_2{-}H)_4Ca$]	−19.95	−0.12	−2.48	0.24	0.90	−21.40
TS4 (M4 → M5)	−34.50	0.13	−1.88	0.20	−0.70	−36.76
M4 [$HCa(\mu_2{-}H)_2CaH$]	−39.65	0.20	−2.08	0.20	−1.20	−42.54
M5 [$HCa(\mu_2{-}H)_3Ca$]	−41.78	0.08	−2.14	0.21	0.29	−43.34
Ca_2 + 2 H_2	0.00	0.00	0.00	0.00	0.00	0.00

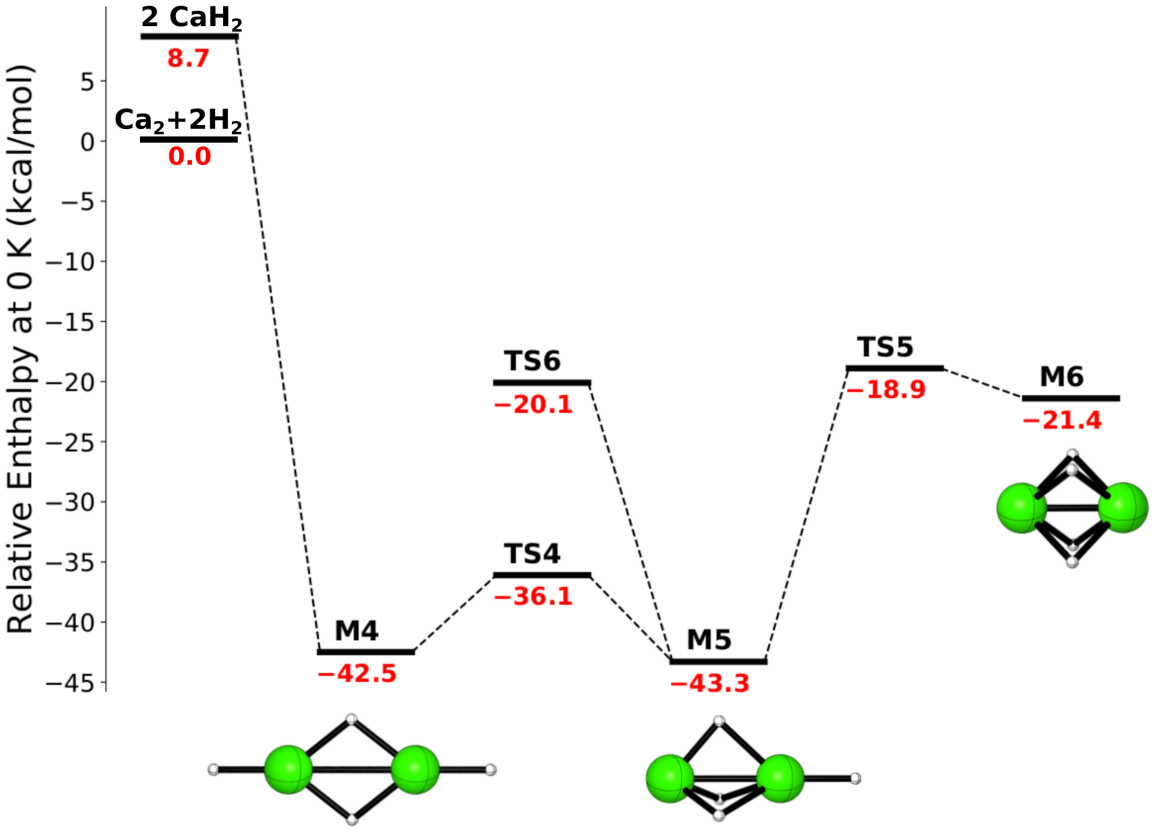

Figure 3.4: Potential enthalpy diagram for Ca_2H_4 at 0 K. TS6 connects M5 to M5'

In addition to the three Ca_2H_4 minima, we optimized a C_{2v} symmetric stationary point with two terminal hydrogens on the same calcium atom. This stationary point lies slightly above the energy of the tetrabridged Ca_2H_4 isomer, and is bound with respect to dissociation. In accord with the results of Kaupp and Schleyer,[100] this stationary point has a symmetry breaking imaginary frequency leading to the tribridged isomer (M5). Thus the C_{2v} structure was identified as a transition state (TS6) directly connecting tribridged isomers.

Previous theoretical computations disagreed whether the dibridged or tribridged structure would be the global minimum. Table 3.9 shows a focal point comparison of the tribridged electronic energy relative to the dibridged electronic energy. At the CCSDT(Q)/DZ level of theory the dibridged structure is lower in energy. However, as we increase the size of the basis set the tribridged structure becomes increasingly more favorable. This trend is related to the increase in polarizability following the addition of basis functions. As the basis set is enlarged, the computed polarizability of the calcium atoms is increased,[129] which lowers the energy of the tribridged and tetrabridged structures relative to the dibridged structure. By examining the incremental changes in energy in Table 3.9, we observe a tight convergence of the electronic energy to both the complete basis set (CBS) and full configuration interaction (FCI) limits. We can estimate the margin of error as the largest incremental correction (excluding δ_{ZPVE}) when calculating $\Delta H_{0\mathrm{K}}$. The largest correction comes from the extrapolation of the CCSD(T) energies to the complete basis set limit which is approximately 0.24 kcal mol^{-1}; thus we can be confident that the tribridged constitutional isomer is the lowest energy isomer at 0K.

While the tribridged isomer is enthalpically favored at low temperatures, it should be noted that the dibridged isomer has a larger entropy. As the temperature is increased the Gibbs free energy [$\Delta G(T)$] between the tribridged and dibridged structure is reduced. Around 300 K, the dibridged structure has the more favorable ΔG, indicating that equilibrium will tend toward the dibridged isomer at moderate to high temperatures.

Table 3.9: Focal Point Analysis (FPA) of tribridged Ca_2H_4 (M5) relative to dibridged Ca_2H_4 (M4). Energies are in kcal mol^{-1}. The symbol δ indicates an incremental change in energy from the preceding level of theory.

Basis	ΔE_e HF	$+\delta$ MP2	$+\delta$ CCSD	$+\delta$ (T)	$+\delta$ T	$+\delta$ (Q)	ΔE_e Net
DZ	+4.41	−3.19	+0.92	−0.48	−0.07	−0.03	[+1.56]
TZ	+4.07	−5.30	+1.10	−0.78	−0.09	[−0.03]	[−1.03]
QZ	+3.91	−5.80	+1.12	−0.88	[−0.09]	[−0.03]	[−1.77]
5Z	+3.89	−5.98	+1.12	−0.92	[−0.09]	[−0.03]	[−2.01]
CBS	[+3.89]	[−6.17]	[+1.12]	[−0.96]	[−0.09]	[−0.03]	[−2.25]

$\Delta H_{0K} = \Delta E_{FPA} + \delta_{CR} + \delta_{DBOC} + \delta_{ZPVE} + \delta_{VPT2}$
$-2.25 - 0.06 + 0.01 + 1.49 - 0.06 = -0.87$ kcal mol^{-1}

Dibridged Ca_2H_4 is principally formed from the barrierless dimerization of CaH_2 within the matrix. The interconversion of the dibridged to tribridged is hindered by an energetic barrier of 6.8 kcal mol^{-1} corresponding to TS4; however, this barrier is submerged significantly below the energy released from the dimerization of CaH_2 (51.6 kcal mol^{-1}). If the dissipation of internal energy to the matrix is slow relative to the rearrangement of vibrational energy within the molecule, then the Ca_2H_4 will be able to rearrange from the dibridged structure to the energetically favorable tribridged structure. On the other hand, if the matrix quickly dissipates the internal energy of Ca_2H_4, it would become kinetically trapped as the dibridged isomer. Since the dissipation rate is dependent on the polarizability of the matrix gas, it is more likely to observe the tribridged isomer in the lighter matrices such as neon and the dibridged isomer in heavier matrices such as krypton.

The fundamental vibrational frequencies of the Ca_2H_4 minima are provided in Table 3.10. Both matrix isolation infrared spectroscopy studies assigned several peaks to Ca_2H_4. However, previous authors were unable to differentiate whether these peaks arose from the dibridged or tribridged Ca_2H_4 isomers. Table 3.11 lists experimental frequencies assigned to Ca_2H_4 along with the most similar dibridged and tribridged fundamental frequency computed in this study. By comparing the neon, argon, and krypton frequencies, it appears the gas-

Table 3.10: Fundamental vibrational frequencies of Ca_2H_4 isomers with anharmonic intensities. Frequencies are given in cm^{-1} and intensities are given in km mol^{-1}.

Species	Frequencies (Intensities)
M4 [HCa(μ_2−H)$_2$CaH]	1276 (a_g, 0), 1258 (b_{3u}, 566), 1056 (b_{3u}, 1486), 1023 (a_g, 0)
dibridged	952 (b_{1g}, 0), 876 (b_{2u}, 844), 496 (b_{1u}, 732), 245 (b_{3g}, 0)
	229 (b_{2u}, 661), 207 (a_g, 0), 115 (b_{1u}, 652), 107 (b_{2g}, 0)
M5 [HCa(μ_2−H)$_3$Ca]	1223 (a', 551), 1168 (a', 39), 1074 (e, 502), 850 (a', 1122),
tribridged	682 (e, 87), 593 (e, 700), 255 (a', 0), 239 (e, 283)
M6 [Ca(μ_2−H)$_4$Ca]	1099 (a_{1g}, 0), 884 (e_u, 970), 852 (a_{2u}, 1150), 879 (b_{1g}, 0)
tetrabridged	822 (b_{1g}, 0), 681 (e_u, 687), 565 (e_g, 0), 359 (b_{2u}, 0), 305 (a_{1g}, 0)

Table 3.11: Comparison of experimentally observed Ca_2H_4 bands to VPT2 CCSD(T) frequencies for dibridged and tribridged Ca_2H_4. Frequencies are given in cm^{-1}. The VPT2 frequency closest to the experimentally observed frequency is indicated in bold.

Experiment			M4 dibridged		M5 tribridged	
Ne[a]	Ar[a]	Kr[b]	ν	% Error	ν	% Error
1221			1258	3.0%	**1223**	0.2%
1072	1070		1056	1.5%	**1074**	0.2%
	1057	1044	**1056**	0.1%	1074	1.6%
878	874	870	**876**	0.2%	850	3.2%

[a] Wang and Andrews[88]
[b] Xiao et al[87]

phase fundamental frequencies are red-shifted with the increasing polarizability of the matrix environment. Peaks 1 and 2 can be confidently assigned to the tribridged structure, however, 3 and 4 are more accurately attributed to the tribridged structure. Furthermore, the 1258 cm^{-1} frequency of the tribridged isomer and the 1223 cm^{-1} frequency of the dibridged isomer overlap respectively with the CaH stretching frequency (1253 cm^{-1}) and the CaH_2 asymmetric stretching frequency (1215 cm^{-1}). The only Ca_2H_4 VPT2 frequency that is not easily accounted for in the neon and argon matrices is the 850 cm^{-1} frequency of the tribridged isomer, however it is possible that this frequency is blue-shifted to coincide with the 876 cm^{-1} frequency of the dibridged isomer.

Based on the comparison in Table 3.11 it is clear that neither the dibridged nor tribridged structure is solely responsible for all the Ca_2H_4 peaks observed in the neon and argon matrices. Instead, the most plausible explanation is the dibridged and tribridged structures exist in roughly equal magnitudes and collectively describe all the Ca_2H_4 peaks that have been observed in these matrices. On the other hand, in the krypton matrix there is no conclusive evidence for the tribridged isomer, suggesting that only the dibridged Ca_2H_4 isomer is present. The lack of observation of the tribridged isomer in the krypton matrix is consistent with our understanding that the heavier matrices are more likely to kinetically trap the dibridged isomer.

In the gas phase, interconversion between the dibridged and tribridged isomers would not be hindered from vibrational quenching by the matrix. Therefore at low temperatures we would expect to observe predominantly the tribridged isomer in the gas phase. Only the tribridged isomer of Ca_2H_4 has a permanent dipole moment (10.72 Debye units), thus microwave spectroscopy could be used in the gas phase to distinguish between the tribridged and dibridged Ca_2H_4 isomers.

3.5 Conclusions

Three interconvertible isomers were identified for Ca_2H_2. Of these three structures, the dibridged structure was the most enthalpically favored at 0 K, followed by the monobridged structure, and last (surprisingly) the observed linear structure. Despite the thermodynamic favorability of the monobridged and dibridged structures, there is currently only conclusive evidence for the linear Ca_2H_2 structure from the photolysis of calcium in excess hydrogen. We suggest that the linear isomer is intially produced, but is incapable of converting to the more thermodynamically favored constitutional isomers due to vibrational quenching from the matrix. A major goal of future experimental studies is to observe the monobridged and dibridged structures.

Three constitutional isomers for Ca_2H_4 were similarly studied. A near-degeneracy exists between the dibridged and tribridged structures of Ca_2H_4 with the tribridged structure only 0.87 kcal mol^{-1} below the enthalpy of the dibridged structure. Comparison of our VPT2 fundamental frequencies to the unassigned experimental infrared bands from prior studies indicates the coexistence of dibridged and tribridged Ca_2H_4 structures in neon and argon matrices, but only the dibridged structure is observed in a krypton matrix. The results presented in this study should be utilized by future experimental efforts to observe and characterize Ca_2H_2 and Ca_2H_4 species.

Chapter 4

Mechanisms of the Ethynyl Radical Reaction with Molecular Oxygen

4.1 Abstract

The ethynyl radical, C_2H, is a key intermediate in the combustion of various alkynes. Once produced, the ethynyl radical will rapidly react with molecular oxygen to produce a variety of products. This research presents the first comprehensive high level theoretical study of the reaction of the C_2H ($^2\Sigma^+$) radical with molecular oxygen ($^3\Sigma_g^-$). Correlation methods as complete as CCSDT(Q) were used; basis sets as large as cc-pV6Z were adopted. Focal point analysis was employed to approach relative energies within the bounds of chemical accuracy ($\leq$ 1 kcal mol^{-1}). Two dominate reaction pathways from the ethynyl peroxy radical include oxygen–oxygen cleavage from the ethynyl peroxy radical that is initially formed to produce HCCO ($^2A''$) and O (^3P) and an isomerization of the ethynyl peroxy radical to eventually yield HCO ($^2A'$) and CO ($^1\Sigma^+$). The branching ratio between these two competitive reaction pathways was determined to be 1:1 at 298 K. Minor reaction pathways leading to the production of CO_2 ($^1\Sigma_g^+$) and CH ($^2\Pi$, $^4\Sigma^-$, $^2\Delta$) were also characterized. The absence of CCO ($^3\Sigma^-$) and OH ($^2\Pi$) was explained in terms competition with more accessible reaction pathways.

4.2 Introduction

As one of the most abundant polyatomic molecules in the universe,[130] C_2H appears in interstellar clouds,[131–135] carbon-rich stars,[136,137] and low temperature planetary atmospheres such as that of Jupiter and Titan.[138–142] In combustion environments, the ethynyl radical is formed during the oxidation of various alkynes.[143] The most notable reaction involving the ethynyl radical is the combustion of acetylene/O_2 flames. The ethynyl radical can subsequently react with oxygen to form the variety of thermodynamically favorable products identified below:

$$
\begin{aligned}
C_2H + O_2 &\rightarrow HCCO + O & \Delta H_{0K} &= -33.5 \text{ kcal mol}^{-1} \\
&\rightarrow CCO + OH & &-35.9 \text{ kcal mol}^{-1} \\
&\rightarrow CO_2 + CH & &-87.0 \text{ kcal mol}^{-1} \\
&\rightarrow 2\ CO + H & &-137.5 \text{ kcal mol}^{-1} \\
&\rightarrow HCO + CO & &-152.1 \text{ kcal mol}^{-1}
\end{aligned}
$$

Of these potential products, HCCO, CH, CO_2, and CO have been directly observed in the laboratory.[144–151] Kinetic studies for the reaction $C_2H + O_2$ have reported large rate constants with slight negative temperature dependences,[151–154] suggesting the formation of the initial complex of this reaction has a negligible barrier. Furthermore, experimental studies have shown that the rate constant for this reaction is pressure independent,[152,153] which implies that the initially formed complex decomposes rapidly and that re-dissociation into the reactants is prohibitive.

The highly exothermic nature of these reactions often leaves the products in excited electronic or vibrational states.[145,149] The most noticeable electronically excited product is CH ($A\ ^2\Delta$). The electronic relaxation of CH ($A\ ^2\Delta \rightarrow X\ ^2\Pi$) is responsible for the emission of bright blue light (435 nm) that is produced in oxo-acetylene flames. Chemiluminescent CH ($A\ ^2\Delta$) from the reaction $C_2H + O_2$ is regularly used in kinetics studies for time-resolved monitoring of C_2H concentration.[155–158] Hence, the specific reaction $C_2H + O_2 \rightarrow CO_2 + CH\ (^2\Delta)$ has received multiple kinetics studies.[159–161] While there has been a plethora of experiments devoted to this reaction, no theoretical study has sought to explain the production of CH ($^2\Delta$). To produce the methylidene in an excited state, the ground state C_2HO_2 adduct must undergo a surface crossing.[161] However, the location of the intersection between these electronic states has not been established. In order to provide a more complete model, we considered multiple electronic surfaces in our investigation of the $C_2H + O_2$ reaction.

In 1998, Peeters and coworkers[162] published the first theoretical study on the reaction of C_2H and O_2. They used the B3LYP functional with the 6-311++G(d,p) basis set

to optimize stationary points, obtain harmonic vibrational frequencies, and compute relative energies. Later, in 2004, Li and coworkers[163] examined the same reaction also using B3LYP/6-311++G(d,p) to compute equilibrium geometries and harmonic vibrational frequencies; however, they appended QCISD(T)/6-311++G(d,p) corrections to improve the accuracy of their energies. Despite using similar levels of theory, these authors predicted two qualitatively different potential energy surfaces (see Figure 4.1). Discrepancies in their potential energy surfaces led the authors to fundamentally different conclusions concerning the relative yields of the products. In order to resolve the discrepancy between the current theoretical models and to provide reliable energies for future kinetic models, we have comprehensively characterized the reaction of C_2H with O_2 using highly reliable ab initio methods.

The most favorable initial reaction is for the triplet oxygen to attack the radical center on the terminal carbon of the ethynyl to form the ethynyl peroxy radical (labeled M1, see Figure 4.1). Since the bond is formed between two radical centers, the reaction is expected to proceed without an entrance barrier. At this stage, the oxygen–oxygen bond can cleave, producing the ketenyl radical (HCCO) and atomic oxygen. However, if the ethynyl peroxy radical persists, the reaction will continue through either a COO three-membered ring (dioxirenyl, S1) or a CCOO four-membered ring (dioxetenyl, S3). The former was shown by the previous theoretical studies[162,163] to readily form from the energized ethynyl peroxy radical. The latter requires an isomerization of the hydrogen on the ethynyl peroxy radical; however, experimental studies on deuterated ethynyl demonstrated negligible isotopic dependence, which suggests that a hydrogen isomerization is not along the main reaction pathway.[153] Alternatively, the oxygen can attach to the intermediate carbon and subsequently form the four-membered CCOO ring (dioxetenyl, S3), but this addition is unlikely to compete with the barrierless addition of the oxygen to the terminal carbon, especially at low temperatures.

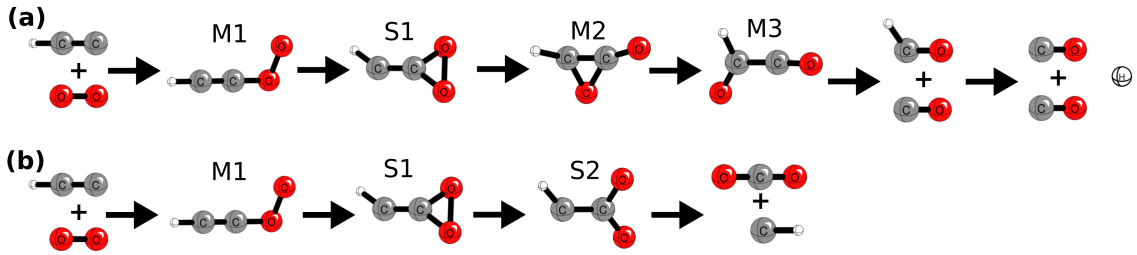

Figure 4.1: Minimum energy pathway according to (a) Peeters and coworkers[162] and (b) Li and coworkers.[163] Stationary points have been labeled with the convention used in this study.

As stated earlier, the existing theoretical models disagree concerning the fate of dioxirenyl. Here we summarize the results from the two studies. Peeters and coworkers[162] state that a cleavage of the oxygen-oxygen bond on dioxirenyl (S1) results in the formation of a CCO three-membered ring (oxyrenyloxy, M2). This new isomer readily undergoes another ring-opening reaction with a minimal barrier, leading to oxo-ketene (M3, [HC(O)CO]). The vibrationally excited oxo-ketene then decomposes into carbon monoxide and a formyl radical (HCO). Alternate pathways include direct dissociation from the CCO three-membered ring into CO_2 and CH or a series of unfavorable isomerizations from the oxo-ketene (M3) leading to C_2O and OH. These alternatives face significantly larger barriers and are expected to contribute minimally to the overall reaction.

Li and coworkers[163] did not find the same CCO three-membered ring. Instead, they suggested the oxygen-oxygen bond cleaving of dioxirenyl creates a HCC(O)O carbene (S2). This carbene easily dissociates into the main products CO_2 and CH, but can also isomerize into carbohydroxycarbyne [HOC(O)C, M4]. Carbohydroxycarbyne can then dissociate into ketenylidene (CCO) and a hydroxyl radical (OH), but will primarily isomerize to oxo-ketene, ultimately producing carbon monoxide.

While these two studies agree that the same products are possible, qualitative differences between their potential energy surfaces result in different expectations for the relative abun-

dances of carbon monoxide and carbon dioxide. Furthermore, quantitative differences in the relative barrier heights for the dissociation of the ethynyl peroxy radical dramatically change the predicted abundance of HCCO reported by the different authors. In this study, we have considered pathways from both of the previous studies in an attempt to transform their potential energy surfaces into one comprehensive model for this reaction.

4.3 Methods

Restricted Hartree–Fock (RHF) and restricted open-shell Hartree–Fock (ROHF) methods were used, respectively, to describe the reference electronic wave functions of the closed-shell and open-shell species. Equilibrium geometries of stationary points (both minima and transition states) were optimized with CFOUR 1.0[110] using coupled cluster with single, double, and perturbative triple excitations [CCSD(T)][164,165] and the ANO2 basis set.[166] The ANO family of basis sets from Almlöf and Taylor refers to various truncations of the set of atomic natural orbitals. The ANO0, ANO1, and ANO2 basis sets are comparable in size to the cc-pVDZ, cc-pVTZ, and cc-pVQZ basis sets of Dunning and coworkers,[12] respectively, the former having more Gaussian primitives per contraction.

Harmonic vibrational frequencies were obtained for the CCSD(T)/ANO1 optimized geometries at the same level of theory using finite difference of analytic gradients. These frequencies were used to characterize the stationary points as minima or transition states. The lowest energy pathways between minima connected by a transition state were computed through the intrinsic reaction coordinate (IRC) method[167,168] as implemented in PSI4.[169] CCSD(T)/ANO0 analytic gradients were used during the IRC procedure; these gradients were computed with the CFOUR 1.0 package through the PSI4/CFOUR interface. Natural Bond Order (NBO) analysis was carried out for various minima using NBO 5.0.[170] The NBO analysis was performed at CCSD(T)/ANO0 optimized geometries using CCSD/cc-pVDZ densities computed with Q-CHEM 5.0.[171]

Electronic energies of stationary points along the $C_2H + O_2$ reaction were computed according to the focal point analysis (FPA) of Allen and coworkers.[23–26] The focal point analysis is designed to systematically converge to both the electron correlation limit and the basis set limit. Electron correlation methods up to CCSDT(Q) and basis sets as large as cc-pV6Z were used in this study. Complete basis set (CBS) energies were obtained for various correlation treatments by extrapolating the Hartree–Fock energies and correlation energies using a three-point exponential equation[21] and a two-point inverse cubic equation,[22] respectively:

$$E_{\mathrm{ref}}(X) = E_{\mathrm{HF}}^{\infty} + ae^{-bX} \tag{4.1}$$

$$E_{\mathrm{corr}}(X) = E_{\mathrm{corr}}^{\infty} + aX^{-3} \tag{4.2}$$

The CCSDT(Q)/CBS energies were obtained through additive corrections for the expansion of the correlation treatment from perturbative triples [CCSD(T)] to full triples [CCSDT] (designated δ_{T}) and from full triples [CCSDT] to perturbative quadruples [CCSDT(Q)] (designated $\delta_{(\mathrm{Q})}$). These corrections were obtained using the cc-pVTZ and cc-pVDZ basis sets, respectively. The CCSDT(Q)/B ansatz was used for the CCSDT(Q) computations as recommended by Martin.[172] CCSD(T)/cc-pVXZ (X = D, T, Q, 5, 6) single point energies were computed using the MOLPRO 2010 quantum chemistry package.[70] The CCSDT/cc-pVTZ and CCSDT(Q)/cc-pVDZ corrections were obtained using the MRCC 2015 package.[111] The total electronic energy was calculated as the sum of the CCSD(T)/CBS energy and the CCSDT and CCSDT(Q) increments:

$$\Delta E_{\mathrm{CCSDT(Q)/CBS}} = \Delta E_{\mathrm{CCSD(T)/CBS}} + \delta_{\mathrm{CCSDT}} + \delta_{\mathrm{CCSDT(Q)}} \tag{4.3}$$

All of the above computations were carried out using the CCSD(T)/ANO2 starting point geometries.

Additional corrections were made to account for approximations used during the CCSD(T) computations. To account for the core-correlation neglected under the frozen-core approximation the CCSD(T)/cc-pCVQZ energies with all electrons correlated were computed (δ_{core}). A scalar relativistic correction (δ_{rel}) was obtained using second-order direct perturbation theory (DPT2)[27] at the CCSD(T)/cc-pCVQZ level of theory with all the electrons correlated. The limitations of the clamped-nuclei approximation were treated by an adiabatic diagonal Born–Oppenheimer correction (δ_{DBOC})[29,30] performed at the HF/ANO2 level of theory. Finally, the zero-point vibrational energy (δ_{ZPVE}) from the CCSD(T)/ANO1 harmonic vibrational frequencies was appended to obtain the relative enthalpies at 0 K ($\Delta H_{0\mathrm{K}}$):

$$\Delta H_{0\mathrm{K}} = \Delta E_{\mathrm{CCSDT(Q)/CBS}} + \delta_{\mathrm{CORE}} + \delta_{\mathrm{REL}} + \delta_{\mathrm{DBOC}} + \delta_{\mathrm{ZPVE}} \tag{4.4}$$

All multireference computations were performed with the MOLPRO 2010 package.[70] A complete active-space self-consistent field (CASSCF) reference wave function was used as the starting point for all multireference computations. The active space for the CASSCF computations initially consisted of the π-space of O_2 (6 electrons, 4 orbitals) and the π-space of the ethynyl radical (5 electrons, 5 orbitals). In C_s symmetry this becomes 11 electrons spread among 5 a' and 4 a'' orbitals. The CI coefficients of a CASSCF(11, 9) wave function were used as a diagnostic for potential multireference problems. If the ratio between C_1^2 and C_0^2 exceeded 0.2, the stationary point was treated with the methods described in this section. For these stationary points, single reference coupled cluster methods may be insufficient to describe the static correlation of the species.

In order to estimate barrier heights associated with multireference transition states, a relaxed scan was performed over the particular internal coordinate that best represented the reaction coordinate. For each coordinate a constrained geometry optimization was performed using second-order multireference perturbation theory (CASPT2).[173–175] The electronic en-

ergy at each optimized geometry was computed using multireference configuration interaction with single and double excitations including the Davidson correction (MRCISD+Q).[176–178]

To obtain accurate relative energies for multireference stationary points, we adopted a method by Klippenstein, Douberly, Harding, Miller, and co-workers first used to study the propargyl peroxy radical.[179,180] The geometry of each multireference stationary point was reoptimized using MRCISD+Q/cc-pVDZ. At each of these geometries, there was a low-lying quartet electronic state that was relatively single-reference. The electronic energy of the quartet electronic state was obtained using the focal point approach explained above. Then the doublet-quartet splitting was computed by comparing the MRCISD+Q(11,9)/cc-pVQZ energy for the different electronic states. Finally, the composite electronic energy of the doublet state was calculated by subtracting the doublet-quartet splitting from the CCSDT(Q)/CBS energy of the quartet state:

$$E^{Db}_{\text{composite}} = E^{Qt}_{\text{CCSDT(Q)/CBS}} - \left(E^{Qt}_{\text{MRCISD+Q/cc-pVQZ}} - E^{Db}_{\text{MRCISD+Q/cc-pVQZ}}\right) \tag{4.5}$$

The ground electronic state of the ethynyl peroxy radical is $^2A''$. However, at certain points along the potential energy surface, the $^2A'$ and $^4A''$ electronic surfaces intersect the $^2A''$ surface. The close proximity of these excited electronic surfaces enables non-adiabatic reaction paths to exist. In the case of $^2A'' \longleftrightarrow {}^2A'$ the symmetry-forbidden electronic transition is allowed through mixing of the states in C_1 symmetry and in the case of $^2A'' \longleftrightarrow {}^4A''$ the spin-forbidden intersystem crossing may be accomplished through spin-orbit coupling.[181,182] Dynamical calculations would quantify the contributions of these non-adiabatic reaction paths to the overall reaction mechanism; however, such calculations are outside the scope of this study.

Potential surface crossings were scanned for by computing the electronic energy of these states along the $^2A''$ IRC trajectories. Some low-lying stationary points on the $^2A'$ and $^4A''$ electronic surfaces were identified from the scans. To distinguish structures optimized on the

different electronic surfaces we have used the letters 'M', 'S', and 'Q' to denote minima on the $^2A''$, $^2A'$, and $^4A''$ electronic surfaces, respectively. Equilibrium geometries and harmonic vibrational frequencies for these stationary points were obtained using the same methods for the $^2A''$ stationary points.

4.4 Results and Discussion

The focal point tables for all of the stationary points showed excellent convergence to the CBS limit. The tables also display good convergence toward the full configuration interaction (FCI) limit as evidenced by the CCSDT(Q) correction. The relative enthalpies computed for the products (see Table 4.1) agree with experimental values within one kcal mol^{-1}, pointing to the accuracy of the methods used in this study. Overall we find the error in the relative enthalpies of species in this study to be within chemical accuracy ($\leq$1 kcal mol^{-1}).

The structures of minima and transition states are sketched in Figures 4.2 and 4.3, respectively. A potential enthalpy diagram for the reaction of C_2H + O_2 is shown in Figure 4.4. The relative enthalpies of the products, intermediates, and transition states are given in Tables 4.1, 4.2, and 4.3, respectively. The relative barrier heights for several reaction steps are compared in Table 4.4. The following sections describe the most thermodynamically favorable reaction pathways for the production of various products. It should be noted that dynamical calculations would provide further insight into the reaction mechanisms; however, such calculations are outside the scope of the present study.

The addition of O_2 to the terminal carbon on the ethynyl radical proceeds without an entrance barrier, forming the ethynyl peroxy radical (HCCOO, M1, see Figure 4.2). Upon formation of the ethynyl peroxy radical, the reaction will bifurcate between competing reaction pathways. The most direct decomposition pathway consists of an oxygen-oxygen cleavage on the ethynyl peroxy radical to produce a ketenyl radical (HCCO $^2A''$) and an oxygen atom (see Figure 4.5). The transition state for this decomposition (TS1) was identified

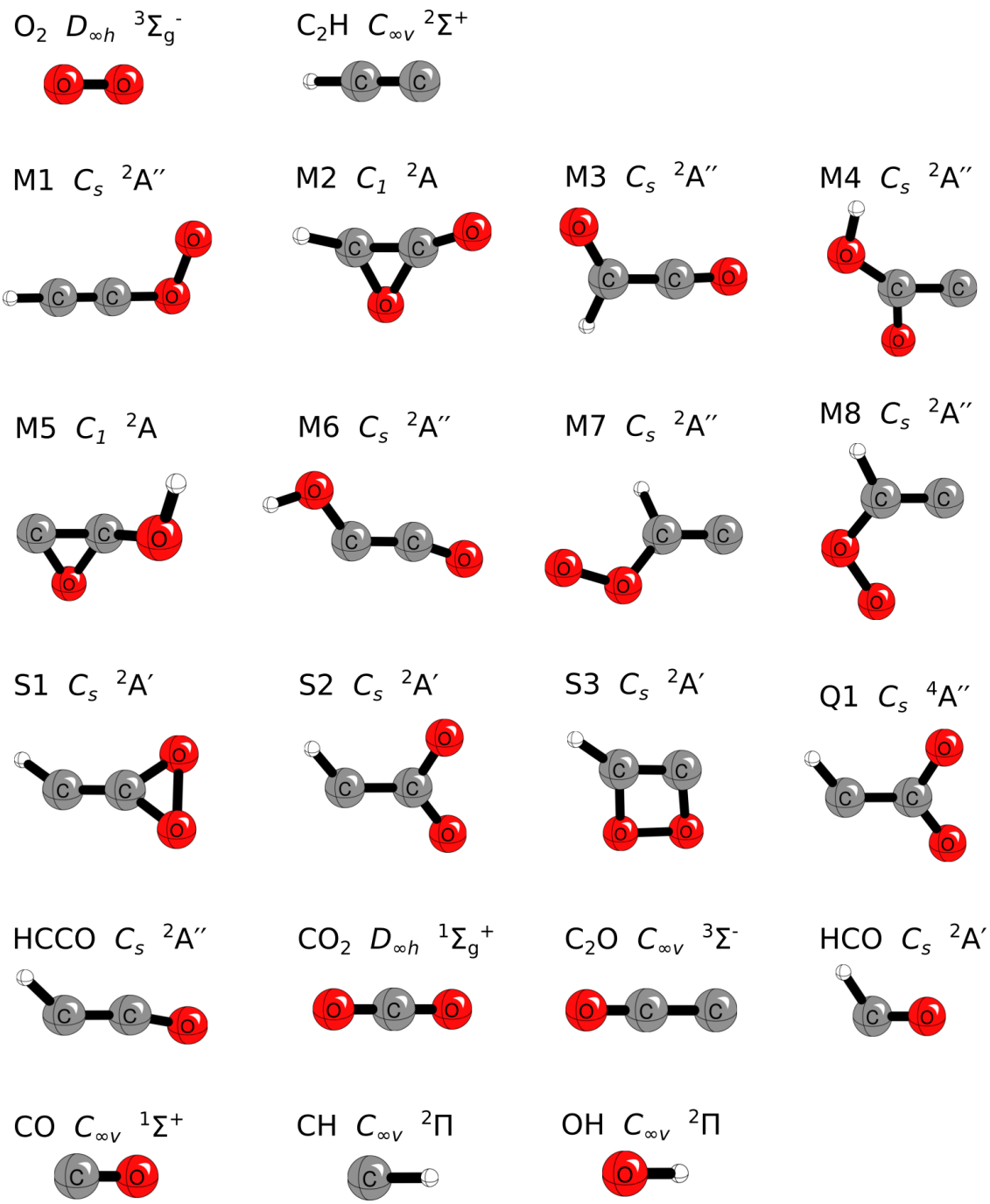

Figure 4.2: Qualitative geometries of minima along the $C_2H + O_2$ reaction pathways. 'M', 'S', and 'Q' correspond to C_2HO_2 minima on the $^2A''$, $^2A'$, and $^4A''$ electronic potential surfaces, respectively.

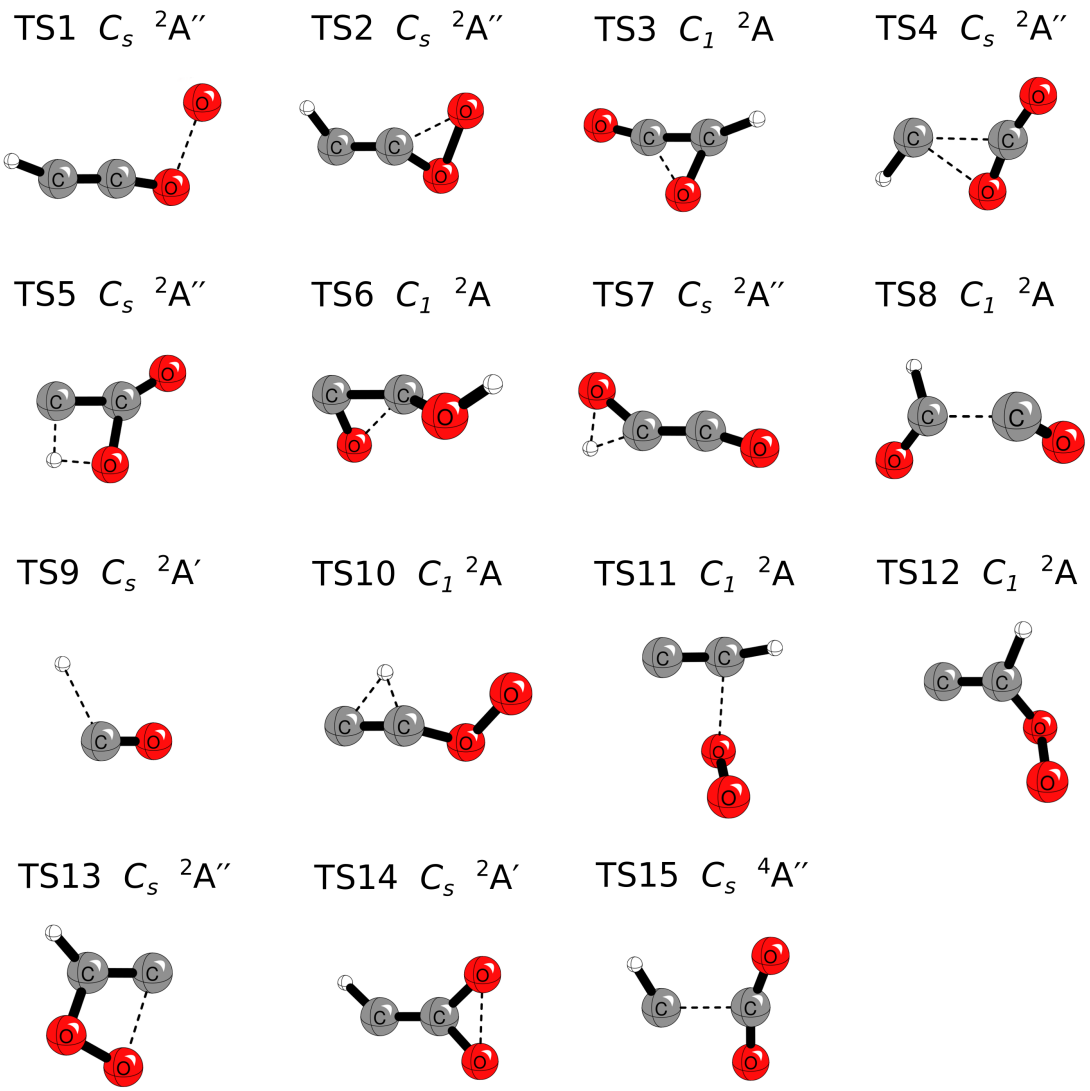

Figure 4.3: Qualitative geometries of transition states along the $C_2H + O_2$ reaction pathways.

Table 4.1: Enthaplies at 0 K (ΔH_{0K}) of products relative to reactants $C_2H + O_2$ in kcal mol^{-1}. CBS denotes the CCSD(T)/CBS relative energy. Delta (δ) denotes the change in relative energy with respect to the preceding level of theory or various additional corrections. See Methods section for details.

Product	CBS	δ_T	$\delta_{(Q)}$	δ_{CORE}	δ_{REL}	δ_{DBOC}	δ_{ZPVE}	Total	Exp.[a]
HCCO + O	−34.65	−0.26	0.90	−0.18	−0.03	0.07	0.62	−33.53	−33.5
CCO + OH	−36.23	−0.55	0.95	0.32	−0.08	0.03	−0.55	−36.11	−35.9
CO_2 + CH	−89.20	0.43	0.85	0.27	0.01	0.09	−0.20	−87.75	−87.0
2 CO + H	−134.40	0.62	0.82	0.30	0.01	−0.15	−5.27	−138.07	−137.5
HCO + CO	−153.51	0.28	0.81	0.09	−0.08	0.06	−0.16	−152.51	−152.1

[a] Active Thermochemical Tables [183]

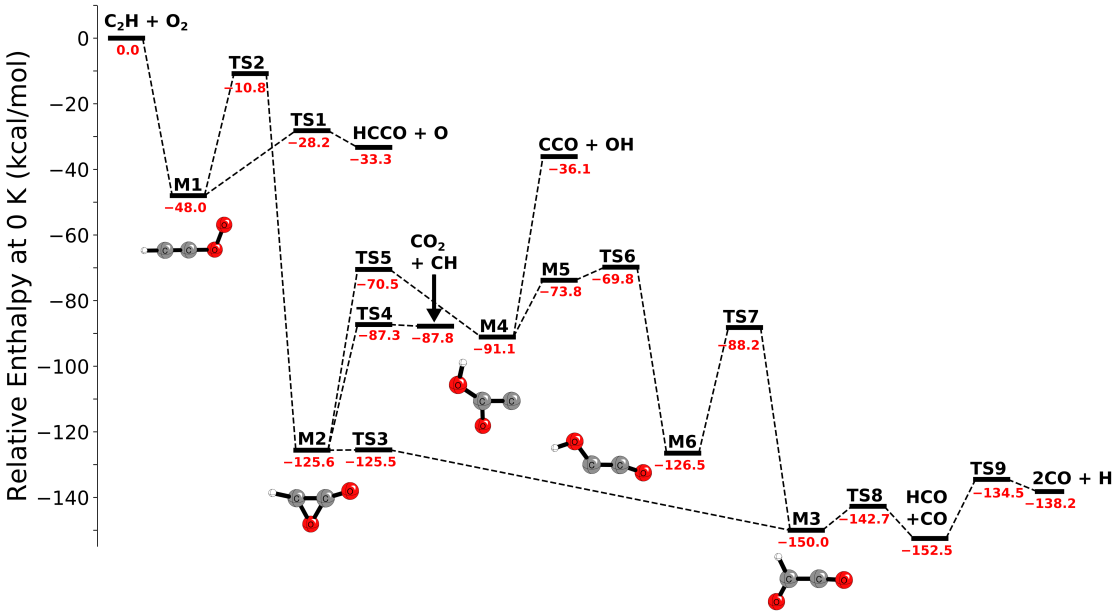

Figure 4.4: Potential enthalpy diagram for the $^2A''$ C_2H + O_2 reaction mechanism. High energy reaction pathways and non-adiabatic reaction pathways are shown in Figure 4.9 and Figure 4.12, respectively. Energies were predicted at the CCSDT(Q)/CBS level of theory. Relative enthalpies were computed by appending the ZPVE and other electronic corrections to the CCSD(T)/CBS energies. Refer to the Energetics section for more information. * TS3 reflects a non-ZPVE corrected enthalpy.

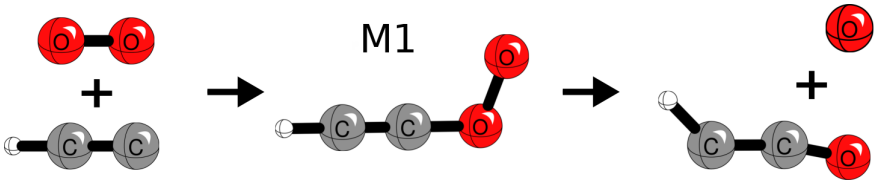

Figure 4.5: Reaction pathway for the production of HCCO (^{2}A$''$) + O(^{3}P) from C_2H + O_2

Table 4.2: Enthaplies at 0 K (ΔH_{0K}) of minima relative to reactants $C_2H + O_2$ in kcal mol^{-1}. CBS denotes the CCSD(T)/CBS relative energy. Delta (δ) denotes the change in relative energy with respect to the preceding level of theory or various additional corrections. See Methods section for details.

Species	CBS	δ_T	$\delta_{(Q)}$	δ_{CORE}	δ_{REL}	δ_{DBOC}	δ_{ZPVE}	Total
M1	−50.70	−0.21	0.38	−0.50	0.05	−0.04	3.05	−47.97
M2	−129.84	0.17	0.55	−0.29	0.14	−0.02	3.72	−125.57
M3	−154.71	0.23	0.50	−0.47	0.12	0.13	4.20	−150.01
M4	−96.18	−0.08	0.63	0.20	0.10	−0.04	4.23	−91.14
M5	−78.11	−0.06	0.75	0.30	0.17	−0.05	3.29	−73.71
M6	−131.17	0.13	0.38	−0.46	0.20	−0.04	4.49	−126.47
M7	−5.56	−0.74	0.61	0.36	−0.05	0.01	2.12	−3.25
M8	−3.48	−1.14	0.47	0.47	−0.09	0.01	2.14	−1.62
S1	−48.84	0.64	−0.03	0.02	0.06	−0.03	2.64	−45.54
S2	−59.98[a]	−1.40	0.96	0.20	0.13	0.46	2.86	−56.77
S3	−38.67	0.45	−0.06	0.16	0.10	−0.03	4.29	−33.76
Q1	−73.19	0.41	0.54	0.36	0.13	0.00	2.52	−69.23

[a] Doublet-quartet splitting has been included in the CBS value.

as multireference, and was treated using the doublet-quartet composite method described previously (see Equation 4.5). The barrier height for this decomposition is predicted to be 19.8 kcal mol^{-1}, which is in good agreement with the barrier height obtained from the MRCISD+Q scan displayed in Figure 4.6. The activation energy for this decomposition is signifcantly less than the reverse decompostion back into the reactants, thus confirming the negligible pressure dependence observed.

The barrier for the decomposition of the ethynyl peroxy radical is within 1 kcal mol^{-1} of the barrier for the isomerization of the ethynyl peroxy radical to oxyrenlyoxy (M2) (see "CO Production Pathways"). This result agrees well with several experimental studies that report both HCCO and CO as major products.[147,151] However, our result contradicts the previous theoretical studies that concluded the isomerization pathway should dominate the decomposition pathway.[162,163] The difference between the composite result and previous

Table 4.3: Enthaplies at 0 K (ΔH_{0K}) of products relative to reactants $C_2H + O_2$ in kcal mol^{-1}. CBS denotes the CCSD(T)/CBS relative energy. Delta (δ) denotes the change in relative energy with respect to the preceding level of theory or various additional corrections. See Methods section for details.

Species	CBS	δ_T	$\delta_{(Q)}$	δ_{CORE}	δ_{REL}	δ_{DBOC}	δ_{ZPVE}	Total
TS1	−29.77[a]	−0.67	0.84	0.50	−0.06	0.05	0.92	−28.19
TS2	−10.90	−1.24	−0.37	0.12	−0.09	1.25[b]	1.71	−10.77
TS2′	−28.91	−0.63	−0.28	−0.09	0.01	−0.03	1.35	−28.58
TS3	−129.84	0.21	0.50	−0.29	0.14	−0.02	3.28	−126.02
TS4	−90.11	0.33	0.65	0.31	0.01	0.04	1.43	−87.34
TS5	−71.33	0.06	0.17	0.23	0.03	−0.01	0.36	−70.49
TS6	−73.23	−0.38	0.54	0.57	0.08	0.00	2.60	−69.82
TS7	−88.36	0.12	−0.29	−0.41	0.10	0.05	0.61	−88.18
TS8	−144.82	−0.33	0.62	0.08	−0.02	0.08	1.71	−142.68
TS9	−130.87	0.25	0.77	0.31	−0.19	0.04	−4.80	−134.49
TS10	−2.08	−0.22	0.53	0.27	−0.05	0.00	0.28	−1.27
TS11	8.26[a]	−0.33	−0.24	0.61	−0.13	0.02	0.36	8.55
TS12	3.09	−0.60	0.66	0.38	−0.07	0.02	1.82	5.30
TS13	−1.51	−1.28	−0.77	0.56	−0.08	0.14	2.64	−0.30
TS15	−60.37	−0.25	0.65	0.27	0.15	−0.01	1.33	−58.23

[a] Doublet-quartet splitting has been included in the CBS value.

[b] Abnormally large DBOC for TS2 is likely the result of a nearby surface crossing between the $^2A''$ and $^2A'$ electronic surfaces. This DBOC is excluded from our "Total" energies.

Table 4.4: Comparison of the barrier heights for reactions on the $C_2H + O_2$ potential energy surface in kcal mol^{-1}

Reaction	This research[a]	Peeters[b]	Li[c]
M1 [HCCOO] → S1 (dioxrenyl)	19.4[d]	20.0[e]	24.3
M1 [HCCOO] → M7 [HC(C)OO]	46.7	46.5	
M1 [HCCOO] → HCCO + O	19.8	17.1[e]	45.7
M2 (oxyrenyloxy)→ M3 [HC(O)CO]	0.1[f]	0.1	
M2 (oxyrenyloxy)→ M4 [HOC(O)C]	55.1		
M2 (oxyrenyloxy)→ CO_2 + CH	38.2	37.3	
M3 [HC(O)CO] → HCO + CO	7.3	10.7	5.5
M4 [HOC(O)C] → M6 [HOCCO]	21.3	7.6[g]	20.3
M4 [HOC(O)C] → CCO + OH	55.0	49.0[h]	51.2
M6 [HOCCO] → M3 [HC(O)CO]	38.3	40.4	38.6
$C_2H + O_2$ → M7 [*trans*-HC(C)OO]	8.6	6.0	17.0
M7 [*trans*-HC(C)OO] → M8 [*cis*-HC(C)OO]	6.9		2.9[i]
M8 [*trans*-HC(C)OO] → M3 [HC(O)CO]	1.3	0.3[f]	3.4
HCO → H + CO	18.0		20.8

[a] CCSDT(Q)/CBS, see Methods section.
[b] B3LYP/6-311++G(d,p) [162]
[c] QCISD(T)/6-311++G(d,p) [163]
[d] Nonadiabatic limit, see "CO Production Pathways"
[e] Peeters recomputed the relative energies of these transition states with CCSD(T)/6-311++G(d,p) and the M1 → P1 barrier was 15 kcal mol^{-1} higher than the M1 → S1
[f] non-ZPVE corrected barrier height. ZPVE corrected barrier is negative.
[g] The barrier reported by Peeters [162] is for *cis*-carbohydroxycarbyne.
[h] The dissociation of carbohydroxycarbyne proceeds without an exit barrier.
[i] B3LYP/6-311++G(d,p)

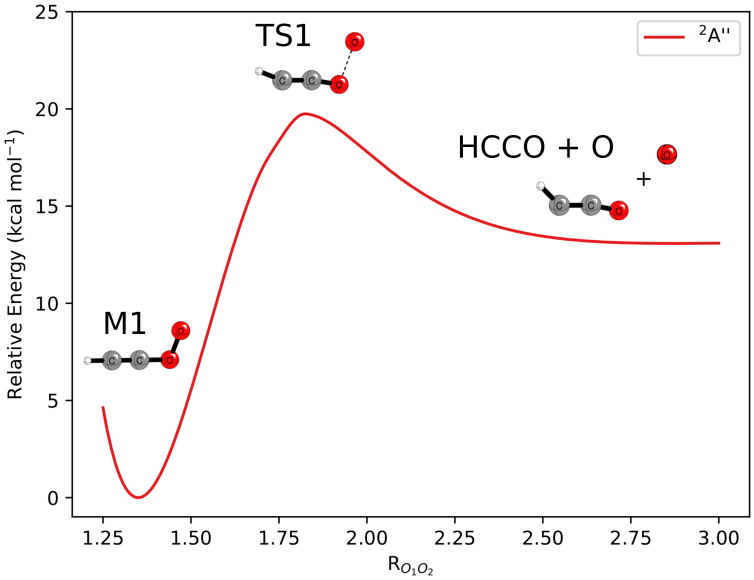

Figure 4.6: MRCISD+Q(7,7)/cc-pVTZ//CASPT2(7,7)/cc-pVTZ relaxed potential energy surface scan of the reaction mechanism connecting the ethynyl peroxy radical (HCCOO, M1) to the ketenyl radical (HCCO) and atomic oxygen. The O–O distance was varied in increments of 0.05 Å while all other geometric parameters were optimized.

theoretical work appears due to the insufficiency of single reference methods to account for the static correlation of the decomposition transition state (TS1). However, the composite approach used in this study should provide an accurate representation of both static and dynamic correlation of the species at the transition state.

The barrierless reaction of the initial reactants to form the ethynyl peroxy radical (HCCOO, M1) also provides the adduct with enough internal energy to isomerize to oxyrenyloxy (M2) through TS2. On the $^2A''$ electronic surface this isomerization consists of a distortion of the HCCO linear structure, followed by the transient formation of a COO three member ring, then immediate cleavage of the O-O bond and formation of the CCO three member ring in oxyrenlyoxy. The direct connection between M1 and M2 through TS2 is in disagreement with Peeters[162] and Li[163] whom insist the ethynyl peroxy radical first forms dioxirenyl. While

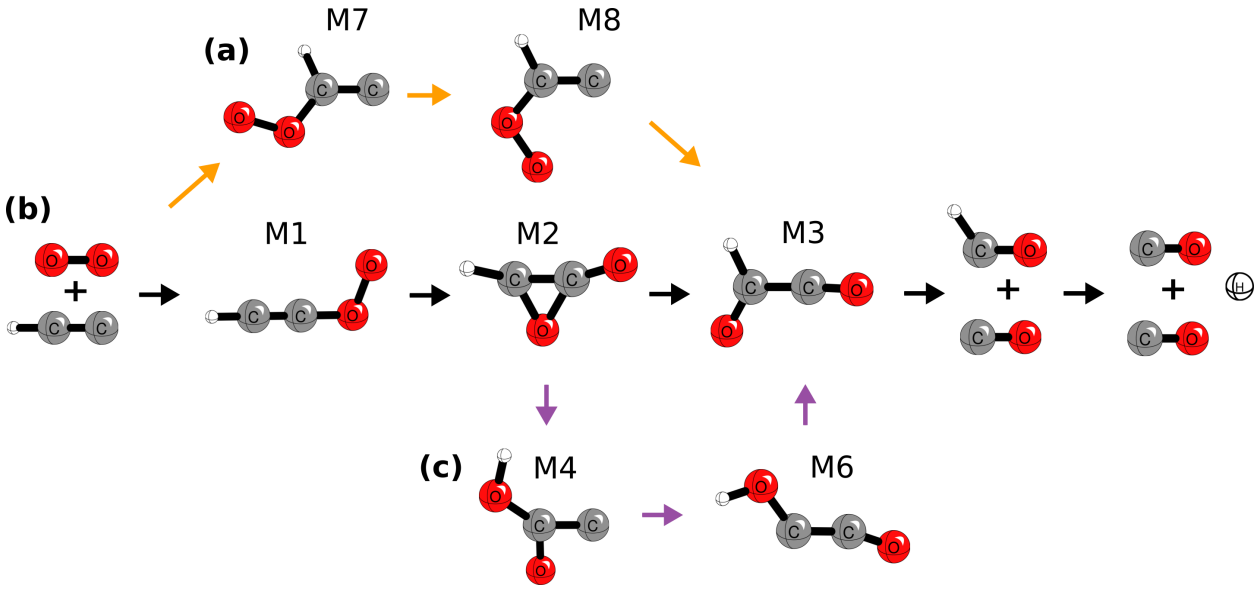

Figure 4.7: Reaction pathways for the production of HCO and CO from $C_2H + O_2$. The minimum energy pathway for the production of HCO **(b)** is illustrated with black arrows. Alternative reaction pathways **(a)** and **(c)** are illustrated with orange and purple arrows, respectively.

the IRC between M1 and M2 passes through a COO ring structure we were unable to locate a minimum for such a structure on the $^2A''$ electronic surface. Dioxirenyl (S1) does, however, exist as a shallow minimum on the nearby $^2A'$ electronic surface.

The $^2A'$ electronic state of the ethynyl peroxy radical, which lies only about 17 kcal mol^{-1} above the $^2A''$ ground state, becomes lower in energy as the adduct approaches TS2. The crossing of these electronic surfaces is examined in Figure 4.8. Hence, it is likely the isomerization of the ethynyl peroxy radical (HCCOO, M1) to oxyrenyloxy (M2) can proceed on the $^2A'$ electronic surface, which is significantly lower in energy. On the $^2A'$ electronic surface, the COO ring is stabilized, allowing dioxirenyl (S1) to exist as a local minimum. A cleavage of the oxygen-oxygen bond lowers the energy of the $^2A''$ state relative to the $^2A'$ state and the $^2A''$ once again becomes the ground electronic state. Therefore, M1 [HCCOO] $\rightarrow$ M2 [oxyrenlyoxy] can be enhanced through the non-adiabatic reaction pathway M1 $\rightarrow$ S1 $\rightarrow$

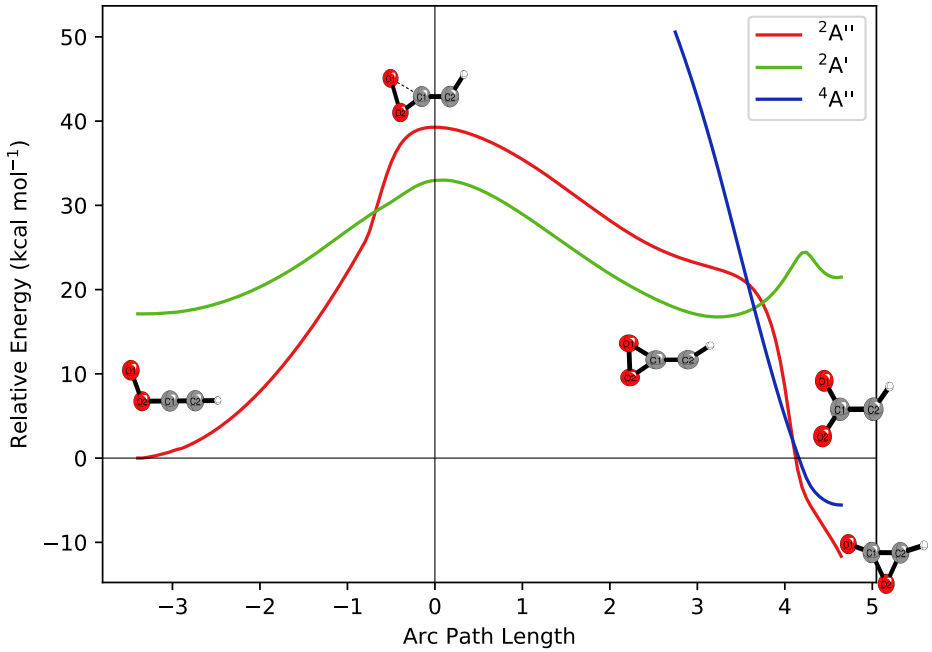

Figure 4.8: CCSD(T)/ANO0 potential energy surface scan of the $^2A''$ (red), $^2A'$ (green), and $^4A''$ (blue) electronic surfaces along the intrinisic reaction coordinate of TS2. Positive and negative directions correspond to the formation of M2 (oxyrenlyoxy) and M1 (ethynyl peroxy radical), respectively.

M2, making the isomerization pathway more competitive with the immediate decomposition pathway discussed in the previous section.

The isomerization of the ethynyl peroxy radical (HCCOO, M1) to oxyrenyloxy (M2) can be explained in terms of two limiting cases. In the adiabatic limit the isomerization takes place exclusively on the $^2A''$ electronic surface. The adiabatic pathway encounters a barrier of 37.2 kcal mol^{-1}, which can be understood as an upper bound for the true barrier. Contrarily, the isomerization could switch (during an excursion to C_1 symmetry) between the $^2A''$ and $^2A'$ electronic surfaces; this would be the non-adiabatic limit for the isomerization. In the non-adiabatic limit the reaction would proceed through a similar transition state on the $^2A'$ electronic surface, namely TS2′. The non-adiabatic reaction barrier was determined to be 19.4

kcal mol^{-1}, which is considerably lower than the adiabatic limit. The non-adiabatic reaction barrier is also slightly lower in energy than the barrier to the decomposition of the ethynyl peroxy radical (M1 [HCCOO]) (see "HCCO Production Pathway") While the efficiency of the non-adiabatic crossing is uncertain, the observation of CO as a major product implies that the non-adiabatic limit aligns better with experimental studies.

We can estimate the branching ratio of the decomposition reaction (M1 [HCCOO] $\rightarrow$ HCCO + O) to the isomerization reaction (M1 [HCCOO] $\rightarrow$ M2 [oxyrenlyoxy]) by comparing the rate constants for these reactions:

$$\frac{k_1}{k_2} = \frac{Q_1}{Q_2} e^{-\left(\Delta H_1^{\ddagger} - \Delta H_2^{\ddagger}\right)/RT} \tag{4.6}$$

where Q_i and $\Delta H_i^{\ddagger}$ correspond, respectively, to the canonical partition function and barrier height for transition state i. Using the non-adiabatic limit (19.4 kcal mol^{-1}) for the isomerization reaction and a temperature of 298 K, the branching ratio was determined to be approximately 1:1. Considering an uncertainty of 1 kcal mol^{-1} in the relative enthalpies of TS1 and TS2, the branching ratio between the isomerization and decomposition pathways could range from 1:5 to 5:1. This result is in good agreement Laufer and Lechleider, who computed rate constants of 1.0×10^{12} cm^3 molecule^{-1} s^{-1} and 4.0×10^{12} cm^3 molecule^{-1} s^{-1} for the reactions $C_2H + O_2 \rightarrow HCCO + O$ and $C_2H + O_2 \rightarrow HCO + CO$, respectively.[147]

Upon formation of oxyrenyloxy (M2) the adduct has a considerable amount of internal energy, which allows passage over several small barriers. The most accessible pathway is the ring-opening reaction leading to oxo-ketene [HC(O)CO, M3]. Without the ZPVE, the activation energy for this reaction is only 0.1 kcal mol^{-1}. Inclusion of the ZPVE for this barrier lowers the relative energy of the transition state below the energy of oxyrenlyoxy. Whether this reaction is barrierless or simply near barrierless is unclear. Regardless, the oxyrenlyoxy (M2) will be short-lived in light of oxo-ketene (M3). The oxo-ketene (M3) can then dissociate into HCO + CO with a 15.0 kcal mol^{-1} barrier. Finally, the vibrationally

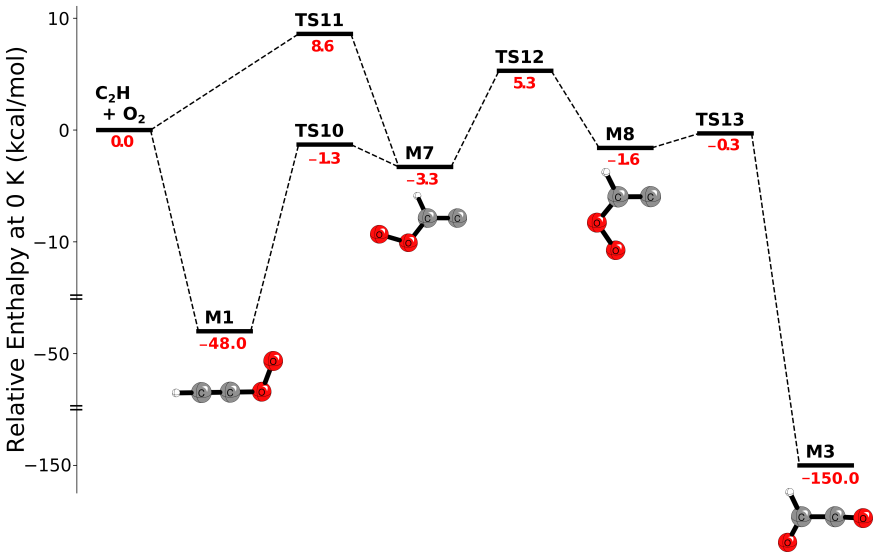

Figure 4.9: High energy pathways for the $C_2H + O_2$ reaction mechanism. The energy axis has been modified for clarity.

excited formyl radical can further decompose into carbon monoxide and a hydrogen atom. Altogether the minimum energy pathway for the production of carbon monoxide is described as $C_2H + O_2 \rightarrow$ M1 [HCCOO] $\rightarrow$ M2 $\rightarrow$ M3 [HC(O)CO] $\rightarrow$ HCO + CO $\rightarrow$ 2 CO + H; this reaction pathway is sketched in Figure 4.7b.

Alternatively, oxo-ketene can be produced through two pathways found to be less favorable. One such pathway includes a hydrogen isomerization leading from the oxyrenyloxy (M2) to carbohydroxycarbyne [HOC(O)C, M4]. Two rotamers exist for carbohydroxycarbyne: one with the hydrogen atom facing toward the opposite oxygen (*cis*) and the other with the hydrogen facing away (*trans*).[184] Regardless of the orientation of the hydrogen atom, an isomerization of the oxygen between the adjacent carbons ultimately produces *cis*-hydroxyketenyl [HOCCO, M6]. The isomerization of carbohydroxycarbyne to hydroxyketenyl proceeds through a C_1 CCO three member ring, M5. M5 exists as a shallow minimum on the CCSD(T)/ANO2 electronic surface; however inclusion of the ZPVE makes the ring opening

of M5 → M4 a barrierless reaction. Hydroxyketenyl [HOCCO, M6] can further isomerize to oxo-ketene [HC(O)CO, M3] through a hydrogen transfer with a barrier of 38.3 kcal mol^{-1}. Altogether this pathway is $C_2H + O_2 \rightarrow$ M1 [HCCOO] → M2 [oxyrenyloxy] → M4 [HOC(O)C] → M5 → M6 [HOCCO] → M3 [HC(O)CO] → HCO + CO; this reaction pathway is sketched in Figure 4.7c. While the isomerization from M2 → M4 is accessible through the excess energy released when oxyrenyloxy is formed, it has to compete with the more favorable, direct M2 → M3 pathway. This suggests that this reaction channel contributes minimally to the production of CO.

An additional reaction pathway, shown in Figure 4.9 the oxygen molecule binding to the central carbon of the ethynyl radical to form the *trans*-vinylidenyl peroxy radical (M7). Unlike the oxygen addition to the terminal carbon, this reaction will encounter an entrance barrier. The transition state for the production of the vinylidenyl peroxy radical (TS11) was identified as multireference and hence was treated using the doublet-quartet method (see Equation 4.5). A barrier height of 8.6 kcal mol^{-1} was obtained for the addition of O_2 to the central carbon of the ethynyl radical, implying this reaction will only take place at higher temperatures. M7 can also be formed through a hydrogen isomerization from the ethynyl peroxy radical; however, this isomerization will have to compete with the two energetically more favorable reactions, namely the isomerization to oxyrenlyoxy (M2) and decomposition to HCCO + O. A rotation around the C–O bond forms M8, the *cis* isomer of M7. The *cis*-vinylidenyl peroxy radical readily undergoes a near-barrierless isomerization to oxo-ketene (M3). The reaction path between M8 and M3 features the transient formation of cyclic dioxetenyl; however, we were unable to optimize cyclic dioxetenyl as a minimum on this potential energy surface. Similar to dioxirenyl, a scan over the IRC corresponding to TS13 revealed that dioxetenyl (S3) is a minimum on the nearby $^2A'$ electronic surface, but not the $^2A''$ electronic surface. These high energy pathways are shown in Figure 4.7a and 4.9 and can be described as $C_2H + O_2 \rightarrow$ M7 [*trans*-HC(C)OO] → M8 [*cis*-HC(C)OO] → M3 [HC(O)CO] → HCO + CO or

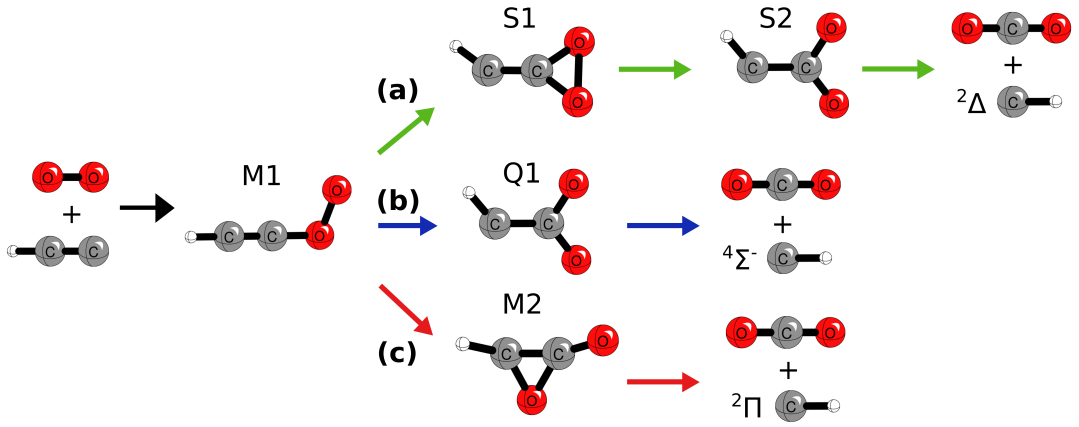

Figure 4.10: Reaction pathways for the production of CO_2 + CH. Pathways **(a)**, **(b)**, and **(c)** correspond to the production of methylidene (CH) in its $^2\Delta$, $^4\Sigma^-$, and $^2\Pi$ electronic states, respectively.

alternatively $C_2H + O_2 \rightarrow$ M1 [HCCOO] $\rightarrow$ M7 [*trans*-HC(C)OO] $\rightarrow$ M8 [*cis*-HC(C)OO] $\rightarrow$ M3 [HC(O)CO] $\rightarrow$ HCO + CO.

Carbon dioxide and ground state methlyidene ($^2\Pi$) can be produced from the ring opening of oxyrenlyoxy (M2, see Figure 4.4 and 4.10c). This dissociation is more favorable than the isomerization to carbohydroxycarbyne, but nevertheless it must compete with the near barrierless reaction M2 $\rightarrow$ M3. While the exit barrier for the decomposition of oxyrenlyoxy (M2) is large, the reverse reaction is nearly barrierless (<0.5 kcal mol^{-1}). The small entrance barrier for CO_2 + CH is in good agreement with previous theoretical and experimental studies that report a small activation energy for this reaction.[185,186] Experimental studies have reported relative CO_2/CO yields in excess of 1:4,[148,149] which would be unexpected given the relative barrier heights for TS3 (0.1 kcal mol^{-1}) and TS4 (38.3 kcal mol^{-1}). Furthermore, many experimental studies have observed methlyidene in excited electronic states such as $^2\Delta$.[145,146,159–161] These observations suggest there are alternative reaction paths to supplement the production of CO_2.

The production of excited methlyidene requires the reaction to proceed through a surface crossing. The most probable location for a surface crossing along this reaction coordinate is during the isomerization of the ethynyl peroxy radical. In the previous section, surface crossings between the $^2A'$ and $^2A''$ were discussed. The crossings between these adiabatic surfaces allow for the non-adiabatic reaction M1 $\rightarrow$ S1 (see Figure 4.8). Upon cleavage of the oxygen-oxygen bond, dioxirenyl (S1) can revert back to the $^2A''$ electronic state. However, if the reaction continues on the $^2A'$ electronic state, then a HCC(O)O carbene (S2) will be produced. This carbene is reminiscent of the third adduct reported by Li et al along their minimum energy pathway.[163] Wave function diagnostics on this carbene revealed heavily multireference character for this structure; thus it was treated using the doublet-quartet method described previously (see Equation 4.5). The bond cleaving transition state leading from dioxirenyl to HCC(O)O (TS14) was likewise multireference; however we were unable to optimize the geometry of this transition state. The relative energy of TS14 was estimated from a relaxed potential energy surface scan over the OCO bond angle on dioxirenyl (see Figure 4.11).

While dioxirenyl (S2) is a local minimum on the $^2A'$ electronic surface, we were unable to optimize a similar structure as a stationary point on the $^2A''$ electronic surface. This is in agreement with Peeters and coworkers, who also failed to find HCC(O)O as a local minimum on the $^2A''$ electronic surface.[185] Dissociation of this $^2A'$ carbene yields CO_2 and CH $^2\Delta$, where the lone pair on the carbene contributes to the π electrons on the $^2\Delta$ CH diatomic. This reaction pathway is summarized as $C_2H + O_2 \rightarrow$ M1 [HCCOO] $\rightarrow$ S1 $\rightarrow$ S2 [HCC(O)O] $\rightarrow CO_2 +$ CH ($^2\Delta$) and is sketched in Figure 4.10a.

The small doublet-quartet splitting of the HCC(O)O carbene allows the $^4A''$ electronic surface to approach or even intersect the $^2A'$ and $^2A''$ electronic surfaces. Figure 4.8 shows how the $^4A''$ electronic surface intersects the doublet electronic surfaces. The near degeneracy of these electronic states during the isomerization of the ethynyl peroxy radical encourages

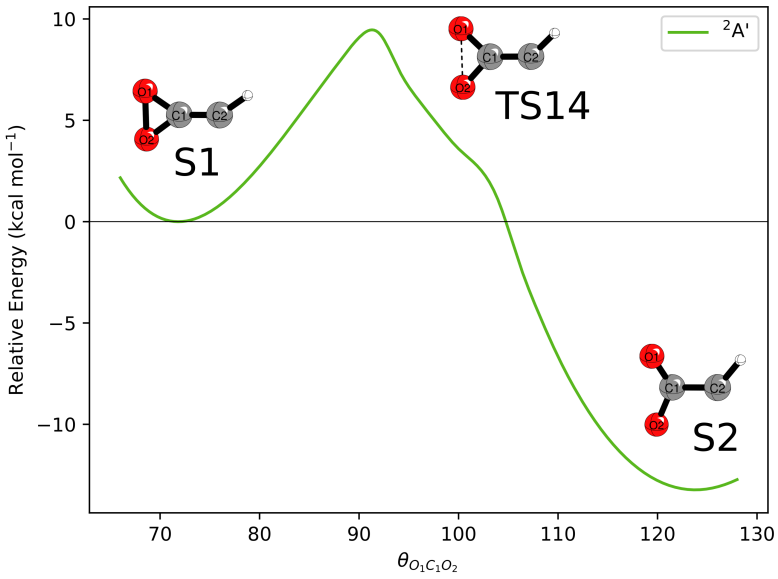

Figure 4.11: MRCISD+Q(11,9)/cc-pVTZ//CASPT2(11,9)/cc-pVDZ relaxed potential energy surface scan of the reaction mechanism from S1 [dioxirenyl] →TS14→S2 [HCC(O)O]. The OCO bond angle was varied in increments of 2.0° while all other geometric parameters were optimized. $\theta = 72°$ corresponds to S1 and $\theta = 124°$ corresponds to S2.

intersystem crossing (ISC) as the transition probability depends exponentially on the energy difference between these adiabatic states.[181,182] Thus, the formally spin-forbidden transition between the $^2A''$ and $^4A''$ electronic states becomes possible during the isomerization M1 → M2. Upon ISC the reaction will continue on the $^4A''$ potential energy surface, dissociating into the products CO_2 and CH $^4\Sigma^-$. The ISC reaction can be summarized as $C_2H + O_2$ → M1 [HCCOO] → Q1 [HCC(O)O] → CO_2 + CH ($^4\Sigma^-$) and is sketched in Figure 4.10b. Despite the near degeneracy of the ^{2}A″ and ^{4}A″ electronic surfaces, the spin-orbit coupling between these states is expected to be small and the ISC reaction will likely contribute only minimally to the overall $C_2H + O_2$ reaction. The reaction pathways leading to the production of CO_2 and CH ($^2\Pi$, $^4\Sigma^-$, and $^2\Delta$) are illustrated in Figure 4.12.

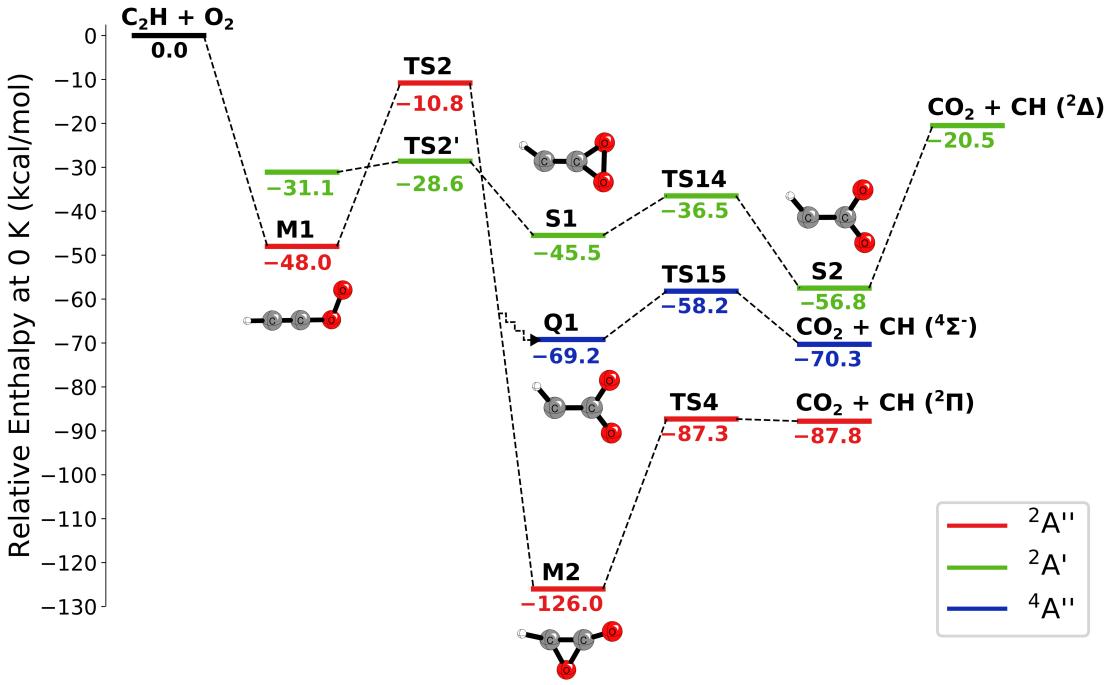

Figure 4.12: Non-adiabatic energy pathways for the $C_2H + O_2$ reaction mechanism. The $^2A''$ (red), $^2A'$ (green), and $^4A''$ (blue) electronic states lead to the production of $^2\Pi$, $^2\Delta$, and $^4\Sigma^-$ methylidene, respectively. Intersystem crossing (M1 $\rightarrow$ Q1) is denoted by a zigzag dashed line. The relative enthalpy of TS14 was estimated from a relaxed surface scan from S1 $\rightarrow$ S2. Experimental excitation energies were used for the relative enthalpies of CO_2 + CH ($^4\Sigma^-$, $^2\Delta$).[125]

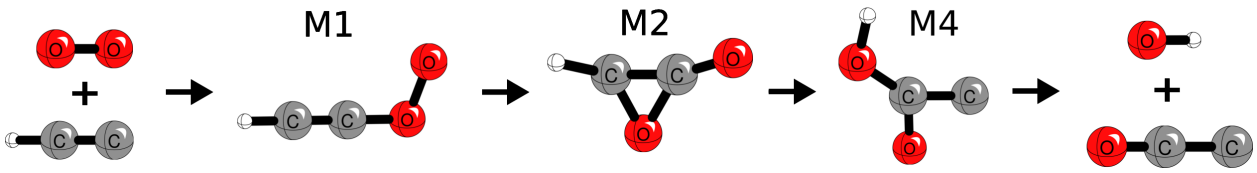

Figure 4.13: Reaction pathway for the production of CCO + OH

Table 4.5: Carbon-carbon bond length (in Å) and quadratic force constant (in mdyne $Å^{-2}$) at the CCSD(T)/ANO2 level of theory, and natural bond order (NBO) with CCSD/cc-pVDZ. Ethane (C_2H_6), ethylene (C_2H_4), and acetylene (C_2H_2) were computed at the same level of theory and are given as a reference.

Species	R_{CC}	k_{CC}	NBO
C_2H	1.211	17.13	3.00
HCCO	1.302	9.57	2.07
CCO	1.367	6.29	1.81
M1	1.203	17.20	2.81
M2	1.360	7.26	1.16
M3	1.396	5.74	1.39
M4	1.390	5.76	1.30
M5	1.456	5.17	1.04
M6	1.320	8.44	1.93
M7	1.327	8.55	1.95
S1	1.293	10.63	1.92
S3	1.331	12.41	1.42
Q1	1.437	5.21	1.23
C_2H_2	1.206	16.29	2.97
C_2H_4	1.334	9.42	2.00
C_2H_6	1.526	4.58	1.00

Finally, CCO and OH can be produced from the dissociation of carbohydroxycarbyne (M4). This reaction pathway can be described as M1 [HCCOO] → M2 [oxyrenlyoxy] → M4 [HOC(O)C] → CCO + OH and is illustrated in Figure 4.13. However, this dissociation must compete with the isomerization of carbohydroxycarbyne to hydroxyketenyl [M6, HOCCO] which is significantly more favorable thermodynamically. Furthermore, carbohydroxycarbyne is only produced on a minor reaction pathway requiring a hydrogen isomerization of either oxo-ketene M3 [HC(O)CO] or oxyrenyloxy M2. Thus CCO and OH are produced in marginal amounts, if at all.

An interesting facet of the $C_2H + O_2$ reaction is the cleavage of the ethynyl C–C triple bond to produce CO or CO_2. The direct cleavage of a triple bond would be unfeasible. However, through a series of isomerizations the bond order of the carbon-carbon bond is reduced to allow for C–C cleavage on a weaker bond. Table 4.5 shows the C–C bond length, force constant, and natural bond order of species along the reaction pathways. For comparison, we have also included the respective parameters for ethane, ethylene, and acetylene obtained at the same level of theory. The carbon-carbon bond retains its bond order during formation of the ethynyl peroxy radical. However, upon isomerization of the ethynyl peroxy radical M1 [HCCOO] $\rightarrow$ M2 [oxyrenlyoxy], the C–C bond order is dramatically reduced. When considering the non-adiabatic reaction M1 ($^2A''$) $\rightarrow$ S1 ($^2A'$) $\rightarrow$ M2 (^2A), it appears that the bond order is reduced in a step-wise fashion: triple (ethynyl peroxy radical) to double (dioxirenyl) to single (oxyrenyloxy) bond. The ring opening of M2 to M3 marginally increases the C–C bond order, but the relative stability of CO allows this bond to be cleaved with a small activation energy.

Alternatively, when the oxygen attacks the intermediate carbon to form the vinylidenyl peroxy radical, the donation of the ethynyl π electrons reduces the molecule to a C–C double bond immediately. The bond order is further reduced upon oxygen isomerization to form the relatively weak bond in the oxo-ketene M3. It is also interesting to note the C–C bond order is reduced during the decompostion of the ethynyl radical to produce ketenyl radical. The double bond on the ketenyl radical can be explained in terms of relative energies of the tautomers ethynol (HCCOH) and ketene (H_2CCO).

4.5 Conclusions

Coupled cluster methods with large ANO basis sets have been used to study the rapid reaction of the C_2H radical with molecular oxygen. Two major reaction pathways were identifed: first the isomerization of the ethynyl peroxy radical to ultimately yield HCO plus

CO the most exothermic products (-152 kcal mol^{-1}). We also examined the decomposition of the ethynyl peroxy radical to immediately yield a ketenyl radical [HCCO] and atomic oxygen. For the former, the isomerization of the ethynyl peroxy radical is aided by crossings between the $^2A''$ and $^2A'$ electronic surfaces. During the isomerization reaction, the C–C bond order is reduced in a step-wise fashion in order to allow for the C–C cleavage on the oxo-ketene [HC(O)CO] radical. The decomposition of the ethynyl peroxy radical to HCCO plus O features a transition state with strong multireference character; a MRCISD+Q and CCSDT(Q) composite approach was used on this transition state to accurately determine the static and dynamic correlation of this stationary point. The branching ratio between the isomerization pathway and the decomposition pathway was predicted to be 1:1 at 298 K, suggesting HCO and HCCO should be produced in equal magnitudes at moderate to high temperatures, in good agreement with experimental studies.[147]

Perhaps the most surprising result of the $C_2H + O_2$ reaction is that the least exothermic ($C_2H + O_2 \rightarrow HCCO + O$, $\Delta H = -34$ kcal mol^{-1}) of the five reactions noted in the introduction takes place at a magnitude equal to the most exothermic reaction ($C_2H + O_2 \rightarrow HCO + CO$, $\Delta H = -152$ kcal mol^{-1}). CO_2 and CH can also be produced from the isomerization pathway, but the CO_2 to CO yield ratio is expected to be minor. Surface crossings between the $^2A''$, $^2A'$, and $^4A''$ electronic states during the isomerization of the ethynyl peroxy radical provide efficient pathways for the production of excited CH and increase the overall CO_2 to CO yield ratio. While CCO and OH are thermodynamically possible products, competition with more accessible reaction pathways will dramatically hinder the production of these products.

Chapter 5

Conclusive Determination of Ethynyl Radical Hydrogen-Abstraction Energetics and Kinetics

---

Bowman, M.C.; Burke, A.D.; Turney, J.M.; Schaefer, H.F., submitted to *Mol. Phys.*

5.1 Abstract

The ethynyl radical (C_2H) is ubiquitous, appearing in a variety of environments from interstellar space to oxy-acetylene flames. Under these diverse conditions, ethynyl has a high affinity to abstract hydrogen atoms from nearby molecules. In this study, C_2H + HX $\rightarrow$ C_2H_2 + X, X = CH_3, NH_2, OH, F, PH_2, SH, Cl, C_2H, CN, and NC reactions have been examined at a rigorously high level of theory. Various additive corrections have been appended to the coupled cluster framework to converge the relative enthalpy of stationary points on the C_2H + HX surfaces to subchemical accuracy ($\leq$ 0.5 kcal mol^{-1}). The barriers for the abstraction of a hydrogen from ammonia (NH_3), phosphine (PH_3), and hydrogen sulfide (H_2S) are submerged below the relative enthalpy of their reactant asymptotes by 2.75, 2.48, and 1.39 kcal mol^{-1}, respectively. Therefore, these reactions are expected to occur rapidly even at low temperatures. Hydrogen (H_2), methane (CH_4), water (H_2O), and hydrogen chloride (HCl) are predicted to have moderate barriers to abstraction of 2.64, 0.77, 3.82, and 2.19 kcal mol^{-1}, respectively, suggesting these reactions will likewise be significant to various systems at moderate to high temperatures. Accurate kinetics were obtained for the C_2H + H_2, CH_4, and H_2O reactions over a wide range of temperatures with excellent agreement to present experimental rate constants.

5.2 Introduction

The ethynyl radical, C_2H ($^2\Sigma^+$), is one of the most prevalent polyatomic radicals in interstellar space[132–134,187] and planetary atmospheres,[138,141] often in concentrations great enough to distinguish between the ^{13}CCH and C^{13}CH isotopologues.[135,188] In these environments, ethynyl radicals are thought to play an important role in the formation of polyynes which lead to larger molecules such as polycyclic aromatic hydrocarbons (PAHs) and fullerenes.[189] Moreover, the ethynyl radical is a common intermediate in the combustion of various alkynes

under fuel-rich conditions.[190–192] Thus, there is a high demand to accurately model ethynyl radical reactions over a wide range of temperatures.

Among the most prevalent reactions for the ethynyl radical is hydrogen-atom abstraction. In reactions with hydrogen-containing molecules, hydrogen abstraction is often the main reaction pathway or at least a viable alternative. These abstractions are thermodynamically driven by the relatively large dissociation energy of acetylene's *sp*-hybridized C–H bond. Kinetic studies have revealed large rate constants for the reaction of C_2H with various saturated hydrocarbons over a wide range of temperatures, suggesting the barriers to abstraction are moderately low.[193–196] This is in agreement with theoretical results which claim moderate to low barrier heights for several H-atom donors.[197,198] In the particular case of C_2H + NH_3, a slight negative temperature dependence has been observed for the hydrogen abstraction, consistent with a barrierless reaction.[199,200] These results have been corroborated by theoretical studies which have computed a submerged barrier due to the formation of strongly bound NH_3–C_2H hydrogen-bonded complex.[201,202] Furthermore, the small mass of hydrogen suggests that many of these reactions will proceed at low temperatures, regardless of the barrier height, due to tunneling. The importance of tunneling has been confirmed by several kinetics studies which have demonstrated a large isotopic dependence at moderate to low temperatures.[158,193,200,203]

At present, experimental and theoretical studies on ethynyl radical hydrogen abstractions have primarily studied hydrocarbon H-atom donors. Nguyen and coworkers examined this reaction with a wide variety of H-atom donors with the MPW1K/6-311++G(3df,2p) method,[197] but this modest level of theory is not sufficient to make reliable predictions for the kinetics of unstudied reactions. Quantitatively accurate kinetic models require the barrier height of reactions to be determined within a small fraction of one kcal mol^{-1}; however, few theoretical studies on these reactions can boast such precision. In this study we have performed a high-level *ab initio* characterization of hydrogen abstraction reactions of the ethynyl radical

with various small hydrogen-containing molecules. The hydrogen donor molecules have been selected in part due to their importance in astrochemistry or combustion chemistry, but they also serve as archetypes for the possible bonds that could be cleaved in reactions involving larger donors. A composite approach has been employed in order to converge energies within subchemical accuracy ($\leq$ 0.5 kcal mol^{-1}). In conjunction with canonical transition state theory, these highly accurate energies have been used to determine reliable rate constants for future kinetic studies.

5.3 Methods

Equilibrium geometries for stationary points on the C_2H + HX reactive surfaces were optimized to a RMS energy gradient of 1.0×10^{-7} using the explicitly correlated CCSD(T)-F12a method.[204] To account for the long-range interactions present among pre-reactive complexes and transition states, the aug-cc-pVTZ-F12 basis sets recently developed by Martin and coworkers were employed.[205] A restricted open-shell Hartree–Fock (ROHF) reference was used for all open-shell computations to avoid issues with spin contamination prevalent with the ethynyl radical. Harmonic vibrational frequencies were obtained at the CCSD(T)-F12a/aug-cc-pVTZ-F12 optimized geometries using the same level of theory.

Electronic energies were computed according to the focal point analysis (FPA) of Allen and coworkers[25,26] for the CCSD(T)-F12a/aug-cc-pVTZ-F12 stationary points. The convergence to the one-particle basis set limit was examined with aug-cc-pV(X+d)Z basis sets.[206] MOLPRO 2010.1[70] was used to compute the CCSD(T)-F12a/aug-cc-pVTZ-F12 geometries and frequencies as well as the CCSD(T)/aug-cc-pV(X+d)Z energies. The CCSD(T) complete basis set (CBS) energies were obtained by extrapolating the Hartree–Fock energy and correlation energies using a three-point exponential equation[21] and a two-point inverse cubic equation,[22] respectively:

$$E_{\mathrm{ref}}(X) = E_{\mathrm{HF}}^{\infty} + ae^{-bX} \tag{5.1}$$

$$E_{\mathrm{corr}}(X) = E_{\mathrm{corr}}^{\infty} + aX^{-3} \tag{5.2}$$

The CCSDT(Q) energy was approximated through an additive correction for the expansion of the correlation treatment from perturbative triples [CCSD(T)] to perturbative quadruples [CCSDT(Q)/B] (designated $\delta_{\mathrm{T(Q)}}$) using the aug-cc-pV(D+d)Z basis set with MRCC 2015.[111] Additional corrections were made to amend the approximations used during the CCSD(T) computations. The core-correlation neglected under the frozen-core approximation (δ_{CORE}) was accounted for by computing the CCSD(T)/aug-cc-pCVQZ energy with all electrons correlated. A scalar relativistic correction (δ_{REL}) was obtained with the spin-free X2C-1e method[28] using the X2C-recontracted aug-cc-pCVTZ basis sets presently available on the CFOUR website.[207] Given the small reduced mass of the transfered hydrogen atom, the limitations of the clamped-nuclei approximation were also considered by an adiabatic diagonal Born–Oppenheimer correction (δ_{DBOC})[29,30] performed at the ROHF/aug-cc-pVTZ level of theory. Both the relativistic correction and the diagonal Born–Oppenheimer correction have been evaluated with CFOUR 2.0.[110] An experimental shift for the spin-orbit splitting (δ_{SO}) was included for the products OH, F, SH, and Cl.[125,208] Finally, the zero-point vibrational energies (δ_{ZPVE}) from the CCSD(T)-F12a/aug-cc-pVTZ-F12 harmonic vibrational frequencies were appended to obtain the relative enthalpies at 0 K ($\Delta H_{0\mathrm{K}}$) as shown in equation 5.3.

$$\Delta H_{0\mathrm{K}} = \Delta E_{\mathrm{CCSD(T)/CBS}} + \delta_{\mathrm{ZPVE}} + \delta_{\mathrm{T(Q)}} + \delta_{\mathrm{CORE}} + \delta_{\mathrm{REL}} + \delta_{\mathrm{DBOC}} \left(+\delta_{\mathrm{SO}}\right) \tag{5.3}$$

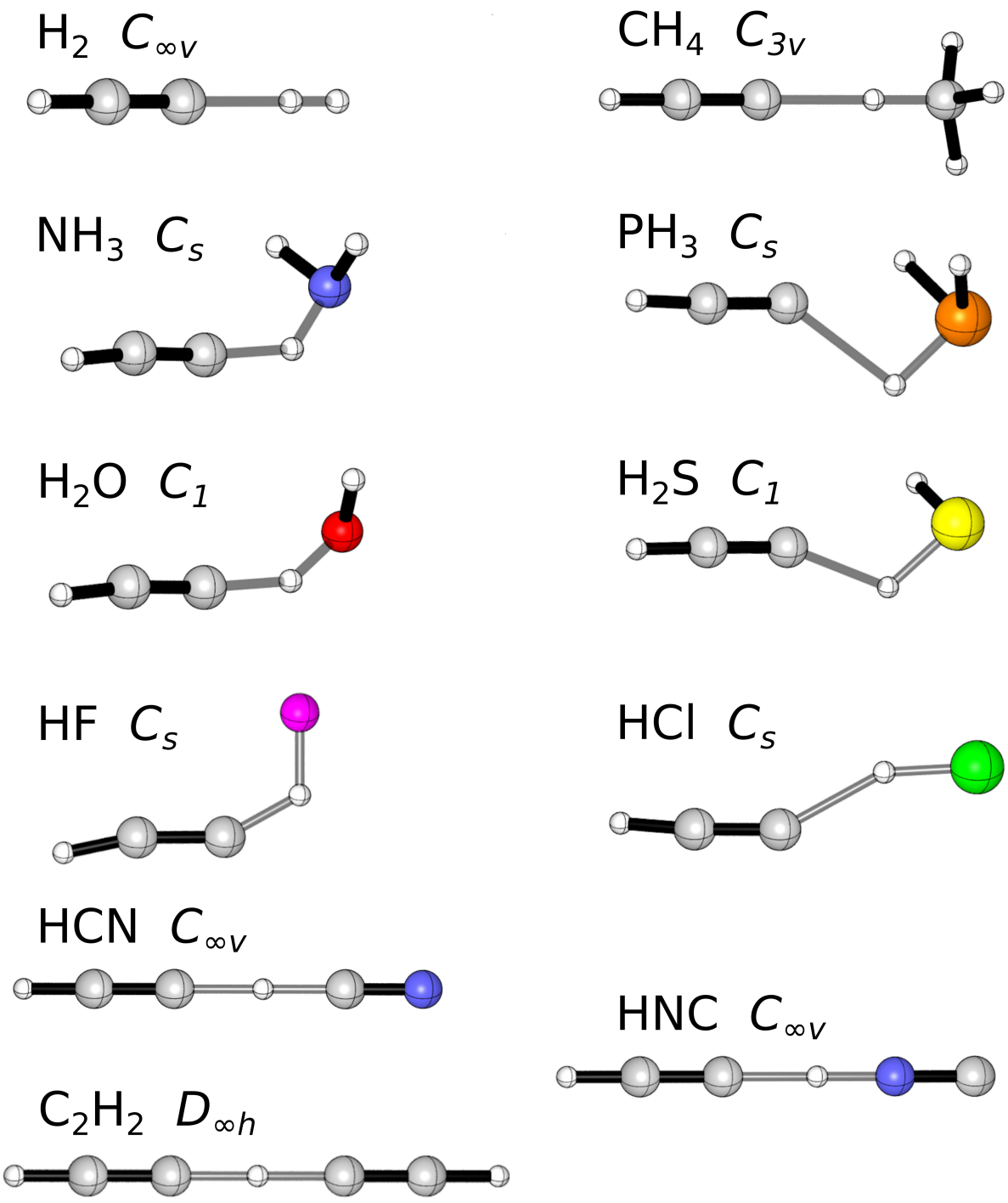

Figure 5.1: Qualitative geometries of C_2H + HX transition states.

Table 5.1: Enthaplies at 0 K (ΔH_{0K}) in kcal mol^{-1} for products (C_2H_2 + X) relative to reactants (C_2H + HX). δ denotes various corrections. See Methods section for details.

Donor	CBS[a]	δ_{ZPVE}	$\delta_{T(Q)}$	δ_{CORE}	δ_{REL}	δ_{DBOC}	δ_{SO}	Total	Exp.[b]
H_2	−29.77	1.48	0.27	−0.34	0.14	−0.02		−28.25	−28.43
CH_4	−26.90	−1.65	0.27	−0.16	0.12	−0.02		−28.34	−28.33
NH_3	−24.04	−1.83	0.26	−0.04	0.04	0.07		−25.54	−25.69
H_2O	−13.63	−0.36	0.35	−0.12	−0.01	0.04	−0.20	−13.93	−14.06
HF	2.20	1.86	0.43	−0.16	−0.07	0.00	−0.39	3.87	3.56
PH_3	−51.67	1.13	0.30	−0.18	−1.57	−0.03		−52.01	
H_2S	−43.20	2.08	0.30	−0.14	−1.87	−0.03	−0.54	−43.38	
HCl	−31.76	3.49	0.30	−0.11	−0.40	−0.03	−0.84	−29.33	−29.48
HCN	−7.12	0.70	−0.38	0.18	0.07	−0.02		−6.58	−6.68
HNC	−22.04	1.03	−0.55	−0.02	0.03	−0.01		−21.55	−21.57

[a] CBS denotes the CCSD(T)/CBS relative energy.
[b] Active Thermochemical Tables v1.22e[209]

Results

5.4 Results and Discussion

Table 5.1 shows the reaction enthalpies at 0 K for C_2H H-abstractions. As demonstrated in the final two columns of Table 5.1, the agreement between our computed reaction enthalpies and the experimentally determined reaction enthalpies is excellent. The mean absolute error (MAE) between our computed enthalpies and the experimental enthalpies is 0.13 kcal mol^{-1}, and the largest deviation is the hydrogen fluoride reaction at a discrepancy of 0.31 kcal mol^{-1}. The root mean squared error (RMSE) is only 0.16 kcal mol^{-1}, and therefore the 95 % confidence interval (2σ) is 0.32 kcal mol^{-1}.

Figure 5.1 illustrates the geometries of each hydrogen abstraction transition state. Table 5.2 shows the relative enthalpy of each transition state compared to its respective reactants.

Since the majority of these reactions feature an early barrier, the spin-orbit splitting at the transition state has been regarded as negligible. While the energetics of the products were determined to have an uncertainty of 0.32 kcal mol^{-1} in Table 5.1, the relative energetics of transition states are more sensitive to the level of theory employed. For this reason, we expect barrier heights to be reliable to within about 0.4 kcal mol^{-1}. At 300 K, an uncertainty of 0.4 kcal mol^{-1} corresponds to an uncertainty in the rate constant of about a factor of 2, which is sufficient for accurate kinetics. Of the corrections listed in Table 5.2, δ_{ZPVE} is noticeably the largest, contributing up to 40% of the total relative enthalpy for some transition states. This suggests that accurate barrier heights require not only accurate electronic energies, but reliable vibrational frequencies as well. Furthermore, δ_{REL} is the largest for third row donors, PH_3, H_2S, and HCl. Without δ_{REL} the barrier heights of period 3 donors would not be converged to the accuracy required for quantitative predictions. The abstraction of a hydrogen from silane (SiH_4) is expected to have a comparable contribution from scalar relativisitic effects. For fourth row donors such as germane (GeH_4), arsine (AsH_3), hydrogen selenide (H_2Se), or hydrogen bromide (HBr), the relativistic effects will contribute significantly more and a computational approach that directly incorporates scalar relativity would likely be more appropriate.

As shown in Table 5.2, C_2H + NH_3, PH_3 and H_2S have transition states submerged below the relative enthalpies of the separate reactants, suggesting these reactions will be rapid even at low temperatures. On the other hand, the hydrogen abstractions from the strong X–H bonds in HF, HCN, HNC, and C_2H_2 encounter barriers in excess of 6 kcal mol^{-1}; therefore, these reactions are unlikely to contribute at most temperatures. This is in agreement with experimental and previous theoretical studies which have shown the C_2H + C_2H_2 and C_2H + HCN reactions are dominated by C_2H insertion instead of H-abstraction at moderate to low temperatures.[203,210–212] As intermediate cases, C_2H + H_2, H_2O, CH_4 and HCl have moderate

Table 5.2: Enthaplies at 0 K (ΔH_{0K}) in kcal mol^{-1} for C_2H + HX transition states relative to reactants. δ denotes the various corrections. See Methods section for details.

Donor	CBS[a]	δ_{ZPVE}	$\delta_{\mathrm{T(Q)}}$	δ_{CORE}	δ_{REL}	δ_{DBOC}	Total
H_2	2.14	0.57	−0.06	−0.03	−0.01	0.03	2.64
CH_4	1.27	−0.42	−0.27	0.00	0.18	0.01	0.77
NH_3	−2.29	−0.48	−0.14	0.04	0.08	0.04[b]	−2.75
H_2O	5.60	−1.81	−0.16	0.01	0.05	0.13[b]	3.82
HF	14.95	−1.04	−0.42	0.21	0.00	0.03	13.73
PH_3	−3.71	0.93	−0.25	−0.04	0.62	−0.02	−2.48
H_2S	−2.33	0.61	−0.31	−0.06	0.71	−0.01	−1.39
HCl	1.94	−0.80	−0.18	−0.04	0.92	0.35	2.19
HCN	11.52	−2.80	−0.18	0.07	0.12	−0.01	8.72
HNC	10.77	−3.74	−0.72	0.06	−0.01	−0.01	6.35
C_2H_2	12.53	−2.62	−0.04	0.00	0.14	0.41	10.42

[a] CBS denotes the CCSD(T)/CBS relative energy.
[b] δ_{DBOC} evaluated with UHF-CCSD/cc-pVDZ

barriers less than 5 kcal mol^{-1}. These reactions will be orders of magnitude slower than their barrierless counterparts, yet they are necessary to confidently model chemical systems.

Table 5.3 compares the reaction enthalpies ($\Delta_r H$), barrier heights ($\Delta H^{\ddagger}$), main transition state geometry features (as illustrated in Figure 5.2), and the transition state imaginary mode frequency ($\omega^{\ddagger}$) of C_2H + HX abstractions. The reactions have been listed in order of decreasing exothermicity ($\Delta_r H$) in order to determine whether these hydrogen abstractions follow the Evans–Polanyi principle, which proposes the barrier height for similar reactions is inversely proportional to the reaction exothermicity. The reactions, in general, appear to follow the Evans–Polanyi principle with one noticeable exception, namely C_2H + NH_3. By comparing to ammonia's neighbors CH_4 and H_2O on the periodic table, one might expect the abstraction of a hydrogen from ammonia to encounter a modest barrier of approximately 2-3 kcal mol^{-1}. Instead, the barrier height for ammonia lies 2.1 kcal mol^{-1} below the reactant asymptote.

Table 5.3: Reaction enthalpies (ΔH_r), reaction barrier heights ($\Delta H^{\ddagger}$), geometries, and transition state imaginary frequencies ($\omega^{\ddagger}$) for C_2H + HX hydrogen abstractions at the CCSDT(Q)/CBS//CCSD(T)-F12a/aug-cc-pVTZ-F12 level of theory. Refer to Figure 5.2 for the definition of geometrical parameters. Energies given in kcal mol^{-1}, bond distances given in Angstrom, and imaginary vibrational frequencies given in cm^{-1}.

Donor	$\Delta_r H$	$\Delta H^{\ddagger}$	R_{CH}	ΔR_{XH}[a]	θ_1	θ_2	$\omega^{\ddagger}$
PH_3	−52.0	−2.5	2.044	0.6%	144.6	102.4	$248i$
H_2S	−43.4	−1.4	1.731	3.5%	158.9	114.6	$855i$
HCl	−29.3	2.2	1.684	3.3%	149.2	152.6	$378i$
CH_4	−28.3	0.8	1.740	3.4%	180.0	180.0	$208i$[b]
H_2	−28.3	2.6	1.754	3.9%	180.0	180.0	$506i$
NH_3	−25.5	−2.8	1.550	7.5%	−176.0	131.9	$757i$
HNC	−21.6	6.4	1.390	15.3%	180.0	180.0	$2495i$
H_2O	−14.1	3.8	1.368	13.8%	−175.6	145.7	$1441i$
HCN	−6.6	8.7	1.335	16.1%	180.0	180.0	$1667i$
C_2H_2	0.0	10.4	1.276	20.0%	180.0	180.0	$1511i$
HF	3.9	13.8	1.229	28.2%	−151.3	119.0	$1532i$

[a] $\Delta R_{\mathrm{XH}} = (R_{\mathrm{XH,TS}} - R_{\mathrm{XH,eq}}) / R_{\mathrm{XH,eq}}$
[b] CCSD(T)/aug-cc-pVTZ harmonic vibrational frequency

The submerged barrier for the NH_3 hydrogen abstraction is in agreement with previous experimental studies which report rate constants above 10^{-11} cm^3 s^{-1} molecule^{-1} with a slight negative temperature dependence. Previous theoretical studies have also examined the unexpected submerged C_2H + NH_3 barrier and have attributed this phenomenon to a strongly bound NH_3–C_2H pre-reactive complex (PRC) with a favorable alignment for H-abstraction.[199,202] Our computations confirm this hypothesis, with the NH_3 PRC lying 3.8 kcal mol^{-1} below the separate reactants.

Hammond's postulate, namely, how closely the transition state matches the isolated reactants depends on the exothermicity of the reaction, has also been considered for these reactions. The degree to which the transition state resembles the isolated reactants has been quantified using two different metrics: (a) the distance between the terminal carbon on

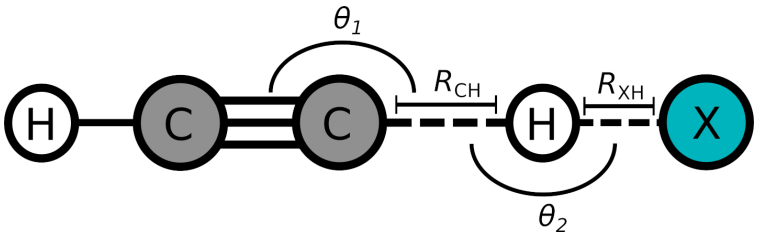

Figure 5.2: Illustration of C_2H + HX transition state geometry features

the ethynyl and (b) the abstracted hydrogen in the transition state (R_{CH}) and the relative elongation of the donor bond being cleaved at the transition state (ΔR_{XH}). In general, a good correlation exists between the reaction enthalpy ($\Delta_r H$) with the distance between the reactant fragments (R_{CH}) as well as with the donor bond elongation (ΔR_{XH}). For example, in the most exothermic reaction, C_2H + PH_3, the terminal carbon is separated from the abstracted hydrogen by a distance of over 2.0 Å and the elongation of the P–H bond is less than 1% at the transition state. On the other hand for the less exothermic C_2H + HCN reaction, the terminal carbon and abstracted hydrogen are only separated by 1.335 Å and the elongation of the C-H bond on hydrogen cyanide is over 16%.

Rate constants for the C_2H + H_2, CH_4, H_2O, and HCl reactions were obtained over a wide range of temperatures using canonical transition state theory:[31,32]

$$k_{\mathrm{TST}}(T) = \kappa(T)\frac{k_B T}{h}\frac{Q_{\mathrm{TS}}(T)}{Q_{\mathrm{R}}(T)}\exp\left(\frac{-\Delta H^{\ddagger}}{k_B T}\right) \tag{5.4}$$

where $Q_{\mathrm{TS}}(T)$ and $Q_{\mathrm{R}}(T)$ are the partition functions of the transition state and reactants, respectively, and $\Delta H^{\ddagger}$ is the barrier height for the reaction computed using equation 5.3. The tunneling transmission coefficient, $\kappa(T)$, was determined with an asymmetric Eckart barrier given the relative enthalpies of the pre-reactive complex, transition state, and products for each reaction, as well as the imaginary harmonic vibrational frequency corresponding to the reaction mode at the transition state.[36] Despite its simplicity, several kinetics studies

have shown that an Eckart tunneling model provides reasonable transmission coefficients for hydrogen transfer reactions when compared to more robust models such as small curvature tunneling.[213–215]

For C_2H + H_2, CH_4, and H_2O, comprehensive *ab initio* studies have unequivocally demonstrated that hydrogen abstraction is the dominant reaction pathway at most temperatures for these reactions, allowing for direct comparisons to be made with experimental rate constants.[201,216–218] Previous theoretical studies on these reactions have shown the rate constants to be sensitive to the treatment of low frequency vibrational modes at the transition state.[158,219] Accordingly, the lowest frequency mode in the C_2H + H_2O transition state (hindered OH rotation), the lowest frequency mode in the C_2H + CH_4 transition state (degenerate C-H-C bending), and the two lowest frequency modes in the C_2H + H_2 transition state (degenerate C-C-H bending and H_2 axisymmetric hindered rotation) have been treated using one-dimensional anharmonic models. Relaxed 1-D surface scans were performed along these modes at the CCSD(T)-F12a/aug-cc-pVTZ-F12//MP2/aug-cc-pVTZ level of theory and the anharmonic vibrational eigenstates and partition functions were determined using the BEx1D program.[220]

Table 5.4: Comparison of rate constants obtained using a harmonic oscillator model for all vibrational modes (HO) with rate constants obtained by using a 1-D anharmonic model for low frequency modes (Anharm). See Results and Discussion section for details. Rate constants given in cm^3 $molecule^{-1}$ s^{-1}.

	H_2		CH_4		H_2O		HCl
T (K)	HO	Anharm[a]	HO	Anharm[b]	HO	Anharm[c]	HO
50	8.34×10^{-18}	5.44×10^{-18}	1.51×10^{-14}	1.81×10^{-14}	5.12×10^{-15}	4.87×10^{-16}	4.55×10^{-17}
100	1.15×10^{-15}	7.34×10^{-16}	1.98×10^{-13}	1.77×10^{-13}	1.48×10^{-15}	9.03×10^{-16}	5.94×10^{-16}
150	2.04×10^{-14}	1.21×10^{-14}	6.73×10^{-13}	5.40×10^{-13}	1.72×10^{-15}	1.91×10^{-15}	1.34×10^{-14}
175	5.54×10^{-14}	3.12×10^{-14}	1.01×10^{-12}	7.85×10^{-13}	2.19×10^{-15}	2.85×10^{-15}	3.78×10^{-14}
200	1.23×10^{-13}	6.60×10^{-14}	1.42×10^{-12}	1.07×10^{-12}	2.92×10^{-15}	4.25×10^{-15}	8.66×10^{-14}
225	2.37×10^{-13}	1.21×10^{-13}	1.89×10^{-12}	1.38×10^{-12}	3.98×10^{-15}	6.29×10^{-15}	1.71×10^{-13}
250	4.12×10^{-13}	2.00×10^{-13}	2.43×10^{-12}	1.72×10^{-12}	5.45×10^{-15}	9.17×10^{-15}	3.01×10^{-13}
275	6.60×10^{-13}	3.05×10^{-13}	3.03×10^{-12}	2.10×10^{-12}	7.45×10^{-15}	1.31×10^{-14}	4.88×10^{-13}
295	9.19×10^{-13}	4.09×10^{-13}	3.55×10^{-12}	2.42×10^{-12}	9.48×10^{-15}	1.72×10^{-14}	6.86×10^{-13}
298	9.63×10^{-13}	4.26×10^{-13}	3.64×10^{-12}	2.47×10^{-12}	9.82×10^{-15}	1.79×10^{-14}	7.20×10^{-13}
300	9.93×10^{-13}	4.38×10^{-13}	3.69×10^{-12}	2.50×10^{-12}	1.01×10^{-14}	1.84×10^{-14}	7.43×10^{-13}
325	1.42×10^{-12}	6.00×10^{-13}	4.43×10^{-12}	2.93×10^{-12}	1.34×10^{-14}	2.51×10^{-14}	1.07×10^{-12}
350	1.96×10^{-12}	7.92×10^{-13}	5.23×10^{-12}	3.39×10^{-12}	1.76×10^{-14}	3.37×10^{-14}	1.49×10^{-12}
375	2.62×10^{-12}	1.01×10^{-12}	6.11×10^{-12}	3.88×10^{-12}	2.27×10^{-14}	4.42×10^{-14}	2.00×10^{-12}
400	3.40×10^{-12}	1.27×10^{-12}	7.06×10^{-12}	4.40×10^{-12}	2.90×10^{-14}	5.71×10^{-14}	2.60×10^{-12}
500	7.98×10^{-12}	2.57×10^{-12}	1.17×10^{-11}	6.76×10^{-12}	6.75×10^{-14}	1.36×10^{-13}	6.12×10^{-12}
1000	7.90×10^{-11}	1.53×10^{-11}	6.01×10^{-11}	2.65×10^{-11}	8.88×10^{-13}	1.66×10^{-12}	5.72×10^{-11}
1500	2.63×10^{-10}	3.63×10^{-11}	1.66×10^{-10}	6.10×10^{-11}	3.78×10^{-12}	6.35×10^{-12}	1.77×10^{-10}
2000	5.97×10^{-10}	6.37×10^{-11}	3.48×10^{-10}	1.11×10^{-10}	1.02×10^{-11}	1.56×10^{-11}	3.75×10^{-10}
3000	1.84×10^{-09}	1.31×10^{-10}	9.95×10^{-10}	2.61×10^{-10}	3.89×10^{-11}	5.09×10^{-11}	1.02×10^{-09}
4000	4.04×10^{-09}	2.08×10^{-10}	2.09×10^{-09}	4.78×10^{-10}	9.62×10^{-11}	1.12×10^{-10}	2.01×10^{-09}
5000	7.35×10^{-09}	2.89×10^{-10}	3.72×10^{-09}	7.65×10^{-10}	1.89×10^{-10}	1.99×10^{-10}	3.34×10^{-09}

[a] C–C–H bending motion (π) and H_2 internal rotation (π) treated as anharmonic vibrations
[b] C–H–C bending motion (e) treated as anharmonic vibration
[c] H–O–H–C torsion treated as a hindered rotation

A comparison of the rate constants computed with strictly harmonic oscillator partition functions and the rate constants computed with anharmonic vibrational partition functions for the lowest vibrational modes of the transition state is provided in Table 5.4. At low temperatures the difference between the harmonic oscillator and anharmonic rate constants is small; however, at higher temperatures the harmonic rate constants are noticeably different than the anharmonic rate constants. At 300 K the H_2 and CH_4 rate constants are reduced by a factor of 2.27 and 1.48, respectively, and the H_2O rate constant increased by a factor of 1.82. At high temperatures the harmonic and anharmonic rate constants for $C_2H + H_2O$ appear to coalesce, but the harmonic and anharmonic rate constants for $C_2H + H_2$ and $C_2H + CH_4$ continue to diverge from each other. At 5000 K, the difference between the harmonic and anharmonic rate constants for $C_2H + H_2$ is a factor of 25.4. This is far greater than the variational contribution for this reaction computed by Zhang[221] as well as the difference between Eckart tunneling and SCT. Therefore, future theoretical studies are encouraged to prioritize anharmonic treatments of low frequency modes in order to achieve accurate rate constants in the moderate to high temperature region.

Due to its simplicity as a pentatomic system and its importance to astrochemistry, numerous theoretical and experimental studies over the past three decades have focused on the $C_2H + H_2$ hydrogen abstraction. Comparisons may be drawn between the theoretical results presented here and the ample previous theoretical studies on $C_2H + H_2$ as shown in Table 5.5. The works of Sherrill[225] and Truhlar[227] also provide an exhaustive comparison of various *ab initio* methods for the $C_2H + H_2$ reaction. In Table 5.5, our results may be considered as the current highest level of theory, incorporating a robust geometry as well as various incremental corrections to the electronic energy. The next highest levels of theory include the CCSD(T)/aug-cc-pWCVTZ results from Miyoshi,[158] the CCSD(T)-F12/aug-cc-pVTZ results from Yang,[226] and the W1 results from Truhlar.[227] Our results closely agree with these other high levels of theory; however, papers that employed basis sets smaller than

Table 5.5: Comparison of $C_2H + H_2$ abstraction at various levels of theory. Enthalpies are given in kcal mol^{-1}, bond distances are given in Angstrom, and frequencies are given in cm^{-1}.

Theory	$\Delta H^{\ddagger}$	ΔH_r	R_{CH}	$\omega^{\ddagger}$
CCSDT(Q)/CBS//CCSD(T)-F12a/aVTZ-F12[a]	2.64	−28.3	1.75	$506i$
MPW1K/6-311++G**[b]	1.48	−29.4	1.92	
QCISD(T)/cc-pVTZ//MP2/cc-pVTZ[c]	2.86	−33.0	1.75	$607i$
QCISD(T)/aVTZ//QCISD/cc-pVTZ[d]	2.30	−30.1	1.69	608i
G2//QCISD/6-311+G**[e]	2.52	−29.0	1.66	$679i$
CCSD(T)/aVTZ//CCSD(T)/6-311++G(2df,2pd)[f]	3.06		1.72	$555i$
CCSD(T)/cc-pVTZ//CCSD(T)/cc-pVDZ[g]	3.30	−29.5	1.72	$527i$
CCSD(T)/cc-pwCVDZ[h]	4.25		1.70	$614i$
CCSD(T)/aug-cc-pwCVTZ[h]	2.70		1.75	$523i$
CCSD(T)-F12a/aug-cc-pVTZ[i]	2.61[k]	−28.2[k]	1.74	
W1//BMC-CCSD/(aug-)cc-pVTZ[j]	2.64[k]	−28.8[k]	1.77	
Active Thermochemical Tables		−28.4		

[a] This work
[b] Nguyen et al [197]
[c] Kurosaki and Takayanagi [222]
[d] Ju and Wang [223,224]
[e] Zhang et al [221]
[f] Peeters et al [216]
[g] Temelso et al [225]
[h] Matsugi et al [158]
[i] Chen et al [226]
[j] Zheng et al [227] aug-cc-pVTZ used for carbon
[k] δ_{ZPVE} has been added for comparison

aug-cc-pVTZ received noticeably different results. This reaffirms the conventional wisdom that triple-ζ basis sets should be used with correlation methods in order to achieve highly accurate results, but it further suggests that a set of diffuse functions are necessary on heavy atoms to properly compute the barrier heights for early barrier bimolecular reactions.

Our computed rate constants for the $C_2H + H_2$ hydrogen abstraction are illustrated in Figure 5.3. For comparison the VTST/Anharm/SCT theoretical rate constants of Miyoshi (solid red),[158] as well as various experimentally determined rate constants have been included. Both Miyoshi[158] and our rate constants have been determined using an anharmonic vibrational partition function for the lowest two degenerate vibrational modes at the $C_2H + H_2$ transition state. The Tokyo group also employed variational transition state theory (VTST) as well as small curvature tunneling (SCT), whereas these treatments were outside the scope of

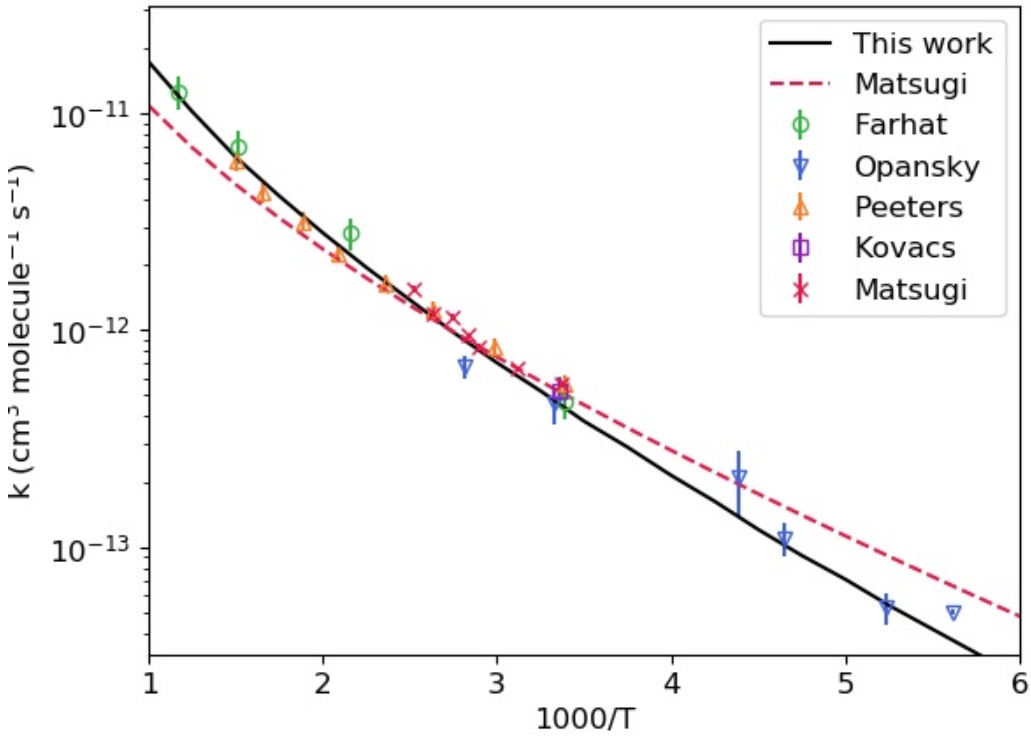

Figure 5.3: Rate coefficients for the $C_2H + H_2 \rightarrow C_2H_2 + H$ reaction. Theoretical rate constants are illustrated as solid curves and experimental rate constants are given as points with error bars.[158,196,216,228,229]

our present research. It has been previously mentioned that Eckart tunneling performs on par with SCT for hydrogen transfer reactions at moderate temperatures.[213–215] Previous work by Zhang and coworkers[221] employed VTST and SCT on the $C_2H + H_2$ reaction and demonstrated the differences between variational transition state theory and conventional transition state theory are negligible at 300 K and only about 15% at 1000 K. Given that variational transition state theory only lowers the calculated rate constants relative to conventional transition state theory, our computed rate constants may be interpreted as upper-bounds for the rate constant in the high-temperature region.

In order to match experimental results, Miyoshi also reduced their barrier height for this reaction by 0.3 kcal mol^{-1}. Without this scaling their computed rate constants would have been considerably slower at moderate to low temperatures. Nevertheless, our theoretically predicted rate constants (solid black) closely match both the theoretical rate constants from Miyoshi (dashed red), as well the experimentally determined rate constants at and above 300 K. At temperatures below 300 K, there is an observable difference between our theoretical rate constants and the work of Miyoshi. Based off the low-temperature kinetics from Opansky and Leone[196] it is unclear which set of rate constants is more accurate in this region. The computed rate constants in this work over the range 100 K to 1000 K was fit to a modified Arrhenius equation:

$$k_{H_2}(T) = 7.29 \times 10^{-16}\ T^{1.566}\ e^{-738.1/T}\ \text{cm}^3\ \text{molecule}^{-1}\ \text{s}^{-1} \tag{5.5}$$

This expression is similar to the fit obtained by Miyoshi for the range 150 K to 2000 K of $2.34{\times}10^{-15}\ T^{1.312} \exp(-615.9/T)$, with a slightly greater temperature dependence in both the prefactor and the exponential.

As methane is the smallest hydrocarbon, several studies have examined the $C_2H + CH_4$ abstraction. The barrier for hydrogen abstraction from CH_4 is less than 1 kcal mol^{-1}; therefore, for the $C_2H + CH_4$ reaction, it is especially important to determine the relative enthalpy

Table 5.6: Comparison of C_2H + CH_4 abstraction at various levels of theory. Enthalpies are given in kcal mol^{-1}, bond distances are given in Angstrom, and frequencies are given in cm^{-1}.

Theory	$\Delta H^{\ddagger}$	ΔH_r	R_{CH}	$\omega^{\ddagger}$
CCSDT(Q)/CBS//CCSD(T)-F12a/aVTZ-F12[a]	0.77	−28.3	1.74	$208i$[e]
MPW1K/6-311++G**[b]	4.71	−31.2	1.89	
MP2/cc-pVDZ [c]	1.74		1.72	$284i$
MP4(SDQ)/aug-cc-pVDZ[c]	0.86		1.71	$306i$
CCSD(T)/cc-pVTZ//M06-2X/6-311++G**[d]	0.38	−29.2	1.67	$455i$
CCSD(T)/cc-pVTZ//CCSD(T)/cc-pVDZ[e]	1.70	−29.0	1.68	$247i$
Active Thermochemical Tables		−28.3		

[a] This work
[b] Nguyen et al[197]
[c] Matsugi et al[158]
[e] Temelso et al[225]
[d] Dash and Rajakumar[198]
[e] CCSD(T)/aug-cc-pVTZ frequency

of the transition state to a high degree of accuracy. Table 5.6 provides a comparison of theoretical results for the C_2H + CH_4 reaction. Both Temelso et al[225] and Dash and Rajakumar[198] computed the CCSD(T)/cc-pVTZ electronic energy at each stationary point; however, these studies employed different levels of theory to optimize the geometries and determine the harmonic vibrational frequencies. Due to differences in the zero point vibrational energies, Temelso et al predicted a barrier height of 1.70 kcal mol^{-1} while Dash and Rajakumar predicted a very different barrier height of 0.38 kcal mol^{-1}. The importance of using an appropriate level of theory to compute the Hessian is reiterated by examining how the transition state's imaginary frequency ($\omega^{\ddagger}$) changes with respect to different levels of theory. While M06-2X/6-311++G** is usually considered to be a reasonable level of theory to determine geometries and vibrational frequencies, it obtains an imaginary frequency for the C_2H + CH_4 transition state that is over twice the value computed at the CCSD(T)/aug-cc-pVTZ level of theory. Since the imaginary frequency is related to the width of the barrier, this error would likely correspond to a significant overestimation of the transmission coefficient and lead to inaccurate kinetics at low temperatures.

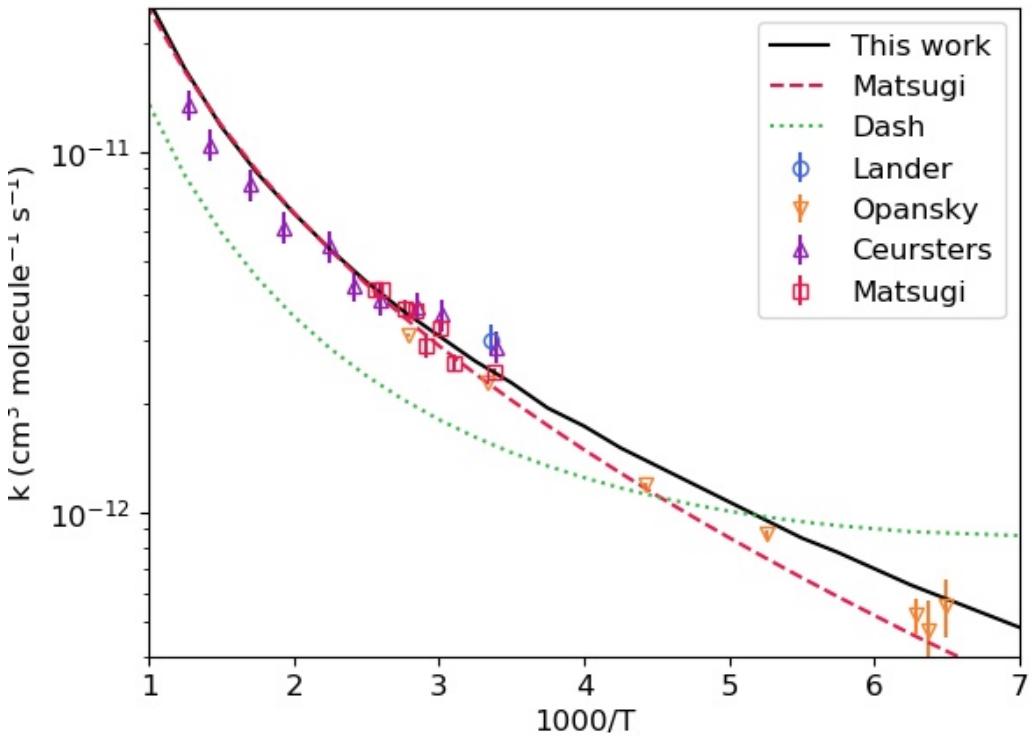

Figure 5.4: Rate coefficients for the $C_2H + CH_4 \rightarrow C_2H_2 + CH_3$ reaction. Theoretical rate constants are illustrated as solid curves and experimental rate constants are given as points with error bars.[158,194,198,217,230]

The C_2H + CH_4 hydrogen abstraction is noticeably faster than the C_2H + H_2 reaction at moderate temperatures despite their similar exothermicities. This is due to the decreased barrier height and increased statistical probability of the C_2H + CH_4 transition state. Figure 5.4 illustrates our calculated rate constants for the C_2H + CH_4 reaction in comparison to previous theoretical and experimental studies. At moderate to high temperatures our calculated rate constants (solid black) closely match the experimentally observed rate constants as well the theoretically predicted rate constants from Miyoshi (dashed red).[158] Similar to Figure 5.3 at temperatures below 300 K, there is once again a discrepancy between the rate constants calculated in this work and the rate constants calculated by Miyoshi.[158] Given the limited number of kinetics studies performed at low temperatures, it is ambiguous which curve is more reliable; however, it should be noted that Miyoshi reduced their computed barrier height by 0.3 kcal mol^{-1} to replicate the experimental rate constants around 300 K.

On the other hand, Dash and Rajakumar (dotted green) also used VTST/SCT, but they did not scale their barrier height value of 0.38 kcal mol^{-1}. The rate constants predicted by Dash and Rajakumar slightly underestimate the experimental rate constants at moderate to high temperatures and overestimate the rate constant at low temperatures. The underestimation at moderate temperatures is likely the result of inaccuracy in the M06-2X harmonic vibrational frequencies. At the M06-2X/6-311++G** level of theory the lowest degenerate vibrational frequency was 87 cm^{-1}, whereas at the MP4(SDQ)/aug-cc-pVDZ and CCSD(T)/aug-cc-pVTZ levels of theory the lowest degenerate vibrational frequency was 48 cm^{-1} and 41 cm^{-1}. While the discrepancy in this vibrational mode would only have a modest impact on the ZPVE, it would significantly reduce the vibrational partition function for the transition state leading to inaccurate predictions for the rate constant at moderate temperatures. Alternatively, at low temperatures the overestimation in the rate constant by Dash and Rajakumar is likely the result of an underestimation in the barrier height for this reaction.

The theoretically predicted rate constants have been fit to a modified Arrhenius equation:

$$k_{CH_4}(T) = 4.20 \times 10^{-17}\ T^{1.935}\ e^{-189.6/T}\ \text{cm}^3\ \text{molecule}^{-1}\ \text{s}^{-1} \tag{5.6}$$

A similar expression was obtained by Miyoshi of $5.53{\times}10^{-16}\ T^{1.582} \exp(-208.2/T)$ over the temperature range 150-2000 K. On the other hand, Dash and Rajakumar obtained an expression with a negative activation energy: $4.69{\times}10^{-19}\ T^{2.44} \exp(331/T)$

An initial experimental study on the C_2H + H_2O by Van Look and Peeters[211], observed rate constants as fast as 10^{-11} cm^3 molecule^{-1} s^{-1} at 295 K, suggesting a barrierless or near-barrierless reaction. Due to the moderate barrier expected for the hydrogen abstraction, Van Look and Peeters suggested the reaction proceeded through the initial formation of a C_2H_3O complex that isomerizes and dissociates into ketene (H_2CCO) and a hydrogen radical. Later, a comprehensive *ab initio* study performed Ding et al[218] demonstrated the formation of a C_2H_3O complex is hindered by barriers in excess of 27 kcal mol^{-1} while the minimum reaction pathway is a direct abstraction of a hydrogen from H_2O with a barrier of 3.7 kcal mol^{-1}. Ding and coworkers performed TST calculations with a correction factor for VTST/SCT at the MP2/6-311G** level of theory and obtained rate constants that were four orders of magnitude slower than the rates observed by Van Look and Peeters. A later joint theoretical and experimental study by Peeters and coworkers sought to resolve this apparent discrepancy.[219] They observed rate constants of $2.3{\times}10^{-13}$, $7.2{\times}10^{-13}$, and $7.7{\times}10^{-13}$ cm^3 molecule^{-1} s^{-1} at 550 K, 770 K, and 825 K, respectively. Complementary rate constants were computed with CCSD(T) and CASPT2 which closely matched the experimentally determined rate constants.

As shown in Table 5.7, the barrier height computed in this study is slightly less than the barrier height obtained by Carl and coworkers at the CCSD(T)/6-311++G(3df,2p) level of theory and slightly greater than the barrier height obtained by the same authors using CASPT2.[219]

Table 5.7: Comparison of C_2H + H_2O abstraction at various levels of theory. Enthalpies are given in kcal mol^{-1}, bond distances are given in Angstrom, and frequencies are given in cm^{-1}.

Theory	$\Delta H^{\ddagger}$	ΔH_r	R_{CH}	$\omega^{\ddagger}$
CCSDT(Q)/CBS//CCSD(T)-F12a/aVTZ-F12[a]	3.82	−13.9	1.37	$1441i$
MPW1K/6-311++G**[b]	2.15	−18.7	1.46	
QCISD(T)/CBS//B3LYP/6-311++G**[c]	4.60	−13.4		$669i$
CASPT2(13,12)/ANO-L//CCSD(T)/6-311++G**[d]	3.59			
CCSD(T)/6-311+G(3df,2p)//QCISD/6-311G**[e]	3.70	−15.2	1.40	$1638i$
CCSD(T)/6-311++G(3df,2p)[d]	4.06	−15.3	1.42	
Active Thermochemical Tables		−14.1		

[a] This work
[b] Nguyen et al[197]
[c] Senosiain et al[231]
[d] Carl et al[219]
[e] Ding et al[218]

Figure 5.5 illustrates the theoretical and experimental rate constants for the C_2H + H_2O reaction. The CASPT2 rate constants computed by Carl[219] appear to be the most consistent with experiment. This is surprising because the CCSD(T) results presented by Carl[219] as well as the coupled cluster results presented in this work are at a higher level of theory than the multireference CASPT2 treatment. At the CCSD(T)/aug-cc-pVDZ level of theory the $\mathcal{T}_1$ diagnostic for the C_2H + H_2O transition state is 0.023, significantly below the conventional threshold of 0.045 for requiring multireference methods in open-shell species.[18] Given the flexibility in determining the active space it is likely the agreement between CASPT2 and the experimental rate constants is fortuitous and does not demonstrate any need for a multireference treatment in this system. Moreover, the rate constants computed in this study are in good agreement with the experimental rate constants from Carl and coworkers. The agreement between our results would be further bolstered with variational transition state theory, which would slightly lower the computed rate constants in the high temperature region. Therefore, it is likely that our determined rate constants will prove to be more

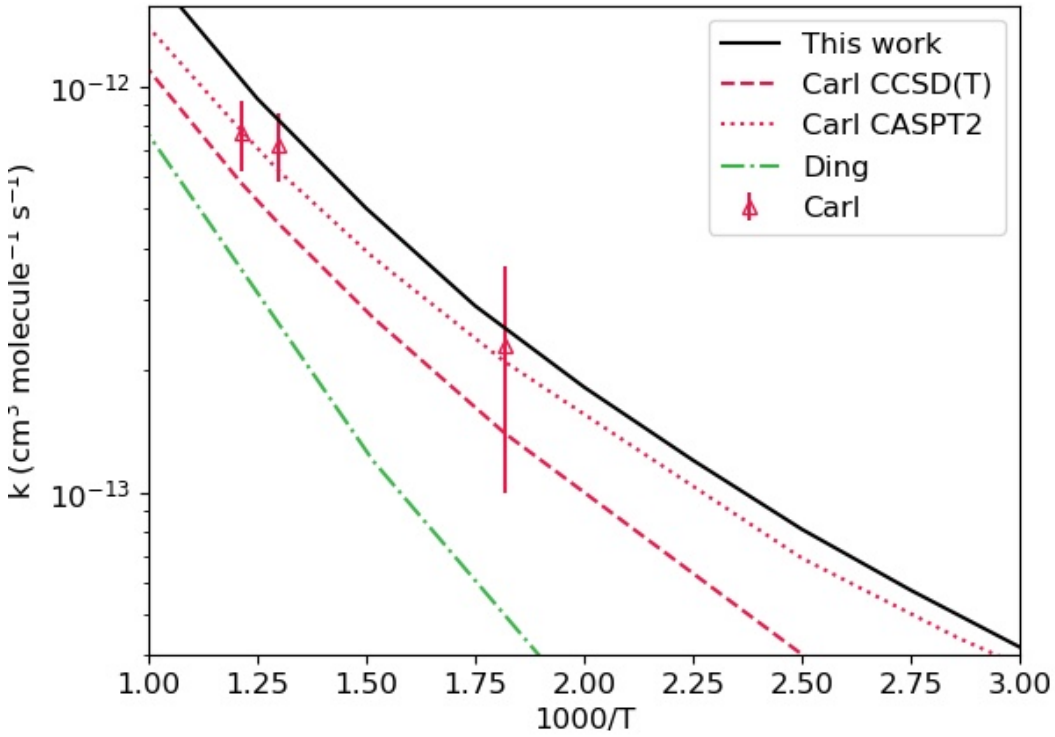

Figure 5.5: Rate coefficients for the $C_2H + H_2O \rightarrow C_2H_2 + OH$ reaction. Theoretical rate constants are illustrated as solid curves and experimental rate constants are given as points with approximate error bars.[218,219]

accurate if future kinetics studies examine the $C_2H + H_2O$ kinetics in the temperature range of 200 - 400 K.

The theoretically predicted rate constants for the $C_2H + H_2O$ reaction over the range 200 K to 2000 K have been fit to a modified Arrhenius equation:

$$k_{H_2O}(T) = 1.38 \times 10^{-20}\ T^{2.784}\ e^{-462.1/T}\ \text{cm}^3\ \text{molecule}^{-1}\ \text{s}^{-1} \tag{5.7}$$

This expression is similar to the equation given by Carl et al over the same temperature range of $(2.2 \pm 0.1) \times 10^{-21}\ T^{3.05}\ \exp\left[-\left(-376 \pm 100\right)/T\right]\ \text{cm}^3\ \text{molecule}^{-1}\ \text{s}^{-1}$

5.5 Conclusions

The energetics of ethynyl radical hydrogen abstractions have been determined using highly accurate *ab initio* methods. In accord with the Evans–Polanyi principle, a strong correlation between the barrier height ($\Delta H^{\ddagger}$) and the reaction enthalpy ($\Delta_r H$) was observed, with the highly exothermic C_2H + PH_3 and C_2H + H_2S abstractions featuring submerged barriers and the modestly exothermic abstractions C_2H + HCN and C_2H + HNC encountering substantial barriers. However, the C_2H + NH_3 reaction significantly deviates from the Evans–Polanyi principle due to the formation of a strongly bound complex prior to hydrogen abstraction. This complex lowers the relative enthalpy of the transition state below the respective reactants.

Accurate kinetics were obtained for the C_2H + H_2, CH_4, and H_2O reactions employing an Eckart tunneling model and anharmonic vibrational partition functions for low frequency vibrational modes at the transition state. Excellent agreement with the best experimental results was demonstrated for our computed rate constants without adjusting the barrier height. The results presented in this study will serve useful in modeling and may be used to guide future experimental studies.

Chapter 6

Concluding Remarks

Quantum chemical *ab initio* methods such as coupled-cluster theory have been demonstrated to provide highly accurate results for a wide variety of chemical systems. The introductory chapter of this thesis included a brief overview of commonly used *ab initio* methods. When *ab initio* methods are combined with basis set extrapolation and auxiliary corrections, sub-chemical accuracies of ≤ 0.5 kcal mol^{-1} may be obtained. These highly accurate results may be used to provide conclusive interpretations of previous experiments as well as guide the efforts of future experimental studies. The four projects described in this thesis showcase highly accurate coupled-cluster methods as they are applied to theoretically challenging systems.

In Chapter 2, the methyl anion (CH_3^-) was studied using large correlation-consistent basis sets. This study explored the anomalous basis set sensitivity of the methyl anion with special attention given to the umbrella vibrational mode. Contrary to expectation, it was shown that non-augmented (cc-pVXZ) and singly augmented (aug-cc-pVXZ) basis sets display false convergence patterns whereas the doubly augmented (d-aug-cc-pVXZ) approaches the true basis set limit.

In Chapter 3, the energetics and anharmonic vibrational spectra of Ca_2H_2 and Ca_2H_4 constitutional isomers were determined using convergent coupled-cluster methods and second order vibrational perturbation theory (VPT2). A comparison of matrix isolation experiments

with our computed frequencies for the Ca_2H_2 isomers revealed only the linear Ca_2H_2 structure has been definitively observed, which is surprising because the monobridged and dibridged Ca_2H_2 structures are significantly lower in energy. On the other hand, our VPT2 frequencies for Ca_2H_4 isomers revealed the nearly degenerate dibridged Ca_2H_4 and tribridged Ca_2H_4 structures were simultaneously observed in both neon and argon matrices.

In Chapter 4, the energetic profile of the $C_2H + O_2$ reaction was thoroughly investigated using coupled-cluster theory. Two main reaction pathways from the HCCOO peroxy radical include a cleavage of the O–O bond which directly yields HCCO ($^2A''$) + O (^3P) and an isomerization which ultimately yields HCO ($^2A'$) + CO. Around 298 K, the branching ratio between these two competitive reaction pathways was determined to be about 1:1, which agrees with experimental studies.

In Chapter 5, the kinetics and energetics of hydrogen abstractions of the C_2H radical from various H-atom donors were examined. In general, these reactions behave according to Hammond's postulate as well as the Evans–Polanyi principle with a noticeable exception to the $C_2H + NH_3$ hydrogen abstraction. For the $C_2H + H_2$, CH_4, H_2O, and NH_3 reactions, our theoretically predicted rate constants were observed to be in excellent agreement with present experimental results. This confirms that our kinetics are reliable for modeling purposes even for hydrogen abstractions where experimental rate constants have not yet been reported.

Appendix A

Supporting Information for Chapter 2

Table S1: Absolute CCSD(T) energies (kcal mol^{-1}), geometries (Åand degrees), and harmonic vibrational frequencies (cm^{-1})

Basis	ζ	R_{CH}	θ	$\omega_1(a_1)$	$\omega_2(a_1)$	$\omega_3(e)$	$\omega_4(e)$
cc-pV	DZ	1.144	28.10	2689	1121	2732	1454
	TZ	1.119	25.97	2771	1040	2814	1455
	QZ	1.113	24.74	2809	980	2865	1445
	5Z	1.109	22.97	2850	906	2919	1432
	6Z	1.106	21.86	2871	858	2950	1426
	CBS	1.104	20.73	2888	803	2976	1422
aug-cc-pV	DZ	1.121	21.14	2853	809	2947	1397
	TZ	1.105	20.22	2890	784	2980	1421
	QZ	1.102	19.85	2903	761	2999	1420
	5Z	1.101	19.46	2912	737	3012	1419
	6Z	1.100	19.21	2917	722	3019	1419
	CBS	1.100	19.09	2921	712	3024	1418
d-aug-cc-pV	DZ	1.114	18.50	2897	639	3013	1394
	TZ	1.101	18.39	2922	663	3028	1417
	QZ	1.099	18.48	2926	665	3034	1417
	5Z	1.099	18.49	2926	663	3036	1411
	CBS	1.098	18.51	2929	661	3040	1412
t-aug-cc-pV	DZ	1.114	18.24	2900	602	3019	1393
	TZ	1.101	18.27	2924	650	3031	1418

Energies are relative to the d-aug-cc-pV(TQ5)Z energy

Appendix B

Supporting Information for Chapter 3

B.1 Products

Incremental Focal Point Analysis (kcal mol^{-1}) of 2 CaH ($^2\Sigma^+$) relative to Ca_2 + H_2:

Basis	ΔE_e HF	$+\delta$ MP2	$+\delta$ CCSD	$+\delta$ (T)	$+\delta$ T	$+\delta$ (Q)	ΔE_e Net
DZ	+11.43	+20.81	−2.05	+1.85	−0.01	+0.33	[+32.36]
TZ	+11.47	+19.69	−3.72	+2.83	−0.17	[+0.33]	[+30.43]
QZ	+11.27	+19.39	−4.26	+3.01	[−0.17]	[+0.33]	[+29.57]
5Z	+11.26	+19.31	−4.56	+3.08	[−0.17]	[+0.33]	[+29.25]
CBS	[+11.26]	[+19.23]	[−4.88]	[+3.16]	[−0.17]	[+0.33]	[+28.93]

Incremental Focal Point Analysis (kcal mol^{-1}) of CaH_2 + Ca relative to Ca_2 + H_2:

Basis	ΔE_e HF	$+\delta$ MP2	$+\delta$ CCSD	$+\delta$ (T)	$+\delta$ T	$+\delta$ (Q)	ΔE_e Net
DZ	+4.13	+7.72	−3.66	+1.36	+0.14	+0.27	[+9.97]
TZ	+4.64	+6.35	−3.99	+2.01	+0.05	[+0.27]	[+9.34]
QZ	+4.53	+5.86	−4.01	+2.15	[+0.05]	[+0.27]	[+8.85]
5Z	+4.53	+5.71	−4.08	+2.20	[+0.05]	[+0.27]	[+8.69]
CBS	[+4.54]	[+5.55]	[−4.15]	[+2.26]	[+0.05]	[+0.27]	[+8.52]

Incremental Focal Point Analysis (kcal mol^{-1}) of 2 CaH_2 relative to Ca_2 + 2 H_2:

Basis	ΔE_e HF	$+\delta$ MP2	$+\delta$ CCSD	$+\delta$ (T)	$+\delta$ T	$+\delta$ (Q)	ΔE_e Net
DZ	+10.09	+11.97	−6.17	+1.78	+0.08	+0.36	[+18.11]
TZ	+11.01	+8.57	−6.65	+2.85	−0.06	[+0.36]	[+16.07]
QZ	+10.76	+7.23	−6.59	+3.00	[−0.06]	[+0.36]	[+14.69]
5Z	+10.75	+6.84	−6.69	+3.07	[−0.06]	[+0.36]	[+14.27]
CBS	[+10.77]	[+6.43]	[−6.80]	[+3.15]	[−0.06]	[+0.36]	[+13.85]

B.2 Minima

M1 [HCaCaH] $D_{\infty h}$

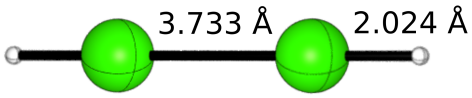

Level of Theory:
Geometry: CCSD(T)/QZ
Harmonics: CCSD(T)/QZ
Anharmonics: CCSD(T)/TZ
Wavefunction Diagnostics:
$T_1 = 0.011$
$D_1 = 0.037$

Figure S1: M1

Cartesian Coordinates (Å):

Ca	0.0000000000	0.0000000000	-1.8666839110
Ca	0.0000000000	0.0000000000	1.8666839110
H	0.0000000000	0.0000000000	-3.8905587102
H	0.0000000000	0.0000000000	3.8905587102

Rotational Constants (GHz): 0.0, 1.631, 1.631

Vibrational Frequencies (cm^{-1}):

Mode	Symmetry	ω	$\delta\nu$	ν	Intensity
1	σ_g^+	1300.3	−36.3	1264.0	0.0
2	σ_g^+	151.7	−0.6	151.0	0.0
3	π_g	144.4	22.9	167.3	0.0
4	σ_u^-	1287.9	−43.0	1244.9	1683.9
5	π_u	130.1	10.3	140.4	428.3

Incremental Focal Point Analysis (kcal mol^{-1}):

Basis	ΔE_e HF	$+\delta$ MP2	$+\delta$ CCSD	$+\delta$ (T)	$+\delta$ T	$+\delta$ (Q)	ΔE_e Net
DZ	−2.72	+9.71	−4.78	+0.86	−0.02	+0.25	[+3.30]
TZ	−2.62	+5.80	−5.63	+1.49	−0.15	[+0.25]	[−0.86]
QZ	−2.77	+4.59	−5.52	+1.58	[−0.15]	[+0.25]	[−2.03]
5Z	−2.78	+4.16	−5.51	+1.61	[−0.15]	[+0.25]	[−2.42]
CBS	[−2.77]	[+3.72]	[−5.51]	[+1.64]	[−0.15]	[+0.25]	[−2.82]

M2 [Ca(μ_2-H)CaH] C_s

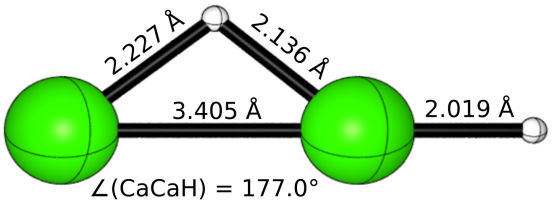

Figure S2: M2

Level of Theory:
Geometry: CCSD(T)/QZ
Harmonics: CCSD(T)/QZ
Anharmonics: CCSD(T)/TZ
Wavefunction Diagnostics:
$T_1 = 0.021$
$D_1 = 0.091$

Cartesian Coordinates (Å):

Ca	0.0207918523	0.0000000000	-1.6563291001
Ca	0.0150922579	0.0000000000	1.7490613730
H	-0.0817695443	0.0000000000	-3.6730098568
H	-1.3451359629	0.0000000000	-0.0144214354

Rotational Constants (GHz): 2.038, 2.053, 272.155

Dipole Moment (Debye): 0.0, 0.0, 2.79

Vibrational Frequencies (cm^{-1}):

Mode	Symmetry	ω	$\delta\nu$	ν	Intensity
1	a'	1304.2	−34.4	1269.7	811.1
2	a'	1042.3	−83.6	958.4	52.8
3	a'	843.0	−46.4	796.6	729.5
4	a'	214.0	4.7	218.7	247.8
5	a'	163.9	−3.8	160.1	25.6
6	a''	136.9	11.4	148.3	313.4

Incremental Focal Point Analysis (kcal mol^{-1}):

Basis	ΔE_e HF	$+\delta$ MP2	$+\delta$ CCSD	$+\delta$ (T)	$+\delta$ T	$+\delta$ (Q)	ΔE_e Net
DZ	−3.24	+4.10	−3.95	+0.03	−0.08	+0.15	[−2.98]
TZ	−3.22	+0.05	−4.00	+0.29	−0.21	[+0.15]	[−6.94]
QZ	−3.48	−1.24	−3.89	+0.29	[−0.21]	[+0.15]	[−8.38]
5Z	−3.50	−1.70	−3.93	+0.30	[−0.21]	[+0.15]	[−8.90]
CBS	[−3.50]	[−2.17]	[−3.98]	[+0.30]	[−0.21]	[+0.15]	[−9.42]

M3 [Ca(μ_2-H)$_2$Ca] D_{2h}

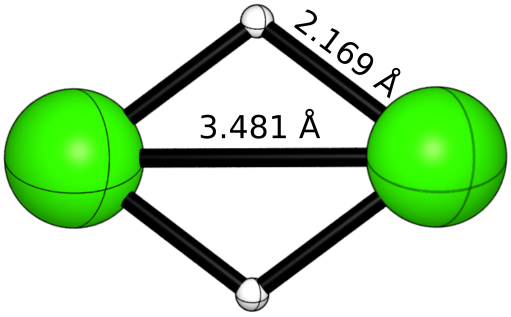

Level of Theory:
Geometry: CCSD(T)/QZ
Harmonics: CCSD(T)/QZ
Anharmonics: CCSD(T)/TZ
Wavefunction Diagnostics:
$T_1 = 0.026$
$D_1 = 0.117$

Figure S3: M3

Cartesian Coordinates (Å):

Ca	0.0000000000	0.0000000000	1.7403045964
Ca	0.0000000000	0.0000000000	-1.7403045964
H	0.0000000000	1.2954015373	0.0000000000
H	0.0000000000	-1.2954015373	0.0000000000

Rotational Constants (GHz): 2.053, 2.082, 149.398

Vibrational Frequencies (cm^{-1}):

Mode	Symmetry	ω	$\delta\nu$	ν	Intensity
1	a_g	1012.0	−26.6	985.4	0.0
2	a_g	224.1	−7.5	216.5	0.0
3	b_{1g}	1030.1	−73.9	956.2	0.0
4	b_{1u}	434.5	−12.7	421.7	4.9
5	b_{2u}	829.7	−28.9	800.8	122.6
6	b_{3u}	1071.8	−66.9	1004.9	25.0

Incremental Focal Point Analysis (kcal mol^{-1}):

Basis	ΔE_e HF	$+\delta$ MP2	$+\delta$ CCSD	$+\delta$ (T)	$+\delta$ T	$+\delta$ (Q)	ΔE_e Net
DZ	+4.32	−9.43	−2.73	−4.37	+0.54	−0.40	[−12.07]
TZ	+4.41	−11.98	−2.61	−4.60	+0.50	[−0.40]	[−14.67]
QZ	+4.11	−12.89	−2.47	−4.72	[+0.50]	[−0.40]	[−15.87]
5Z	+4.08	−13.15	−2.54	−4.77	[+0.50]	[−0.40]	[−16.27]
CBS	[+4.09]	[−13.42]	[−2.61]	[−4.81]	[+0.50]	[−0.40]	[−16.66]

M4 [HCa(μ_2-H)$_2$CaH] D_{2h}

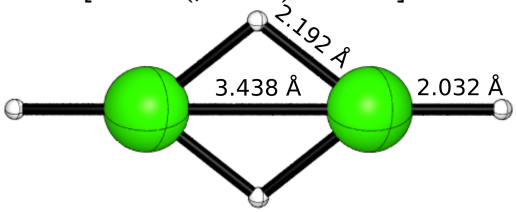

Figure S4: M4

Level of Theory:
Geometry: CCSD(T)/QZ
Harmonics: CCSD(T)/QZ
Anharmonics: CCSD(T)/TZ
Wavefunction Diagnostics:
$T_1 = 0.009$
$D_1 = 0.028$

Cartesian Coordinates (Å):

Ca	0.0000000000	0.0000000000	1.7191306432
Ca	0.0000000000	0.0000000000	-1.7191306432
H	0.0000000000	1.3606949333	0.0000000000
H	0.0000000000	-1.3606949333	0.0000000000
H	0.0000000000	0.0000000000	-3.7512220621
H	0.0000000000	0.0000000000	3.7512220621

Rotational Constants (GHz): 1.879, 1.905, 135.404

Vibrational Frequencies (cm^{-1}):

Mode	Symmetry	ω	$\delta\nu$	ν	Intensity	VCI
1	a_g	1309.7	−37.3	1272.4	0.0	1264.9
2	a_g	1009.3	13.3	1022.6	0.0	996.6
3	a_g	212.0	−5.4	206.6	0.0	209.1
4	b_{1g}	1008.8	−57.0	951.8	0.0	933.9
5	b_{1g}	241.9	3.3	245.2	0.0	241.1
6	b_{2g}	87.8	22.8	110.6	0.0	179.0
7	b_{1u}	498.4	−2.4	496.0	731.9	519.9
8	b_{1u}	103.2	15.4	118.6	651.8	169.0
9	b_{2u}	904.4	−28.1	876.3	844.0	849.5
10	b_{2u}	223.5	5.6	229.1	611.1	236.2
11	b_{3u}	1299.5	−42.0	1257.5	566.3	1237.7
12	b_{3u}	1120.7	−64.3	1056.4	1486.1	1035.7

Incremental Focal Point Analysis (kcal mol^{-1}):

Basis	ΔE_e HF	$+\delta$ MP2	$+\delta$ CCSD	$+\delta$ (T)	$+\delta$ T	$+\delta$ (Q)	ΔE_e Net
DZ	−37.87	+8.44	−5.00	+1.42	+0.03	+0.33	[−32.66]
TZ	−37.07	+3.49	−5.25	+2.20	−0.13	[+0.33]	[−36.43]
QZ	−37.40	+1.78	−5.15	+2.27	[−0.13]	[+0.33]	[−38.30]
5Z	−37.40	+1.26	−5.25	+2.31	[−0.13]	[+0.33]	[−38.87]
CBS	[−37.37]	[+0.71]	[−5.35]	[+2.36]	[−0.13]	[+0.33]	[−39.45]

M5 [HCa(μ_2-H)$_3$Ca] C_{3v}

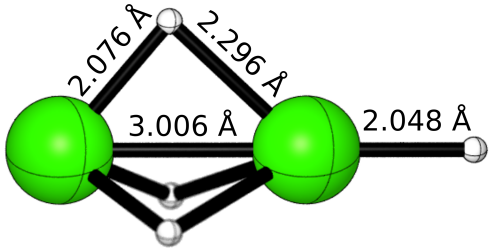

Level of Theory:
Geometry: CCSD(T)/QZ
Harmonics: CCSD(T)/QZ
Anharmonics: CCSD(T)/DZ
Wavefunction Diagnostics:
$T_1 = 0.011$
$D_1 = 0.029$

Figure S5: M5

Cartesian Coordinates (Å):

Ca	0.0000000000	0.0000000000	1.4663417338
Ca	-0.0000000000	0.0000000000	-1.5398961593
H	1.5833387792	0.0000000000	-0.1965133772
H	-0.7916693896	-1.3712116056	-0.1965133772
H	-0.7916693896	1.3712116056	-0.1965133772
H	0.0000000000	0.0000000000	3.5143782916

Rotational Constants (GHz): 2.558, 2.558, 66.667

Dipole Moment (Debye): 0.0, 0.0, 10.72

Vibrational Frequencies (cm^{-1}):

Mode	Symmetry	ω	$\delta\nu$	ν	Intensity
1	a'	1260.8	−37.8	1223.0	550.6
2	a'	1229.7	−61.5	1168.2	39.2
3	a'	911.3	−60.9	850.4	1121.8
4	a'	262.2	−7.5	254.7	0.0
5	e	1114.8	−41.2	1073.6	502.2
6	e	726.8	−45.0	681.8	88.6
7	e	622.2	−29.2	593.0	700.3
8	e	236.5	2.5	239.0	283.4

Incremental Focal Point Analysis (kcal mol^{-1}):

Basis	ΔE_e HF	$+\delta$ MP2	$+\delta$ CCSD	$+\delta$ (T)	$+\delta$ T	$+\delta$ (Q)	ΔE_e Net
DZ	−33.46	+5.25	−4.08	+0.94	−0.05	+0.31	[−31.10]
TZ	−33.00	−1.81	−4.15	+1.42	−0.23	[+0.31]	[−37.46]
QZ	−33.49	−4.01	−4.03	+1.39	[−0.23]	[+0.31]	[−40.06]
5Z	−33.51	−4.72	−4.13	+1.39	[−0.23]	[+0.31]	[−40.88]
CBS	[−33.48]	[−5.46]	[−4.23]	[+1.39]	[−0.23]	[+0.31]	[−41.70]

M6 [Ca(μ_2-H)$_4$Ca] D_{4h}

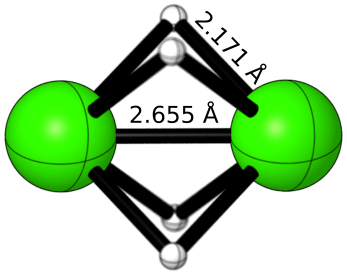

Level of Theory:
Geometry: CCSD(T)/QZ
Harmonics: CCSD(T)/QZ
Anharmonics: CCSD(T)/TZ
Wavefunction Diagnostics:
$T_1 = 0.014$
$D_1 = 0.041$

Figure S6: M6

Cartesian Coordinates (Å):

Ca	0.0000000000	0.0000000000	1.3277090839
Ca	0.0000000000	0.0000000000	-1.3277090839
H	1.7177315542	0.0000000000	0.0000000000
H	0.0000000000	-1.7177315542	0.0000000000
H	0.0000000000	1.7177315542	0.0000000000
H	-1.7177315542	0.0000000000	0.0000000000

Rotational Constants (GHz): 3.432, 3.432, 42.483

Vibrational Frequencies (cm^{-1}):

Mode	Symmetry	ω	$\delta\nu$	ν	Intensity
1	a_{1g}	1149.5	−50.9	1098.6	0.0
2	a_{1g}	325.8	−21.0	304.8	0.0
3	b_{1g}	906.6	−84.4	822.2	0.0
4	b_{2g}	912.0	−32.7	879.3	0.0
5	e_g	662.5	−97.1	565.4	0.0
6	a_{2u}	984.0	−131.6	852.4	1150.5
7	b_{2u}	443.2	−83.9	359.3	0.0
8	e_u	1000.1	−115.9	884.2	969.8
9	e_u	722.5	−41.4	681.1	687.1

Incremental Focal Point Analysis (kcal mol^{-1}):

Basis	ΔE_e HF	$+\delta$ MP2	$+\delta$ CCSD	$+\delta$ (T)	$+\delta$ T	$+\delta$ (Q)	ΔE_e Net
DZ	+0.40	−0.61	−2.71	−0.02	−0.15	+0.26	[−2.84]
TZ	−0.40	−10.72	−2.51	−0.02	−0.38	[+0.26]	[−13.77]
QZ	−1.06	−13.87	−2.35	−0.26	[−0.38]	[+0.26]	[−17.67]
5Z	−1.11	−14.85	−2.47	−0.32	[−0.38]	[+0.26]	[−18.87]
CBS	[−1.10]	[−15.88]	[−2.58]	[−0.39]	[−0.38]	[+0.26]	[−20.07]

B.3 Transition States

TS1 [M1 ↔ M2]

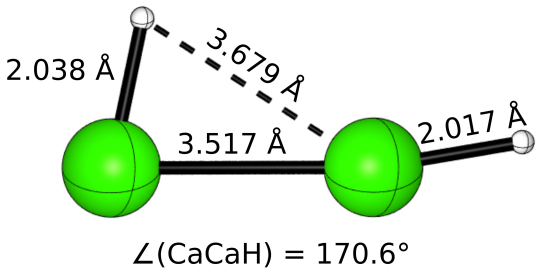

Level of Theory:
Geometry: CCSD(T)/QZ
Harmonics: CCSD(T)/QZ
Wavefunction Diagnostics:
$T_1 = 0.018$
$D_1 = 0.072$

Figure S7: TS1

Cartesian Coordinates (Å):

Ca	-0.0388331350	0.0000000000	-1.7879951405
Ca	-0.0185263908	0.0000000000	1.7290865569
H	1.9571521570	0.0000000000	-1.3746679637
H	0.3237076095	0.0000000000	3.7171248854

Rotational Constants (GHz): 1.887, 1.916, 125.073

Harmonic Vibrational Frequencies (cm^{-1}):
$[a']$ 1301 $[a'']$ 138
$[a']$ 1201
$[a']$ 176
$[a']$ 141
$[a']$ $414i$

Incremental Focal Point Analysis (kcal mol^{-1}):

Basis	ΔE_e HF	$+\delta$ MP2	$+\delta$ CCSD	$+\delta$ (T)	$+\delta$ T	$+\delta$ (Q)	ΔE_e Net
DZ	+11.51	+7.35	−4.16	+0.23	−0.15	+0.20	[+14.98]
TZ	+11.45	+2.67	−4.59	+0.67	−0.31	[+0.20]	[+10.08]
QZ	+11.24	+1.28	−4.54	+0.71	[−0.31]	[+0.20]	[+8.57]
5Z	+11.22	+0.73	−4.55	+0.72	[−0.31]	[+0.20]	[+8.00]
CBS	[+11.22]	[+0.16]	[−4.56]	[+0.73]	[−0.31]	[+0.20]	[+7.43]

TS2 [M2 ↔ M3]

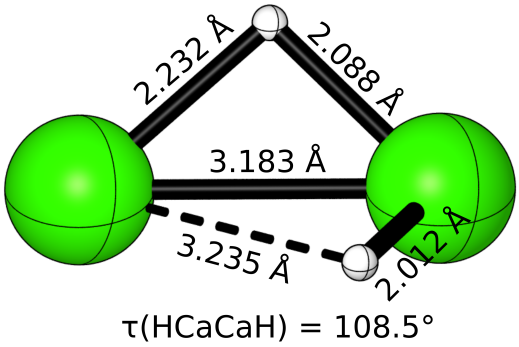

Level of Theory:
Geometry: CCSD(T)/QZ
Harmonics: CCSD(T)/QZ
Wavefunction Diagnostics:
$T_1 = 0.028$
$D_1 = 0.122$

Figure S8: TS2

Cartesian Coordinates (Å):

Ca	-0.0262236978	-0.0266326153	-1.5776078551
Ca	0.0020137363	-0.0162044547	1.6050905027
H	-0.8581004550	1.1676405901	-0.0807079782
H	1.8207919405	0.5357442965	-1.0121194880

Rotational Constants (GHz): 2.428, 2.456, 86.925

Harmonic Vibrational Frequencies (cm^{-1}):

[a] 1256
[a] 1063
[a] 786
[a] 466
[a] 216
[a] $372i$

Incremental Focal Point Analysis (kcal mol^{-1}):

Basis	ΔE_e HF	$+\delta$ MP2	$+\delta$ CCSD	$+\delta$ (T)	$+\delta$ T	$+\delta$ (Q)	ΔE_e Net
DZ	+13.34	+1.81	−3.84	−0.91	−0.35	+0.02	[+10.06]
TZ	+13.03	−3.20	−3.90	−0.82	−0.21	[+0.02]	[+4.92]
QZ	+12.69	−4.76	−3.81	−0.88	[−0.21]	[+0.02]	[+3.05]
5Z	+12.65	−5.34	−3.87	−0.91	[−0.21]	[+0.02]	[+2.33]
CBS	[+12.65]	[−5.96]	[−3.94]	[−0.94]	[−0.21]	[+0.02]	[+1.63]

TS3 [M2 ↔ M2]

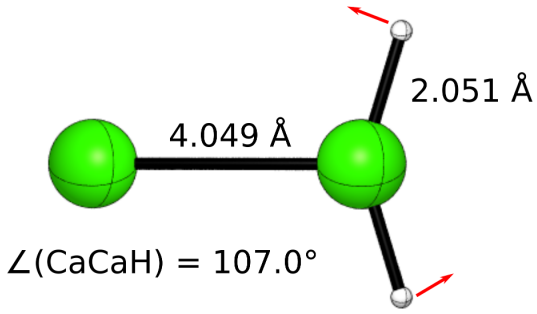

Level of Theory:
Geometry: CCSD(T)/QZ
Harmonics: CCSD(T)/QZ
Wavefunction Diagnostics:
$T_1 = 0.014$
$D_1 = 0.057$

Figure S9: TS3

Cartesian Coordinates (Å):

Ca	0.0000000000	0.0000000000	-1.9601554665
Ca	0.0000000000	0.0000000000	2.0889192444
H	0.0000000000	1.9609228149	-2.5600989227
H	0.0000000000	-1.9609228149	-2.5600989227

Rotational Constants (GHz): 11.445, 1.477, 65.198

Harmonic Vibrational Frequencies (cm^{-1}):

$[a_1]$ 1290 $[b_1]$ 143 $[b_2]$ 1226
$[a_1]$ 274 $[b_2]$ $58i$
$[a_1]$ 82

Incremental Focal Point Analysis (kcal mol^{-1}):

Basis	ΔE_e HF	$+\delta$ MP2	$+\delta$ CCSD	$+\delta$ (T)	$+\delta$ T	$+\delta$ (Q)	ΔE_e Net
DZ	+3.52	+4.93	−3.30	+0.81	+0.03	+0.21	[+6.21]
TZ	+3.81	+2.53	−3.34	+1.25	−0.06	[+0.21]	[+4.41]
QZ	+3.68	+1.81	−3.32	+1.32	[−0.06]	[+0.21]	[+3.64]
5Z	+3.67	+1.60	−3.38	+1.35	[−0.06]	[+0.21]	[+3.39]
CBS	[+3.67]	[+1.37]	[−3.45]	[+1.39]	[−0.06]	[+0.21]	[+3.14]

TS4 [M4 ↔ M5]

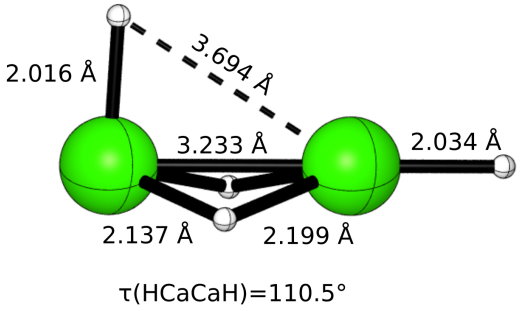

Level of Theory:
Geometry: CCSD(T)/QZ
Harmonics: CCSD(T)/QZ
Wavefunction Diagnostics:
$T_1 = 0.011$
$D_1 = 0.032$

Figure S10: TS4

Cartesian Coordinates (Å):

Ca	-0.0342337971	0.0000000000	1.6412469180
Ca	0.0095673719	0.0000000000	-1.5916399183
H	-0.5177970839	1.3536556151	0.0593662170
H	-0.5177970839	-1.3536556151	0.0593662170
H	0.0371173529	0.0000000000	-3.6250553028
H	1.9793192481	0.0000000000	1.5337366544

Rotational Constants (GHz): 2.201, 2.209, 61.368

Harmonic Vibrational Frequencies (cm^{-1}):

$[a']$ 1297	$[a'']$ 1008
$[a']$ 1291	$[a'']$ 907
$[a']$ 1118	$[a'']$ 462
$[a']$ 1013	$[a'']$ 243
$[a']$ 605	
$[a']$ 260	
$[a']$ 168	
$[a']$ $253i$	

Incremental Focal Point Analysis (kcal mol^{-1}):

Basis	ΔE_e HF	$+\delta$ MP2	$+\delta$ CCSD	$+\delta$ (T)	$+\delta$ T	$+\delta$ (Q)	ΔE_e Net
DZ	−29.50	+6.98	−4.66	+1.16	−0.02	+0.32	[−25.72]
TZ	−28.92	+1.06	−4.81	+1.81	−0.19	[+0.32]	[−30.74]
QZ	−29.35	−0.90	−4.71	+1.83	[−0.19]	[+0.32]	[−33.01]
5Z	−29.36	−1.50	−4.81	+1.85	[−0.19]	[+0.32]	[−33.69]
CBS	[−29.34]	[−2.13]	[−4.91]	[+1.88]	[−0.19]	[+0.32]	[−34.38]

TS5 [M5 ↔ M6]

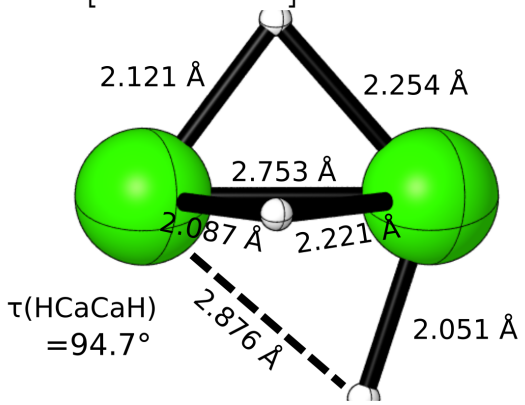

Level of Theory:
Geometry: CCSD(T)/QZ
Harmonics: CCSD(T)/QZ
Wavefunction Diagnostics:
$T_1 = 0.014$
$D_1 = 0.042$

Figure S11: TS5

Cartesian Coordinates (Å):

Ca	0.0088970719	0.0000000000	1.3815011294
Ca	-0.0213019239	0.0000000000	-1.3712506861
H	0.1306651205	1.6493635592	0.1087810383
H	0.1306651205	-1.6493635592	0.1087810383
H	-1.7031456868	0.0000000000	0.1288988145
H	1.9350853520	0.0000000000	-0.7540623039

Rotational Constants (GHz): 3.174, 3.199, 41.297

Harmonic Vibrational Frequencies (cm^{-1}):

$[a']$ 1185	$[a'']$ 1077
$[a']$ 1169	$[a'']$ 844
$[a']$ 999	$[a'']$ 744
$[a']$ 891	$[a'']$ 581
$[a']$ 722	
$[a']$ 552	
$[a']$ 333	
$[a']$ $416i$	

Incremental Focal Point Analysis (kcal mol^{-1}):

Basis	ΔE_e HF	$+\delta$ MP2	$+\delta$ CCSD	$+\delta$ (T)	$+\delta$ T	$+\delta$ (Q)	ΔE_e Net
DZ	+0.86	+0.75	−3.28	+0.16	−0.16	+0.27	[−1.40]
TZ	+0.36	−8.45	−3.14	+0.28	−0.37	[+0.27]	[−11.07]
QZ	−0.25	−11.30	−3.00	+0.10	[−0.37]	[+0.27]	[−14.55]
5Z	−0.29	−12.20	−3.11	+0.06	[−0.37]	[+0.27]	[−15.65]
CBS	[−0.28]	[−13.15]	[−3.21]	[+0.01]	[−0.37]	[+0.27]	[−16.74]

TS6 [M5 ↔ M5]

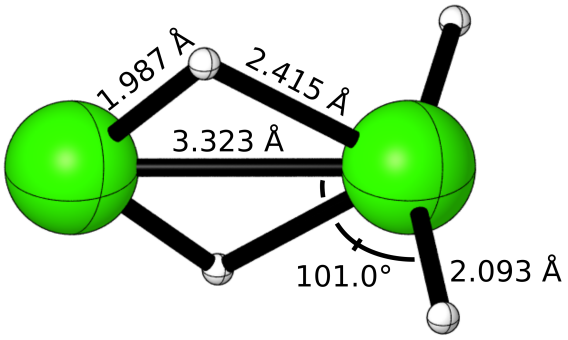

Level of Theory:
Geometry: CCSD(T)/QZ
Harmonics: CCSD(T)/QZ
Wavefunction Diagnostics:
$T_1 = 0.012$
$D_1 = 0.037$

Figure S12: TS6

Cartesian Coordinates (Å):

Ca	0.0000000000	0.0000000000	-1.7041825128
Ca	0.0000000000	0.0000000000	1.6191248212
H	0.0000000000	1.4310774680	-0.3261232328
H	0.0000000000	-1.4310774680	-0.3261232328
H	-2.0548888039	0.0000000000	2.0172518114
H	2.0548888039	0.0000000000	2.0172518114

Rotational Constants (GHz): 2.120, 2.160, 39.980

Harmonic Vibrational Frequencies (cm^{-1}):

$[a_1]$ 1379	$[a_2]$ 390	$[b_1]$ 1147	$[b_2]$ 1312
$[a_1]$ 1219		$[b_1]$ 526	$[b_2]$ 507
$[a_1]$ 740		$[b_1]$ 259i	$[b_2]$ 260
$[a_1]$ 272			
$[a_1]$ 112			

Incremental Focal Point Analysis (kcal mol^{-1}):

Basis	ΔE_e HF	$+\delta$ MP2	$+\delta$ CCSD	$+\delta$ (T)	$+\delta$ T	$+\delta$ (Q)	ΔE_e Net
DZ	−3.01	+7.07	−5.01	+1.11	−0.06	+0.32	[+0.42]
TZ	−2.43	+1.47	−5.17	+1.78	−0.22	[+0.32]	[−4.25]
QZ	−2.86	−0.35	−5.07	+1.82	[−0.22]	[+0.32]	[−6.36]
5Z	−2.88	−0.92	−5.16	+1.85	[−0.22]	[+0.32]	[−7.02]
CBS	[−2.86]	[−1.52]	[−5.27]	[+1.88]	[−0.22]	[+0.32]	[−7.68]

Appendix C

Supporting Information for Chapter 4

C.1 Products

Incremental Focal Point Analysis (kcal mol^{-1}) of HCCO + O:

Basis	ROHF	+δMP2	+δCCSD	+δ(T)	+δT	+δ(Q)	Net
DZ	−80.39	+52.23	−13.34	+1.80	−0.04	+0.90	[−38.83]
TZ	−77.74	+54.16	−16.06	+3.30	−0.26	[+0.90]	[−35.70]
QZ	−77.56	+55.11	−16.58	+3.61	[−0.26]	[+0.90]	[−34.78]
5Z	−77.50	+55.59	−16.75	+3.73	[−0.26]	[+0.90]	[−34.28]
6Z	−77.42	+55.82	−16.83	+3.78	[−0.26]	[+0.90]	[−34.01]
CBS	[−77.39]	[+56.12]	[−16.94]	[+3.85]	[−0.26]	[+0.90]	[−33.71]

Incremental Focal Point Analysis (kcal mol^{-1}) of HCO + CO:

Basis	ROHF	+δMP2	+δCCSD	+δ(T)	+δT	+δ(Q)	Net
DZ	−159.18	+11.30	−6.39	+0.31	+0.17	+0.81	[−152.99]
TZ	−158.94	+12.72	−6.94	+0.73	+0.28	[+0.81]	[−151.35]
QZ	−159.59	+12.46	−7.11	+0.91	[+0.28]	[+0.81]	[−152.24]
5Z	−159.55	+12.27	−7.10	+0.97	[+0.28]	[+0.81]	[−152.32]
6Z	−159.51	+12.16	−7.09	+1.00	[+0.28]	[+0.81]	[−152.34]
CBS	[−159.49]	[+12.01]	[−7.07]	[+1.04]	[+0.28]	[+0.81]	[−152.42]

Incremental Focal Point Analysis (kcal mol^{-1}) of 2 CO + H:

Basis	ROHF	+δMP2	+δCCSD	+δ(T)	+δT	+δ(Q)	Net
DZ	−156.34	+20.41	−5.17	+0.36	+0.43	+0.82	[−139.48]
TZ	−154.68	+24.78	−5.85	+1.01	+0.62	[+0.82]	[−133.29]
QZ	−155.10	+25.16	−6.12	+1.29	[+0.62]	[+0.82]	[−133.32]
5Z	−154.83	+25.15	−6.18	+1.38	[+0.62]	[+0.82]	[−133.03]
6Z	−154.75	+25.12	−6.20	+1.43	[+0.62]	[+0.82]	[−132.96]
CBS	[−154.73]	[+25.07]	[−6.23]	[+1.48]	[+0.62]	[+0.82]	[−132.96]

Incremental Focal Point Analysis (kcal mol^{-1}) of CO_2 + CH:

Basis	ROHF	+δMP2	+δCCSD	+δ(T)	+δT	+δ(Q)	Net
DZ	−107.11	+26.32	−9.92	+1.34	+0.50	+0.85	[−88.02]
TZ	−106.85	+27.25	−11.22	+2.33	+0.43	[+0.85]	[−87.21]
QZ	−107.12	+26.84	−11.50	+2.57	[+0.43]	[+0.85]	[−87.93]
5Z	−107.03	+26.67	−11.50	+2.66	[+0.43]	[+0.85]	[−87.93]
6Z	−106.97	+26.59	−11.50	+2.70	[+0.43]	[+0.85]	[−87.90]
CBS	[−106.95]	[+26.48]	[−11.49]	[+2.76]	[+0.43]	[+0.85]	[−87.93]

Incremental Focal Point Analysis (kcal mol^{-1}) of C_2O + OH:

Basis	ROHF	+δMP2	+δCCSD	+δ(T)	+δT	+δ(Q)	Net
DZ	−68.87	+44.41	−14.93	+2.45	−0.30	+0.95	[−36.28]
TZ	−68.45	+45.47	−16.81	+3.48	−0.55	[+0.95]	[−35.91]
QZ	−68.85	+45.74	−17.14	+3.65	[−0.55]	[+0.95]	[−36.20]
5Z	−68.96	+45.90	−17.19	+3.70	[−0.55]	[+0.95]	[−36.15]
6Z	−68.93	+46.04	−17.25	+3.74	[−0.55]	[+0.95]	[−36.00]
CBS	[−68.92]	[+46.23]	[−17.32]	[+3.79]	[−0.55]	[+0.95]	[−35.82]

C.2 Intermediates

M1 (ethynyl peroxy radical)

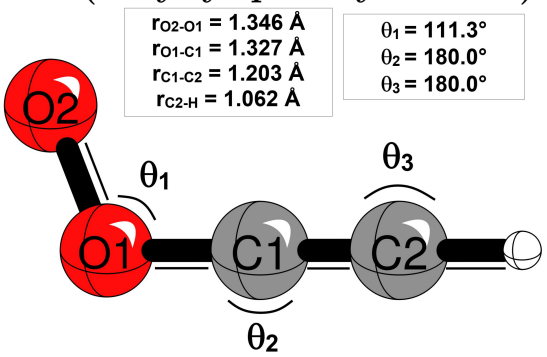

Level of Theory:
Geometry: CCSD(T)/ANO2
Harmonics: CCSD(T)/ANO2
Wavefunction Diagnostics:
CASSCF(11,9) $C_0^2 = 0.899$
CASSCF(11,9) $C_1^2 = 0.014$
CASSCF(11,9) $C_2^2 = 0.007$

Figure S1: M1

Cartesian Coordinates (Å):

C	0.6694701018	-0.1477239513	0.0000000000
C	1.8108837369	0.2329301511	0.0000000000
H	2.8184971642	0.5689627472	0.0000000000
O	-0.5894129714	-0.5675533577	0.0000000000
O	-1.4490348053	0.4677785697	0.0000000000

Rotational Constants (GHz): 4.966, 5.501, 51.093

Harmonic Vibrational Frequencies (cm^{-1}):

$[a']$ 3473	$[a'']$ 586
$[a']$ 2193	$[a'']$ 351
$[a']$ 1084	
$[a']$ 978	
$[a']$ 656	
$[a']$ 596	
$[a']$ 217	

Incremental Focal Point Analysis (kcal mol^{-1}):

Basis	ROHF	+δMP2	+δCCSD	+δ(T)	+δT	+δ(Q)	Net
DZ	−45.61	+14.76	−12.49	−0.35	−0.04	+0.38	[−43.34]
TZ	−47.11	+11.87	−13.46	−0.45	−0.21	[+0.38]	[−48.98]
QZ	−46.82	+10.97	−13.74	−0.48	[−0.21]	[+0.38]	[−49.90]
5Z	−46.75	+10.60	−13.79	−0.50	[−0.21]	[+0.38]	[−50.26]
6Z	−46.66	+10.44	−13.79	−0.50	[−0.21]	[+0.38]	[−50.33]
CBS	[−46.63]	[+10.21]	[−13.78]	[−0.50]	[−0.21]	[+0.38]	[−50.52]

M2 (oxyrenyloxy)

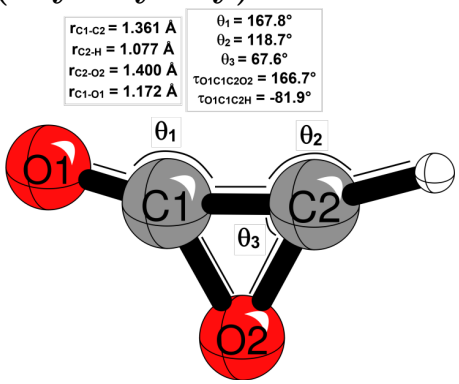

Level of Theory:
Geometry: CCSD(T)/ANO2
Harmonics: CCSD(T)/ANO2
Wavefunction Diagnostics:
CASSCF(11,9) $C_0^2 = 0.921$
CASSCF(11,9) $C_1^2 = 0.012$
CASSCF(11,9) $C_2^2 = 0.008$

Figure S2: M2

Cartesian Coordinates (Å):

C	0.3290331581	0.1752180221	0.0129643610
C	-0.9242094889	0.6993073694	-0.0540876141
O	1.4802754245	-0.0440252029	0.0017531378
O	-0.9299640374	-0.6990941374	0.0064595344
H	-1.6471785321	1.3810191720	0.3593065154

Rotational Constants (GHz): 48.666, 4.430, 4.165

Harmonic Vibrational Frequencies (cm^{-1}):

$[a']$ 3259	$[a']$ 671
$[a']$ 2063	$[a']$ 571
$[a']$ 1180	$[a']$ 505
$[a']$ 1143	$[a']$ 235
$[a']$ 920	

Incremental Focal Point Analysis (kcal mol^{-1}):

Basis	ROHF	+δMP2	+δCCSD	+δ(T)	+δT	+δ(Q)	Net
DZ	−115.54	−2.82	−1.38	−1.33	+0.07	+0.55	[−120.44]
TZ	−117.49	−6.25	−1.62	−1.40	+0.18	[+0.55]	[−126.03]
QZ	−117.68	−7.79	−1.74	−1.42	[+0.18]	[+0.55]	[−127.90]
5Z	−117.77	−8.42	−1.72	−1.42	[+0.18]	[+0.55]	[−128.59]
6Z	−117.71	−8.70	−1.69	−1.41	[+0.18]	[+0.55]	[−128.78]
CBS	[−117.69]	[−9.08]	[−1.66]	[−1.41]	[+0.18]	[+0.55]	[−129.11]

M3 (oxo-ketene)

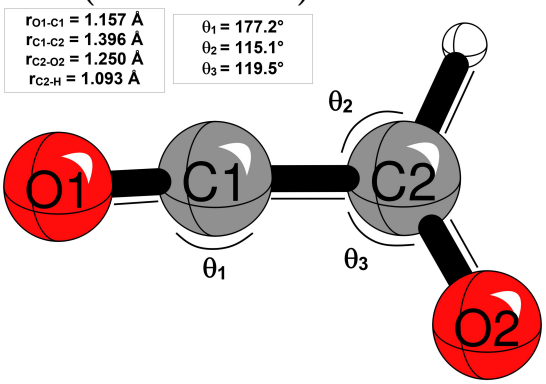

Level of Theory:
Geometry: CCSD(T)/ANO2
Harmonics: CCSD(T)/ANO2
Wavefunction Diagnostics:
CASSCF(11,9) $C_0^2 = 0.912$
CASSCF(11,9) $C_1^2 = 0.021$
CASSCF(11,9) $C_2^2 = 0.012$

Figure S3: M3

Cartesian Coordinates (Å):

C	0.6251961539	-0.1510530160	0.0000000000
C	-0.7257952414	-0.5028039968	0.0000000000
H	-0.9243206320	-1.5774052207	0.0000000000
O	1.7289983996	0.1944228752	0.0000000000
O	-1.5952844900	0.3955166699	0.0000000000

Rotational Constants (GHz): 56.644, 5.034, 4.623

Harmonic Vibrational Frequencies (cm^{-1}):

[a′] 3069	[a″] 786
[a′] 2134	[a″] 217
[a′] 1525	
[a′] 1349	
[a′] 994	
[a′] 673	
[a′] 196	

Incremental Focal Point Analysis (kcal mol^{-1}):

Basis	ROHF	+δMP2	+δCCSD	+δ(T)	+δT	+δ(Q)	Net
DZ	−142.98	−3.31	+0.09	−1.26	−0.09	+0.50	[−147.05]
TZ	−143.29	−7.27	+0.50	−1.26	+0.23	[+0.50]	[−150.59]
QZ	−143.89	−8.97	+0.51	−1.27	[+0.23]	[+0.50]	[−152.89]
5Z	−144.02	−9.54	+0.57	−1.27	[+0.23]	[+0.50]	[−153.53]
6Z	−143.99	−9.79	+0.61	−1.27	[+0.23]	[+0.50]	[−153.71]
CBS	[−143.98]	[−10.13]	[+0.66]	[−1.26]	[+0.23]	[+0.50]	[−153.99]

M4 (*trans*-carbohydroxycarbyne)

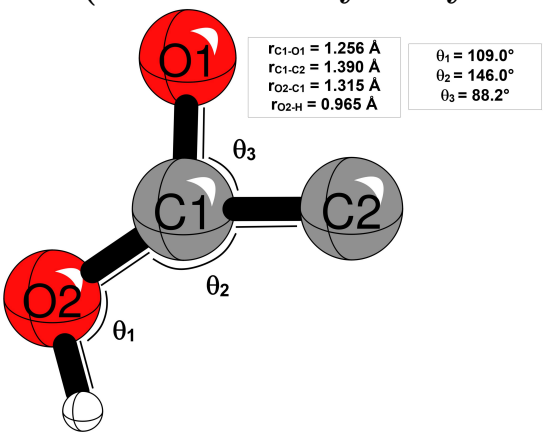

Level of Theory:
Geometry: CCSD(T)/ANO2
Harmonics: CCSD(T)/ANO2
Wavefunction Diagnostics:
CASSCF(11,9) $C_0^2 = 0.935$
CASSCF(11,9) $C_1^2 = 0.011$
CASSCF(11,9) $C_2^2 = 0.006$

Figure S4: M4

Cartesian Coordinates (Å):

C	0.0590373423	-0.1014629852	0.0000000000
C	-1.0286384861	-0.9667546729	0.0000000000
O	1.3697941425	0.0006809294	0.0000000000
H	1.7536266739	-0.8843505144	0.0000000000
O	-0.7528565086	0.8564591532	0.0000000000

Rotational Constants (GHz): 21.181, 9.203, 6.415

Harmonic Vibrational Frequencies (cm^{-1}):

[a′] 3806	[a″] 558
[a′] 1706	[a″] 487
[a′] 1463	
[a′] 1180	
[a′] 949	
[a′] 519	
[a′] 292	

Incremental Focal Point Analysis (kcal mol^{-1}):

Basis	ROHF	+δMP2	+δCCSD	+δ(T)	+δT	+δ(Q)	Net
DZ	−87.94	+7.15	−6.72	−1.52	−0.19	+0.63	[−88.59]
TZ	−88.79	+3.70	−6.93	−1.52	−0.08	[+0.63]	[−92.99]
QZ	−88.99	+2.25	−7.00	−1.52	[−0.08]	[+0.63]	[−94.72]
5Z	−89.04	+1.68	−6.93	−1.52	[−0.08]	[+0.63]	[−95.27]
6Z	−88.99	+1.46	−6.90	−1.51	[−0.08]	[+0.63]	[−95.40]
CBS	[−88.97]	[+1.16]	[−6.86]	[−1.50]	[−0.08]	[+0.63]	[−95.63]

M5 (*trans*)

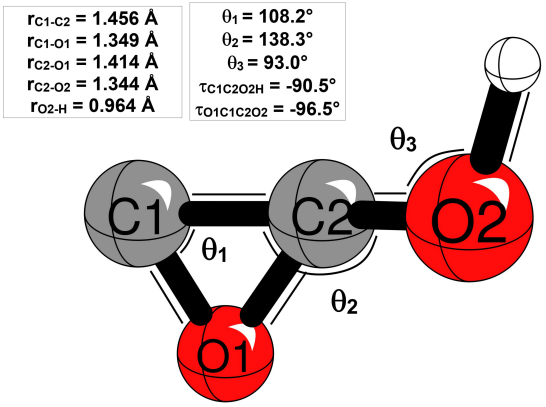

Level of Theory:
Geometry: CCSD(T)/ANO2
Harmonics: CCSD(T)/ANO2
Wavefunction Diagnostics:
CASSCF(11,9) $C_0^2 = 0.944$
CASSCF(11,9) $C_1^2 = 0.006$
CASSCF(11,9) $C_2^2 = 0.005$

Figure S5: M5

Cartesian Coordinates (Å):

C	0.1957195182	0.1817198536	-0.3936904051
C	-1.0467564303	0.7048771187	0.1558265123
O	1.3993974714	-0.0819355033	0.1432647387
H	1.9422081996	0.7098233067	0.0605504982
O	-0.8832936257	-0.6279489551	0.0313746651

Rotational Constants (GHz): 32.027, 7.932, 6.784

Harmonic Vibrational Frequencies (cm^{-1}):

3817	658
1473	436
1277	327
1176	236
904	

Incremental Focal Point Analysis (kcal mol^{-1}):

Basis	ROHF	+δMP2	+δCCSD	+δ(T)	+δT	+δ(Q)	Net
DZ	−71.04	+10.39	−9.21	+0.07	−0.06	+0.75	[−69.10]
TZ	−73.14	+7.24	−9.36	+0.05	−0.29	[+0.75]	[−74.75]
QZ	−73.4	+5.89	−9.46	+0.07	[−0.29]	[+0.75]	[−76.44]
5Z	−73.55	+5.25	−9.43	+0.08	[−0.29]	[+0.75]	[−77.20]
6Z	−73.53	+5.01	−9.41	+0.08	[−0.29]	[+0.75]	[−77.38]
CBS	[−73.51]	[+4.68]	[−9.37]	[+0.09]	[−0.29]	[+0.75]	[−77.66]

M6 (*cis*-hydroxyketenyl)

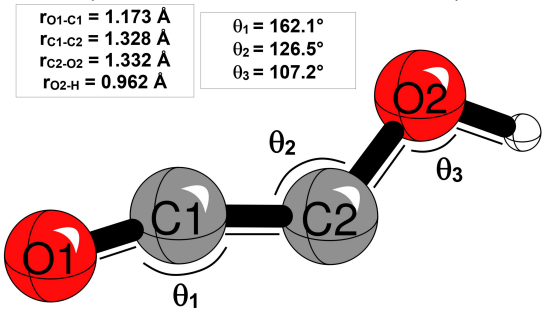

Level of Theory:
Geometry: CCSD(T)/ANO2
Harmonics: CCSD(T)/ANO2
Wavefunction Diagnostics:
CASSCF(11,9) $C_0^2 = 0.898$
CASSCF(11,9) $C_1^2 = 0.016$
CASSCF(11,9) $C_2^2 = 0.010$

Figure S6: M6

Cartesian Coordinates (Å):

C	0.5878624820	0.4563461185	0.0000000000
C	-0.6505651441	-0.0242784934	0.0000000000
O	1.7143211183	-0.2553868089	0.0000000000
H	2.4456365568	0.3698911187	0.0000000000
O	-1.8213765069	-0.0920734387	0.0000000000

Rotational Constants (GHz): 132.201, 4.382, 4.242

Harmonic Vibrational Frequencies (cm^{-1}):

[a′] 3816 [a″] 569
[a′] 2075 [a″] 352
[a′] 1487
[a′] 1287
[a′] 569
[a′] 264

Incremental Focal Point Analysis (kcal mol^{-1}):

Basis	ROHF	+δMP2	+δCCSD	+δ(T)	+δT	+δ(Q)	Net
DZ	−122.37	−0.09	−3.02	−1.81	−0.01	+0.37	[−126.94]
TZ	−123.19	−3.33	−3.45	−1.83	+0.11	[+0.37]	[−131.32]
QZ	−123.66	−4.91	−3.52	−1.80	[+0.11]	[+0.37]	[−133.41]
5Z	−123.76	−5.45	−3.45	−1.79	[+0.11]	[+0.37]	[−133.97]
6Z	−123.73	−5.66	−3.41	−1.77	[+0.11]	[+0.37]	[−134.10]
CBS	[−123.72]	[−5.94]	[−3.37]	[−1.74]	[+0.11]	[+0.37]	[−134.30]

M7 (*trans*-vinylidenyl peroxy radical)

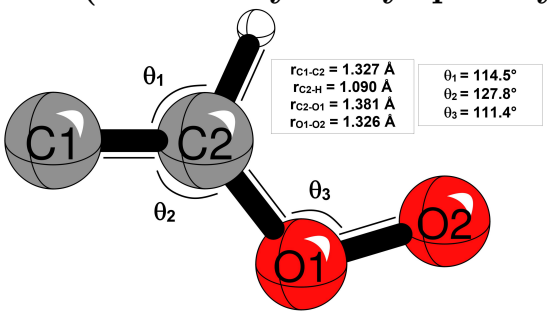

Level of Theory:
Geometry: CCSD(T)/ANO2
Harmonics: CCSD(T)/ANO2
Wavefunction Diagnostics:
CASSCF(11,9) $C_0^2 = 0.888$
CASSCF(11,9) $C_1^2 = 0.031$
CASSCF(11,9) $C_2^2 = 0.031$

Figure S7: M7

Cartesian Coordinates (Å):

C	1.9499537934	0.0573872829	0.0000000000
C	0.6752402453	-0.3130441840	0.0000000000
H	0.5186593114	-1.3913565331	0.0000000000
O	-0.4429865150	0.4979788687	0.0000000000
O	-1.5592152502	-0.2185071235	0.0000000000

Rotational Constants (GHz): 63.999, 5.411, 4.989

Harmonic Vibrational Frequencies (cm^{-1}):

[a′] 3135 [a″] 665
[a′] 1650 [a″] 82
[a′] 1147
[a′] 1109
[a′] 911
[a′] 521
[a′] 261

Incremental Focal Point Analysis (kcal mol^{-1}):

Basis	ROHF	+δMP2	+δCCSD	+δ(T)	+δT	+δ(Q)	Net
DZ	−11.25	+31.29	−22.94	+0.86	−0.46	+0.61	[−1.89]
TZ	−11.22	+29.47	−23.96	+1.07	−0.74	[+0.61]	[−4.78]
QZ	−10.92	+28.95	−24.22	+1.05	[−0.74]	[+0.61]	[−5.27]
5Z	−10.94	+28.66	−24.27	+1.03	[−0.74]	[+0.61]	[−5.65]
6Z	−10.87	+28.55	−24.27	+1.04	[−0.74]	[+0.61]	[−5.69]
CBS	[−10.85]	[+28.39]	[−24.27]	[+1.04]	[−0.74]	[+0.61]	[−5.82]

M8 (*cis*-vinylidenyl peroxy radical)

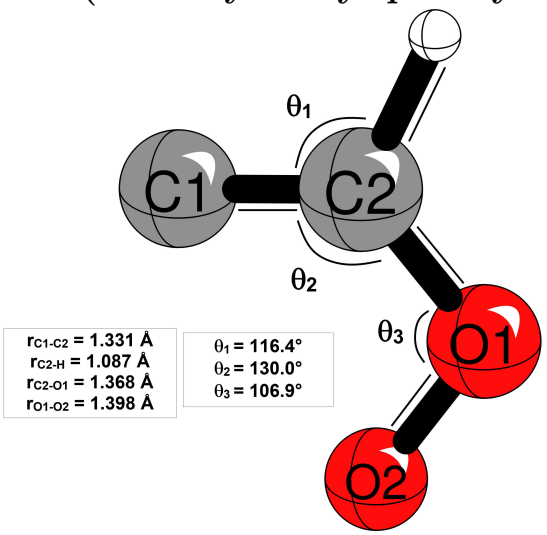

Level of Theory:
Geometry: CCSD(T)/ANO2
Harmonics: CCSD(T)/ANO2
Wavefunction Diagnostics:
CASSCF(11,9) $C_0^2 = 0.885$
CASSCF(11,9) $C_1^2 = 0.033$
CASSCF(11,9) $C_2^2 = 0.026$

Figure S8: M8

Cartesian Coordinates (Å):

C	1.4752052662	0.6509984767	0.0000000000
C	0.7647051841	-0.4743529726	0.0000000000
H	1.3292150053	-1.4032819234	0.0000000000
O	-0.5913952111	-0.6579572846	0.0000000000
O	-1.1728243689	0.6138505566	0.0000000000

Rotational Constants (GHz): 22.242, 8.085, 5.930

Harmonic Vibrational Frequencies (cm^{-1}):

$[a']$ 3162	$[a'']$ 684
$[a']$ 1661	$[a'']$ 180
$[a']$ 1123	
$[a']$ 1021	
$[a']$ 867	
$[a']$ 611	
$[a']$ 188	

Incremental Focal Point Analysis (kcal mol^{-1}):

Basis	ROHF	+δMP2	+δCCSD	+δ(T)	+δT	+δ(Q)	Net
DZ	−8.69	+30.87	−23.78	+0.47	−0.80	+0.47	[−1.46]
TZ	−8.11	+29.22	−24.65	+0.61	−1.14	[+0.47]	[−3.61]
QZ	−7.65	+28.83	−24.81	+0.56	[−1.14]	[+0.47]	[−3.73]
5Z	−7.65	+28.57	−24.82	+0.54	[−1.14]	[+0.47]	[−4.03]
6Z	−7.58	+28.47	−24.81	+0.53	[−1.14]	[+0.47]	[−4.05]
CBS	[−7.56]	[+28.33]	[−24.78]	[+0.52]	[−1.14]	[+0.47]	[−4.15]

S1 (dioxirenyl)

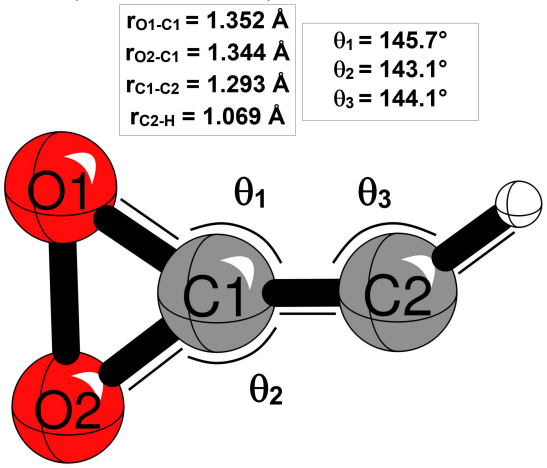

Level of Theory:
Geometry: CCSD(T)/ANO2
Harmonics: CCSD(T)/ANO2
Wavefunction Diagnostics:
CASSCF(11,9) $C_0^2 = 0.880$
CASSCF(11,9) $C_1^2 = 0.059$
CASSCF(11,9) $C_2^2 = 0.021$

Figure S9: S1

Cartesian Coordinates (Å):

C	0.3046213385	-0.0110034207	0.0000000000
C	1.5966252400	-0.0658421278	0.0000000000
H	2.4884457950	0.5233795831	0.0000000000
O	-0.8036066494	-0.7722097377	0.0000000000
O	-0.7795763454	0.7968845532	0.0000000000

Rotational Constants (GHz): 25.238, 8.714, 6.478

Harmonic Vibrational Frequencies (cm^{-1}):

[a′] 3369	[a″] 646
[a′] 1854	[a″] 416
[a′] 1063	
[a′] 967	
[a′] 654	
[a′] 635	
[a′] 398	

Incremental Focal Point Analysis (kcal mol^{-1}):

Basis	ROHF	+δMP2	+δCCSD	+δ(T)	+δT	+δ(Q)	Net
DZ	−30.82	−1.79	−7.04	−2.01	+0.45	−0.03	[−41.24]
TZ	−32.33	−5.85	−6.49	−2.38	+0.64	[−0.03]	[−46.44]
QZ	−31.93	−7.19	−6.36	−2.51	[+0.64]	[−0.03]	[−47.38]
5Z	−31.93	−7.70	−6.30	−2.54	[+0.64]	[−0.03]	[−47.86]
6Z	−31.86	−7.92	−6.27	−2.55	[+0.64]	[−0.03]	[−47.99]
CBS	[−31.83]	[−8.21]	[−6.24]	[−2.56]	[+0.64]	[−0.03]	[−48.23]

S2 [HCC(O)O]

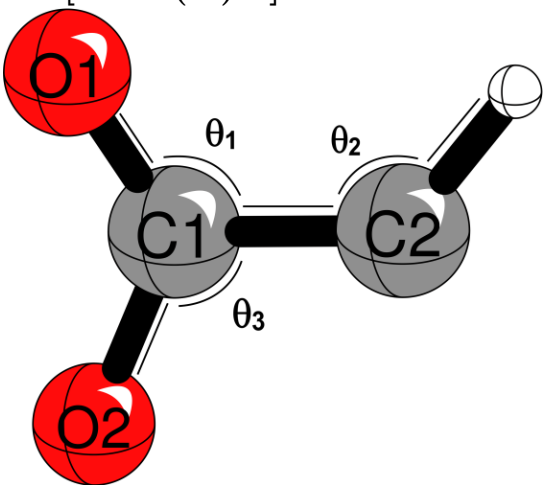

Level of Theory:
Geometry: MRCISD+Q(9,8)/cc-pVDZ
Frequencies: CASSCF(13,9)/cc-pVDZ
Program: MOLPRO 2010
Wavefunction Diagnostics:
CASSCF(11,9) $C_0^2 = 0.430$
CASSCF(11,9) $C_1^2 = 0.213$
CASSCF(11,9) $C_2^2 = 0.182$

Figure S10: S2

Equilibrium Geometry (Å, °):

Theory	Bond Distance				Bond Angle		
	C_1–C_2	C_1–O_1	C_1–O_2	C_2–H	θ_1	θ_2	θ_3
CASPT2(11,9)/cc-pVQZ	1.413	1.223	1.354	1.083	121.6	128.3	113.5
MRCISD+Q(9,8)/cc-pVDZ	1.451	1.219	1.380	1.098	123.4	128.1	113.1

Harmonic Vibrational Frequencies (cm^{-1}):

[a′] 3452 [a″] 687
[a′] 1760 [a″] 416
[a′] 1357
[a′] 1197
[a′] 979
[a′] 887
[a′] 658

Incremental Focal Point Analysis (kcal mol^{-1}) for $^4A'$ state:

Basis	ROHF	+δMP2	+δCCSD	+δ(T)	+δT	+δ(Q)	Net
DZ	-94.33	+44.60	-16.77	+2.45	-1.02	+0.96	[-64.11]
TZ	-92.31	+44.80	-18.40	+3.28	-1.40	[+0.96]	[-63.07]
QZ	-92.10	+44.88	-18.92	+3.39	[-1.40]	[+0.96]	[-63.19]
5Z	-92.07	+44.93	-19.12	+3.43	[-1.40]	[+0.96]	[-63.27]
6Z	-91.98	+44.97	-19.22	+3.46	[-1.40]	[+0.96]	[-63.21]
CBS	[-91.95]	[+45.03]	[-19.36]	[+3.49]	[-1.40]	[+0.96]	[-63.23]

Doublet Quartet Splitting: 2.81 kcal mol^{-1}

S3 (dioxetenyl)

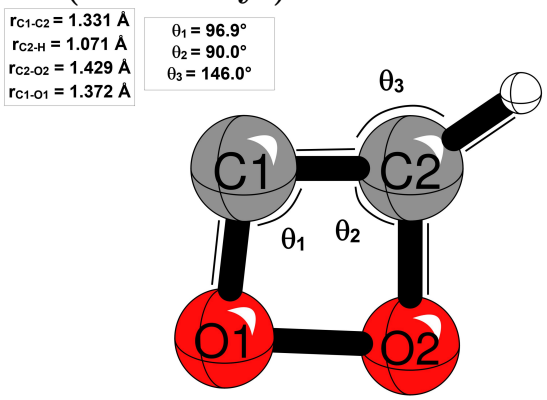

Level of Theory:
Geometry: CCSD(T)/ANO2
Harmonics: CCSD(T)/ANO2
Wavefunction Diagnostics:
CASSCF(11,9) $C_0^2 = 0.871$
CASSCF(11,9) $C_1^2 = 0.034$
CASSCF(11,9) $C_2^2 = 0.031$

Figure S11: S3

Cartesian Coordinates (Å):

C	-0.9969519239	-0.2671166365	0.0000000000
C	0.1135587018	-1.0010755165	0.0000000000
O	1.0027586335	0.0433860044	0.0000000000
O	-0.2097368732	0.9255260872	0.0000000000
H	-2.0674190351	-0.2771912982	0.0000000000

Rotational Constants (GHz): 18.935, 15.233, 8.442

Harmonic Vibrational Frequencies (cm^{-1}):

[a′] 3353	[a″] 680
[a′] 1577	[a″] 543
[a′] 1182	
[a′] 1135	
[a′] 963	
[a′] 862	
[a′] 707	

Incremental Focal Point Analysis (kcal mol^{-1}):

Basis	ROHF	+δMP2	+δCCSD	+δ(T)	+δT	+δ(Q)	Net
DZ	−15.43	−3.53	−7.15	−2.57	+0.20	−0.06	[−28.53]
TZ	−18.05	−8.17	−6.22	−3.12	+0.45	[−0.06]	[−35.16]
QZ	−17.96	−9.75	−6.09	−3.25	[+0.45]	[−0.06]	[−36.66]
5Z	−18.16	−10.55	−5.99	−3.31	[+0.45]	[−0.06]	[−37.61]
6Z	−18.13	−10.88	−5.94	−3.33	[+0.45]	[−0.06]	[−37.88]
CBS	[−18.11]	[−11.34]	[−5.87]	[−3.35]	[+0.45]	[−0.06]	[−38.27]

Q1 [HCC(O)O]

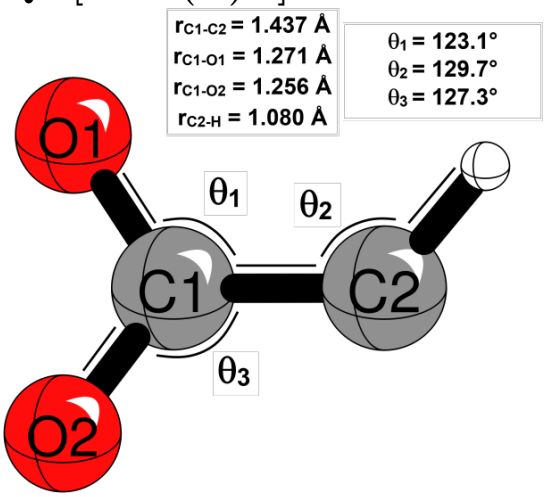

Level of Theory:
Geometry: CCSD(T)/ANO2
Harmonics: CCSD(T)/ANO2
Wavefunction Diagnostics:
CASSCF(11,9) $C_0^2 = 0.885$
CASSCF(11,9) $C_1^2 = 0.033$
CASSCF(11,9) $C_2^2 = 0.026$

Figure S12: Q1

Cartesian Coordinates (Å):

C	0.0608265064	-0.0453966610	0.0000000000
C	1.4728460405	-0.3145240017	0.0000000000
H	2.3056562149	0.3728451608	0.0000000000
O	-0.8739235423	-0.8839060055	0.0000000000
O	-0.4219738760	1.1304396949	0.0000000000

Rotational Constants (GHz): 14.739, 10.869, 6.256

Harmonic Vibrational Frequencies (cm^{-1}):

[a′] 3247 [a″] 646
[a′] 1690 [a″] 416
[a′] 1024
[a′] 899
[a′] 897
[a′] 560
[a′] 385

Incremental Focal Point Analysis (kcal mol^{-1}):

Basis	ROHF	+δMP2	+δCCSD	+δ(T)	+δT	+δ(Q)	Net
DZ	−79.74	+10.75	−1.57	−1.20	+0.24	+0.54	[−70.98]
TZ	−78.31	+9.06	−1.81	−0.93	+0.41	[+0.54]	[−71.04]
QZ	−78.33	+8.40	−1.89	−0.95	[+0.41]	[+0.54]	[−71.82]
5Z	−78.35	+8.18	−1.93	−0.96	[+0.41]	[+0.54]	[−72.11]
6Z	−78.27	+8.14	−1.99	−0.96	[+0.41]	[+0.54]	[−72.13]

C.3 Transition States

TS1 (M1 → HCCO + O)

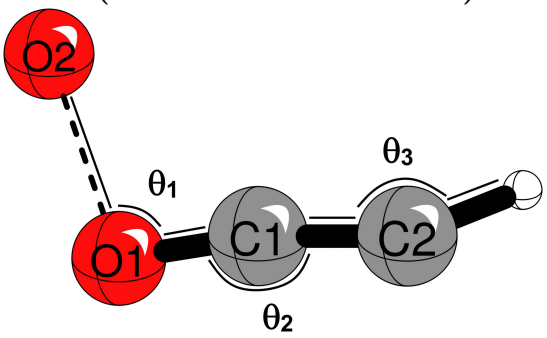

Wavefunction Diagnostics:
CASSCF(11,9) $C_0^2 = 0.688$
CASSCF(11,9) $C_1^2 = 0.142$
CASSCF(11,9) $C_2^2 = 0.051$

Figure S13: TS1 (M1 → HCCO + O)

Equilibrium Geometry (Å, °):

Theory	Bond Distance				Bond Angle		
:	C_1–C_2	C_1–O_2	O_1–O_2	C_2–H	θ_1	θ_2	θ_3
CCSD(T)/cc-pVTZ	1.234	1.239	1.836	1.062	108.2	178.4	182.6
CASPT2/cc-pVTZ	1.233	1.230	1.766	1.059	110.1	179.1	183.2
MRCISD+Q/cc-pVTZ	1.233	1.227	1.820	1.059	109.6	179.0	182.6

Harmonic Vibrational Frequencies (cm^{-1}):

Theory	a′						a″		
CCSD(T)/cc-pVTZ	3464	1880	1160	530	313	194	551i	518	461
CASPT2/cc-pVTZ	3510	1876	1113	558	340	201	677i	501	272i
MRCISD+Q/cc-pVDZ	3498	1915	1076	625	530	211	613i	557	235

Incremental Focal Point Analysis (kcal mol^{-1}) of $^4A''$ state:

Basis	ROHF	+δMP2	+δCCSD	+δ(T)	+δT	+δ(Q)	Net
DZ	−36.10	+40.11	−12.88	+0.76	−0.38	+0.84	[−7.63]
TZ	−33.14	+39.10	−14.92	+1.50	−0.67	[+0.84]	[−7.29]
QZ	−32.71	+38.86	−15.35	+1.51	[−0.67]	[+0.84]	[−7.53]
5Z	−32.61	+38.85	−15.51	+1.50	[−0.67]	[+0.84]	[−7.59]
6Z	−32.52	+38.85	−15.56	+1.51	[−0.67]	[+0.84]	[−7.55]
CBS	[−32.49]	[+38.85]	[−15.64]	[+1.52]	[−0.67]	[+0.84]	[−7.59]

Doublet Quartet Splitting: 22.01 kcal mol^{-1}

TS2 (M1 → M2)

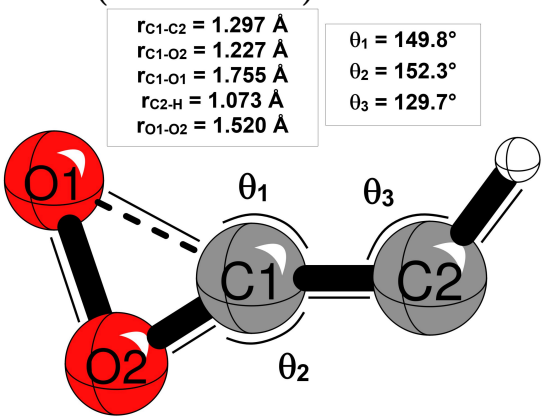

Level of Theory:
Reference: ROHF
Geometry: CCSD(T)/ANO2
Frequencies: EOM-CCSD/ANO2
Program: CFOUR 1.0, VCC
Wavefunction Diagnostics:
CASSCF(11,9) $C_0^2 = 0.825$
CASSCF(11,9) $C_1^2 = 0.008$
CASSCF(11,9) $C_2^2 = 0.008$

Figure S14: TS2 (M1 → M2)

Cartesian Coordinates (Å):

C	0.4274867229	0.0101932768	0.0000000000
C	1.7290839676	-0.1265560147	0.0000000000
O	-0.5576900706	0.7677945209	0.0000000000
O	-1.2044242201	-0.6144938986	0.0000000000
H	2.2881147511	-1.0474808898	0.0000000000

Rotational Constants (GHz): 30.139, 7.066, 5.724

Harmonic Vibrational Frequencies (cm^{-1}):

[a′] 3172 [a″] 1009
[a′] 1645 [a″] 560
[a′] 962
[a′] 762
[a′] 599
[a′] 432
[a′] 528i

Incremental Focal Point Analysis (kcal mol^{-1}) of $^2A''$ state

Basis	ROHF	+δMP2	+δCCSD	+δ(T)	+δT	+δ(Q)	Net
DZ	+10.30	+0.89	−9.69	−4.60	−1.81	−0.37	[−5.28]
TZ	+8.91	−3.84	−8.78	−4.92	−1.24	[−0.37]	[−10.22]
QZ	+9.18	−5.38	−8.50	−5.10	[−1.24]	[−0.37]	[−11.41]
5Z	+9.14	−6.06	−8.35	−5.19	[−1.24]	[−0.37]	[−12.06]
6Z	+9.21	−6.33	−8.28	−5.21	[−1.24]	[−0.37]	[−12.22]
CBS	[+9.23]	[−6.69]	[−8.19]	[−5.24]	[−1.24]	[−0.37]	[−12.51]

TS2′ (M1 → S1)

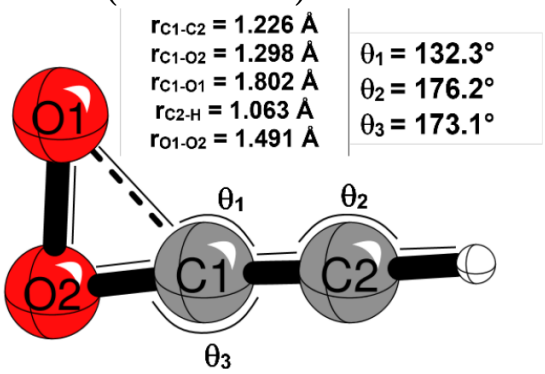

Level of Theory:
Reference: ROHF
Geometry: CCSD(T)/ANO2
Frequencies: CCSD/ANO1
Program: CFOUR 1.0, VCC
Wavefunction Diagnostics:
CASSCF(11,9) $C_0^2 = 0.856$
CASSCF(11,9) $C_1^2 = 0.031$
CASSCF(11,9) $C_2^2 = 0.002$

Figure S15: TS2′ (M1 → S1)

Cartesian Coordinates (Å):

C	0.4854617048	-0.1924821070	0.0000000000
C	1.6527981881	0.1816919765	0.0000000000
O	-0.6943674363	-0.7346317235	0.0000000000
O	-1.0762367572	0.7066631290	0.0000000000
H	2.6408792916	0.5723581178	0.0000000000

Rotational Constants (GHz): 28.407, 7.337, 5.831

Harmonic Vibrational Frequencies (cm^{-1}):

[a′] 3465 [a″] 496
[a′] 1968 [a″] 309
[a′] 1067
[a′] 789
[a′] 531
[a′] 289
[a′] 622i

Incremental Focal Point Analysis (kcal mol^{-1}) of $^2A'$ state:

Basis	ROHF	+δMP2	+δCCSD	+δ(T)	+δT	+δ(Q)	Net
DZ	-8.87	+0.67	-10.00	-3.11	-0.48	-0.28	[-22.07]
TZ	-9.95	-3.49	-10.10	-3.64	-0.63	[-0.28]	[-28.09]
QZ	-9.45	-4.58	-10.18	-3.84	[-0.63]	[-0.28]	[-28.96]
5Z	-9.37	-5.03	-10.20	-3.92	[-0.63]	[-0.28]	[-29.44]
6Z	-9.28	-5.24	-10.18	-3.95	[-0.63]	[-0.28]	[-29.56]
CBS	[-9.25]	[-5.52]	[-10.16]	[-3.99]	[-0.63]	[-0.28]	[-29.82]

TS3 (M2 → M3)

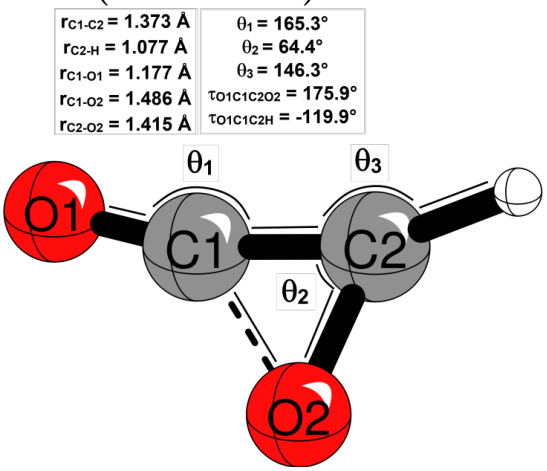

Level of Theory:
Geometry: CCSD(T)/ANO1
Harmonics: CCSD(T)/ANO1
Wavefunction Diagnostics:
CASSCF(11,9) $C_0^2 = 0.915$
CASSCF(11,9) $C_1^2 = 0.011$
CASSCF(11,9) $C_2^2 = 0.008$

Figure S16: TS3 (M2 → M3)

Cartesian Coordinates (Å):

C	0.3120723076	-0.1579198687	-0.0032229593
C	-0.9470413863	-0.7024969006	-0.0551511545
O	1.4756904847	0.0210241962	0.0088530719
O	-0.8945935973	0.7098339008	0.0085698509
H	-1.6619612362	-1.3544132882	0.4185361554

Rotational Constants (GHz): 30.906, 8.078, 6.439

Harmonic Vibrational Frequencies (cm^{-1}):

3270	621
2078	560
1195	482
1158	$227i$
932	

Incremental Focal Point Analysis (kcal mol^{-1}):

Basis	ROHF	+δMP2	+δCCSD	+δ(T)	+δT	+δ(Q)	Net
DZ	−113.85	−4.83	−0.55	−1.57	+0.09	+0.50	[−120.21]
TZ	−115.87	−8.37	−0.76	−1.68	+0.21	[+0.50]	[−125.98]
QZ	−116.09	−9.96	−0.86	−1.71	[+0.21]	[+0.50]	[−127.91]
5Z	−116.18	−10.60	−0.83	−1.71	[+0.21]	[+0.50]	[−128.61]
6Z	−116.12	−10.89	−0.80	−1.71	[+0.21]	[+0.50]	[−128.81]
CBS	[−116.10]	[−11.28]	[−0.75]	[−1.70]	[+0.21]	[+0.50]	[−129.12]

TS4 (M2 → CO_2 + CH)

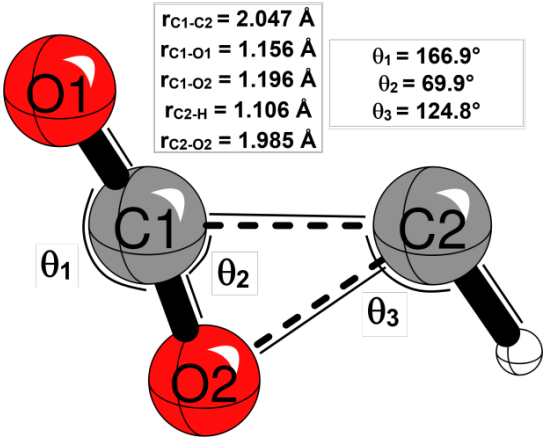

Level of Theory:
Geometry: CCSD(T)/ANO2
Harmonics: CCSD(T)/ANO2
Wavefunction Diagnostics:
CASSCF(11,9) $C_0^2 = 0.934$
CASSCF(11,9) $C_1^2 = 0.008$
CASSCF(11,9) $C_2^2 = 0.007$

Figure S17: TS4 (M2 → CO_2 + CH)

Cartesian Coordinates (Å):

C	-0.3900303930	0.1564827238	0.0000000000
C	1.3823599378	-0.8679188199	0.0000000000
H	2.3827491219	-0.3966837121	0.0000000000
O	-1.4220171158	-0.3646140203	0.0000000000
O	0.5273984726	0.9233554180	0.0000000000

Rotational Constants (GHz): 20.011, 7.513, 5.462

Harmonic Vibrational Frequencies (cm^{-1}):

[a′] 2995 [a″] 635
[a′] 2291 [a″] 53
[a′] 1271
[a′] 898
[a′] 571
[a′] 288
[a′] 417i

Incremental Focal Point Analysis (kcal mol^{-1}):

Basis	ROHF	+δMP2	+δCCSD	+δ(T)	+δT	+δ(Q)	Net
DZ	−94.23	+14.03	−6.38	−0.85	+0.33	+0.65	[−86.45]
TZ	−93.79	+12.62	−6.86	−0.48	+0.33	[+0.65]	[−87.53]
QZ	−93.83	+11.64	−7.05	−0.41	[+0.33]	[+0.65]	[−88.66]
5Z	−93.69	+11.24	−7.05	−0.38	[+0.33]	[+0.65]	[−88.90]
6Z	−93.61	+11.06	−7.03	−0.36	[+0.33]	[+0.65]	[−88.96]
CBS	[−93.58]	[+10.81]	[−7.01]	[−0.33]	[+0.33]	[+0.65]	[−89.14]

TS5 (M2 → M4)

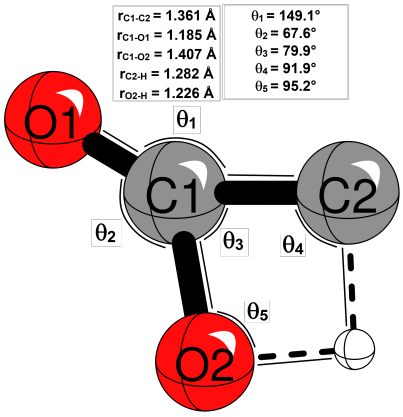

Level of Theory:
Geometry: CCSD(T)/ANO2
Harmonics: CCSD(T)/ANO2
Wavefunction Diagnostics:
CASSCF(11,9) $C_0^2 = 0.927$
CASSCF(11,9) $C_1^2 = 0.015$
CASSCF(11,9) $C_2^2 = 0.007$

Figure S18: TS5 (M2 → M4)

Cartesian Coordinates (Å):

C	-0.2337423958	-0.1239333593	0.0000000000
C	0.8970738828	-0.9926821144	0.0000000000
O	0.8056229100	0.8250180923	0.0000000000
H	1.7107201094	-0.0018205920	0.0000000000
O	-1.4110706188	0.0128244836	0.0000000000

Rotational Constants (GHz): 22.070, 9.107, 6.447

Harmonic Vibrational Frequencies (cm^{-1}):

[a′] 2373 [a″] 593
[a′] 1919 [a″] 195
[a′] 1022
[a′] 963
[a′] 641
[a′] 550
[a′] $1553i$

Incremental Focal Point Analysis (kcal mol^{-1}):

Basis	ROHF	+δMP2	+δCCSD	+δ(T)	+δT	+δ(Q)	Net
DZ	−51.68	−8.01	−2.74	−3.48	+0.06	+0.17	[−65.68]
TZ	−51.36	−11.63	−2.42	−3.73	+0.23	[+0.17]	[−69.09]
QZ	−51.28	−13.05	−2.36	−3.82	[+0.23]	[+0.17]	[−70.45]
5Z	−51.27	−13.60	−2.28	−3.84	[+0.23]	[+0.17]	[−70.93]
6Z	−51.20	−13.83	−2.24	−3.83	[+0.23]	[+0.17]	[−71.05]
CBS	[−51.18]	[−14.15]	[−2.18]	[−3.83]	[+0.23]	[+0.17]	[−71.27]

TS6 (M5 → M6)

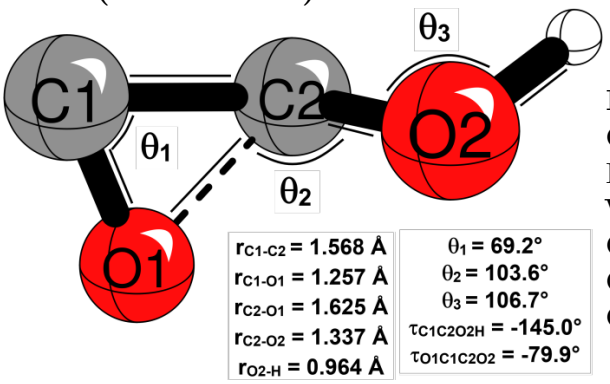

Level of Theory:
Geometry: CCSD(T)/ANO2
Harmonics: CCSD(T)/ANO2
Wavefunction Diagnostics:
CASSCF(11,9) $C_0^2 = 0.922$
CASSCF(11,9) $C_1^2 = 0.020$
CASSCF(11,9) $C_2^2 = 0.011$

Figure S19: TS6 (M5 → M6)

Cartesian Coordinates (Å):

C	0.3135795896	0.3729225423	-0.4575077579
C	-1.0539890979	0.6045297027	0.2731549352
O	1.3473680499	-0.1502172546	0.2102977005
H	2.1425639296	0.2700089447	-0.1367383692
O	-0.9268853689	-0.6001180207	-0.0633733624

Rotational Constants (GHz): 1.025, 0.255, 0.227

Harmonic Vibrational Frequencies (cm^{-1}):

3815	436
1501	402
1252	320
1189	636 i
645	

Incremental Focal Point Analysis (kcal mol^{-1}):

Basis	ROHF	+δMP2	+δCCSD	+δ(T)	+δT	+δ(Q)	Net
DZ	−60.02	+3.50	−8.20	−1.66	−0.38	+0.54	[−66.22]
TZ	−61.30	+0.72	−7.94	−1.87	[−0.38]	[+0.54]	[−70.24]
QZ	−61.50	−0.53	−7.93	−1.91	[−0.38]	[+0.54]	[−71.72]
5Z	−61.60	−1.19	−7.84	−1.93	[−0.38]	[+0.54]	[−72.40]
CBS	[−61.66]	[−1.87]	[−7.75]	[−1.95]	[−0.38]	[+0.54]	[−73.07]

TS7 (M6 → M3)

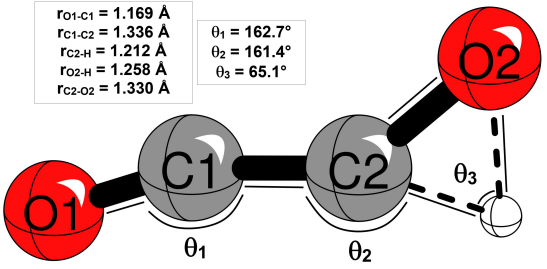

Level of Theory:
Geometry: CCSD(T)/ANO2
Harmonics: CCSD(T)/ANO2
Wavefunction Diagnostics:
CASSCF(11,9) $C_0^2 = 0.881$
CASSCF(11,9) $C_1^2 = 0.013$
CASSCF(11,9) $C_2^2 = 0.009$

Figure S20: TS7 (M6 → M3)

Cartesian Coordinates (Å):

C	0.6816188208	0.0625159524	0.0000000000
C	-0.5966953711	-0.3254547451	0.0000000000
H	-1.5836614716	-1.0283320607	0.0000000000
O	-1.8146607925	0.2087854125	0.0000000000
O	1.8507330275	0.0532756498	0.0000000000

Rotational Constants (GHz): 161.53, 4.217, 4.110

Harmonic Vibrational Frequencies (cm^{-1}):

[a′] 2638 [a″] 348
[a′] 2079 [a″] 269
[a′] 1393
[a′] 879
[a′] 571
[a′] 253
[a′] 2070 i

Incremental Focal Point Analysis (kcal mol^{-1}):

Basis	ROHF	+δMP2	+δCCSD	+δ(T)	+δT	+δ(Q)	Net
DZ	−57.09	−23.88	+5.64	−5.75	−0.15	−0.29	[−81.54]
TZ	−58.13	−26.86	+5.52	−6.10	+0.12	[−0.29]	[−85.74]
QZ	−58.62	−28.39	+5.68	−6.14	[+0.12]	[−0.29]	[−87.65]
5Z	−58.78	−28.91	+5.84	−6.14	[+0.12]	[−0.29]	[−88.17]
6Z	−58.77	−29.17	+5.92	−6.13	[+0.12]	[−0.29]	[−88.32]
CBS	[−58.76]	[−29.52]	[+6.04]	[−6.12]	[+0.12]	[−0.29]	[−88.53]

TS8 (M3 → HCO + CO)

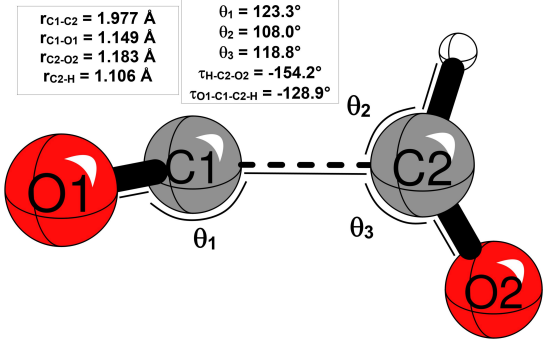

Level of Theory:
Geometry: CCSD(T)/ANO2
Harmonics: CCSD(T)/ANO2
Wavefunction Diagnostics:
CASSCF(11,9) $C_0^2 = 0.885$
CASSCF(11,9) $C_1^2 = 0.017$
CASSCF(11,9) $C_2^2 = 0.013$

Figure S21: TS8 (M3 → HCO + CO)

Cartesian Coordinates (Å):

C	0.9528909116	-0.3688137509	-0.3488314941
C	-0.9387091307	-0.4617931411	0.2170569556
H	-1.2033092966	-1.5266612077	0.3539351599
O	-1.6676796314	0.4187084820	-0.0871647165
O	1.7328593351	0.3006382742	0.1637259062

Rotational Constants (GHz): 37.457, 4.278, 4.004

Harmonic Vibrational Frequencies (cm^{-1}):

2901	325
1976	257
1827	84
1192	$467i$
635	

Incremental Focal Point Analysis (kcal mol^{-1}):

Basis	ROHF	+δMP2	+δCCSD	+δ(T)	+δT	+δ(Q)	Net
DZ	−136.36	−0.48	−3.56	−1.58	−0.33	+0.62	[−141.69]
TZ	−136.42	−0.83	−3.82	−1.54	−0.16	[+0.62]	[−142.15]
QZ	−137.03	−1.68	−3.90	−1.51	[−0.16]	[+0.62]	[−143.67]
5Z	−137.00	−2.11	−3.87	−1.51	[−0.16]	[+0.62]	[−144.03]
6Z	−136.95	−2.30	−3.84	−1.49	[−0.16]	[+0.62]	[−144.14]
CBS	[−136.93]	[−2.56]	[−3.81]	[−1.48]	[−0.16]	[+0.62]	[−144.33]

TS9 (HCO → CO)

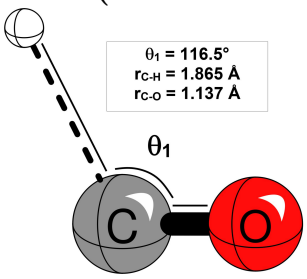

Level of Theory:
Geometry: CCSD(T)/ANO2
Harmonics: CCSD(T)/ANO2
Wavefunction Diagnostics:
CASSCF(11,9) $C_0^2 = 0.885$
CASSCF(11,9) $C_1^2 = 0.017$
CASSCF(11,9) $C_2^2 = 0.013$

Figure S22: TS9 (HCO → CO)

Cartesian Coordinates (Å):

```
C       -0.5623589009      0.2114919107      0.0000000000
H       -1.7996740007     -1.1837910012      0.0000000000
O        0.5352990942     -0.0840797719      0.0000000000
```

Rotational Constants (GHz): 245.074, 43.408, 36.877
Harmonic Vibrational Frequencies (cm^{-1}):
[a'] 2103
[a'] 384
[a'] 801i

Incremental Focal Point Analysis (kcal mol^{-1}):

Basis	ROHF	+δMP2	+δCCSD	+δ(T)	+δT	+δ(Q)	Net
DZ	-145.11	+16.54	-6.39	-0.03	+0.12	+0.77	[-134.10]
TZ	-143.79	+19.99	-7.18	+0.49	+0.25	[+0.77]	[-129.47]
QZ	-144.30	+20.09	-7.47	+0.71	[+0.25]	[+0.77]	[-129.95]
5Z	-144.07	+19.97	-7.53	+0.79	[+0.25]	[+0.77]	[-129.82]
6Z	-144.00	+19.90	-7.55	+0.82	[+0.25]	[+0.77]	[-129.80]
CBS	[-143.98]	[+19.79]	[-7.57]	[+0.87]	[+0.25]	[+0.77]	[-129.86]

TS10 (M1 → M7)

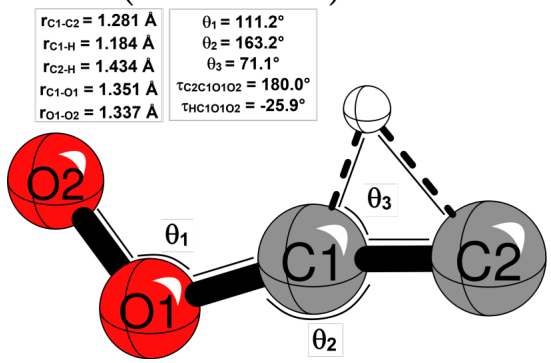

Level of Theory:
Geometry: CCSD(T)/ANO2
Harmonics: CCSD(T)/ANO2
Wavefunction Diagnostics:
CASSCF(11,9) $C_0^2 = 0.934$
CASSCF(11,9) $C_1^2 = 0.019$
CASSCF(11,9) $C_2^2 = 0.008$

Figure S23: TS10 (M1 → M7)

Cartesian Coordinates (Å):

C	-0.6871237724	-0.0110191743	-0.0099618834
C	-1.9582454030	0.1459625584	-0.0238455471
H	-0.9430313870	1.0846343821	0.3578612265
O	0.5485289805	-0.5562995992	0.0244074486
O	1.4955482472	0.3867180609	-0.0215923262

Rotational Constants (GHz): 56.538, 5.416, 4.957

Harmonic Vibrational Frequencies (cm^{-1}):

2545	501
1888	291
1090	133
994	$323i$
752	

Incremental Focal Point Analysis (kcal mol^{-1}):

Basis	ROHF	+δMP2	+δCCSD	+δ(T)	+δT	+δ(Q)	Net
DZ	+0.28	+19.16	−16.60	−0.71	−0.21	+0.52	[+2.44]
TZ	+0.26	+16.86	−17.45	−0.69	−0.43	[+0.52]	[−0.92]
QZ	+0.64	+16.29	−17.68	−0.74	[−0.43]	[+0.52]	[−1.39]
5Z	+0.68	+16.06	−17.73	−0.76	[−0.43]	[+0.52]	[−1.66]
6Z	+0.75	+15.95	−17.74	−0.76	[−0.43]	[+0.52]	[−1.69]
CBS	[+0.68]	[+15.80]	[−17.80]	[−0.77]	[−0.43]	[+0.52]	[−1.82]

TS11 ($C_2H + O_2 \rightarrow$ M7)

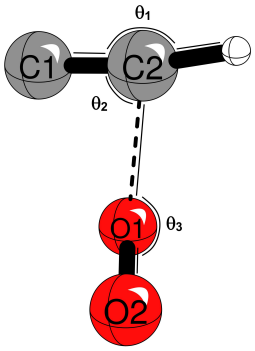

Level of Theory:
Geometry: CCSD(T)/ANO1
Harmonics: CCSD(T)/ANO1
Wavefunction Diagnostics:
CASSCF(11,9) $C_0^2 = 0.690$
CASSCF(11,9) $C_1^2 = 0.153$
CASSCF(11,9) $C_2^2 = 0.021$

Figure S24: TS11 ($C_2H + O_2 \rightarrow$ M7)

Geometry (Å):

Theory	C_1–C_2	C_1–O_2	O_1–O_2	C_2–H	θ_1	θ_2	θ_3	$\tau_{O_1O_2C_1C_2}$
CCSD(T)/ANO1	1.291	2.179	1.214	1.072	115.1	83.1	171.8	96.2
CASPT2/cc-pVTZ	1.296	1.763	1.213	1.068	113.2	92.7	160.2	98.7
MRCISD+Q/cc-pVDZ	1.306	1.933	1.199	1.078	113.2	91.6	163.7	97.0

Harmonic Vibrational Frequencies (cm^{-1}):

CCSD(T)/ANO1	3367	1684	1511	636	551	293	126	88	235i
CASPT2/cc-pVTZ	3407	1696	1270	838	604	438	236	156	695i
MRCISD+Q/cc-pVDZ	3462	1731	1346	751	555	397	204	137	442i

Incremental Focal Point Analysis (kcal mol^{-1}) of ^2A state:

Basis	ROHF	+δMP2	+δCCSD	+δ(T)	+δT	+δ(Q)	Net
DZ	+51.26	−12.86	−14.61	−12.51	−2.39	−2.45	[+6.73]
TZ	+52.83	−15.78	−11.89	−13.27	−2.09	[−2.45]	[+7.36]
QZ	+52.96	−16.5	−11.14	−13.52	[−2.09]	[−2.45]	[+7.26]
5Z	+52.96	−16.86	−10.82	−13.63	[−2.09]	[−2.45]	[+7.10]
CBS	[+52.94]	[−17.24]	[−10.49]	[−13.75]	[−2.09]	[−2.45]	[+6.91]

Incremental Focal Point Analysis (kcal mol^{-1}) of ^4A state:

Basis	ROHF	+δMP2	+δCCSD	+δ(T)	+δT	+δ(Q)	Net
DZ	+29.55	+15.36	-12.60	-0.18	-0.13	-0.24	[+31.76]
TZ	+31.08	+15.18	-13.23	-0.10	-0.33	[-0.24]	[+32.36]
QZ	+31.26	+15.32	-13.43	-0.16	[-0.33]	[-0.24]	[+32.43]
5Z	+31.27	+15.36	-13.49	-0.20	[-0.33]	[-0.24]	[+32.38]
6Z	+31.33	+15.40	-13.52	-0.20	[-0.33]	[-0.24]	[+32.44]
CBS	[+31.35]	[+15.45]	[-13.56]	[-0.21]	[-0.33]	[-0.24]	[+32.46]

Doublet Quartet Splitting: 24.77 kcal mol^{-1}

TS12 (M7 → M8)

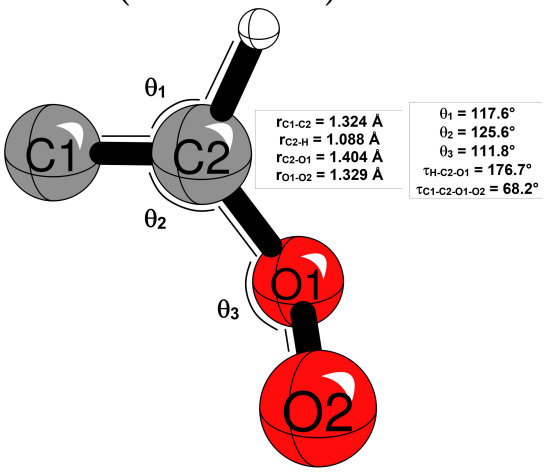

Level of Theory:
Geometry: CCSD(T)/ANO2
Harmonics: CCSD(T)/ANO2
Wavefunction Diagnostics:
CASSCF(11,9) $C_0^2 = 0.920$
CASSCF(11,9) $C_1^2 = 0.030$
CASSCF(11,9) $C_2^2 = 0.026$

Figure S25: TS12 (M7 → M8)

Cartesian Coordinates (Å):

C	1.6342182246	-0.5352132564	-0.1424550817
C	0.7634450649	0.3873039977	0.2352632301
H	1.0999223076	1.1369944177	0.9479723202
O	-0.5459526599	0.5250606046	-0.2535721226
O	-1.3221716403	-0.4857343792	0.1242130031

Rotational Constants (GHz): 28.372, 6.643, 5.762

Harmonic Vibrational Frequencies (cm^{-1}):

[a_1] 3153	[a_1] 721
[a_1] 1636	[a_1] 457
[a_1] 1124	[a_1] 212
[a_1] 1039	[a_1] 162 i
[a_1] 933	

Incremental Focal Point Analysis (kcal mol^{-1}):

Basis	ROHF	+δMP2	+δCCSD	+δ(T)	+δT	+δ(Q)	Net
DZ	−8.99	+31.57	−22.91	+1.00	−0.38	+0.66	[+0.72]
TZ	−8.87	+29.59	−23.89	+1.19	−0.60	[+0.66]	[−1.92]
QZ	−8.58	+29.00	−24.08	+1.17	[−0.60]	[+0.66]	[−2.44]
5Z	−8.62	+28.68	−24.11	+1.14	[−0.60]	[+0.66]	[−2.86]
6Z	−8.55	+28.56	−24.10	+1.14	[−0.60]	[+0.66]	[−2.91]
CBS	[−8.53]	[+28.39]	[−24.09]	[+1.14]	[−0.60]	[+0.66]	[−3.06]

TS13 (M8 → M3)

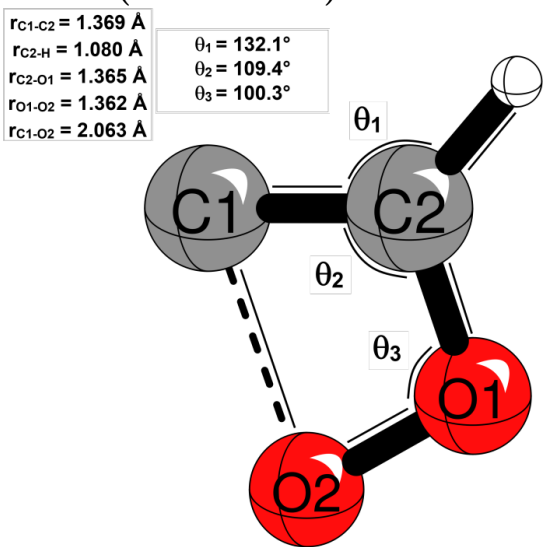

Level of Theory:
Reference: ROHF
Geometry: CCSD(T)/ANO1
Frequencies: EOM-CCSD/ANO1
Program: CFOUR 1.0, VCC
Wavefunction Diagnostics:
CASSCF(11,9) $C_0^2 = 0.884$
CASSCF(11,9) $C_1^2 = 0.034$
CASSCF(11,9) $C_2^2 = 0.017$

Figure S26: TS13 (M8 → M3)

Cartesian Coordinates (Å):

C	2.1043850600	1.4616966800	0.0000000000
C	1.4883981800	-1.0507657800	0.0000000000
H	2.6325170300	-2.7402639200	0.0000000000
O	-1.0776120700	-1.3054511800	0.0000000000
O	-1.7837045800	1.1698165500	0.0000000000

Rotational Constants (GHz): 18.883, 11.796, 7.260

Harmonic Vibrational Frequencies (cm^{-1}):

[a′] 3194	[a″] 865
[a′] 1447	[a″] 411
[a′] 1163	
[a′] 1085	
[a′] 981	
[a′] 704	
[a′] 879 i	

Incremental Focal Point Analysis (kcal mol^{-1}):

Basis	ROHF	+δMP2	+δCCSD	+δ(T)	+δT	+δ(Q)	Net
DZ	+1.76	+26.13	−25.45	−1.24	−1.26	−0.77	[−3.02]
TZ	+1.95	+24.05	−25.40	−1.25	−1.28	[−0.77]	[−4.88]
QZ	+2.24	+23.43	−25.34	−1.28	[−1.28]	[−0.77]	[−5.17]
5Z	+2.22	+23.07	−25.27	−1.31	[−1.28]	[−0.77]	[−5.52]
6Z	+2.28	+22.90	−25.23	−1.31	[−1.28]	[−0.77]	[−5.58]
CBS	[+2.31]	[+22.67]	[−25.17]	[−1.31]	[−1.28]	[−0.77]	[−3.55]

TS15 (Q1 → CO_2 + CH ($^4\Sigma^-$))

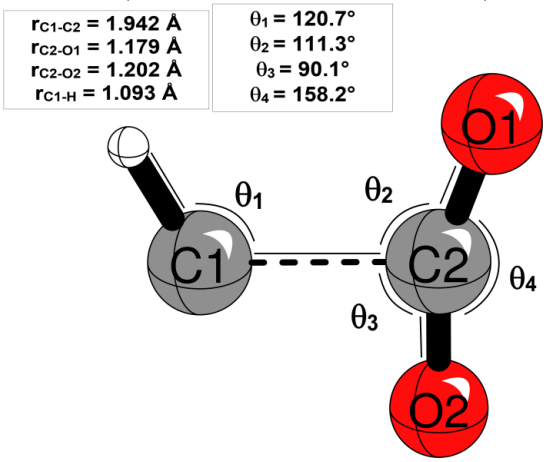

Level of Theory:
Reference: ROHF
Geometry: CCSD(T)/ANO2
Frequencies: CCSD/ANO1
Program: CFOUR 1.0, VCC
Wavefunction Diagnostics:
CASSCF(11,9) $C_0^2 = 0.923$
CASSCF(11,9) $C_1^2 = 0.009$
CASSCF(11,9) $C_2^2 = 0.006$

Figure S27: TS15 (Q1 → CO_2 + CH ($^4\Sigma^-$))

Cartesian Coordinates (Å):

C	0.2894192826	0.1636645270	0.0000000000
C	-1.3637457153	-0.8550020584	0.0000000000
H	-1.3463517438	-1.9478301152	0.0000000000
O	-0.3395346171	1.1877902530	0.0000000000
O	1.2303680185	-0.5463912473	0.0000000000

Rotational Constants (GHz): 12.553, 9.869, 5.525
Harmonic Vibrational Frequencies (cm^{-1}):
[a′] 3091 [a″] 653
[a′] 2131 [a″] 378
[a′] 1227
[a′] 623
[a′] 560
[a′] 267
[a′] 578 i

Incremental Focal Point Analysis (kcal mol^{-1}):

Basis	ROHF	+δMP2	+δCCSD	+δ(T)	+δT	+δ(Q)	Net
DZ	−81.57	+23.71	−3.15	−0.41	−0.12	+0.65	[−60.91]
TZ	−81.27	+25.69	−4.63	+0.16	−0.25	[+0.65]	[−59.65]
QZ	−81.35	+25.94	−5.25	+0.25	[−0.25]	[+0.65]	[−60.01]
5Z	−81.26	+26.07	−5.51	+0.29	[−0.25]	[+0.65]	[−60.01]
6Z	−81.17	+26.15	−5.65	+0.32	[−0.25]	[+0.65]	[−59.95]
CBS	[−81.14]	[+26.26]	[−5.83]	[+0.35]	[−0.25]	[+0.65]	[−59.97]

Appendix D

Supporting Information for Chapter 5

D.1 Products

Incremental Focal Point Analysis Table (kcal mol^{-1}) for $C_2H + H_2 \rightarrow C_2H_2 + H$:

Basis	ROHF	+δMP2	+δCCSD	+δ(T)	+δT	+δ(Q)	Net
aug-cc-pVDZ	-34.93	-0.72	+7.18	-0.30	+0.24	+0.03	[-28.49]
aug-cc-pVTZ	-34.37	-1.16	+6.60	-0.46	[+0.24]	[+0.03]	[-29.21]
aug-cc-pVQZ	-34.30	-1.31	+6.47	-0.49	[+0.24]	[+0.03]	[-29.35]
aug-cc-pV5Z	-34.29	-1.34	+6.44	-0.50	[+0.24]	[+0.03]	[-29.41]
CBS LIMIT	[-34.30]	[-1.36]	[+6.40]	[-0.50]	[+0.24]	[+0.03]	[-29.49]

Incremental Focal Point Analysis Table (kcal mol^{-1}) for $C_2H + CH_4 \rightarrow C_2H_2 + CH_3$:

Basis	ROHF	+δMP2	+δCCSD	+δ(T)	+δT	+δ(Q)	Net
aug-cc-pVDZ	-29.60	+1.77	+2.25	+0.42	+0.22	+0.05	[-24.89]
aug-cc-pVTZ	-30.11	+1.08	+1.88	+0.48	[+0.22]	[+0.05]	[-26.41]
aug-cc-pVQZ	-30.00	+0.84	+1.87	+0.48	[+0.22]	[+0.05]	[-26.54]
aug-cc-pV5Z	-29.99	+0.77	+1.89	+0.49	[+0.22]	[+0.05]	[-26.58]
CBS LIMIT	[-30.00]	[+0.70]	[+1.91]	[+0.49]	[+0.22]	[+0.05]	[-26.63]

Incremental Focal Point Analysis Table (kcal mol^{-1}) for $C_2H + NH_3 \rightarrow C_2H_2 + NH_2$:

Basis	ROHF	+δMP2	+δCCSD	+δ(T)	+δT	+δ(Q)	Net
aug-cc-pVDZ	-31.58	+8.10	-0.77	+0.64	+0.15	+0.11	[-23.35]
aug-cc-pVTZ	-31.91	+7.73	-1.16	+0.82	[+0.15]	[+0.11]	[-24.26]
aug-cc-pVQZ	-31.72	+7.89	-1.15	+0.85	[+0.15]	[+0.11]	[-23.87]
aug-cc-pV5Z	-31.70	+7.92	-1.15	+0.86	[+0.15]	[+0.11]	[-23.82]
CBS LIMIT	[-31.71]	[+7.95]	[-1.15]	[+0.87]	[+0.15]	[+0.11]	[-23.78]

Incremental Focal Point Analysis Table (kcal mol^{-1}) for $C_2H + H_2O \rightarrow C_2H_2 + OH$:

Basis	ROHF	+δMP2	+δCCSD	+δ(T)	+δT	+δ(Q)	Net
aug-cc-pVDZ	-27.05	+15.48	-2.66	+0.84	+0.16	+0.18	[-13.04]
aug-cc-pVTZ	-27.76	+15.42	-3.33	+1.23	[+0.16]	[+0.18]	[-14.11]
aug-cc-pVQZ	-27.51	+15.77	-3.35	+1.29	[+0.16]	[+0.18]	[-13.46]
aug-cc-pV5Z	-27.51	+15.87	-3.37	+1.31	[+0.16]	[+0.18]	[-13.36]
CBS LIMIT	[-27.53]	[+15.97]	[-3.39]	[+1.33]	[+0.16]	[+0.18]	[-13.28]

Incremental Focal Point Analysis Table (kcal mol^{-1}) for C_2H + HF → C_2H_2 + F:

Basis	ROHF	+δMP2	+δCCSD	+δ(T)	+δT	+δ(Q)	Net
aug-cc-pVDZ	-18.05	+22.04	-3.29	+0.82	+0.23	+0.20	[+1.95]
aug-cc-pVTZ	-18.30	+22.39	-4.33	+1.49	[+0.23]	[+0.20]	[+1.68]
aug-cc-pVQZ	-18.11	+23.05	-4.39	+1.59	[+0.23]	[+0.20]	[+2.56]
aug-cc-pV5Z	-18.14	+23.13	-4.43	+1.62	[+0.23]	[+0.20]	[+2.60]
CBS LIMIT	[-18.19]	[+23.21]	[-4.48]	[+1.65]	[+0.23]	[+0.20]	[+2.63]

Incremental Focal Point Analysis Table (kcal mol^{-1}) for C_2H + PH_3 → C_2H_2 + PH_2:

Basis	ROHF	+δMP2	+δCCSD	+δ(T)	+δT	+δ(Q)	Net
aug-cc-pVDZ	-50.58	-3.52	+3.75	+0.22	+0.23	+0.06	[-49.83]
aug-cc-pVTZ	-51.07	-4.39	+3.42	+0.16	[+0.23]	[+0.06]	[-51.60]
aug-cc-pVQZ	-50.86	-4.47	+3.51	+0.16	[+0.23]	[+0.06]	[-51.37]
aug-cc-pV5Z	-50.84	-4.51	+3.53	+0.16	[+0.23]	[+0.06]	[-51.36]
CBS LIMIT	[-50.84]	[-4.55]	[+3.56]	[+0.17]	[+0.23]	[+0.06]	[-51.37]

Incremental Focal Point Analysis Table (kcal mol^{-1}):

Basis	ROHF	+δMP2	+δCCSD	+δ(T)	+δT	+δ(Q)	Net
aug-cc-pVDZ	-45.54	+0.47	+2.59	+0.57	+0.21	+0.09	[-41.61]
aug-cc-pVTZ	-46.10	-0.07	+1.96	+0.61	[+0.21]	[+0.09]	[-43.30]
aug-cc-pVQZ	-45.90	-0.10	+2.05	+0.62	[+0.21]	[+0.09]	[-43.03]
aug-cc-pV5Z	-45.88	-0.09	+2.08	+0.64	[+0.21]	[+0.09]	[-42.96]
CBS LIMIT	[-45.88]	[-0.08]	[+2.11]	[+0.65]	[+0.21]	[+0.09]	[-42.90]

Incremental Focal Point Analysis Table (kcal mol^{-1}) for C_2H + HCl → C_2H_2 + Cl:

Basis	ROHF	+δMP2	+δCCSD	+δ(T)	+δT	+δ(Q)	Net
aug-cc-pVDZ	-36.96	+3.72	+1.42	+0.73	+0.21	+0.11	[-30.77]
aug-cc-pVTZ	-37.48	+3.40	+0.59	+0.91	[+0.21]	[+0.11]	[-32.26]
aug-cc-pVQZ	-37.33	+3.62	+0.68	+0.93	[+0.21]	[+0.11]	[-31.78]
aug-cc-pV5Z	-37.30	+3.74	+0.69	+0.96	[+0.21]	[+0.11]	[-31.60]
CBS LIMIT	[-37.30]	[+3.87]	[+0.69]	[+0.98]	[+0.21]	[+0.11]	[-31.43]

Incremental Focal Point Analysis Table (kcal mol^{-1}) for C_2H + HCN → C_2H_2 + CN:

Basis	ROHF	+δMP2	+δCCSD	+δ(T)	+δT	+δ(Q)	Net
aug-cc-pVDZ	+1.39	-7.58	+0.43	-1.47	-0.27	-0.11	[-7.62]
aug-cc-pVTZ	+1.63	-7.53	+0.49	-1.77	[-0.27]	[-0.11]	[-7.55]
aug-cc-pVQZ	+1.59	-7.46	+0.57	-1.82	[-0.27]	[-0.11]	[-7.50]
aug-cc-pV5Z	+1.59	-7.47	+0.61	-1.85	[-0.27]	[-0.11]	[-7.50]
CBS LIMIT	[+1.59]	[-7.49]	[+0.65]	[-1.88]	[-0.27]	[-0.11]	[-7.50]

Incremental Focal Point Analysis Table (kcal mol^{-1}) for C_2H + HNC → C_2H_2 + CN:

Basis	ROHF	+δMP2	+δCCSD	+δ(T)	+δT	+δ(Q)	Net
aug-cc-pVDZ	-8.58	-15.16	+3.65	-1.67	-0.12	-0.43	[-22.32]
aug-cc-pVTZ	-8.12	-15.50	+3.71	-2.11	[-0.12]	[-0.43]	[-22.56]
aug-cc-pVQZ	-8.08	-15.47	+3.84	-2.20	[-0.12]	[-0.43]	[-22.46]
aug-cc-pV5Z	-8.07	-15.54	+3.88	-2.23	[-0.12]	[-0.43]	[-22.52]
CBS LIMIT	[-8.08]	[-15.61]	[+3.93]	[-2.27]	[-0.12]	[-0.43]	[-22.59]

D.2 Pre-Reactive Complexes

$C_2H + H_2$

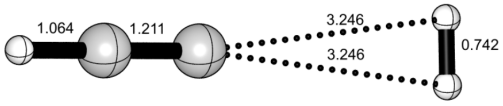

Figure S1: PRC1 ($C_2H + H_2$)

Level of Theory:

Reference:	ROHF
Geometry:	CCSD(T)-F12a/aug-cc-pVTZ-F12
Frequencies:	CCSD(T)-F12a/aug-cc-pVTZ-F12
Program:	MOLPRO 2010.1

Wavefunction Diagnostics:

T_1: 0.015

D_1: 0.031

Cartesian Coordinates (Å):

C	0.0000000000	0.0000000000	-0.3798059876
C	0.0000000000	0.0000000000	0.8309620035
H	0.0000000000	0.0000000000	1.8954310413
H	0.0000000000	0.3710089050	-3.6357896653
H	0.0000000000	-0.3710089050	-3.6357896653

Rotational Constants (GHz): 12.456, 12.542, 1821.310

Harmonic Vibrational Frequencies (cm^{-1}):

a_1:	4395	3443	2017	77
b_1:			373	12
b_2:		375	123	16

Incremental Focal Point Analysis Table (kcal mol^{-1}):

Basis	ROHF	+δMP2	+δCCSD	+δ(T)	+δT	+δ(Q)	Net
aug-cc-pVDZ	+0.08	-0.44	+0.03	-0.05	-0.00	-0.00	[-0.38]
aug-cc-pVTZ	+0.15	-0.39	+0.04	-0.05	[-0.00]	[-0.00]	[-0.25]
aug-cc-pVQZ	+0.16	-0.37	+0.04	-0.05	[-0.00]	[-0.00]	[-0.22]
aug-cc-pV5Z	+0.17	-0.36	+0.04	-0.05	[-0.00]	[-0.00]	[-0.21]
CBS LIMIT	[+0.17]	[-0.36]	[+0.04]	[-0.05]	[-0.00]	[-0.00]	[-0.20]

$C_2H + CH_4$

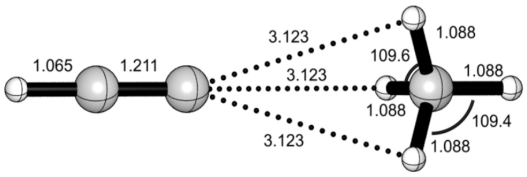

Figure S2: PRC2 (C_2H + CH_4)

Level of Theory:

Reference:	ROHF
Geometry:	CCSD(T)-F12a/aug-cc-pVTZ-F12
Frequencies:	CCSD(T)-F12a/aug-cc-pVTZ-F12
Program:	MOLPRO 2010.1

Wavefunction Diagnostics:

T_1: 0.013

D_1: 0.031

Cartesian Coordinates (Å):

C	-0.0000000000	0.0000000000	2.0941338545
H	-0.0000000000	0.0000000000	3.1586422043
C	-0.0000000000	0.0000000000	0.8831544939
C	0.0000000000	0.0000000000	-2.4272590280
H	1.0264851043	0.0000000000	-2.0658878666
H	-0.5132425521	-0.8889621769	-2.0658878666
H	-0.5132425521	0.8889621769	-2.0658878666
H	0.0000000000	0.0000000000	-3.5153391491

Rotational Constants (GHz): 2.976, 2.976, 158.619

Harmonic Vibrational Frequencies (cm^{-1}):

a_1:	3443	3152	3029	2016	1341	59
e:	3151	1568	1343	380	77	16

Incremental Focal Point Analysis Table (kcal mol^{-1}):

Basis	ROHF	+δMP2	+δCCSD	+δ(T)	+δT	+δ(Q)	Net
aug-cc-pVDZ	+0.29	-1.54	+0.23	-0.19	+0.00	-0.01	[-1.22]
aug-cc-pVTZ	+0.57	-1.37	+0.24	-0.19	[+0.00]	[-0.01]	[-0.77]
aug-cc-pVQZ	+0.60	-1.31	+0.24	-0.19	[+0.00]	[-0.01]	[-0.66]
aug-cc-pV5Z	+0.61	-1.28	+0.24	-0.19	[+0.00]	[-0.01]	[-0.63]
CBS LIMIT	[+0.62]	[-1.25]	[+0.23]	[-0.19]	[+0.00]	[-0.01]	[-0.60]

$C_2H + NH_3$

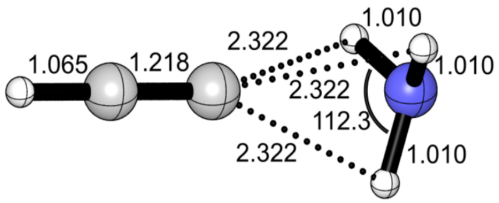

Figure S3: PRC3 (C_2H + NH_3)

Level of Theory:

Reference:	ROHF
Geometry:	CCSD(T)-F12a/aug-cc-pVTZ-F12
Frequencies:	CCSD(T)-F12a/aug-cc-pVTZ-F12
Program:	MOLPRO 2010.1

Wavefunction Diagnostics:

T_1: 0.032

D_1: 0.119

Cartesian Coordinates (Å):

C	0.0000000000	0.0000000000	-1.7654172575
C	0.0000000000	0.0000000000	-0.5473053486
H	0.0000000000	0.0000000000	-2.8306704324
N	-0.0000000000	0.0000000000	1.8494697794
H	0.9683756059	0.0000000000	1.5630192335
H	-0.4841878029	0.8386378751	1.5630192335
H	-0.4841878029	-0.8386378751	1.5630192335

Rotational Constants (GHz): 4.776, 4.776, 178.227

Harmonic Vibrational Frequencies (cm^{-1}):

a_1:	3492	3431	1981	722	270
e:	3660	1618	575	379	26

Incremental Focal Point Analysis Table (kcal mol^{-1}):

Basis	ROHF	+δMP2	+δCCSD	+δ(T)	+δT	+δ(Q)	Net
aug-cc-pVDZ	+30.80	-22.27	+3.74	-2.80	+0.12	-0.30	[+9.29]
aug-cc-pVTZ	+31.78	-22.36	+4.24	-3.10	[+0.12]	[-0.30]	[+10.39]
aug-cc-pVQZ	+32.03	-22.17	+4.44	-3.15	[+0.12]	[-0.30]	[+10.97]
aug-cc-pV5Z	+32.06	-22.03	+4.47	-3.16	[+0.12]	[-0.30]	[+11.17]
CBS LIMIT	[+32.06]	[-21.88]	[+4.51]	[-3.17]	[+0.12]	[-0.30]	[+11.34]

$C_2H + H_2O$

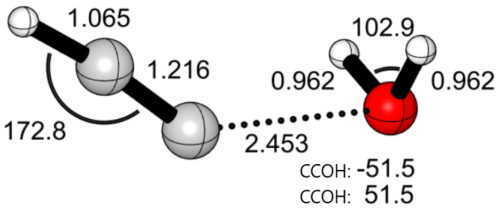

Figure S4: PRC4 ($C_2H + H_2O$)

Level of Theory:

Reference: ROHF
Geometry: CCSD(T)-F12a/aug-cc-pVTZ-F12
Frequencies: CCSD(T)-F12a/aug-cc-pVTZ-F12
Program: Molpro 2010.1

Wavefunction Diagnostics:

T_1: 0.021
D_1: 0.070

Cartesian Coordinates (Å):

C	0.1998532607	0.0000000000	1.7255968666
H	0.5917686606	0.0000000000	2.7158060787
C	-0.3859589491	0.0000000000	0.6597344340
O	0.0271363658	0.0000000000	-1.7588872237
H	0.5975963592	-0.7596081855	-1.6104349388
H	0.5975963592	0.7596081855	-1.6104349388

Rotational Constants (GHz): 4.845, 4.745, 111.889

Harmonic Vibrational Frequencies (cm^{-1}):

a':	3794	3434	1964	1640	521	309	136	69
a'':						3905	522	294

Incremental Focal Point Analysis Table (kcal mol^{-1}):

Basis	ROHF	+δMP2	+δCCSD	+δ(T)	+δT	+δ(Q)	Net
aug-cc-pVDZ	+2.92	-5.01	+0.43	-0.97	-0.07	-0.02	[-2.72]
aug-cc-pVTZ	+3.51	-5.24	+0.52	-1.05	[-0.07]	[-0.02]	[-2.35]
aug-cc-pVQZ	+3.57	-5.18	+0.58	-1.08	[-0.07]	[-0.02]	[-2.20]
aug-cc-pV5Z	+3.60	-5.14	+0.59	-1.08	[-0.07]	[-0.02]	[-2.13]
CBS LIMIT	[+3.61]	[-5.10]	[+0.61]	[-1.09]	[-0.07]	[-0.02]	[-2.07]

C_2H + HF

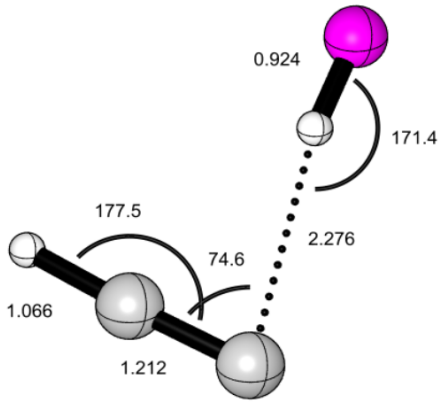

Level of Theory:

Reference:	ROHF
Geometry:	CCSD(T)-F12a/aug-cc-pVTZ-F12
Frequencies:	CCSD(T)-F12a/aug-cc-pVTZ-F12
Program:	MOLPRO 2010.1

Wavefunction Diagnostics:

T_1: 0.013

D_1: 0.030

Figure S5: PRC5 (C_2H + HF)

Cartesian Coordinates (Å):

C	-0.6688417025	0.0000000000	-1.3733647768
C	0.5431757073	0.0000000000	-1.3544064054
H	1.6074252396	0.0000000000	-1.2916114431
H	-0.0969945401	0.0000000000	0.8298536105
F	-0.0006868604	0.0000000000	1.7490251080

Rotational Constants (GHz): 4.805, 4.330, 43.829

Harmonic Vibrational Frequencies (cm^{-1}):

a':	3990	3429	2008	540	361	132	90
a'':						381	345

Incremental Focal Point Analysis Table (kcal mol^{-1}):

Basis	ROHF	+δMP2	+δCCSD	+δ(T)	+δT	+δ(Q)	Net
aug-cc-pVDZ	-2.06	-1.92	+0.43	-0.36	+15.63	+0.71	[+12.42]
aug-cc-pVTZ	-2.06	-2.07	+0.50	-0.34	[+15.63]	[+0.71]	[+12.37]
aug-cc-pVQZ	-1.97	-1.97	+0.53	-0.34	[+15.63]	[+0.71]	[+12.59]
aug-cc-pV5Z	-1.94	-1.93	+0.53	-0.34	[+15.63]	[+0.71]	[+12.66]
CBS LIMIT	[-1.93]	[-1.88]	[+0.53]	[-0.34]	[+15.63]	[+0.71]	[+12.72]

$C_2H + PH_3$

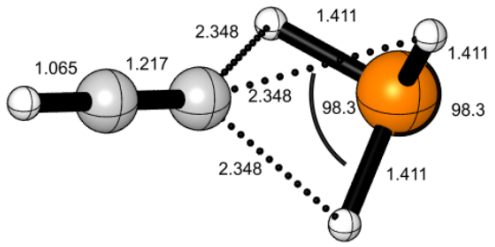

Level of Theory:

Reference:	ROHF
Geometry:	CCSD(T)-F12a/aug-cc-pVTZ-F12
Frequencies:	CCSD(T)-F12a/aug-cc-pVTZ-F12
Program:	MOLPRO 2010.1

Wavefunction Diagnostics:

T_1: 0.033

D_1: 0.121

Figure S6: PRC6 ($C_2H + PH_3$)

Cartesian Coordinates (Å):

C	-0.0000000000	0.0000000000	1.2253408023
C	-0.0000000000	0.0000000000	2.4427426929
H	-0.0000000000	0.0000000000	3.5079061713
P	0.0000000000	0.0000000000	-1.4610779264
H	-1.2324261844	0.0000000000	-0.7732050106
H	0.6162130922	-1.0673123840	-0.7732050106
H	0.6162130922	1.0673123840	-0.7732050106

Rotational Constants (GHz): 2.933, 2.933, 110.037

Harmonic Vibrational Frequencies (cm^{-1}):

a_1:	3432	2429	1981	826	144
e:	2450	1107	568	220	69

Incremental Focal Point Analysis Table (kcal mol^{-1}):

Basis	ROHF	+δMP2	+δCCSD	+δ(T)	+δT	+δ(Q)	Net
aug-cc-pVDZ	+9.69	-13.07	+1.83	-2.10	-0.04	-0.20	[-3.90]
aug-cc-pVTZ	+10.05	-13.59	+2.00	-2.35	[-0.04]	[-0.20]	[-4.13]
aug-cc-pVQZ	+10.14	-13.62	+2.02	-2.41	[-0.04]	[-0.20]	[-4.10]
aug-cc-pV5Z	+10.16	-13.61	+2.02	-2.43	[-0.04]	[-0.20]	[-4.10]
CBS LIMIT	[+10.16]	[-13.60]	[+2.02]	[-2.45]	[-0.04]	[-0.20]	[-4.10]

$C_2H + H_2S$

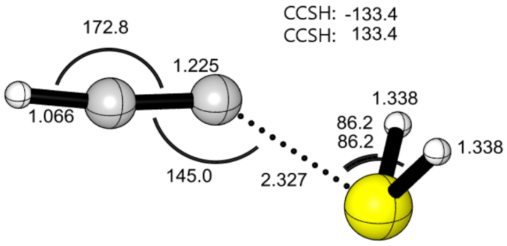

Figure S7: PRC7 (C_2H + H_2S)

Level of Theory:

Reference: ROHF
Geometry: CCSD(T)-F12a/aug-cc-pVTZ-F12
Frequencies: CCSD(T)-F12a/aug-cc-pVTZ-F12
Program: Molpro 2010.1

Wavefunction Diagnostics:

T_1: 0.017
D_1: 0.040

Cartesian Coordinates (Å):

C	0.0000000000	0.3347874050	1.0574481031
C	0.0000000000	-0.1689045255	2.1739514034
H	0.0000000000	-0.4826336724	3.1926130075
S	0.0000000000	-0.0984446914	-1.2284594798
H	0.9708937623	0.8185920415	-1.3125240116
H	-0.9708937623	0.8185920415	-1.3125240116

Rotational Constants (GHz): 3.719, 3.765, 92.131

Harmonic Vibrational Frequencies (cm^{-1}):

a':	3421	2720	1930	1187	600	495	288	89
a'':					2736	617	462	29

Incremental Focal Point Analysis Table (kcal mol^{-1}):

Basis	ROHF	+δMP2	+δCCSD	+δ(T)	+δT	+δ(Q)	Net
aug-cc-pVDZ	+7.80	-20.70	+6.57	-2.57	+0.25	-0.29	[-8.94]
aug-cc-pVTZ	+8.31	-22.03	+7.32	-2.83	[+0.25]	[-0.29]	[-9.28]
aug-cc-pVQZ	+8.46	-22.23	+7.51	-2.91	[+0.25]	[-0.29]	[-9.21]
aug-cc-pV5Z	+8.48	-22.27	+7.54	-2.94	[+0.25]	[-0.29]	[-9.23]
CBS LIMIT	[+8.48]	[-22.31]	[+7.58]	[-2.97]	[+0.25]	[-0.29]	[-9.27]

C_2H + HCl

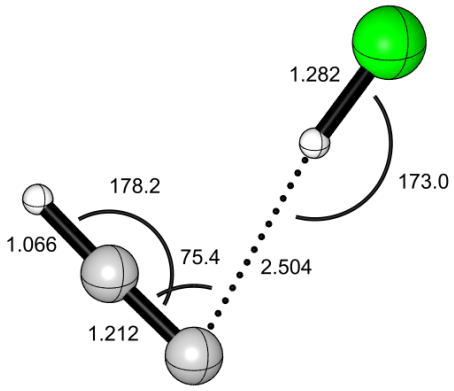

Level of Theory:

Reference:	ROHF
Geometry:	CCSD(T)-F12a/aug-cc-pVTZ-F12
Frequencies:	CCSD(T)-F12a/aug-cc-pVTZ-F12
Program:	MOLPRO 2010.1

Wavefunction Diagnostics:

T_1: 0.013

D_1: 0.030

Figure S8: PRC8 (C_2H + HCl)

Cartesian Coordinates (Å):

C	-0.6657830137	0.0000000000	-2.1962436174
C	0.5451441120	0.0000000000	-2.1515645962
H	1.6083700566	0.0000000000	-2.0792902224
H	-0.1231791209	0.0000000000	0.2487395945
Cl	-0.0013536091	0.0000000000	1.5250221322

Rotational Constants (GHz): 2.522, 2.385, 43.884

Harmonic Vibrational Frequencies (cm^{-1}):

a':	3432	2920	2011	449	265	88	74
a'':						369	228

Incremental Focal Point Analysis Table (kcal mol^{-1}):

Basis	ROHF	+δMP2	+δCCSD	+δ(T)	+δT	+δ(Q)	Net
aug-cc-pVDZ	-0.62	-2.44	+0.69	-0.36	+0.02	-0.03	[-2.75]
aug-cc-pVTZ	-0.51	-2.50	+0.81	-0.37	[+0.02]	[-0.03]	[-2.59]
aug-cc-pVQZ	-0.45	-2.44	+0.83	-0.38	[+0.02]	[-0.03]	[-2.45]
aug-cc-pV5Z	-0.43	-2.42	+0.83	-0.38	[+0.02]	[-0.03]	[-2.41]
CBS LIMIT	[-0.43]	[-2.39]	[+0.84]	[-0.38]	[+0.02]	[-0.03]	[-2.38]

D.3 Transition States

$C_2H + H_2$

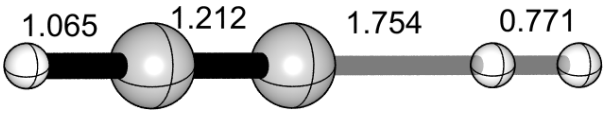

Figure S9: TS1 (C_2H+H_2→C_2H_2+H)

Level of Theory:

Reference:	ROHF
Geometry:	CCSD(T)-F12a/aug-cc-pVTZ-F12
Frequencies:	CCSD(T)-F12a/aug-cc-pVTZ-F12
Program:	MOLPRO 2010.1

Wavefunction Diagnostics:

T_1: 0.018

D_1: 0.049

Cartesian Coordinates (Å):

C	0.0000000000	0.0000000000	-0.4635470464
C	0.0000000000	0.0000000000	0.7482216866
H	0.0000000000	0.0000000000	1.8128562939
H	0.0000000000	0.0000000000	-2.2171512458
H	0.0000000000	0.0000000000	-2.9879973506

Rotational Constants (GHz): 19.020, 19.020

Harmonic Vibrational Frequencies (cm^{-1}):

σ^+:	3628	3441	2007	506i
π :		515	384	58

Incremental Focal Point Analysis Table (kcal mol^{-1}):

Basis	ROHF	+δMP2	+δCCSD	+δ(T)	+δT	+δ(Q)	Net
aug-cc-pVDZ	+8.93	-6.85	+0.49	-0.69	-0.02	-0.04	[+1.83]
aug-cc-pVTZ	+9.43	-7.11	+0.56	-0.81	[-0.02]	[-0.04]	[+2.02]
aug-cc-pVQZ	+9.53	-7.18	+0.60	-0.84	[-0.02]	[-0.04]	[+2.05]
aug-cc-pV5Z	+9.54	-7.18	+0.61	-0.84	[-0.02]	[-0.04]	[+2.07]
CBS LIMIT	[+9.54]	[-7.18]	[+0.62]	[-0.85]	[-0.02]	[-0.04]	[+2.08]

$C_2H + CH_4$

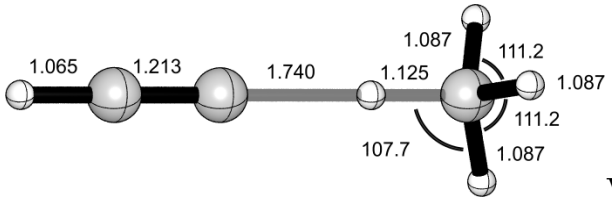

Figure S10: TS2 (C_2H+CH_4→C_2H_2+CH_3)

Level of Theory:

Reference:	ROHF
Geometry:	CCSD(T)-F12a/aug-cc-pVTZ-F12
Frequencies:	CCSD(T)-F12a/aug-cc-pVTZ
Program:	MOLPRO 2010.1

Wavefunction Diagnostics:

T_1: 0.018

D_1: 0.054

Cartesian Coordinates (Å):

C	0.0000000000	0.0000000000	-1.9179929079
C	0.0000000000	0.0000000000	-0.7052659365
H	0.0000000000	0.0000000000	-2.9826643985
H	0.0000000000	0.0000000000	1.0345984353
C	0.0000000000	0.0000000000	2.1599004103
H	1.0355660772	0.0000000000	2.4898743180
H	-0.5177830389	0.8968265300	2.4845825455
H	-0.5177830389	-0.8968265300	2.4845825455

Rotational Constants (GHz): 3.700, 3.700, 155.850

Harmonic Vibrational Frequencies (cm^{-1}):

a_1:	3440	3068	2294	1990	1278	$201i$
e:	3177	1506	1299	527	191	41

Incremental Focal Point Analysis Table (kcal mol^{-1}):

Basis	ROHF	+δMP2	+δCCSD	+δ(T)	+δT	+δ(Q)	Net
aug-cc-pVDZ	+9.65	-9.10	+1.25	-1.16	-0.16	-0.10	[+0.37]
aug-cc-pVTZ	+10.17	-9.28	+1.37	-1.30	[-0.16]	[-0.10]	[+0.69]
aug-cc-pVQZ	+10.31	-9.27	+1.43	-1.33	[-0.16]	[-0.10]	[+0.87]
aug-cc-pV5Z	+10.33	-9.22	+1.44	-1.33	[-0.16]	[-0.10]	[+0.94]
CBS LIMIT	[+10.34]	[-9.17]	[+1.45]	[-1.34]	[-0.16]	[-0.10]	[+1.00]

$C_2H + NH_3$

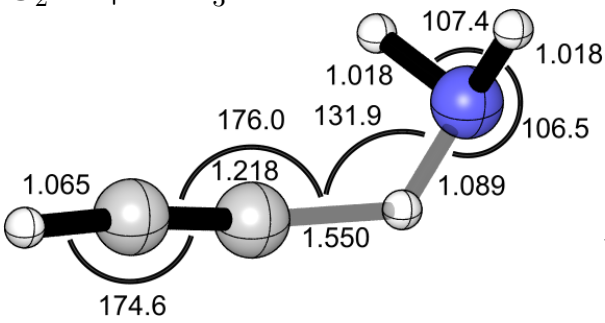

Figure S11: TS3 (C_2H+NH_3→C_2H_2+NH_2)

Level of Theory:

Reference: ROHF
Geometry: CCSD(T)-F12a/aug-cc-pVTZ-F12
Frequencies: CCSD(T)-F12a/aug-cc-pVTZ-F12
Program: Molpro 2010.1

Wavefunction Diagnostics:

T_1: 0.025
D_1: 0.089

Cartesian Coordinates (Å):

C	-0.2365787439	0.0000000000	0.5640080139
C	0.1316873338	0.0000000000	1.7253846135
H	0.3564224220	0.0000000000	2.7668237887
H	-0.5995958541	0.0000000000	-0.9427501443
N	0.0185454664	0.0000000000	-1.8387330599
H	0.6176926068	-0.8201266598	-1.7768266399
H	0.6176926068	0.8201266598	-1.7768266399

Rotational Constants (GHz): 4.894, 4.857, 144.361

Harmonic Vibrational Frequencies (cm^{-1}):

a':	3472	3430	2258	1955	1609	891	613	342	90	$757i$
a'':						3569	1504	608	505	106

Incremental Focal Point Analysis Table (kcal mol^{-1}):

Basis	ROHF	+δMP2	+δCCSD	+δ(T)	+δT	+δ(Q)	Net
aug-cc-pVDZ	+17.05	-22.67	+5.79	-2.86	+0.19	-0.33	[-2.84]
aug-cc-pVTZ	+17.89	-22.39	+6.06	-3.19	[+0.19]	[-0.33]	[-2.78]
aug-cc-pVQZ	+18.08	-23.43	+6.19	-3.28	[+0.19]	[-0.33]	[-2.58]
aug-cc-pV5Z	+18.12	023.39	+6.23	-3.30	[+0.19]	[-0.33]	[-2.49]
CBS LIMIT	[+18.13]	[-23.36]	[+6.26]	[-3.32]	[+0.19]	[-0.33]	[-2.43]

$C_2H + H_2O$

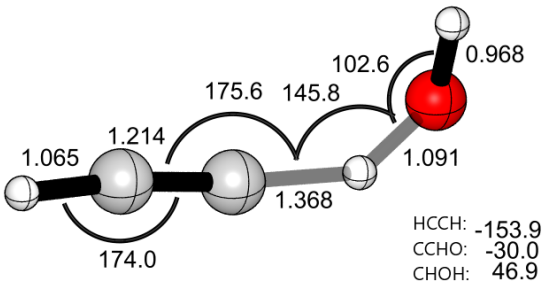

Level of Theory:

Reference:	ROHF
Geometry:	CCSD(T)-F12a/aug-cc-pVTZ-F12
Frequencies:	CCSD(T)-F12a/aug-cc-pVTZ-F12
Program:	MOLPRO 2010.1

Wavefunction Diagnostics:

T_1: 0.025

D_1: 0.081

Figure S12: TS4 (C_2H+H_2O→C_2H_2+OH)

Cartesian Coordinates (Å):

C	0.0561015586	-0.1787746287	0.5742144336
C	-0.0340447634	0.1000290208	1.7518699946
H	0.1641580109	-0.3896898916	-0.7730527736
O	-0.0393366736	0.0100536031	-1.7675780044
H	0.2674769900	0.9249635384	-1.6946923524
H	-0.0700668433	0.2435047315	2.8066417427

Rotational Constants (GHz): 4.867, 4.934, 286.890

Harmonic Vibrational Frequencies (cm^{-1}):

a:	3778	3436	2032	1621	1140	617
	596	547	329	146	104	1441i

Incremental Focal Point Analysis Table (kcal mol^{-1}):

Basis	ROHF	+δMP2	+δCCSD	+δ(T)	+δT	+δ(Q)	Net
aug-cc-pVDZ	+24.44	-21.00	+4.47	-2.84	+0.23	-0.39	[+4.92]
aug-cc-pVTZ	+24.78	-21.39	+4.43	-3.09	[+0.23]	[-0.39]	[+4.58]
aug-cc-pVQZ	+25.07	-21.26	+4.59	-3.15	[+0.23]	[-0.39]	[+5.09]
aug-cc-pV5Z	+25.12	-21.13	+4.61	-3.16	[+0.23]	[-0.39]	[+5.28]
CBS LIMIT	[+25.13]	[-20.98]	[+4.62]	[-3.18]	[+0.23]	[-0.39]	[+5.44]

$C_2H + HF$

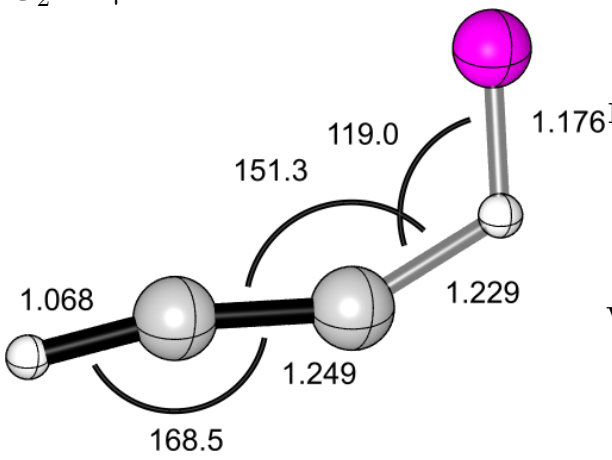

Level of Theory:

Reference:	ROHF
Geometry:	CCSD(T)-F12a/aug-cc-pVTZ-F12
Frequencies:	CCSD(T)-F12a/aug-cc-pVTZ-F12
Program:	MOLPRO 2010.1

Wavefunction Diagnostics:

T_1: 0.083

D_1: 0.334

Figure S13: TS5 (C_2H+HF→C_2H_2+F)

Cartesian Coordinates (Å):

C	-0.5191116660	0.0000000000	0.5550499938
C	0.2777936073	0.0000000000	1.5170068820
H	-0.7517375553	0.0000000000	-0.6518291037
F	0.1509643851	0.0000000000	-1.4058077563
H	0.7818871447	0.0000000000	2.4581143583

Rotational Constants (GHz): 6.702, 6.225, 87.400

Harmonic Vibrational Frequencies (cm^{-1}):

a':	3405	2078	1720	693	486	169	1532i
a'':						722	588

Incremental Focal Point Analysis Table (kcal mol^{-1}):

Basis	ROHF	+δMP2	+δCCSD	+δ(T)	+δT	+δ(Q)	Net
aug-cc-pVDZ	+28.05	-6.02	-5.76	-3.29	-0.79	+0.37	[+12.57]
aug-cc-pVTZ	+29.77	-6.67	-5.30	-3.93	[-0.79]	[+0.37]	[+13.46]
aug-cc-pVQZ	+30.21	-6.64	-4.95	-4.05	[-0.79]	[+0.37]	[+14.15]
aug-cc-pV5Z	+30.30	-6.57	-4.84	-4.10	[-0.79]	[+0.37]	[+14.37]
CBS LIMIT	[+30.32]	[-6.50]	[-4.72]	[-4.14]	[-0.79]	[+0.37]	[+14.53]

$C_2H + PH_3$

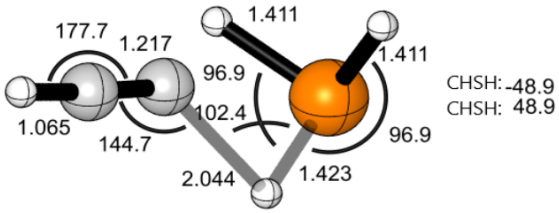

Figure S14: TS6 (C_2H+PH_3→C_2H_2+PH_2)

Level of Theory:

Reference:	ROHF
Geometry:	CCSD(T)-F12a/aug-cc-pVTZ-F12
Frequencies:	CCSD(T)-F12a/aug-cc-pVTZ-F12
Program:	MOLPRO 2010.1

Wavefunction Diagnostics:

T_1: 0.032

D_1: 0.116

Cartesian Coordinates (Å):

C	0.0000000000	0.0468785119	1.2503752792
C	0.0000000000	-0.0231015197	2.4658398083
H	0.0000000000	-0.0411522198	3.5308913204
H	0.0000000000	-1.0384143889	-0.4820823998
P	0.0000000000	-0.0224939976	-1.4791438224
H	1.0548949468	0.7437330581	-0.9394557809
H	-1.0548949468	0.7437330581	-0.9394557809

Rotational Constants (GHz): 2.865, 2.865, 112.422

Harmonic Vibrational Frequencies (cm^{-1}):

a':	3432	2443	2348	1977	1113	852	569	167	64	248i
a'':						2456	1105	566	263	54

Incremental Focal Point Analysis Table (kcal mol^{-1}):

Basis	ROHF	+δMP2	+δCCSD	+δ(T)	+δT	+δ(Q)	Net
aug-cc-pVDZ	+9.64	-13.04	+1.81	-2.09	-0.05	-0.20	[-3.93]
aug-cc-pVTZ	+10.06	-13.52	+2.01	-2.33	[-0.05]	[-0.20]	[-4.04]
aug-cc-pVQZ	+10.15	-13.55	+2.05	-2.39	[-0.05]	[-0.20]	[-3.99]
aug-cc-pV5Z	+10.17	-13.54	+2.05	-2.40	[-0.05]	[-0.20]	[-3.97]
CBS LIMIT	[+10.18]	[-13.52]	[+2.05]	[-2.42]	[-0.05]	[-0.20]	[-3.97]

$C_2H + H_2S$

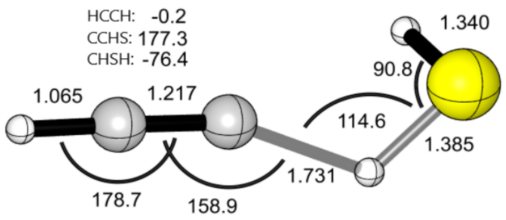

Figure S15: TS7 (C_2H+H_2S→C_2H_2+SH)

Level of Theory:

Reference: ROHF
Geometry: CCSD(T)-F12a/aug-cc-pVTZ-F12
Frequencies: CCSD(T)-F12a/aug-cc-pVTZ-F12
Program: Molpro 2010.1

Wavefunction Diagnostics:

T_1: 0.032
D_1: 0.114

Cartesian Coordinates (Å):

C	0.0446379089	-0.0256863831	-2.4196819237
C	-0.0543683046	0.0449837814	-1.2084455293
H	0.1088182887	-0.0794118069	-3.4817266782
H	-0.7696687829	0.3519939597	0.3380970261
S	0.0317478019	0.0243745438	1.4189968945
H	-0.2330149590	-1.2778294155	1.2431181136

Rotational Constants (GHz): 3.006, 3.025, 195.593

Harmonic Vibrational Frequencies (cm^{-1}):

a:	3431	2715	2215	1970	1142	594
	586	387	200	53	41	855i

Incremental Focal Point Analysis Table (kcal mol^{-1}):

Basis	ROHF	+δMP2	+δCCSD	+δ(T)	+δT	+δ(Q)	Net
aug-cc-pVDZ	+14.65	-17.41	+2.67	-2.60	-0.03	-0.28	[-2.99]
aug-cc-pVTZ	+15.11	-18.03	+3.19	-2.87	[-0.03]	[-0.28]	[-2.91]
aug-cc-pVQZ	+15.25	-18.12	+3.39	-2.94	[-0.03]	[-0.28]	[-2.74]
aug-cc-pV5Z	+15.28	-18.11	+3.43	-2.96	[-0.03]	[-0.28]	[-2.68]
CBS LIMIT	[+15.29]	[-18.10]	[+3.47]	[-2.98]	[-0.03]	[-0.28]	[-2.64]

$C_2H + HCl$

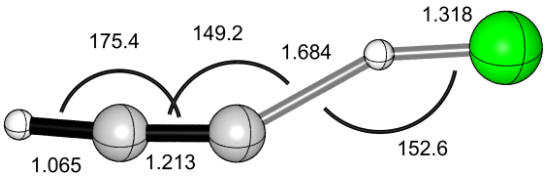

Figure S16: TS8 (C_2H+HCl→C_2H_2+Cl)

Level of Theory:

Reference:	ROHF
Geometry:	CCSD(T)-F12a/aug-cc-pVTZ-F12
Frequencies:	CCSD(T)-F12a/aug-cc-pVTZ-F12
Program:	MOLPRO 2010.1

Wavefunction Diagnostics:

T_1: 0.019

D_1: 0.057

Cartesian Coordinates (Å):

C	0.0000000000	-0.2073715936	1.4389355314
C	0.0000000000	0.0944259246	2.6135066953
H	0.0000000000	0.2687774933	-0.1764054515
Cl	0.0000000000	0.0180778498	-1.4708364061
H	0.0000000000	0.4412612203	3.6207369783

Rotational Constants (GHz): 2.556, 2.567, 558.886

Harmonic Vibrational Frequencies (cm^{-1}):

a':	3435	2179	1973	457	150	49	378i
a'':						431	44

Incremental Focal Point Analysis Table (kcal mol^{-1}):

Basis	ROHF	+δMP2	+δCCSD	+δ(T)	+δT	+δ(Q)	Net
aug-cc-pVDZ	+10.66	-9.78	+1.96	-1.39	-0.04	-0.14	[+1.27]
aug-cc-pVTZ	+11.04	-10.10	+2.22	-1.57	[-0.04]	[-0.14]	[+1.40]
aug-cc-pVQZ	+11.14	-10.11	+2.36	-1.60	[-0.04]	[-0.14]	[+1.61]
aug-cc-pV5Z	+11.16	-10.08	+2.40	-1.61	[-0.04]	[-0.14]	[+1.69]
CBS LIMIT	[+11.17]	[-10.05]	[+2.44]	[-1.62]	[-0.04]	[-0.14]	[+1.76]

C_2H + HCN

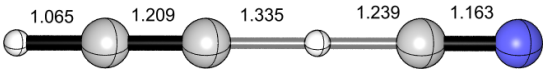

Figure S17: TS9 (C_2H+HCN→C_2H_2+CN)

Level of Theory:

Reference:	ROHF
Geometry:	CCSD(T)-F12a/aug-cc-pVTZ-F12
Frequencies:	CCSD(T)-F12a/aug-cc-pVTZ-F12
Program:	MOLPRO 2010.1

Wavefunction Diagnostics:

T_1: 0.024

D_1: 0.084

Cartesian Coordinates (Å):

C	0.0000000000	0.0000000000	1.3022638885
C	0.0000000000	0.0000000000	2.5114774244
H	0.0000000000	0.0000000000	3.5766391474
H	0.0000000000	0.0000000000	-0.0326747958
C	0.0000000000	0.0000000000	-1.2716140551
N	0.0000000000	0.0000000000	-2.4349485548

Rotational Constants (GHz): 2.390, 2.390

Harmonic Vibrational Frequencies (cm^{-1}):

σ^+:	3439	2208	2047	449	1667i
π:		749	581	195	50

Incremental Focal Point Analysis Table (kcal mol^{-1}):

Basis	ROHF	+δMP2	+δCCSD	+δ(T)	+δT	+δ(Q)	Net
aug-cc-pVDZ	+30.80	-22.27	+3.74	-2.80	+0.12	-0.30	[+9.29]
aug-cc-pVTZ	+31.78	-22.36	+4.24	-3.10	[+0.12]	[-0.30]	[+10.39]
aug-cc-pVQZ	+32.03	-22.17	+4.44	-3.15	[+0.12]	[-0.30]	[+10.97]
aug-cc-pV5Z	+32.06	-22.03	+4.47	-3.16	[+0.12]	[-0.30]	[+11.17]
CBS LIMIT	[+32.06]	[-21.88]	[+4.51]	[-3.17]	[+0.12]	[-0.30]	[+11.34]

C_2H + HNC

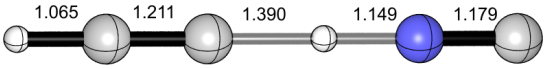

Figure S18: TS10 (C_2H+HNC→C_2H_2+CN)

Level of Theory:

Reference:	ROHF
Geometry:	CCSD(T)-F12a/aug-cc-pVTZ-F12
Frequencies:	CCSD(T)-F12a/aug-cc-pVTZ-F12
Program:	MOLPRO 2010.1

Wavefunction Diagnostics:

T_1: 0.069

D_1: 0.289

Cartesian Coordinates (Å):

C	0.0000000000	0.0000000000	1.2443286139
C	0.0000000000	0.0000000000	2.4552116550
H	0.0000000000	0.0000000000	3.5206050460
H	0.0000000000	0.0000000000	-0.1456733816
N	0.0000000000	0.0000000000	-1.2944670782
C	0.0000000000	0.0000000000	-2.4732074572

Rotational Constants (GHz): 2.521, 2.521

Harmonic Vibrational Frequencies (cm^{-1}):

σ^+:	3435	2104	2026	442	2495i
π:		701	329	146	25

Incremental Focal Point Analysis Table (kcal mol^{-1}):

Basis	ROHF	+δMP2	+δCCSD	+δ(T)	+δT	+δ(Q)	Net
aug-cc-pVDZ	+54.02	-52.77	+13.87	-6.38	-0.02	-0.70	[+8.02]
aug-cc-pVTZ	+55.62	-53.44	+14.73	-7.17	[-0.02]	[-0.70]	[+9.02]
aug-cc-pVQZ	+56.03	-53.37	+15.13	-7.35	[-0.02]	[-0.70]	[+9.72]
aug-cc-pV5Z	+56.10	-53.26	+15.20	-7.40	[-0.02]	[-0.70]	[+9.91]
CBS LIMIT	[+56.10]	[-53.15]	[+15.28]	[-7.45]	[-0.02]	[-0.70]	[+10.05]

$C_2H + C_2H_2$

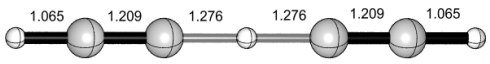

Figure S19: TS11 ($C_2H+C_2H_2 \rightarrow C_2H_2+C_2H$)

Level of Theory:

Reference:	ROHF
Geometry:	CCSD(T)-F12a/aug-cc-pVTZ-F12
Frequencies:	CCSD(T)-F12a/aug-cc-pVTZ-F12
Program:	MOLPRO 2010.1

Wavefunction Diagnostics:

T_1: 0.014

D_1: 0.029

Cartesian Coordinates (Å):

H	0.0000000000	0.0000000000	0.0000000000
C	0.0000000000	0.0000000000	1.2759501666
C	0.0000000000	0.0000000000	-1.2759501666
C	0.0000000000	0.0000000000	2.4853601979
C	0.0000000000	0.0000000000	-2.4853601979
H	0.0000000000	0.0000000000	3.5499434381
H	0.0000000000	0.0000000000	-3.5499434381

Rotational Constants (GHz): 2.374, 2.374

Harmonic Vibrational Frequencies (cm^{-1}):

σ_g^+:	3444	2090	445	$1511i$
π_g:			940	64
σ_u^+:			3443	2034
π_u:		930	743	171

Incremental Focal Point Analysis Table (kcal mol^{-1}):

Basis	ROHF	+δMP2	+δCCSD	+δ(T)	+δT	+δ(Q)	Net
aug-cc-pVDZ	+31.08	-23.70	+5.47	-2.46	+0.26	-0.30	[+10.34]
aug-cc-pVTZ	+32.23	-23.92	+6.02	-2.74	[+0.26]	[-0.30]	[+11.55]
aug-cc-pVQZ	+32.49	-23.72	+6.21	-2.78	[+0.26]	[-0.30]	[+12.16]
aug-cc-pV5Z	+32.52	-23.59	+6.23	-2.78	[+0.26]	[-0.30]	[+12.33]
CBS LIMIT	[+32.52]	[-23.46]	[+6.26]	[-2.79]	[+0.26]	[-0.30]	[+12.49]

D.4 Post-Reactive Complexes

C_2H_2 + NH_2

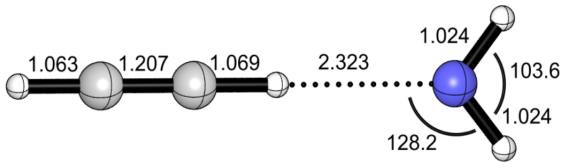

Figure S20: PoRC1 (C_2H_2 + NH_2)

Level of Theory:

Reference: ROHF
Geometry: CCSD(T)-F12a/aug-cc-pVTZ-F12
Frequencies: CCSD(T)-F12a/aug-cc-pVTZ-F12
Program: Molpro 2010.1

Wavefunction Diagnostics:

T_1: 0.012
D_1: 0.029

Cartesian Coordinates (Å):

C	0.0000000000	0.0000000000	0.9489279365
C	0.0000000000	0.0000000000	2.1564020569
H	0.0000000000	0.0000000000	3.2195479044
H	0.0000000000	0.0000000000	-0.1205370739
N	0.0000000000	0.0000000000	-2.4430873658
H	0.0000000000	0.8049349657	-3.0766433123
H	0.0000000000	-0.8049349657	-3.0766433123

Rotational Constants (GHz): 2.790, 2.811, 386.929

Harmonic Vibrational Frequencies (cm^{-1}):

a_1:	3477	3385	3353	1992	1543	118
b_1:			809	638	227	74
b_2:		3482	813	640	174	62

Incremental Focal Point Analysis Table (kcal mol^{-1}):

Basis	ROHF	+δMP2	+δCCSD	+δ(T)	+δT	+δ(Q)	Net
aug-cc-pVDZ	-35.17	+6.75	-0.48	+0.39	+0.15	+0.10	[-27.27]
aug-cc-pVTZ	-34.02	+6.57	-0.92	+0.61	[+0.15]	[+0.10]	[-27.52]
aug-cc-pVQZ	-33.76	+6.82	-0.90	+0.64	[+0.15]	[+0.10]	[-26.94]
aug-cc-pV5Z	-33.73	+6.90	-0.91	+0.66	[+0.15]	[+0.10]	[-26.82]
CBS LIMIT	[-33.73]	[+6.99]	[-0.92]	[+0.67]	[+0.15]	[+0.10]	[-26.74]

$C_2H_2 + PH_2$

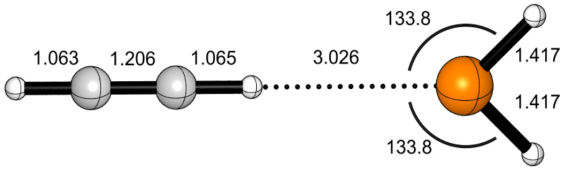

Figure S21: PoRC2 (C_2H_2 + PH_2)

Level of Theory:

Reference: ROHF
Geometry: CCSD(T)-F12a/aug-cc-pVTZ-F12
Frequencies: CCSD(T)-F12a/aug-cc-pVTZ-F12
Program: Molpro 2010.1

Wavefunction Diagnostics:

T_1: 0.013
D_1: 0.029

Cartesian Coordinates (Å):

C	0.0000000000	0.0000000000	2.0538258200
C	0.0000000000	0.0000000000	3.2602823330
H	0.0000000000	0.0000000000	4.3235457214
H	0.0000000000	0.0000000000	0.9887891288
P	0.0000000000	0.0000000000	-2.0371895494
H	0.0000000000	1.0237658865	-3.0174651461
H	0.0000000000	-1.0237658865	-3.0174651461

Rotational Constants (GHz): 1.456, 1.465, 239.194

Harmonic Vibrational Frequencies (cm^{-1}):

a_1:	3491	3395	2405	2000	1122	48
b_1:		2414	757	623	71	34
b_2:		761	626	623	98	33

Incremental Focal Point Analysis Table (kcal mol^{-1}):

Basis	ROHF	+δMP2	+δCCSD	+δ(T)	+δT	+δ(Q)	Net
aug-cc-pVDZ	-50.98	-4.69	+4.00	+0.05	+0.23	+0.04	[-51.35]
aug-cc-pVTZ	-51.36	-5.43	+3.67	-0.00	[+0.23]	[+0.04]	[-52.85]
aug-cc-pVQZ	-51.10	-5.40	+3.76	+0.00	[+0.23]	[+0.04]	[-52.46]
aug-cc-pV5Z	-51.07	-5.42	+3.78	+0.01	[+0.23]	[+0.04]	[-52.42]
CBS LIMIT	[-51.07]	[-5.43]	[+3.80]	[+0.01]	[+0.23]	[+0.04]	[-52.42]

Bibliography

[1] E. Schrödinger, Phys. Rev. **28** (6), 1049 (1926).

[2] M. Born and R. Oppenheimer, Ann. Phys. **389** (20), 457–484 (1927).

[3] J.C. Tully, Theor. Chem. Acc. **103** (3-4), 173–176 (2000).

[4] W. Pauli, Z. Phys. **31** (1), 765–783 (1925).

[5] J.C. Slater, Phys. Rev. **34** (10), 1293 (1929).

[6] C.C.J. Roothaan, Rev. Mod. Phys. **23** (2), 69 (1951).

[7] J. Pople and R. Nesbet, J. Chem. Phys. **22** (3), 571–572 (1954).

[8] C. Roothaan, Rev. Mod. Phys. **32** (2), 179 (1960).

[9] G.A. Segal, J. Chem. Phys. **52** (7), 3530–3533 (1970).

[10] S.F. Boys, Proc. R. Soc. Lon. Ser-A **200** (1063), 542–554 (1950).

[11] R.C. Raffenetti, J. Chem. Phys. **58** (10), 4452–4458 (1973).

[12] T.H. Dunning Jr, J. Chem. Phys. **90** (2), 1007–1023 (1989).

[13] R.A. Kendall, T.H. Dunning Jr and R.J. Harrison, J. Chem. Phys. **96** (9), 6796–6806 (1992).

[14] J. Čížek, J. Chem. Phys. **45** (11), 4256–4266 (1966).

[15] G.D. Purvis III and R.J. Bartlett, J. Chem. Phys. **76** (4), 1910–1918 (1982).

[16] K. Raghavachari, G.W. Trucks, J.A. Pople and M. Head-Gordon, Chem. Phys. Lett. **157** (6), 479–483 (1989).

[17] T.J. Lee, M. Head-Gordon and A.P. Rendell, Chem. Phys. Lett. **243** (5-6), 402–408 (1995).

[18] J.C. Rienstra-Kiracofe, W.D. Allen and H.F. Schaefer, J. Phys. Chem. A **104** (44), 9823–9840 (2000).

[19] G. Das and A.C. Wahl, J. Chem. Phys. **44** (1), 87–96 (1966).

[20] R.J. Buenker, S.D. Peyerimhoff and W. Butscher, Mol. Phys. **35** (3), 771–791 (1978).

[21] D. Feller, J. Chem. Phys. **96** (8), 6104–6114 (1992).

[22] T. Helgaker, W. Klopper, H. Koch and J. Noga, J. Chem. Phys. **106** (23), 9639–9646 (1997).

[23] M.S. Schuurman, S.R. Muir, W.D. Allen and H.F. Schaefer, J. Chem. Phys. **120** (24), 11586–11599 (2004).

[24] J.M. Gonzales, C. Pak, R.S. Cox, W.D. Allen, H.F. Schaefer, A.G. Császár and G. Tarczay, Chem. Eur. J. **9** (10), 2173–2192 (2003).

[25] A.G. Csaszar, W.D. Allen and H.F. Schaefer, J. Chem. Phys. **108** (23), 9751–9764 (1998).

[26] A.L. East and W.D. Allen, J. Chem. Phys. **99** (6), 4638–4650 (1993).

[27] S. Stopkowicz and J. Gauss, J. Chem. Phys. **129** (16), 164119 (2008).

[28] L. Cheng and J. Gauss, J. Chem. Phys. **135** (8), 084114 (2011).

[29] H. Sellers and P. Pulay, Chem. Phys. Lett. **103** (6), 463–465 (1984).

[30] N.C. Handy, Y. Yamaguchi and H.F. Schaefer, J. Chem. Phys. **84** (8), 4481–4484 (1986).

[31] D.G. Truhlar, B.C. Garrett and S.J. Klippenstein, J. Phys. Chem. **100** (31), 12771–12800 (1996).

[32] H. Eyring, J. Chem. Phys. **3** (2), 107–115 (1935).

[33] C.J. Cramer, *Essentials of Computational Chemistry: Theories and Models* (, , 2013).

[34] E. Wigner, Z. Phys. Chem. **19** (1), 203–216 (1932).

[35] C. Eckart, Phys. Rev. **35** (11), 1303 (1930).

[36] H.S. Johnston and J. Heicklen, J. Phys. Chem. **66** (3), 532–533 (1962).

[37] R.T. Skodje, D.G. Truhlar and B.C. Garrett, J. Phys. Chem. **85** (21), 3019–3023 (1981).

[38] D.G. Truhlar and B.C. Garrett, Acc. Chem. Res. **13** (12), 440–448 (1980).

[39] D.G. Truhlar and B.C. Garrett, Annu. Rev. Phys. Chem. **35** (1), 159–189 (1984).

[40] T. Janes, Y. Yang and D. Song, Chem. Comm. **53** (83), 11390–11398 (2017).

[41] L. Capone, R. Whitten, J. Dubach, S. Prasad and W. Huntress, Icarus **28** (3), 367–378 (1976).

[42] W. Borucki, Z. Levin, R. Whitten, R. Keesee, L. Capone, A. Summers, O. Toon and J. Dubach, Icarus **72** (3), 604–622 (1987).

[43] A. Coates, F. Crary, G. Lewis, D. Young, J. Waite and E. Sittler, Geophys. Res. Lett. **34** (22) (2007).

[44] V. Vuitton, P. Lavvas, R. Yelle, M. Galand, A. Wellbrock, G. Lewis, A. Coates and J.E. Wahlund, Planet Space Sci. **57** (13), 1558–1572 (2009).

[45] A. Ali, E. Sittler, D. Chornay, B. Rowe and C. Puzzarini, Planet Space Sci. **109**, 46–63 (2015).

[46] C.E. Dykstra, M. Hereld, R.R. Lucchese, H.F. Schaefer and W. Meyer, J. Chem. Phys. **67** (9), 4071–4075 (1977).

[47] G. Surratt and W. Goddard, Chem. Phys. **23** (1), 39–50 (1977).

[48] G.B. Ellison, P. Engelking and W. Lineberger, J. Am. Chem. Soc. **100** (8), 2556–2558 (1978).

[49] A.M. Oliveira, Y.J. Lu, J.H. Lehman, P.B. Changala, J.H. Baraban, J.F. Stanton and W.C. Lineberger, J. Am. Chem. Soc. **137** (40), 12939–12945 (2015).

[50] S.E. Mitchell, P.M. Conklin and J.W. Farley, J. Chem. Phys. **118** (24), 11017–11025 (2003).

[51] R.R. Squires, Acc. Chem. Res. **25** (10), 461–467 (1992).

[52] C.H. DePuy, S. Gronert, S.E. Barlow, V.M. Bierbaum and R. Damrauer, J. Am. Chem. Soc. **111** (6), 1968–1973 (1989).

[53] N. Tymińska, M. Włoch and A.T. Royappa, Int. J. Quant. Chem. **115** (1), 42–49 (2015).

[54] Z. Tian, B. Chan, M.B. Sullivan, L. Radom and S.R. Kass, Proc. Natl. Acad. Sci. U.S.A. **105** (22), 7647–7651 (2008).

[55] B.L. Poad, N.D. Reed, C.S. Hansen, A.J. Trevitt, S.J. Blanksby, E.G. Mackay, M.S. Sherburn, B. Chan and L. Radom, Chem. Sci. **7** (9), 6245–6250 (2016).

[56] F. Driessler, R. Ahlrichs, V. Staemmler and W. Kutzelnigg, Theor. Chem. Acc. **30** (4), 315–326 (1973).

[57] D.S. Marynick and D.A. Dixon, Proc. Natl. Acad. Sci. U.S.A. **74** (2), 410–413 (1977).

[58] W. Kraemer, V. Špirko, P.A. Malmqvist and B. Roos, J. Mol. Spec. **147** (2), 526–540 (1991).

[59] R. Kari and I. Csizmadia, J. Chem. Phys. **46** (12), 4585–4590 (1967).

[60] R. Kari and I. Csizmadia, J. Chem. Phys. **50** (3), 1443–1448 (1969).

[61] A. Duke, Chem. Phys. Lett. **21** (2), 275–282 (1973).

[62] P.R. Peoples and J.B. Grutzner, J. Am. Chem. Soc. **102** (14), 4709–4715 (1980).

[63] T. Rajamäki, A. Miani and L. Halonen, J. Chem. Phys. **118** (24), 10929–10938 (2003).

[64] D.A. Dixon, D. Feller and K.A. Peterson, J. Phys. Chem. A **101** (49), 9405–9409 (1997).

[65] M. Ragni, A.C.P. Bitencourt, F.V. Prudente, P.R. Barreto and T. Posati, Eur. Phys. J. D **70**, 60 (2016).

[66] D. Feller, J. Chem. Phys. **144** (1), 014105 (2016).

[67] G.S. Tschumper and H.F. Schaefer, J. Chem. Phys. **107** (7), 2529–2541 (1997).

[68] R.A. Kendall, T.H. Dunning Jr and R.J. Harrison, J. Chem. Phys. **96** (9), 6796–6806 (1992).

[69] T.J. Lee and H.F. Schaefer, J. Chem. Phys. **83** (4), 1784–1794 (1985).

[70] H.J. Werner, P.J. Knowles, G. Knizia, F.R.M. amd M. Schutz, P. Celani, T. Korona, R. Lindh, A. Mitrushenkov, G. Rauhut, K.R. Shamasundar, T.B. Adler, R.D. Amos, A. Bernhardsson, A. Berning, D.L. Cooper, M.J.O. Deegan, A.J. Dobbyn, F. Eckert, E. Goll, C. Hampel, A. Hesselmann, G. Hetzer, T. Hre-nar, G. Jansen, C. Koppl, Y. Liu, A.W. Lloyd, R.A. Mata, A.J. May, S.J. McNicholas, W. Meyer, M.E. Mura, A. Nicklass, D.P. O'Neill, P. Palmieri, K. Pfluger, R. Pitzer, M. Reiher, T. Shiozaki, H. Stoll, A.J. Stone, R. Tarroni, T. Thorsteinsson, M. Wang, and A. Wolf, MOLPRO, version 2010.1, a package of ab initio programs 2010.

[71] T.H. Dunning Jr, J. Chem. Phys. **90** (2), 1007–1023 (1989).

[72] A.K. Wilson, T. van Mourik and T.H. Dunning, J. Mol. Spec. **388**, 339–349 (1996).

[73] D.E. Woon and T.H. Dunning Jr, J. Chem. Phys. **100** (4), 2975–2988 (1994).

[74] D. Feller, J. Chem. Phys. **96** (8), 6104–6114 (1992).

[75] T. Helgaker, W. Klopper, H. Koch and J. Noga, J. Chem. Phys. **106** (23), 9639–9646 (1997).

[76] J. Okuda, D. Mukherjee and D. Schuhknecht, Angew. Chem. Int. Ed. **57** (31), 9590–9602 (2018).

[77] S. Harder and J. Brettar, Angew. Chem. Int. Ed. **118** (21), 3554–3558 (2006).

[78] A. Causero, G. Ballmann, J. Pahl, C. Färber, J. Intemann and S. Harder, Dalton Trans. **46** (6), 1822–1831 (2017).

[79] A.S. Wilson, C. Dinoi, M.S. Hill, M.F. Mahon and L. Maron, Angew. Chem. Int. Ed. **57** (47), 15500–15504 (2018).

[80] X. Shi, G. Qin, Y. Wang, L. Zhao, Z. Liu and J. Cheng, Angew. Chem. Int. Ed. (2019).

[81] S. Harder and J. Spielmann, J. Organomet. Chem. **698**, 7–14 (2012).

[82] S. Yadav, R. Dixit, M.K. Bisai, K. Vanka and S.S. Sen, Organometallics **37** (24), 4576–4584 (2018).

[83] J. Spielmann and S. Harder, Eur. J. Inorg. Chem. **2008** (9), 1480–1486 (2008).

[84] J.H. Lim, J.H. Shim, Y.S. Lee, J.Y. Suh, Y.W. Cho and J. Lee **35** (13), 6578–6582 (2010).

[85] J. Hu, Z. Xiong, G. Wu, P. Chen, K. Murata and K. Sakata **159** (1), 116–119 (2006).

[86] E. Grube, S.R. Jensen, U.G. Nielsen and T.R. Jensen **770**, 1155–1163 (2019).

[87] Z. Xiao, R. Hauge and J. Margrave **31** (1), 59–77 (1991).

[88] X. Wang and L. Andrews, J. Phys. Chem. A **108** (52), 11500–11510 (2004).

[89] M. Kaupp, P.v.R. Schleyer, H. Stoll and H. Preuss, J. Chem. Phys. **94** (2), 1360–1366 (1991).

[90] L. von Szentpály, J. Phys. Chem. A **106** (49), 11945–11949 (2002).

[91] P. Garcia-Fernandez, I.B. Bersuker and J.E. Boggs, J. Phys. Chem. A **111** (41), 10409–10415 (2007).

[92] J. Koput, J. Phys. Chem. A **109** (19), 4410–4414 (2005).

[93] T.J. Tague Jr and L. Andrews, J. Am. Chem. Soc. **115** (25), 12111–12116 (1993).

[94] V. Brites and C. Léonard, J. Phys. Chem. A **116** (38), 9484–9489 (2012).

[95] V. Brites, M. Guitou and C. Léonard, J. Chem. Phys. **134** (5), 054314 (2011).

[96] P.J. Bruna, G.A. Di Labio and J.S. Wright, J. Phys. Chem. **96** (15), 6269–6278 (1992).

[97] T.J. Tague Jr and L. Andrews, J. Phys. Chem. **98** (35), 8611–8616 (1994).

[98] X. Wang and L. Andrews, J. Phys. Chem. A **108** (52), 11511–11520 (2004).

[99] E. Magnusson and S. Petrie, J. Phys. Chem. A **107** (35), 6882–6890 (2003).

[100] M. Kaupp and P.v.R. Schleyer, J. Am. Chem. Soc. **115** (24), 11202–11208 (1993).

[101] D. DeFrees, K. Raghavachari, H. Schlegel, J. Pople and P.v.R. Schleyer, J. Phys. Chem. **91** (7), 1857–1864 (1987).

[102] K. Raghavachari, G.W. Trucks, J.A. Pople and M. Head-Gordon, Chem. Phys. Lett. **157** (6), 479–483 (1989).

[103] J. Koput and K.A. Peterson, J. Phys. Chem. A **106** (41), 9595–9599 (2002).

[104] I.S. Lim and Y.S. Lee, J. Chem. Phys. **126** (10), 104307 (2007).

[105] I.S. Kerkines and A. Mavridis, J. Phys. Chem. A **111** (2), 371–374 (2007).

[106] A. Shayesteh, S.F. Alavi, M. Rahman and E. Gharib-Nezhad, Chem. Phys. Lett. **667**, 345–350 (2017).

[107] J.Q. Sun and K. Ruedenberg, J. Chem. Phys. **99** (7), 5257–5268 (1993).

[108] F. Eckert and H.J. Werner, Theor. Chem. Acc. **100** (1-4), 21–30 (1998).

[109] H.H. Nielsen, Rev. Mod. Phys. **23** (2), 90 (1951).

[110] J.F. Stanton, J. Gauss, L. Cheng, M.E. Harding, D.A. Matthews and P.G. Szalay, CFOUR, Coupled-Cluster techniques for Computational Chemistry, a quantum-chemical program package With contributions from A.A. Auer, R.J. Bartlett, U. Benedikt, C. Berger, D.E. Bernholdt, Y.J. Bomble, O. Christiansen, F. Engel, R. Faber, M. Heckert, O. Heun, M. Hilgenberg, C. Huber, T.-C. Jagau, D. Jonsson, J. Jusélius, T. Kirsch, K. Klein, W.J. Lauderdale, F. Lipparini, T. Metzroth, L.A. Mück, D.P. O'Neill, D.R. Price, E. Prochnow, C. Puzzarini, K. Ruud, F. Schiffmann, W. Schwalbach, C. Simmons, S. Stopkowicz, A. Tajti, J. Vázquez, F. Wang, J.D. Watts and the integral packages MOLECULE (J. Almlöf and P.R. Taylor), PROPS (P.R. Taylor), ABACUS (T. Helgaker, H.J. Aa. Jensen, P. Jørgensen, and J. Olsen), and ECP routines by A. V. Mitin and C. van Wüllen. For the current version, see http://www.cfour.de.

[111] M. Kállay, Z. Rolik, J. Csontos, I. Ladjánszki, L. Szegedy, B. Ladóczki, G. Samu, K. Petrov, M. Farkas, P. Nagy *et al.*, See also: http://www.mrcc.hu (2015).

[112] J.M. Merritt, V.E. Bondybey and M.C. Heaven, Science **324** (5934), 1548–1551 (2009).

[113] P. Li, W. Xie and K. Tang, J. Chem. Phys. **133** (8), 084308 (2010).

[114] W.J. Balfour and R.F. Whitlock, Can. J. Phys. **53** (5), 472–485 (1975).

[115] J.C. Miller, B.S. Ault and L. Andrews, J. Chem. Phys. **67** (6), 2478–2487 (1977).

[116] X. Biquard, O. Sublemontier, J. Berlande, M. Gaveau, J. Mestdagh and J. Visticot, J. Chem. Phys. **103** (3), 957–965 (1995).

[117] J. Francis Jr and S. Webber, J. Chem. Phys. **56** (12), 5879–5886 (1972).

[118] C. Vidal, J. Chem. Phys. **72**, 1864 (1980).

[119] O. Allard, A. Pashov, H. Knöckel and E. Tiemann, Phys. Rev. A **66** (4), 042503 (2002).

[120] O. Allard, C. Samuelis, A. Pashov, H. Knöckel and E. Tiemann, Eur. Phys. J. D **26** (2), 155–164 (2003).

[121] D.D. Yang and F. Wang, Theor. Chem. Acc. **131** (2), 1117 (2012).

[122] K. Patkowski, R. Podeszwa and K. Szalewicz **111** (49), 12822–12838 (2007).

[123] N.S. Mosyagin, A.N. Petrov, A.V. Titov and A.V. Zaitsevskii, Int. J. Quant. Chem. **113** (20), 2277–2281 (2013).

[124] D. Petitprez, B. Lemoine, C. Demuynck, J. Destombes and B. Macke, J. Chem. Phys. **91** (8), 4462–4467 (1989).

[125] K.P. Huber and G. Herzberg, *Molecular Spectra and Molecular Structure: IV. Constants of Diatomic Molecules*, Vol. 4, 1st ed. (Springer Science & Business Media, New York, 2013).

[126] J. Chen and T.C. Steimle, J. Chem. Phys. **128** (14), 144312 (2008).

[127] T. Hrenar, H.J. Werner and G. Rauhut, Phys. Chem. Chem. Phys. **7** (17), 3123–3125 (2005).

[128] B. Bussery-Honvault and R. Moszynski, Mol. Phys. **104** (13-14), 2387–2402 (2006).

[129] D.E. Woon and T.H. Dunning Jr, J. Chem. Phys. **100** (4), 2975–2988 (1994).

[130] K. Tucker, M. Kutner and P. Thaddeus, Astrophys. J. **193**, L115–L119 (1974).

[131] W.M. Jackson, Y. Bao and R.S. Urdahl, J. Geophys. Res-Planet **96** (E2), 17569–17572 (1991).

[132] A. Glassgold, R. Lucas and A. Omont, Astron. Astrophys. **157**, 35–48 (1986).

[133] I. Cherchneff and A.E. Glassgold, Astrophys. J. **419**, L41 (1993).

[134] A. Wootten, E. Bozyan, D. Garrett, R. Loren and R. Snell, Astrophys. J. **239**, 844–854 (1980).

[135] A. Heikkilä, L.E. Johansson and H. Olofsson, Astrophys. J. **344**, 817–847 (1999).

[136] J. Goebel, J. Bregman, D. Cooper, D. Goorvitch, S. Langhoff and F. Witteborn, Astrophys. J. **270**, 190–199 (1983).

[137] X. Gu, Y. Guo, F. Zhang, A.M. Mebel and R.I. Kaiser, Faraday Discuss. **133**, 245–275 (2006).

[138] Y.L. Yung, M. Allen and J.P. Pinto, Astrophys. J. Suppl. S. **55** (3), 465–506 (1984).

[139] D. Toublanc, J. Parisot, J. Brillet, D. Gautier, F. Raulin and C. McKay, Icarus **113** (1), 2–26 (1995).

[140] L.M. Lara, E. Lellouch, J. López-Moreno and R. Rodrigo, J. Geophys. Res-Planet **101** (E10), 23261–23283 (1996).

[141] G.R. Gladstone, M. Allen and Y. Yung, Icarus **119** (1), 1–52 (1996).

[142] M. Allen, Y.L. Yung and G.R. Gladstone, Icarus **100** (2), 527–533 (1992).

[143] J.M. Simmie, Prog. Energy Combust. Sci. **29** (6), 599–634 (2003).

[144] W. Lange and H. Gg. Wagner **79** (2), 165–170 (1975).

[145] A. Renlund, F. Shokoohi, H. Reisler and C. Wittig, Chem. Phys. Lett. **84** (2), 293–298 (1981).

[146] A. Renlund, F. Shokoohi, H. Reisler and C. Wittig, J. Phys. Chem. **86** (21), 4165–4170 (1982).

[147] A. Laufer and R. Lechleider, J. Phys. Chem. **88** (1), 66–68 (1984).

[148] D. Lander, K.G. Unfried, J.W. Stephens, G.P. Glass and R. Curl, J. Phys. Chem. **93** (10), 4109–4116 (1989).

[149] H. Su, J. Yang, Y. Ding, W. Feng and F. Kong, Chem. Phys. Lett. **326** (1-2), 73–79 (2000).

[150] J. Stephens, J. Hall, H. Solka, W. Yan, R. Curl and G. Glass, J. Phys. Chem. **91** (22) (1987).

[151] S. Lee and S.R. Leone, Chem. Phys. Lett. **329** (5-6), 443–449 (2000).

[152] B.J. Opansky, P.W. Seakins, J.O.P. Pedersen and S.R. Leone, J. Phys. Chem. **97** (33), 8583–8589 (1993).

[153] H. Thiesemann and C.A. Taatjes, Chem. Phys. Lett. **270** (5-6), 580–586 (1997).

[154] A.B. Vakhtin, D.E. Heard, I.W. Smith and S.R. Leone, Chem. Phys. Lett. **344** (3-4), 317–324 (2001).

[155] D. Chastaing, P.L. James, I.R. Sims and I.W. Smith, Faraday Discuss. **109**, 165–181 (1998).

[156] A.B. Vakhtin, D.E. Heard, I.W. Smith and S.R. Leone, Chem. Phys. Lett. **348** (1-2), 21–26 (2001).

[157] J.E. Murphy, A.B. Vakhtin and S.R. Leone, Icarus **163** (1), 175–181 (2003).

[158] A. Matsugi, K. Suma and A. Miyoshi, Phys. Chem. Chem. Phys. **13** (9), 4022–4031 (2011).

[159] K. Devriendt and J. Peeters, J. Phys. Chem. A **101** (14), 2546–2551 (1997).

[160] R.M. Elsamra, S. Vranckx and S.A. Carl, J. Phys. Chem. A **109** (45), 10287–10293 (2005).

[161] A.N. Arrowsmith, V. Chikan and S.R. Leone, J. Phys. Chem. A **110** (24), 7521–7526 (2006).

[162] R. Sumathi and M.T. Nguyen, J. Phys. Chem. A **102** (41), 8013–8020 (1998).

[163] L. Li, P. Deng, A. Tian, M. Xu and N.B. Wong, J. Phys. Chem. A **108** (20), 4428–4432 (2004).

[164] J. Gauss, W.J. Lauderdale, J.F. Stanton, J.D. Watts and R.J. Bartlett, Chem. Phys. Lett. **182** (3-4), 207–215 (1991).

[165] J.D. Watts, J. Gauss and R.J. Bartlett, J. Chem. Phys. **98** (11), 8718–8733 (1993).

[166] J. Almlöf and P.R. Taylor, J. Chem. Phys. **86** (7), 4070–4077 (1987).

[167] C. Gonzalez and H.B. Schlegel, J. Phys. Chem. **94** (14), 5523–5527 (1990).

[168] K. Fukui, J. Phys. Chem. **74** (23), 4161–4163 (1970).

[169] R.M. Parrish, L.A. Burns, D.G. Smith, A.C. Simmonett, A.E. DePrince III, E.G. Hohenstein, U. Bozkaya, A.Y. Sokolov, R. Di Remigio, R.M. Richard *et al.*, J. Chem. Theory Comput. **13** (7), 3185–3197 (2017).

[170] F. Weinhold and C.R. Landis, Chem. Educ. Res. Pract. **2** (2), 91–104 (2001).

[171] Y. Shao, Z. Gan, E. Epifanovsky, A.T. Gilbert, M. Wormit, J. Kussmann, A.W. Lange, A. Behn, J. Deng, X. Feng *et al.*, Mol. Phys. **113** (2), 184–215 (2015).

[172] J.M. Martin, Mol. Phys. **112** (5-6), 785–793 (2014).

[173] H.J. Werner, Mol. Phys. **89** (2), 645–661 (1996).

[174] P. Celani and H.J. Werner, J. Chem. Phys. **112** (13), 5546–5557 (2000).

[175] P. Celani and H.J. Werner, J. Chem. Phys. **119** (10), 5044–5057 (2003).

[176] H.J. Werner and P.J. Knowles, J. Chem. Phys. **89** (9), 5803–5814 (1988).

[177] P.J. Knowles and H.J. Werner, Chem. Phys. Lett. **145** (6), 514–522 (1988).

[178] S.R. Langhoff and E.R. Davidson, Int. J. Quant. Chem. **8** (1), 61–72 (1974).

[179] C.P. Moradi, A.M. Morrison, S.J. Klippenstein, C.F. Goldsmith and G.E. Douberly, J. Phys. Chem. A **117** (50), 13626–13635 (2013).

[180] C.F. Goldsmith, L.B. Harding, Y. Georgievskii, J.A. Miller and S.J. Klippenstein, J. Phys. Chem. A **119** (28), 7766–7779 (2015).

[181] C.M. Marian, WIREs: Comput. Mol. Sci. **2** (2), 187–203 (2012).

[182] R. Englman and J. Jortner, Mol. Phys. **18** (2), 145–164 (1970).

[183] B. Ruscic, J. Phys. Chem. A **119** (28), 7810–7837 (2015).

[184] K.S. Kim, S. So and H.F. Schaefer, J. Am. Chem. Soc. **104** (6), 1457–1461 (1982).

[185] J. Peeters, I. Langhans, W. Boullart, M.T. Nguyen and K. Devriendt, J. Phys. Chem. **98** (46), 11988–11996 (1994).

[186] M.W. Markus, P. Roth and T. Just, Int. J. Chem. Kinet. **28** (3), 171–179 (1996).

[187] H. Beuther, D. Semenov, T. Henning and H. Linz, Astrophys. J. Lett. **675** (1), L33 (2008).

[188] A. Saleck, R. Simon, G. Winnewisser and J. Wouterloot, Can. J. Phys. **72** (11-12), 747–754 (1994).

[189] Y.L. Sun, W.J. Huang and S.H. Lee, J. Phys. Chem. Lett. **6** (20), 4117–4122 (2015).

[190] J.H. Kiefer, W.A. Von Drasek and W.A. Von Drasek, Int. J. Chem. Kinet. **22** (7), 747–786 (1990).

[191] W. Boullart, K. Devriendt, R. Borms and J. Peeters, J. Phys. Chem. **100** (3), 998–1007 (1996).

[192] N. Hansen, S.J. Klippenstein, P. Westmoreland, T. Kasper, K. Kohse-Höinghaus, J. Wang and T. Cool, Phys. Chem. Chem. Phys. **10** (3), 366–374 (2008).

[193] A.H. Laufer, J. Phys. Chem. **85** (25), 3828–3831 (1981).

[194] D. Lander, K.G. Unfried, G.P. Glass and R. Curl, J. Phys. Chem. **94** (20), 7759–7763 (1990).

[195] B. Ceursters, H.M.T. Nguyen, M.T. Nguyen, J. Peeters and L. Vereecken, Phys. Chem. Chem. Phys. **3** (15), 3070–3074 (2001).

[196] B.J. Opansky and S.R. Leone, J. Phys. Chem. **100** (51), 19904–19910 (1996).

[197] H.M.T. Nguyen, A.K. Chandra, S.A. Carl and M.T. Nguyen, J. Mol. Struct. **732** (1-3), 219–224 (2005).

[198] M.R. Dash and B. Rajakumar, Phys. Chem. Chem. Phys. **17** (5), 3142–3156 (2015).

[199] S.A. Carl, R.M. Elsamra, R.M. Kulkarni, H.M. Nguyen and J. Peeters, J. Phys. Chem. A **108** (17), 3695–3698 (2004).

[200] B. Nizamov and S.R. Leone, J. Phys. Chem. A **108** (17), 3766–3771 (2004).

[201] H.M.T. Nguyen, S.A. Carl, J. Peeters and M.T. Nguyen, Phys. Chem. Chem. Phys. **6** (16), 4111–4117 (2004).

[202] S. Berski and Z. Latajka, Chem. Phys. Lett. **426** (4-6), 273–279 (2006).

[203] M. Koshi, N. Nishida and H. Matsui, J. Phys. Chem. **96** (14), 5875–5880 (1992).

[204] G. Knizia, T.B. Adler and H.J. Werner, J. Chem. Phys. **130** (5), 054104 (2009).

[205] N. Sylvetsky, M.K. Kesharwani and J.M. Martin, J. Chem. Phys. **147** (13), 134106 (2017).

[206] T.H. Dunning Jr, K.A. Peterson and A.K. Wilson, J. Chem. Phys. **114** (21), 9244–9253 (2001).

[207] Recontracted Correlation-consistent Basis Functions `http://slater.chemie.uni-mainz.de/cfour/index.php?n=\Main.RecontractedCorrelation-consistentBasisFunctions`, Accessed: 2020-02-22.

[208] C.E. Moore, *Atomic Energy Levels as Derived from the Analyses of Optical Spectra*, Vol. 1 (US Department of Commerce, National Bureau of Standards, Washington D.C., 1949).

[209] B. Ruscic and D.H. Bross, Active Thermochemical Tables (ATcT) values based on ver. 1.122e of the Thermochemical Network, Argonne National Laboratory (2019); available at ATcT.anl.gov 2019. <https://atct.anl.gov/>.

[210] J. Stephens, J. Hall, H. Solka, W.B. Yan, R. Curl and G. Glass, J. Mol. Struct. **19** (6), 41–60 (1988).

[211] H. Van Look and J. Peeters, J. Phys. Chem. **99** (44), 16284–16289 (1995).

[212] R.J. Hoobler and S.R. Leone, J. Geophys. Res-Planet **102** (E12), 28717–28723 (1997).

[213] F. Zhang and T.S. Dibble, Phys. Chem. Chem. Phys. **13** (40), 17969–17977 (2011).

[214] B. Sirjean, E. Dames, H. Wang and W. Tsang, J. Phys. Chem. A **116** (1), 319–332 (2012).

[215] Y. Sha and T.S. Dibble, Chem. Phys. Lett. **646**, 153–157 (2016).

[216] J. Peeters, B. Ceursters, H.M.T. Nguyen and M.T. Nguyen, J. Chem. Phys. **116** (9), 3700–3709 (2002).

[217] B. Ceursters, H.M.T. Nguyen, J. Peeters and M.T. Nguyen, Chem. Phys. Lett. **329** (5-6), 412–420 (2000).

[218] Y.h. Ding, X. Zhang, Z.s. Li, X.r. Huang and C.c. Sun, J. Phys. Chem. A **105** (35), 8206–8215 (2001).

[219] S.A. Carl, H. Minh Thi Nguyen, R.M. Elsamra, M. Tho Nguyen and J. Peeters, J. Chem. Phys. **122** (11), 114307 (2005).

[220] A. Miyoshi, BEx1D software, rev. 2012.03.12 See http://akrmys.com/bex1d/. .

[221] X. Zhang, Y.h. Ding, Z.s. Li, X.r. Huang and C.c. Sun, J. Phys. Chem. A **104** (36), 8375–8381 (2000).

[222] Y. Kurosaki and T. Takayanagi, J. Chem. Phys. **113** (10), 4060–4072 (2000).

[223] L.P. Ju, T.X. Xie, X. Zhang and K.L. Han, Chem. Phys. Lett. **409** (4-6), 249–254 (2005).

[224] L. Ju and D. Wang, Int. J. Chem. Kinet. **42** (5), 289–298 (2010).

[225] B. Temelso, C.D. Sherrill, R.C. Merkle and R.A. Freitas, J. Phys. Chem. A **110** (38), 11160–11173 (2006).

[226] L. Chen, K. Shao, J. Chen, M. Yang and D.H. Zhang, J. Chem. Phys. **144** (19), 194309 (2016).

[227] J. Zheng, Y. Zhao and D.G. Truhlar, J. Phys. Chem. A **111** (21), 4632–4642 (2007).

[228] S. Farhat, C. Morter and G.P. Glass, J. Phys. Chem. **97** (49), 12789–12792 (1993).

[229] T. Kovács, M.A. Blitz and P.W. Seakins, J. Phys. Chem. A **114** (14), 4735–4741 (2010).

[230] B.J. Opansky and S.R. Leone, J. Phys. Chem. **100** (12), 4888–4892 (1996).

[231] J.P. Senosiain, S.J. Klippenstein and J.A. Miller, J. Phys. Chem. A **109** (27), 6045–6055 (2005).